INFORMATION TO USERS

This manuscript has been reproduced from the microfilm master. UMI films the text directly from the original or copy submitted. Thus, some thesis and dissertation copies are in typewriter face, while others may be from any type of computer printer.

The quality of this reproduction is dependent upon the quality of the copy submitted. Broken or indistinct print, colored or poor quality illustrations and photographs, print bleedthrough, substandard margins, and improper alignment can adversely affect reproduction.

In the unlikely event that the author did not send UMI a complete manuscript and there are missing pages, these will be noted. Also, if unauthorized copyright material had to be removed, a note will indicate the deletion.

Oversize materials (e.g., maps, drawings, charts) are reproduced by sectioning the original, beginning at the upper left-hand corner and continuing from left to right in equal sections with small overlaps. Each original is also photographed in one exposure and is included in reduced form at the back of the book.

Photographs included in the original manuscript have been reproduced xerographically in this copy. Higher quality 6" x 9" black and white photographic prints are available for any photographs or illustrations appearing in this copy for an additional charge. Contact UMI directly to order.

U·M·I

University Microfilms International
A Bell & Howell Information Company
300 North Zeeb Road, Ann Arbor, MI 48106-1346 USA
313/761-4700 800/521-0600

Order Number 9304645

Interface structure in metal/carbon multilayers

Chan, Yuet-Loy, Ph.D.

City University of New York, 1992

300 N. Zeeb Rd.
Ann Arbor, MI 48106

INTERFACE STRUCTURE
IN
METAL/CARBON MULTILAYERS

by

Yuet-Loy Chan

A dissertation Submitted to the Graduate Faculty in Physics in Partial Fulfillment of the requirements for the degree of Doctor of Philosophy, The City University of New York.

1992

This manuscript has been read and accepted for the Graduate Faculty in Physics in satisfaction of the dissertation requirement for the degree of Doctor of Philosophy.

5/22/92
Date

Prof. Pedro A. Montano
Chair Of Examining Committee

5/20/92
Date

Prof. Joseph B. Krieger
Executive Officer

Prof. Lesser Peter

Prof. Frederick W. Smith

Prof. Homma Hitoshi

Dr. Kegang Huang
Supervisory Committee

The City University of New York

ABSTRACT

INTERFACE STRUCTURE IN METAL/CARBON MULTILAYERS

W/C Multilayers

We have studied the structure of W/C multilayers using a diverse numbers of techniques. The samples were prepared by plasma rf sputtering techniques and the modulation and lattice structure were determined by x-ray diffraction and electron microscopy. Electron energy loss spectroscopy was used to obtain a non destructive composition depth profile of the material by changing the impinging electron energy. The measurements were carried out under UHV conditions. All the major electron energy loss peaks of the multilayers were identified. The measurements were performed as a function of temperature, between 293K and 973K. Auger spectroscopy and Rutherford back scattering measurements were also performed in all the samples. We found EELS to be very sensitive to the structural modifications in the samples. We observed the formation of a carbide at the W/C interface. The structure of the interface was identified using surface electron energy loss fine structure and x-ray scattering. We investigated the stability of the multilayers in an oxidizing environment and at high temperatures.

Single crystal TiC[111]

The electron energy loss (EEL) spectra of a TiC [111] single crystal were measured over a wide range of electron primary energies. The electron energy losses below 16 eV were analyzed using the theoretical band calculations of Price and Cooper.[1] The volume and surface plasma excitations were identified from their electron primary energy dependence. Energy losses due to core electrons autoionization effects were identified above 35 eV. We observed a difference in the electronic structure of the surface vs the bulk of TiC. The temperature dependence of EEL spectra was studied between 300 to 1250 K. The reaction of the TiC surface with ethylene and oxygen was also investigated. The ethylene bonding to the TiC surface was found to be very weak. There is evidence of the formation of surface defects on the TiC [111] surface at high temperatures.

Ti/C Multilayers

We have performed an experimental investigation of the structure of Ti/C multilayers. The samples were prepared by conventional techniques and the lattice structure was characterized by x-ray diffraction. The modulation wavelengths of the samples were from 27 to 38 Å , and the total thicknesses between 1350 to 1900 Å. The measurements were analyzed using Fresnel's laws of optics and assuming Gaussian roughness at the interfaces. Rutherford Backscattering (RBS) was employed to characterize the chemical composition of the samples. It was observed that the Ti/C interface is isolated by a thin titanium oxide layer. The electron density of carbon shows a graphitic character. We have found that the interface has a

graphite like atomic arrangement rather than a carbide-like arrangement.

Single crystal α-SiC-6H [0001]

We report a study of the surface composition of α-SiC between room temperature and 1273 K. Electron energy loss spectroscopy was employed to detect the changes in surface structure of silicon carbide as a function of temperature. The electron energy loss spectra were analyzed using the bulk and surface dielectric functions of α-SiC. Auger spectroscopy, RBS, elastic resonance scattering of α-particles from ^{16}O, and surface reflected electron energy loss fine structure were employed to characterize the sample. We observed the formation at rather low temperatures (around 570 K) of a graphitic surface layer on the silicon carbide. We attribute the formation of this layer to carbon migration to the surface. This migration will create carbon vacancies in the bulk. We also found evidence of internal oxidation of the silicon carbide at temperatures of 823 K and above.

Si/C Multilayers

We have studied using angular resolved electron energy loss spectroscopy the structure of silicon/carbon multilayers. The total thickness of the multilayers was between 900 to about 2000 Å. The modulation wavelength of the samples was 14 to 62 Å, as determined from x-ray diffraction. The major electron energy loss peaks were identified. We inferred from the electron energy loss measurements that a carbidic interface is present at the silicon-carbon interface. The

electron energy loss measurements of the multilayers were also carried out at high temperatures, up to 873 K.

We have also studied using x-ray reflectivity, the structure of silicon/carbon multilayers. The measurements were analyzed using Fresnel's laws of optics and assuming Gaussian roughness at the interfaces. We found from the analysis of the data that a carbidic interface forms at the silicon-carbon interface for samples heated in vacuum to 873 K. These results are in very good agreement with electron energy loss measurements.

ACKNOWLEDGMENT

I would like to acknowledge the guidance and encouragement given to me by my thesis adviser, Prof. Pedro A. Montano, a man whose mind always twinkles with new and interesting ideas.

I am pleased to express my gratitude to the Supervisory Committee, in particular, to Prof. Peter Lesser and to Prof. Hitoshi Homma for their helpful and enthusiastic discussions. I wish to thank Professor Frederick W. Smith of City College, CUNY, and Dr. Kegang Huang of ANL for their careful reading of this manuscript and their helpful advice.

I thank all my fellow graduate students for their assistance throughout the study. I thank Dr. Celeste Reyls for her careful reading and thoughtful suggestions. I would also like to thank the AFOSR and the Research Foundation of City University of New York for providing me with full financial support in this work; and the Brooklyn College Computer Center for allowing me to use their facilities.

Finally, I am grateful to my parents and to my wife, Ching-Lin Liu, for their help and confidence in me, especially during the trying moments of graduate student life.

TABLE OF CONTENTS

Page

APPROVAL OF THE EXAMINATION COMMITTEE------------------ ii

ABSTRACT--- iii

ACKNOWLEDGMENT-- vii

TABLE OF CONTENTS-- viii

LIST OF TABLES--- xii

LIST OF FIGURES-- xiv

CHAPTER

1. INTRODUCTION 1

2. THEORETICAL BACKGROUND

2.1 Electron Spectroscopy

2.1. Introduction-- 6

2.1.2 Auger Electron Spectroscopy

2.1.2.1 Introduction -------------------------- 9

2.1.2.2 Example ----------------------------- 15

2.1.3 Electron Energy Loss Spectroscopy

2.1.3.1 Description of EELS ---------------- 16

2.1.3.2 Excitation of Core, Valence, and Collective Electrons and Surface Vibrations------------------------------ 17

2.1.3.3 Inelastic Scattering, Inelastic Scattering Cross Section of electrons---- 20

2.1.3.4 The Dielectric Function and Free

Electron, Bound Electron and
Interband Excitation ---------------- 25
2.1.4 Surface Electron Energy Loss Fine Structure Spectroscopy
2.1.4.1 Introduction -------------------------- 35
2.1.4.2 EXAFS and SEELFS------------------- 37
2.2 Rutherford Back Scattering and α Particles on ^{16}O Resonance Elastic Scattering
2.2.1 Introduction------------------------------------- 41
2.2.2 Kinematic Factor of Elastic Collision--------- 42
2.2.3 Scattering Cross Section ---------------------- 43
2.2.4 Energy Loss ------------------------------------- 43
2.2.5 Example --- 44
2.2.6 ^{16}O resonance Elastic Scattering------------ 45
2.3 X-ray Reflectivity
2.3.1 Introduction------------------------------------- 45
2.3.2 The Refractive Index of Matter
for X-rays of Wavelength λ--------------------- 45
2.3.3 Reflectivity and Fresnel Formula------------ 47
3. EXPERIMENTAL DESCRIPTION AND SAMPLES PREPARATION
3.1 Electron Spectroscopy Apparatus---------------------- 51
3.1.1 Cylindrical Mirror Analyzer Equipment--------- 51
3.1.2 Angle Resolved Spectroscopy Equipment------ 54

3.2 RBS Equipment-- 56
3.3 X-ray Reflectivity Equipment---------------------------- 57
3.4 Sample Preparation-------------------------------------- 59
3.4.1 W/C, Ti/C Multilayers------------------------- 59
3.4.2 Si/C Multilayers------------------------------ 60

4. INTERFACE STRUCTURE AND STABILITY IN W/C MULTILAYERS
4.1 Introduction-- 61
4.2 Experimental-- 62
4.3 Results and Discussion---------------------------------- 65

5. SINGLE CRYSTAL TIC[111]
5.1 Introduction-- 107
5.2 Experimental-- 108
5.3 Results and Discussion---------------------------------- 112

6. INTERFACE STRUCTURE AND STABILITY IN Ti/C MULTILAYERS
6.1 Previous Work--- 137
6.2 Introduction-- 137
6.3 Experimental-- 138
6.4 Results and Discussion---------------------------------- 139

7. SINGLE CRYSTAL of α-SiC-6H [0001]
7.1 Introduction-- 153
7.2 Experimental-- 155

7.3 Results and Discussion---------------------------------- 156

8. INTERFACE STRUCTURE AND STABILITY IN Si/C MULTILAYERS

8.1 Introduction-- 175

8.2 Experimental-- 176

8.3 Results and Discussion---------------------------------- 177

9. CONCLUSION

9.1 W/C Multilayers-- 211

9.2 Single Crystal TiC[111]---------------------------------- 211

9.3 Ti/C Multilayers-- 212

9.4 Single Crystal α-SiC-6H [0001--------------------------- 212

9.5 Si/C Multilayers-- 213

APPENDIX A. Dynamic Structure and Dielectric Function -------- 215

APPENDIX B. Energy-Band Structure of a Single two Dimensional Layer of Graphite--- 220

Bibliography -- 221

LIST OF TABLES

Table		Page
4.1	W and C composition of the multilayers.	65
4.2	Electron energy losses of W/C=6Å/5Å.	74
4.3	Electron energy losses of W/C=6Å/5Å as a function of temperature (E_p=350 eV)	82
4.4	Comparison of near-neighbor distances for the carbon atoms in the W_2C and the experimental measurements (from the solid line in figure 4.13).	89
4.5	Parameters obtained from the fitting of the experimental data for the W/C=6Å/5Å multilayer.	94
4.6	Parameters obtained from the fitting of the experimental data for the W/C=7Å/7Å multilayer before heating.	97
4.7	Parameters obtained from the fitting of the experimental data for the W/C=7Å/7Å multilayer after heating.	99
4.8	Parameters obtained from the fitting of the experimental data for the W/C=10Å/20Å multilayer.	103
4.9	Parameters obtained from the fitting of the experimental data for the W/C=10Å/13Å multilayer.	105
5.1	Electron energy losses of TiC (111).	114
5.2	Electron energy loss peaks in Figure 5.3 and the corresponding transitions according to Figure 5.4.	117
5.3	Electron energy losses (in eV) of clean Ti(100) for Ep=150 eV.	126
6.1	Ti and C composition of the multilayers.	138
6.2	Parameters obtained from the fitting of the experimental data for the Ti/C (26Å/12Å) multilayer.	146
6.3	Parameters obtained from the fitting of the experimental data for the Ti/C (15Å/12Å) multilayer	151

7.1 Comparison of near-neighbor distances for the carbon atoms in the α- SiC-6H and the experimental measurements extracted from Figure 7.4a. 159

7.2 Comparison of near-neighbor distances for the carbon atoms in the graphite and the experimental measurements extracted from Figure 7.4b. 159

8.1 Si and C composition of the multilayers 177

8.2 Parameters obtained from the fitting of the experimental data for the Si/C (10Å/19Å) multilayer. 199

8.3 Parameters obtained from the fitting of the experimental data for the Si/C (25Å/25Å) multilayer after reaction at 873 K. 204

8.4 Parameters obtained from the fitting of the experimental data for the Si/C (29Å/14Å) multilayer. 209

LIST OF FIGURES

Figure		Page
2.1	Universal curve for the electrons mean free path in solids as a function of their energy	7
2.2	Schematic energy distribution of backscattered electrons obtained with an incident beam energy of E_p (eV).	8
2.3	Auger process. (a) X-ray photon or electron incident upon an atom. (b) Ionization of inner shell electron by an impact of electron. (c, d) Processes of de-excitation, (c) emission of x-ray radiation, (e) emission of an Auger electron.	10
2.4	Relative probabilities of relaxation by emission of an Auger electron and by emission of an X-ray photon following creation of an inner vacancy hole in the K shell.	11
2.5	Auger effect in the condensed matter.	12
2.6	Auger spectra of graphite in energy range 0 to 440 eV.	14
2.7	Auger spectra of SiC in the energy range 0 to 440 eV. . .	14
2.8	Auger spectra of TiC in the energy range 0 to 500eV. . . .	15
2.9	(a) Auger peak in the energy distribution function N(E). (b) The first derivative of N(E) for identification of Auger peaks.	16
2.10	A typical EELS in the second derivative mode.	18
2.11	Primary electrons of momentum $\hbar \cdot \vec{k_o}$, after being scattered at an angle θ, with momentum change to $\hbar \cdot \vec{k}$, and with the momentum transfer $\hbar \cdot \vec{q}$ being equal to $\vec{k_o} - \vec{k}$.	21
2.12	A typical diagram of two step [I-E, E-I] scattering process	27

2.13 Maximum and minimum momentum transfer q at three different primary energies. At the small energy loss region, long wavelength approximation is possible. 28

2.14 The dielectric function of ε_1, ε_2 and the loss function of a free electron gas at $\hbar\omega_p$ =15 eV. 31

2.15 The influence of bound electrons in the dielectric function. (a) If the eigenfrequency of the bound electrons ω_n, lies below the plasmon frequency of the free electrons ω_p, the position of $\varepsilon_1(\omega)=0$ will shift to higher values. (c) The reverse takes place if $\omega_n > \omega_p$ . . . 33

2.16 Schematic representation of the interferences of two different incoming and outgoing waves. The outgoing photoelectron (solid line) originated from the central atom (circle) propagate to the neighboring atoms (dashed lines circle). The back scattered waves (dashed lines) interfere with the outgoing waves and give rise to the EXAFS. 36

2.17 Typical X-ray absorption spectrum μx vs E 37

2.18 Interaction of fast electrons with an atom. Many different transitions may happen after an atom is ionized by an energetic incident electron. Continuous white radiation may be produced while the incident electron is decelerated in the field of the nucleus. 39

2.19 Schematic diagram of a typical backscattering experiment in use today. 41

2.20 A typical backscattering spectrum of an ion at energy E_o. M represents the heaviest element, substrate is the lightest. The heavy mass (M) gives a signal at high energies side, then next m. The high energy edge of each peaks is equal to KE_O 44

2.21 A schematic representation of the reflectivity at small angle. 47

3.1 A schematic block diagram of experimental set up for the surface science research. 52

3.2 A typical Cylinder Mirror Analyzer. 53

3.3 Typical experimental arrangement using the electron monochromator (EM50) and VSW hemispherical analyzer. 55

3.4 A schematic diagram of the Concentric Hemispherical Analyzer(CHA). 56

3.5 A typical schematic diagram of a Backscattering spectrometer system. 57

3.6 A typical x-ray reflectivity experimental set- up. 58

4.1 RBS spectra for a W/C multilayer (W/C= 7 Å/7 Å), α-particles at energies of 3.065, 3.05, 3.045, 3.04 MeV. . . 66

4.2 RBS spectrum for a W/C multilayer (W/C= 7Å/7 Å) using protons at 3.0 MeV. 67

4.3 Optical dielectric loss function for graphite and tungsten. 69

4.4 (a) Combined optical dielectric loss function from graphite and tungsten with W/C=6Å/5Å and N=4; (b) combined optical dielectric loss function from graphite and tungsten with W/C=6Å/2Å and N=4. 72

4.5 EEL spectra at room temperature before heating for a W/C multilayer (W/C= 6 Å/5 Å). The spectra were taken for primary energies from 100 to 400 eV. 75

4.6 EEL spectra at room temperature before heating for a W/C multilayer (W/C= 6Å/5 Å). The spectra were taken for primary energies from 500 to 1800 eV. 76

4.7 EEL spectra before heating for a multilayer with W/C= 7Å/7 Å. 78

4.8 EEL spectra as a function of temperature for a 200 eV electron primary energy (W/C= 6Å/5 Å). 80

4.9 EEL spectra as a function of temperature for a 350 eV electron primary energy (W/C= 6 Å/ 5 Å). 81

4.10 Auger spectra around the carbon signal for a W/C multilayer (W/C= 6 Å/5 Å): (a) before heating, (b) after heating and (c) after reaction with oxygen. 83

4.11 EEL spectra for W/C=6Å/5Å, 200 eV electron primary energy. 85

4.12 EEL spectra for W/C=6Å/5Å, 350 eV electron primary energy. 86

4.13 (a) SEELFS spectrum taken at C K-edge; (b) Magnitude of the Fourier transforms of the Carbon K-edge SEELFS spectrum, before heating (dot line) and after reaction (solid line). 88

4.14 (a-d) X-ray specular reflectivity of multilayer of W/C= (6Å/5Å) with 200 periods. The upper curve is the theoretical calculation and is shifted by 1 from the Y axis for illustration. The values of the fitting parameters are shown in Table4.5 and Figure 4.15. The large modulation in this fitting curve is produced by assuming that there is an extra layer which is just embedded between the surface of the substrate and the multilayer with thickness of 53 Å, electron density 2.8x(6.022x10^{23}e/cm^3). Figures 4.14b-4.14d are the expansions of Figure 4.14a. 91

4.15 A comparison of electron density between the known bulk state and the experimental state. The experimental electron densities of W, W_2C and C are from the parameters used to obtain fit in Figure 4.14a. The electron densities of W, W_2C and C are about 10% , 7% and14% less than the known bulk state respectively 94

4.16 X-ray specular reflectivity of multilayer of W/C=7Å/7Å with150 periods. The thin line curve is the theoretical calculation and the coarse line is the experimental data. The values of the fitting parameters are given in Table 4.6 and Figure 4.17. The two peaks at the first Bragg peak position were made up by two different thickness bilayer lattices. In Figure 4.16, we assume that the thickness (Λ) of the bilayer from peak (a) is about 13.18Å and with 23 periods, the thickness from peak (b) is 3.5% least than peak (a) but with 127 periods. . . . 96

4.17 A comparison of electron density between the known bulk state and the experimental state. The experimental electron densities of W, W_2C and C are from the parameters used to obtain fit in Figure 4.16. The electron densities of W, W_2C and C are about 1% , 2% and 8% less than the known bulk state respectively. 97

4.18 X-ray specular reflectivity of multilayer of W/C=7Å/7Å with150 periods after heating. The thin line curve is the theoretical calculation and the coarse line is the experimental data. The values of the fitting parameters are shown in Table4.7 and Figure 4.19. In the theoretical calculation, we used the same model as in Figure 4.16 but the thickness of the bilayer of peak (b) is about 6.5% least than peak (a). 98

4.19 A comparison of electron density between the known bulk state and the experimental state. The experimental electron densities of W, W_2C and C are from the parameters used to obtain fit in Figure 4.18. The electron densities of W, W_2C and C are about 1% , 1% and 2% less than the known bulk state respectively. 99

4.20 X-ray specular reflectivity of multilayer of W/C=10Å/20Å with 65 periods. The thin line curve is the theoretical calculation and the circle line is the experimental data. The values of the fitting parameters are shown in Table 4.8 and Figure 4.21. 102

4.21 A comparison of electron density between the known bulk state and the experimental state. The experimental electron densities of W, W_2C and C are from the parameters used to obtain fit in Figure 4.20. The electron densities of W, W_2C and C are about 16% , 15% and 17% less than the known bulk state respectively. . . 103

4.22 X-ray specular reflectivity of multilayer of W/C=10Å/13Å with 150 periods. The top one (a) is the experimental measurement and the lower one (b) is the theoretical calculation. The values of the simulation parameters are shown in Table4.9 and Figure 4.23. 104

4.23 A Gaussian distribution of the occupation number versus bilayer thickness. The deviation σ used in this model is 1.2 Å. 105

4.24 An illustration of electron density for the known bulk state and the experimental state. The experimental electron densities of W, W_2C and C are from the parameters used to obtain the simulation in Figure 4.22b. The electron densities of W, W_2C and C are about 19% , 15% and 17% less than the known bulk state respectively. 106

5.1 Auger spectra for (a) clean TiC (b) with Oxygen coverage. 110

5.2 EELS spectra for N(E) and $-dN^2/d^2E$ mode as a function of primary electron energy (100 to 350 eV) at 300 ^oK. 111

5.3 EELS spectra at 300 ^oK as a function of primary electron energy (100 to 450 eV). 113

5.4 Partial density of states of TiC (ref. 1); p_1-- p_5, d_1-- d_9 correspond to C-2p and Ti-3d states respectively. 116

5.5 The dot line is the loss function from the optical measurement by Lye & Logothetis. The solid line is the EEL spectrum measured at Ep=200 eV. (the solid line was shifted by 0.5 eV) 119

5.6 Peak intensity vs energy ; (a) intensity of peak d vs primary energies; (b) the ratio of peak f with respect to peak e 120

5.7 Ionization cross section vs U_{nl} for M shell electrons. . . 125

5.8 EELS spectra for Ep =150 eV as a function of temperature (128 ^oK to 1073 ^oK). 128

5.9 EELS spectra for Ep =350 eV as a function of temperature (128 ^oK to 1073 ^oK). 129

5.10 Lower range EELS spectra for Ep =200 eV as a function of temperature (300 ^oK to 1250 ^oK) with oxygen coverage. 130

5.11 Higher range EELS spectra for Ep =200 eV as a function of temperature (300 ^oK to 1250 ^oK) with oxygen coverage. 131

5.12 The reflectivity measurement vs temperature; (a) for Ep=150 eV; (b) for Ep=1000 eV. 133

5.13 EELS spectra at 136 ^ok after Ethylene adsorption as a function of primary electron energy (100 to 450 eV). . 135

5.14 EELS spectra for oxygen coverage on TiC (111) at 300^oK as a function of primary electron energy

(100 to 450 eV). 136

6.1 RBS spectrum for alpha particles at 2.2MeV. 141

6.2 A typical RBS spectrum for alpha particles at 3.05 MeV. 142

6.3 X-ray specular reflectivity of 50 bilayers of [Ti(26Å)/C-(12Å)]. The bold solid line is the theoretical fit to the data. 145

6.4 A comparison of electron density between the known bulk state and the experimental state. The experimental electron densities of Ti and C are from the parameters used to obtain fit in Figure 6.3. The electron densities of Ti and C have changed about 0% and -20% with respect to the known bulk state value. 147

6.5 Schematic diagram of the [Ti(26Å)/C(12 Å)] multilayer near the substrate with interface roughness values. 148

6.6 X-ray specular reflectivity of 50 bilayers of [Ti(15Å)/C-(12Å)]. The bold solid line is the theoretical fit to the data. 150

6.7 A comparison of electron density between the known bulk state and the experimental state. The experimental electron densities of SiO_2, Ti and C are from the parameters used to obtain fit in Figure 6.6. The electron densities of SiO_2, Ti and C have changed about +5% , -2% and -2% with respect to the known bulk state. . . . 151

6.8 Schematic diagram of the [Ti(15Å)/C(12Å)] multilayer near the substrate with the values of the interface roughness. 152

7.1 Angular resolved AS: (a) glancing angle of incidence. (b) angle of incidence 70^0. 157

7.2 Top one is a SEELFS spectrum at the Si L-edge before heating and the bottom one after heating. 160

7.3 Magnitude of the Fourier transform of the SEELFS spectrum of Si: (a) before heating;(b) after heating. 161

7.4 Magnitude of the Fourier transform of the SEELFS spectrum of C: (a) before heating; (b) after heating 162

7.5 Energy loss functions and second derivatives for the surface and bulk of α-SiC 164

7.6 EEL spectra of α-SiC taken at room temperature as a function of electron primary energies. The insert is the expanded spectra of the most important energy loss region 166

7.7 EEL spectra plotted as a function of temperature for Ep=150 eV. 167

7.8 EEL spectra plotted as a function of temperature for Ep=500 eV. 168

7.9 EEL spectra plotted at room temperature, after heating and after reaction with oxygen for Ep=150 eV. 170

7.10 EEL spectra plotted at room temperature, after heating a and after reaction with oxygen for Ep=500 eV. 171

7.11 Angular resolved EEL spectra taken at room temperature for an angle of incidence of 35^0 and angles of reflection of a) 55^0, b)70^0, c) 85^0. All the angles are measured with respect to the normal to crystal face. 172

7.12 This AES spectrum was taken at glancing angle after sputtering($\theta_{in}=72^0$, $\theta_{out}=35^0$). This figure clearly shows a strong carbon peak but no oxygen and silicon. 174

7.13 This is an EELS spectrum measured after sputtering at Ep=200eV. The incident angle is about 35^0, and the detecting angle is about 72^0 with respect to the normal direction. 174

8.1(a) Angular resolved EEL spectrum as a function of electron primary energy for Si(25Å)/C(25Å) at Ep=450-1550eV, the angle of incidence is equal to the angle of reflection=40^0. 178

8.1(b) Angular resolved EEL spectrum as a function of electron primary energy for Si(25Å)/C(25Å) at Ep=1750 - 2600eV, the angle of incidence is equal to the angle of reflection=40^0. 179

8.2(a) Angular resolved EEL spectrum (second derivative) as a function of electron primary energy for Si(25Å)/ C(25Å) at Ep=450 - 1550eV, the angle of incidence is

equal to the angle of reflection $=40^0$. 180

8.2(b) Angular resolved EEL spectrum (second derivative) as a function of electron primary energy for Si(25Å)/C(25Å) at Ep=1750 - 2600eV, the angle of incidence is equal to the angle of reflection $=40^0$ 181

8.3 Angular resolved AS spectrum as a function of electron primary energy for Si(25Å)/C(25Å), the angle of incidence is equal to the angle of reflection$=30^0$, 40^0, 50^0, 60^0, and 70^0 182

8.4(a) Angular resolved EEL spectrum as a function of the angle of reflection for Si(25Å)/C(25Å) at incidence angle 30^0. 184

8.4(b) Angular resolved EEL spectrum as a function of the angle of reflection for Si(25Å)/C(25Å) at incidence angle 40^0. 185

8.4(c) Angular resolved EEL spectrum as a function of the angle of reflection for Si(25Å)/C(25Å) at incidence angle 50^0. 186

8.4(d) Angular resolved EEL spectrum as a function of the angle of reflection for Si(25Å)/C(25Å) at incidence angle 60^0. 187

8.4(e) Angular resolved EEL spectrum as a function of the angle of reflection for Si(25Å)/C(25Å) at incidence angle 70^0. 188

8.5(a) EEL spectrum as a function of temperature for Si(25Å)/C(25Å) multilayer, at Ep=150 eV. 189

8.5(b) EEL spectrum as a function of temperature for Si(25Å)/C(25Å) multilayer, at Ep=350 eV. 190

8.5(c) EEL spectrum as a function of temperature for Si(25Å)/C(25Å) multilayer, at Ep=600 eV. 191

8.6(a) Angular resolved EEL spectrum as a function of electron primary energy for Si(29Å)/C(14Å) at Ep=450-1550eV, the angle of incidence is equal to the angle of reflection$=40^0$. 192

8.6(b) Angular resolved EEL spectrum as a function of electron primary energy for Si(29Å)/C(14Å) at Ep=1750-2650eV,

the angle of incidence is equal to the angle of reflection=40^0. 193

8.7 Angular resolved EEL spectrum as a function of low electron primary energies for Si(29Å)/C(14Å), the angle of incidence is equal to the angle of reflection= 45° 195

8.8 X-ray specular reflectivity for the Si(10Å)/C(19 Å). The full line is the theoretical fit to the data. 197

8.9 A comparison of electron density between the known bulk state and the experimental state. The experimental electron densities of Si, C and topmost layer are from the parameters used to obtain fit in Figure 8.8. The electron densities of Si, and C are about 3%, and 15% less than the known bulk state respectively. 200

8.10 Schematic diagram of the Si(10Å)/C(19Å) multilayer near the substrate with interface roughness values. . . . 201

8.11 X-ray specular reflectivity of 30 bilayers of the [Si(12Å/SiC(10Å)/C(13Å)/SiC(10Å)] on α-Al_2O_3. The solid line is the theoretical fit to the data. 203

8.12 A comparison of electron density between the known bulk state and the experimental state. The experimental electron densities of Si, SiC and C are from the parameters used to obtain fit in Figure 8.11. The electron densities of Si, SiC and C are about 2%, 3% and 15% less than the known bulk state respectively. 205

8.13 Schematic diagram of [Si(12Å/SiC(10Å)/C(13Å)/SiC (10Å)] on α-Al_2O_3 near the substrate with the values of the interface roughness. 206

8.14 Low angle X-ray specular reflectivity of 30 bilayers of the [Si(29Å)/C(14Å)] on float glass. The solid line is the theoretical fit to the data 208

8.15 A comparison of electron density between the known bulk state and the experimental state. The experimental electron densities of Si, and C are from the parameters used to obtain fit in Figure 8.14. The electron densities

of Si, and C are about 2%, and 9% less than the known bulk state respectively. 209

8.16 Schematic diagram of the [Si(29Å)/C(14Å)] multilayer near the substrate with the values of the interface roughness. 210

CHAPTER 1
INTRODUCTION

Multilayers (or superlattices) are artificial lattices that consist of alternating layers of two different types of elements. The thickness of the individual layer is between a few angstroms and a few hundred angstroms. Recent progress in ultra thin layer deposition techniques has made possible the deposition of elements with a regularity of a few angstroms. Supported by these developed deposition techniques, it is also possible to deposit metallic multilayers onto shaped, ultra smooth substrates leading to optics with focusing properties.

Multilayer structures have shown successful promise for the production of xuv and x-ray optical elements. The multilayer coatings can enhance the xuv reflectivity of mirrors over a wide range of angles and at the same time provide spectral selectivity. These coatings consist of different refractive indices in each layer, and are similar to the multilayer mirrors used at longer wavelengths. The multilayers can be used as diffraction grating in soft-x-ray spectrometer for space astronomy, or for microscopy.[2-4] Multilayers can also be used as bandpass reflector that scatters a range of wavelength into a defined solid angle with high efficiency. This bandpass reflector has been applied extensively in producing focused beams of x-rays for x-ray lithography[5] or other techniques where a high flux of x-rays in a range of wavelengths is required in a small area. Thus the development of this new type of optics has important applications in a wide variety of fields, and a full understanding of the micro mechanism is necessary.

In the new lattices, as in the case where the layer thickness

becomes comparable with atomic dimensions, the properties of multilayers take on characteristics representative of new compound materials. These characteristics are not obtained by simply considering the sum of the component materials. The periodic variation of the layers gives rise to a periodic alternation in the electronic potential. One can expect that at the interface, the Fermi level of the element which looses electrons will shift to lower energies, and the Fermi level of the element which takes up the electrons shifts to higher energies, within the respective valence bands. This charge redistribution in the lattices may change the bond structure, and consequently, will have a strong effect on many physical properties.

The semiconductor superlattice materials have been studied extensively in the past two decades. Considerable attention is now given to the man-made one-dimensional periodic structure, referred to as metallic multilayers. Many anomalous physical properties have been reported. For instance, W. M. C. Yang et al.,[6] J. E. Hillard,[7] D. Baral et al.,[8] and D. Wolf et al.[9] have investigated the mechanical properties of metallic superlattices, and they have found an anomalous enhancement in the elastic modulus and in a number of systems. Thaler, Ketterson and Hillard[10] have reported an enhancement in the magnetization density in Cu/Ni systems.

The interest in metallic superlattice materials has come in large measure from the fact that it is possible to produce new materials which do not occur naturally. In this thesis, we have pursued the study of the interface structure in metal/carbon multilayers. We want to study a new class of ultra thin multilayer structure fabricated by two

dissimilar materials (W/C, Ti/C, Si/C). Thin metal /carbon multilayers were selected in order to obtain a more detailed picture of the interface and the accumulation of signals from each layer can enhance the signal received by the detector. Our ambition is to study the electronic structure at the interface, to discover the unique properties of these artificial materials. We attempt to understand whether the metallic multilayers can offer an advantage over the naturally occurring crystalline structures in maintaining high-temperature stability in an oxygen containing environment. The metal-carbon bonds at the interface should be very similar to the bonds in the carbides. The carbides are refractory materials of great importance because of their remarkable stability and strength at high temperature. The multilayers can be used as model systems for high temperature composite materials and for the study of the thermal and chemical stability of the interfaces.

We also have studied some standard crystals (TiC, SiC), since the study of natural single crystals (TiC, SiC) can supply the reference points for the identification of the behavior of these metallic multilayers, especially the electronic excitations. Transition-metal carbides from the IVB, VB and VIB columns of the periodic table are uncommon compounds. In general, the carbides which exhibit the greatest hardness and brittleness represent those materials which are covalently bonded while still preserving a degree of metallic electrical and thermal conductivity. Their melting temperatures[11] are higher than the metallic constituents alone, and thus, place them well among the refractory materials. This combination of properties has made the carbides important in a wide variety of applications.

Titanium carbide is one of the refractory metal monocarbides. Its light weight has made it particularly attractive in aerospace applications. Silicon carbide is also a high temperature, high thermal conductivity material. It offers the electronic device manufacturer many useful features which are not available from other semiconductor materials; in particular, its refractory nature, inertness, and large energy gap (β-SiC=2.2~2.6eV, 2H-SiC=3.3eV, 6H-SiC=2.86 eV)[12] allow high power dissipation and superior reliability.

Recently, heat-fusion research workers[13-14] have discovered that the silicon carbide and titanium carbide are the most promising candidate materials for use as the coating on the first-wall. Because coating materials with low Z like SiC and TiC have high stability against thermal load and neutron bombardment. They can help improve the surface erosion under the impact of plasma particles.

It is our other desire to use surface sensitive techniques to investigate the electronic structure and temperature sensitivity of these single crystals (TiC, SiC).

In this research, we employed a variety of techniques to study the interface structure; Auger spectroscopy (AS), electron energy loss spectroscopy (EELS), surface electron energy loss fine structure (SEELFS), Rutherford back-scattering (RBS) and X-ray reflectivity at small angles to characterize the samples.

This dissertation is divided into 9 chapters. The first chapter explains the objective and motivation of this research. Chapter 2 deals with the theoretical background which is necessary for the understanding of the experimental results. In Chapter 3, we discuss the experimental set-up and sample preparations. In Chapters 4

through 8 we discuss a series of experimental results (AES, EELS, SEELFS, RBS, and X-ray reflectivity). Multilayers of W/C, Ti/C, Si/C are discussed in Chapter 4, 6, and 8, respectively. Single crystals TiC and SiC are discussed in Chapter 5 and 7, respectively. Finally, in Chapter 9, we summarize the results and conclusions of all our investigations.

CHAPTER 2
THEORETICAL BACKGROUND

2.1 Electron Spectroscopy

2.1.1 Introduction

During the past two decades, the advances in ultra-high vacuum technology and electron optics have made the slow-electron scattering from solids into a new probe for microstructure analysis. Surface spectroscopes that make use of electron scattering, like Auger electron spectroscopy (AES), electron energy loss spectroscopy (EELS), and surface electron energy loss fine structure spectroscopy (SEELFS) have been used widely to investigate the chemical and physical properties of surfaces. Electrons with energies between 10 to 1000 eV are ideally suited to investigate the top surface layers of solids. The reason is that their mean free path in solids is only a few atomic layers. The characteristic electron mean free path as a function of electron energy is shown in Figure 2.1.

Electron spectroscopies have found, by far, the widest application in surface analysis for a number of reasons. Electrons can be easily focused into a beam, and then detected. Electrons can also be analyzed with respect to energy or angular distribution. Another advantage of using electrons as a probe is that electrons disappear in the vacuum chamber after being used for surface analysis, whereas atoms or ions do not have such an advantage.

The electron spectroscopes are based on an analysis of the energy distribution of electrons emitted from the sample surface. A

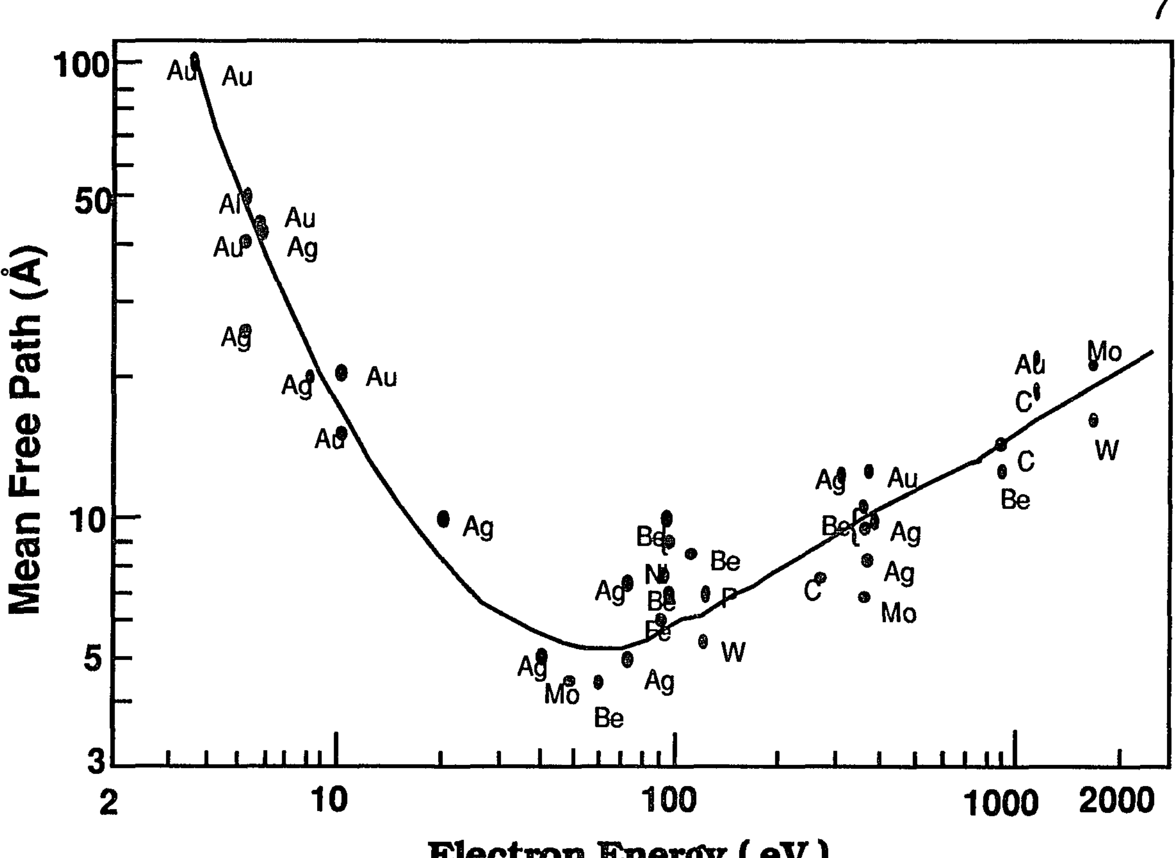

Figure 2.1 Universal curve for the electrons mean free path in solids as a function of their energy.

typical energy distribution spectrum of electrons emitted from a solid that is subjected to bombardment by an electron beam with energy E_p is shown in Figure 2.2. The relative intensity of the different features in the spectrum depends on the intensity of the primary beam, the angle of the incident beam, and the angle of the detecting system.

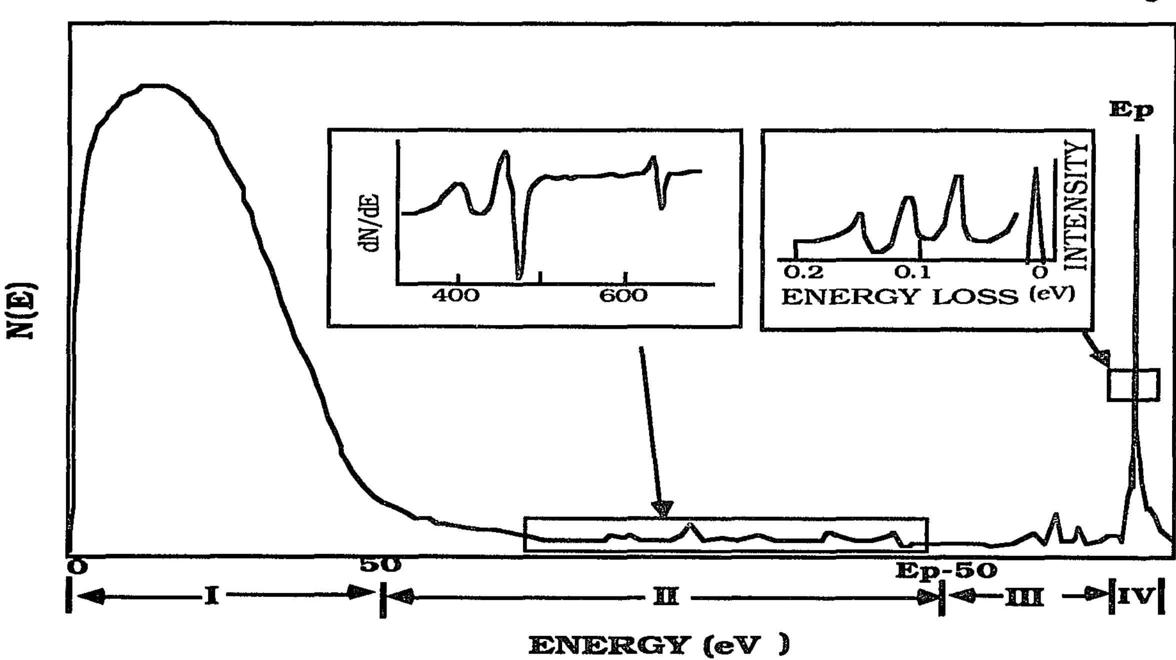

Figure 2.2 Schematic energy distribution of backscattered electrons obtained with an incident beam energy of E_p (eV).

The energy distribution curve, N(E), may be divided into 4 regions:

(1) The large peak located in the very low energy range (region I) represents the so called "true secondary electrons." This broad and huge bump is created by the inelastic collisions between the primary beam and the electrons bound in the solid. When a single primary electron suffers several inelastic collisions, a cascade of secondary electrons is then generated by the transfer of a small amount of energy in each collision.

(2) In region II, the spectrum is a superposition of some small peaks and a smooth background. The transitions in this region are usually caused by the Auger electrons, SEELFS, or ionization losses.

(3) In region III, the characteristics of the spectrum are caused by the energy losses of the primary electrons due to the electronic excitation in the solid, or the collective excitation of the valence electrons in the solid.

(4) In region IV, the sharp peak at energy E_p is due to the elastically reflected electrons. This elastic peak contains the structural information of the bulk and surface. The energy losses of much less than 1 eV are caused by the excitation of the surface vibrations or phonon excitations. They are normally not separated from the elastic peak, unless higher resolution energy analyzer and primary electron beam are used. In this work, we are interested in regions II and III of the electron scattering spectrum.

2.1.2 Auger Electron Spectroscopy

2.1.2.1 Introduction

When a core level electron in a free atom is ionized by x-ray irradiation or by an energetic electron, an inner shell vacancy is created. The excited atoms can release their energy in one of the following processes:

(1) Radiative transitions: An electron from a higher level drops into the "core hole." The available excess energy (E_K - E_{LI}) will be released by the emission of a characteristic x-ray photon.

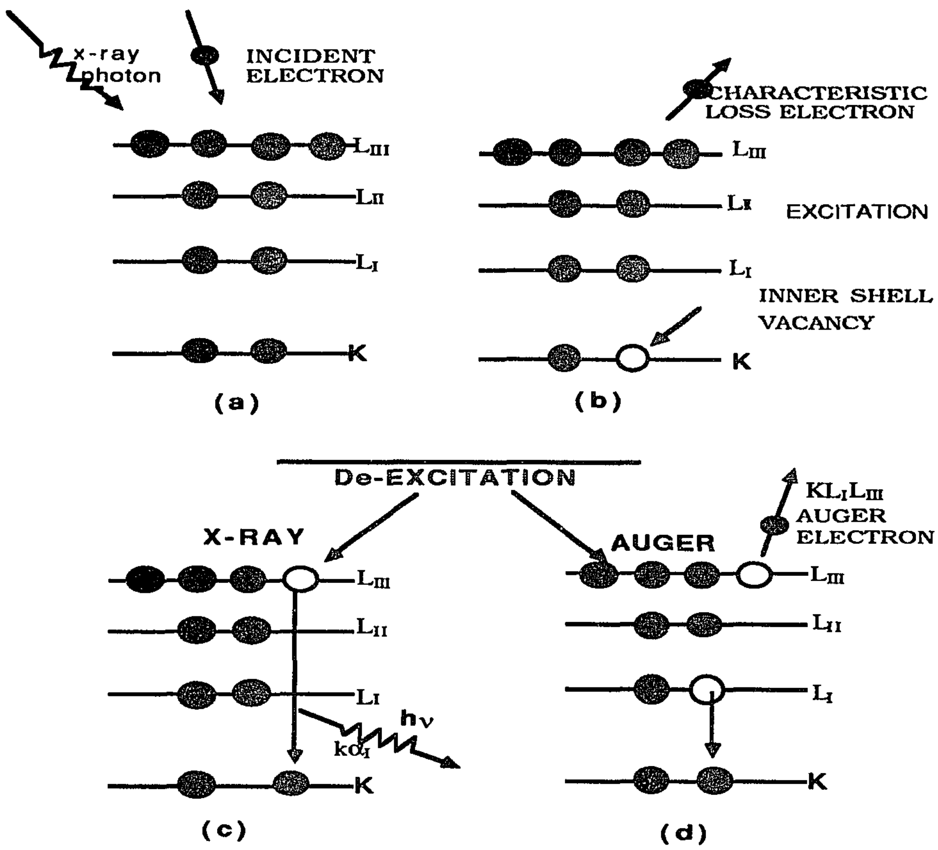

Figure 2.3 Auger process. (a) X-ray photon or electron incident upon an atom. (b) Ionization of inner shell electron by an impact of electron. (c, d) Processes of de-excitation, (c) emission of x-ray radiation, (e) emission of an Auger electron.

(2) Nonradiative transitions: An electron from an outer level fills the "core hole." The extra available energy is transmitted to another electron either in the same level or in an outer level, whereupon the second electron is ejected. This process is called Auger effect (Figure 2.3), and the ejected electrons are called Auger electrons.

The relative probabilities of relaxation by emission of an Auger electron and by emission of an x-ray photon per K-electron vacancy is shown in the Figure 2.4.

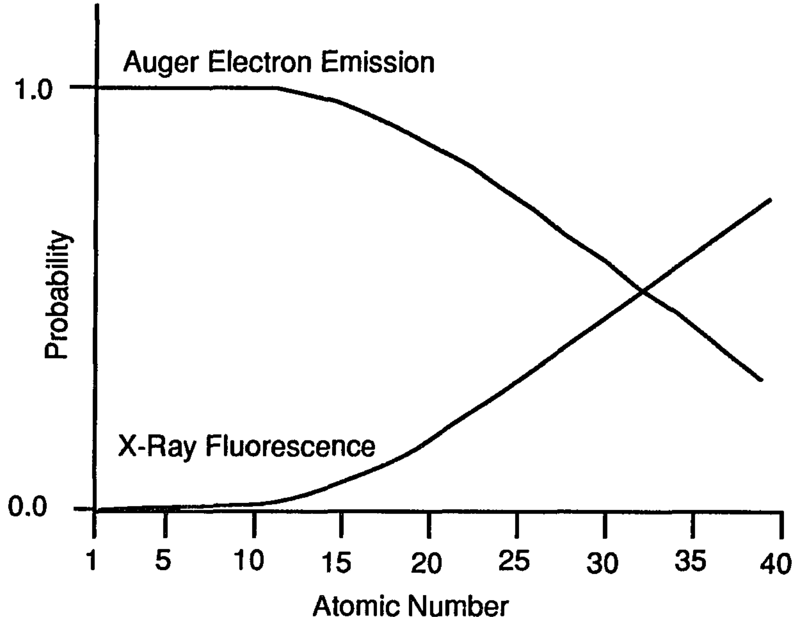

Figure 2.4 Relative probabilities of relaxation by emission of an Auger electron and by emission of an X-ray photon following creation of an inner vacancy hole in the K shell.

In this figure, the probability is plotted as a function of the atomic number. The probability of relaxation by Auger electron emission is favored over that of x-ray emission for lower atomic number.

The Auger electron emission process involves a three-electron transition. There are no strict selection rules, but the transition is mainly controlled by the electrostatic forces between a hole in an incomplete shell and its surrounding electron clouds. For the x-ray emission process, the probability is governed by the selection for dipole transition.

The Auger transition, as described in Figure 2.3, is named in the conventionally used j - j coupling KL_IL_{III}. Generally, the Auger electrons are classified by referring to the energy levels in their production and they are named in the notation $W_pX_qY_r$. (W, X, Y= K,

L, M are the x-ray level notation; p, q, r are the j values). W_p is the level in which the primary vacancy hole is generated, X_q is the level from which an electron fills the vacancy hole, and Y_r is the level from which the Auger electron is ejected. The Auger transition in which the initial vacancy, and one of the electrons that fills this vacancy are in a shell with the same principal quantum number (like $W_pW_qY_r$), is called as a Coster-Kronig transition. Such Auger transitions are very fast. They are observed only in a limited part in the periodic table since the differences in the subshell binding energies must be sufficient to eject an electron from an orbital in the next outer shell.

In the condensed matter, the Auger transitions are more complicated. The reason is that the electrons at the higher level of the solid (outer level) always form an energy band (valence band) with more or less delocalized electronic states and a finite energy width. The Auger electrons can be emitted from the valence band (as in Figure 2.5).

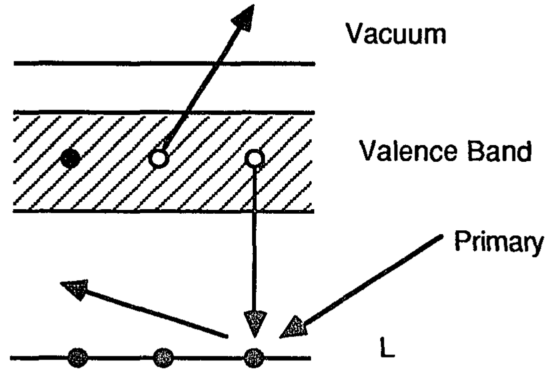

Figure 2.5 Auger effect in the condensed matter.

In these cases, the notation will be changed from $W_pX_qY_r$ to W_pVV. (V here only represents the valence electrons). For example,

in Si, the LMM will be replaced by LVV, if the hole is in the L level, and is filled by an electron from the valence band, and another electron is emitted from the valence band.

The energy of the Auger electrons is a characteristic of the target atom, it can be used to discriminate the elements of a solid from the Auger spectrometer. Therefore, it is very important to have a knowledge of the distribution of Auger electron energies. In the first approximation, the kinetic energy Ewxy of the Auger electron can be calculated as follows:

$$Ewxy = Ew_p(Z) - Ex_q(Z) - Ey_r(Z+1) - \phi_A. \qquad 2.1$$

where $Ew_p(Z)$ is the binding energy of an electron in the state w_p of the neutral atom, $Ex_q(Z)$ is the binding energy of the electron in the level x_q, and $Ey_r(Z+1)$ is the binding energy of the y_r level in the presence of a hole in the level x_q, and is therefore different from $Ey_r(Z)$, and Φ_A is the work function of the analyzer (not the sample). For practical applications, the energy of the Auger electrons can be found from the Handbook.[15]

The AES is one of the most popular and convenient methods to identify unambiguously the composition of solid surfaces. It is capable of uniquely identifying each element, except of course, hydrogen and helium, and is essentially a surface probe, as the data come from the top atomic layers.[16-18] It has been reported[19] that a small amount of contaminants down to 10^{12} atoms/cm^2 range can be detected under high-vacuum conditions. Moreover, the line shape of the Auger peak can always help us to determine the chemical effect of the environment. For example, the carbon line shapes are very different

in graphite and in the compound state of titanium-carbide (see Figure 2.6, 2.7, 2.8).

In this work, the Auger spcetroscopy was used mainly to determine the cleanliness of the samples, the composition of the solid surface, and the chemical effect.

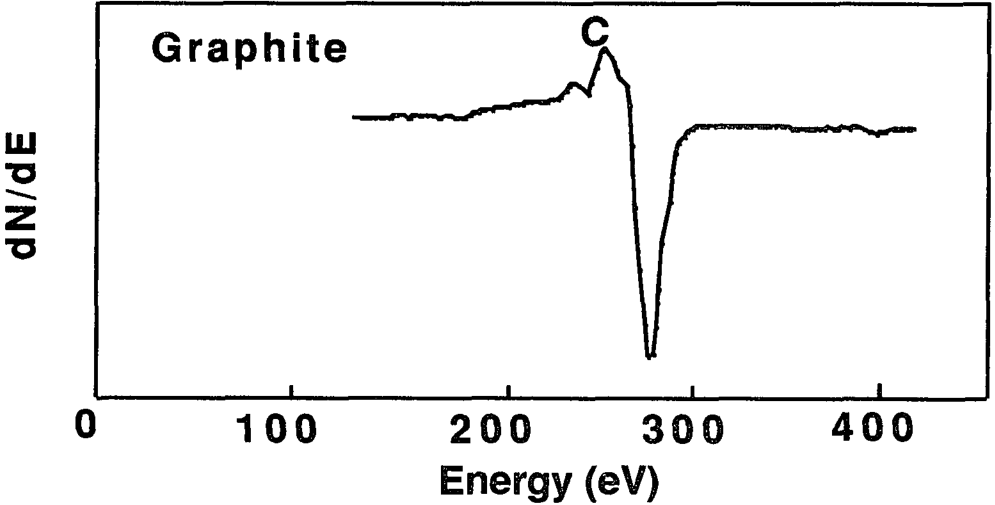

Figure 2.6 Auger spectra of graphite in the energy range 0 to 440 eV.

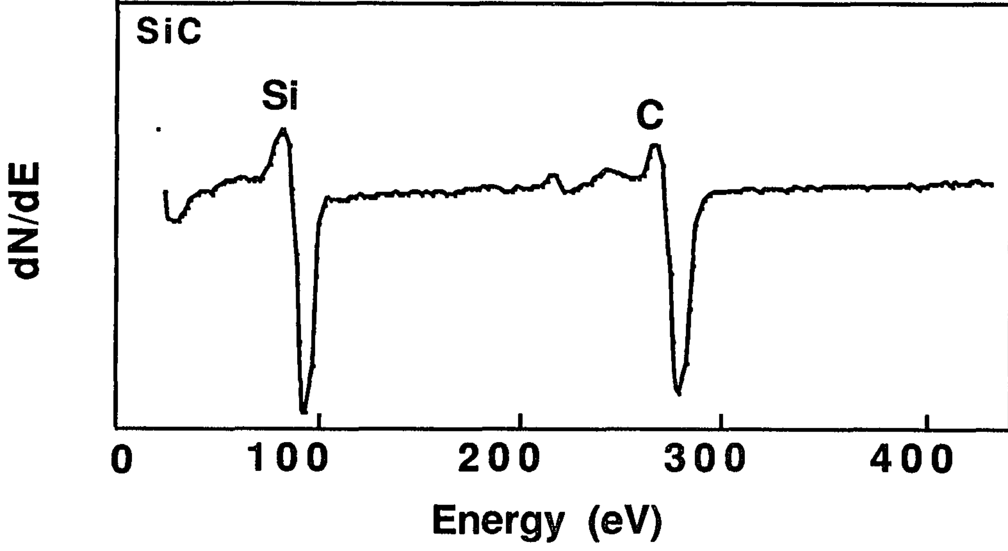

Figure 2.7 Auger spectra of SiC in the energy range 0 to 440 eV.

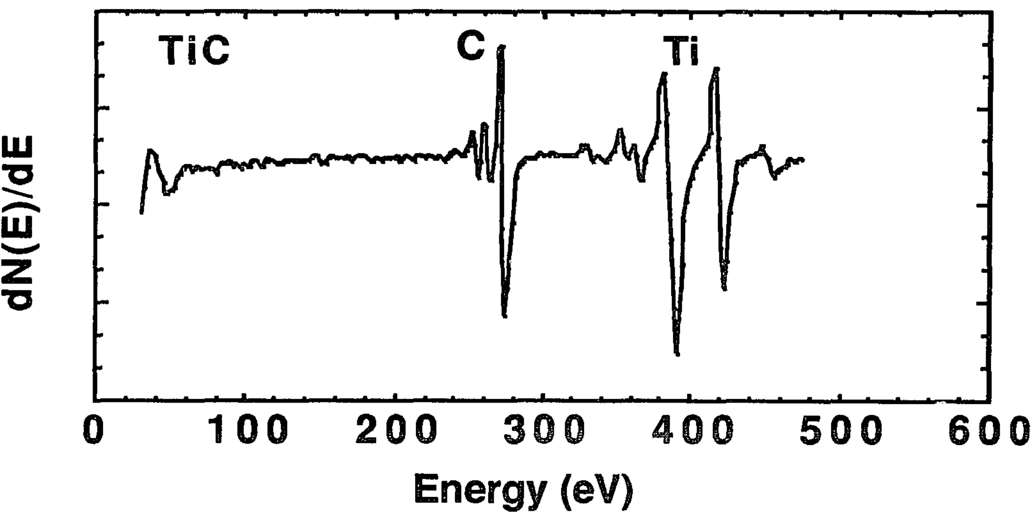

Figure 2.8 Auger spectra of TiC in the energy range 0 to 500eV.

2.1.2.2 Example

In Figures 2.6, 2.7, 2.8, the Auger spectra are shown in the dN(E)/dE mode respectively for graphite, α-SiC-6H, and TiC. It is noted the large differences in the line shapes of carbon between graphite and titanium carbide.

Because of the various energy loss processes (N(E) mode) in their way out of the solid, Auger peaks have a "tail" on their low energy side [see Figure 2.9a] and appear to fall off relatively more rapidly on their high energy side. The first derivative mode of AES is shown in Figure 2.9b. The AES structures usually consist of a main peak followed by additional features on the low-energy side because of different couplings of the Auger transition to the valence band electrons. The energy position of an Auger electron transition energy values is measured in the position of the negative end of the peaks [

see Figure 2.9 b]. The peak-to peak signal strength in the derivative spectrum is usually used as a relative quantitative measure of elemental surface concentration.

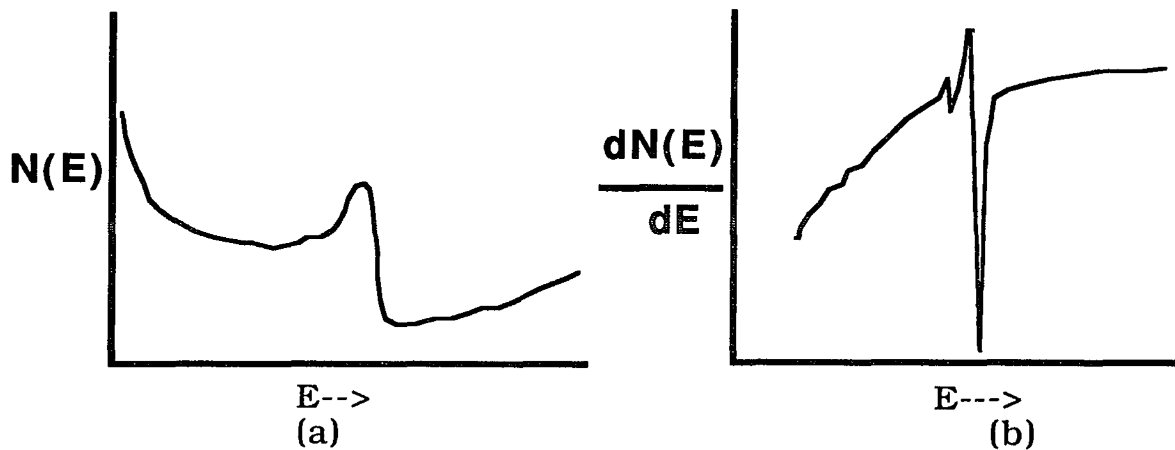

Figure2.9 (a) Auger peak in the energy distribution function N(E). (b) The first derivative of N(E) for identification of Auger peaks.

2.1.3 Electron Energy Loss Spectroscopy

2.1.3.1 Description of EELS

A beam of monoenergetic electrons with certain energy E_p impinges upon the target, part of the primary electrons undergo inelastic scattering. An energy loss of ΔE from these primary electrons will contribute to the excitation of the target electrons. These excitations are mainly caused by one electron or many electrons interactions which are characteristic of the electronic structure of the target. The scattered electrons are detected through the energy analyzer. The recorded electron energy distribution spectrum, with respect to the primary beam, is called electron energy loss spectroscopy (EELS).

EELS can be divided into fast and slow electron energy spectroscopy. Electrons with energies ranging from 10^3 to 10^5 are usually treated as fast electrons, and those with energies that fall below 10^3 are customarily regarded as slow electrons. Fast electron inelastic scattering (FEELS) is usually used at forward small angle transmission scattering measurements. FEELS inelastic scattering has been developed mainly by the experimental work of Raether et al,[20] Geigers,[21] and Boersch[22] and is studied broadly in solids for the past 40 years. The results of the reported FEELS[23] are surprisingly matched in the position of the extreme points and line shape with the loss function $Im(-1/\varepsilon(0,\omega))$ which is derived from optical reflectivity measurements. FEELS is considered as one of the best techniques in detecting the electronic structure in solids. Contrary to FEELS, and because of the short mean free path characteristics, slow electron energy loss spectroscopy (SEELS) can only be used in the reflection scattering measurements. In the past 20 years, SEELS has been extensively used for surface analysis. One important aspect of this spectroscopic technique is the possibility of obtaining a non destructive depth profile of the material by changing the impinging electron energy.

2.1.3.2 Excitation of Core, Valence, and Collective Electrons and Surface Vibrations

An example of a typical EELS in the second derivative mode is shown in Figure 2.10. The characteristic losses can be described mainly in the following four categories:

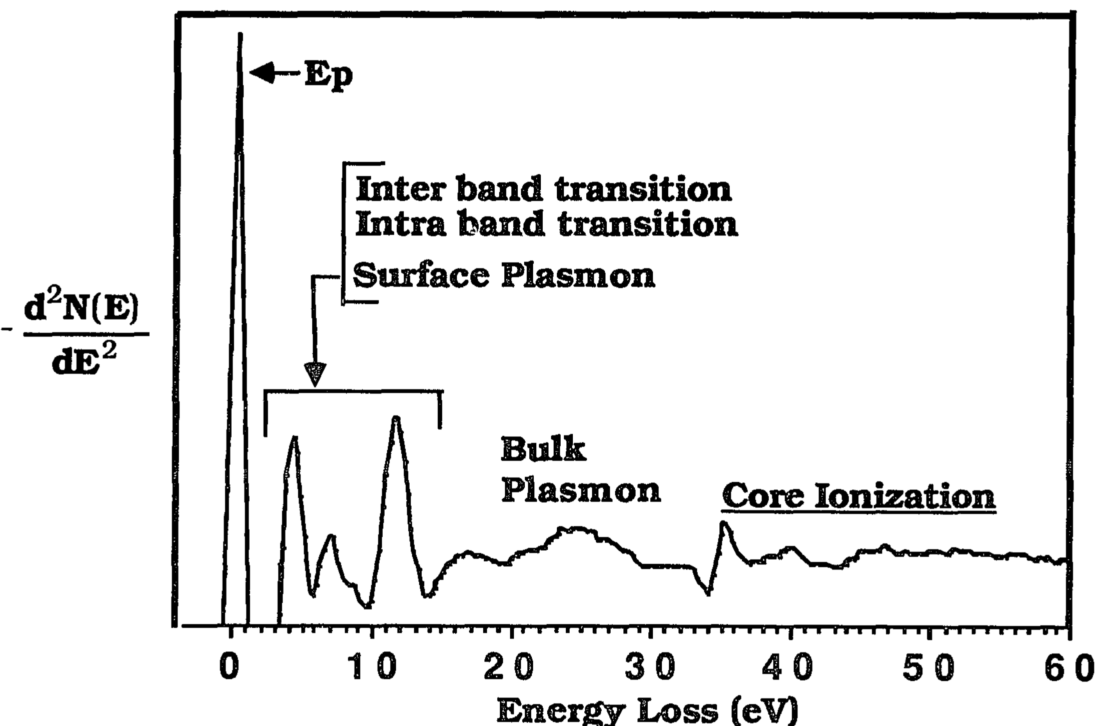

Figure 2.10 A typical EELS in the second derivative mode.

(a) Excitation of Core Electrons: These excitations occur if the primary electron interacts with the inner shell electron, and transfers an amount of energy (ΔE), which is sufficient to raise the core electron into an unfilled state above the Fermi level. The energy loss ΔE can be described as follows:

$$\Delta E \geq E_f - E_B \quad , \qquad 2.2$$

where E_f is the Fermi level energy, and E_B is the binding energy of the core electron. These transitions may provide information about the unoccupied density of states (DOS) in the conduction bands of solids.[24] The threshold energy of the core electrons usually agrees to within a few eV with the known ionization energy of the atom. Thus the core

electron energy loss can provide another easy way of identifying atoms of different types in the target.

(b). One Electron Excitation of Valence Electrons: This excitation involves an energy transfer from a few eV to 20 eV. Usually, an electron in the valence band of a solid may be excited by the incident electron to a higher unfilled level of the same band (intra-band transition) or into another energy band (interband transition). These transitions involve a convolution of the valence and conduction band density of states, and hence are not easy to interpret.

(c). Collective Excitations of Valence Electrons: In solids, the collective oscillations of valence band electrons lead to discrete peaks with characteristic frequency ω_p. These oscillating electrons are called plasmons. The energy of these collective excitation is in the range of 5 to 50 eV. The plasmon frequency ω_p mainly depends on the electron density,[25]

$$\omega_p = \sqrt{\frac{4\pi n_e e^2}{m}} \quad , \qquad 2.3$$

where m is the effective mass of the valence electron, n_e is the electron density, and e is the electron charge.

At the surface of solids, collective excitation can also exist. This kind of excitation is called surface plasmon.[26] Its characteristic frequency ω_s is defined as:

$$\omega_s = \frac{\omega_p}{\sqrt{1+\varepsilon}} \quad , \qquad 2.4$$

where ε is the dielectric constant of the medium outside of the surface.

In reflection electron energy loss spectroscopy, bulk plasmons can be distinguished from surface plasmons by the energy dependence of the loss peak intensity.

(d). Excitation of Surface Vibrations: These excitations are predominantly due to phonon excitation or the vibration of the adsorbed atoms at the surface of the solids. Energy losses of these excitations are usually less than 1 eV, and they can be seen only using a higher resolution EEL spectrometer.

2.1.3.3 Inelastic Scattering and Inelastic Scattering Cross Section of Electrons

Our goal in this section is to discuss briefly the theories which describe the relation between differential cross section, $d^2\sigma/d\omega d\Omega$ and the solid dielectric function $\varepsilon(q,\omega)$.

It is well known that the dielectric function describes the response of the electrons in a solid to an applied electric field. The dielectric function and the differential cross section can be connected together through the transition rate which can be calculated from quantum mechanics. The electron-electron scattering through the Coulomb field involves two main scattering processes: one is the elastic scattering, the other is the inelastic scattering. In EELS, we are interested in the inelastic scattering. The following discussion will closely follow the analysis of references [27-28].

Theoretically, the total Hamiltonian which describes the system, incident electron and the sample, should be considered:

$$H = H_o + \frac{p^2}{2m} + \sum_j \frac{e^2}{|r - r_j|} \qquad 2.5$$

where the first term H_o describes the unperturbed sample system, the second term $p^2/2m$ is the kinetic energy of the incident electron, and the third term is the Coulomb interaction between the incident electron and electrons in the sample. The positions of the incident electron and the electron labeled as j in the sample are denoted by r and r_j, respectively.

The eigenfunction of the unperturbed system has the form

$$| \, l, k_o> = \phi_l(r_1 \, ...r_N)e^{ik_o.r} \quad , \qquad 2.6$$

where $\phi_l(r_1......r_n)$ is the many-body wavefunction for the sample in state l with energy E_l, $\exp(ik_o \cdot r)$ is the plane wavefunction of the incident electron with wave vector k_o. After a small-angle scattering, the wave vector of the incident electron changes to k. In Figure 2.11, a typical representation of the wave vector before and after scattering is shown.

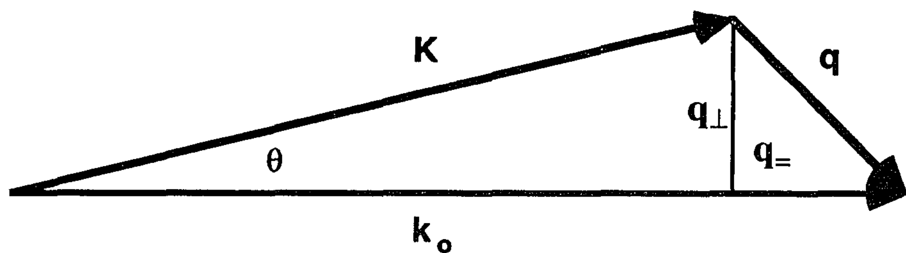

Figure 2.11 Primary electrons of momentum $\hbar \cdot \vec{k_o}$, after being scattered at an angle θ, with momentum change to $\hbar \cdot \vec{k}$, and with the momentum transfer $\hbar \vec{q}$ being equal to $\vec{k_o} - \vec{k}$.

From the first order time perturbation theory, one can calculate the transition rate[29] from the initial state i of energy E_i to the final state f of energy E_f. That is,

$$R_{fi} = \frac{2\pi}{\hbar}|\langle f|H|i\rangle|^2 \, \delta(E_f - E_i \pm \hbar\omega) \quad , \qquad 2.7$$

where $< f \mid H \mid i>$ is the transition matrix.

In the electron scattering system, we define the initial state as $|l_o,k_o>$, and the final state as $|l,k>$. Thus the transition rate is

$$R_{l_o \to l} = \frac{2\pi}{\hbar^2}\left|\langle l,k\left|\sum_j \frac{e^2}{|r-r_j|}\right| l_o,k_o\rangle\right|^2 \delta\left(\frac{E_{lo} - E_l}{\hbar} \pm \hbar\omega\right) \quad . \qquad 2.8$$

After calculating the Coulomb interaction term, we have

$$R_{l_o \to l} = \frac{2\pi}{\hbar^2}\left[\frac{4\pi e^2}{q^2}\right]^2 \left|\langle l\left|\sum_j \exp(i\vec{q}.\vec{r}_j)\right| l_o\rangle\right|^2 \delta\left(\frac{E_{lo} - E_l}{\hbar} \pm \hbar\omega\right) \quad , \qquad 2.9$$

where $\hbar\vec{q}$ is the momentum transfer.

If we replace the delta function by an integral representation,

$$\delta\left(\frac{E_{lo}-E_l}{\hbar} + \omega\right) = \frac{1}{2\pi}\int e^{i\left(\frac{E_{lo} - E_l}{\hbar} + \omega\right)t}\, dt$$
$$= \frac{1}{2\pi}\int e^{(i\omega t)}\, e^{i\left(\frac{E_{lo} - E_l}{\hbar}\right)t}\, dt \ , \qquad 2.10$$

then Eq. 2.9 can be written as follows :

$$R_{l_o \to l}(q,\omega) = \frac{2\pi}{\hbar^2}\left[\frac{4\pi e^2}{q^2}\right]^2 \int dt\, e^{(i\omega t)} \left\langle l_o\left|\sum_j e^{\frac{iE_{lo}t}{\hbar}}\, e^{-iq.r_j} e^{\frac{-iE_{lo}t}{\hbar}}\right| l\right\rangle\left\langle l\left|\sum_j e^{iq.r_j}\right| l_o\right\rangle \ , \qquad 2.11$$

where $\sum_j e^{iq.r_j}$ can be treated as the electron density operator $n_q(r)$. The $e^{\frac{iE_{lo}t}{\hbar}}\, e^{-iq.r_j} e^{\frac{-iE_{lo}t}{\hbar}}$ term can be treated as the Fourier transform of the electron density at time t. The transition rate will then have the form

$$R_{l_o \to l}(q,\omega)= \frac{2\pi}{\hbar^2}\left[\frac{4\pi e^2}{q^2}\right]^2 \int dt\ e^{(i\omega t)} \langle l_o | n_q(t) | l \rangle \langle l | n_{-q} | l_o \rangle . \quad 2.12$$

In real experiments, we measure only the total transition rate $R(q,\omega)$, which is the sum of the final states l for a given energy of the scattered electrons. The total transition rate after getting the sum over the final states is

$$R(q,\omega)= \frac{2\pi}{\hbar^2}\left[\frac{4\pi e^2}{q^2}\right]^2 \int_{-\infty}^{\infty} dt\ \ e^{(i\omega t)} \langle l_o | n_q(t) n_{-q} | l_o \rangle$$

$$= \frac{2\pi}{\hbar}\left[\frac{4\pi e^2}{q^2}\right]^2 S(q,\omega) , \quad 2.13$$

where

$$S(q,\omega)= \frac{2\pi}{\hbar} \int_{-\infty}^{\infty} dt\ \ e^{(i\omega t)} \langle l_o | n_q(t) n_{-q} | l_o \rangle \quad 2.14$$

is called the dynamic structure factor. It is the space-time Fourier transform of the electron density - density correlation function. This dynamic factor is related to the longitudinal dielectric function of the sample as follows:

$$S(q,\omega) = \frac{q^2}{4\pi^2 e^2} \mathrm{Im}\left(\frac{-1}{\varepsilon(q,\omega)}\right) \quad 2.15a$$

$$S(q,\omega) = \frac{q^2}{4\pi^2 e^2}\ \frac{\varepsilon_2}{\varepsilon_1^2 + \varepsilon_2^2} \quad 2.15b$$

where ε is the dielectric function $\varepsilon(q,w)$, $(\varepsilon(q,w) = \varepsilon_1(q,\omega)+i\varepsilon_2(q,\omega))$, which describes the characteristic response of the sample under an

applied electric field. (Details of this relation are described in Appendix A.) Using Eq. 2.15a, Eq. 2.13 can be written as:

$$R(q,\omega)=\frac{8\pi e^2}{\hbar q^2}\,\mathrm{Im}\left(\frac{-1}{\varepsilon}\right) . \qquad 2.16$$

Thus, if ε can be determined from other independent sources, then the transition rate at small angles can be figured out. The differential scattering cross section per atom can then be obtained from the transition rate. Actually, the differential cross section is equal the transition rate divided by the incident flux $\hbar k/m$, the number of atoms in the sample N, and then multiplied by the number of states available for the electron to lose energy between $\hbar\omega$ and $\hbar(\omega+\delta\omega)$. The final result is:

$$\frac{d^2\sigma}{d\omega d\Omega}=\frac{\hbar V}{(\pi e a_o q)^2 N}\mathrm{Im}\left(\frac{-1}{\varepsilon(q,\omega)}\right) , \qquad 2.17$$

where a_o is the Bohr radius, V is the volume for the normalization of the incident electron wave function.

Equation 2.17 describes the differential scattering cross section that an electron experiences in the bulk of the sample. For the electron scattered at the surface, because half of the space is in vacuum, the field inside the medium, which is built up by a moving electron outside, is screened by a factor of $\varepsilon+1$ due to polarization. Thus we have to replace ε by $\varepsilon+1$, and the differential scattering cross section at the surface is:

$$\frac{d^2\sigma}{d\omega d\Omega} = \frac{\hbar V}{(\pi e a_o q)^2 N} \mathrm{Im}\left(\frac{-1}{\varepsilon(q,\omega)+1}\right) . \qquad 2.18$$

In the EELS, the factors $\mathrm{Im}(-1/\varepsilon)$ and $\mathrm{Im}(-1/(\varepsilon+1)$ are customarily called bulk loss function and surface loss function, respectively. Each contains both one-electron (inter-band, intraband) and many electron (plasmon) excitations.

2.1.3.4 The Dielectric Function of Free Electron, Bound Electron and Interband Excitation

The interpretation of the EELS spectra generally uses one of the three models: the dielectric model,[30-32] the density-of-states model,[33-36] or the joint-density of states model that is modified by exchange interactions.[37] Except for the DOS model, the other two directly or indirectly involve the use of the dielectric function. A deeper understanding of the dielectric function is very important.

The dielectric response function of a solid to the electron or photon excitation is determined by either the longitudinal or transverse dielectric function. Both the longitudinal and transverse dielectric functions are equal in the random phase approximation, in the small momentum transfer (q) limit. This equivalence allows us to compare the EELS spectra with the loss spectra derived from optical measurements.

In FEELS, the scattering angle is chosen to be small, the energy loss is small compared with the primary electron beam, and the momentum transfer q is very small. The differential cross section for this scattering process can be described by:[27]

$$\frac{d^2\sigma_{if}}{dEd\Omega} = \frac{4}{a_0^2 q^2}\left|\langle f \,|\, e^{i\vec{q}.\vec{r}} \,|\, i \rangle\right|^2 , \qquad 2.19$$

where q is the momentum transfer, r is the electron distance for the atom. The operator in the matrix elements can be expanded as follows:

$$e^{i\vec{q}.\vec{r}} = 1 + i\vec{q}.\vec{r} - \frac{1}{2}(\vec{q}.\vec{r})^2 + \ldots\ldots , \qquad 2.20$$

therefore, the dipole approximation is valid.

For slow electron energy loss spectroscopy that is measured in the CMA or spherical detector, the scattering angle is very large, if one considers only a one- inelastic-scattering-step process. Actually, multiple-scattering can always happen in the electron scattering process. Most of the acceptable interpretations about the inelastic reflection scattering is that several scattering events are responsible for scattering a number of inelastic electrons into the backward direction. The simplest model that is suggested by E. Bauer, E. Sickfus, and N. R. Avery[35,38,39] is the two-step process in which the electrons experience an elastic scattering, and then follow an inelastic scattering (I-E) or visa versa (E-I). To show the scattering picture, we plot the two-step process[40] in Figure 2.12, which is especially suited for the interpretation of the SEELS measurements using a CMA. In Figure 2.12 (a) $\vec{k_o}$, $\vec{k}$ are the momentum before and after scattering, respectively, and $\vec{q}$ is the momentum transfer. The left hand side of (a), and of (b) describe the I-E scattering, and the right hand side of (a) and of (b) describe the E-I scattering.

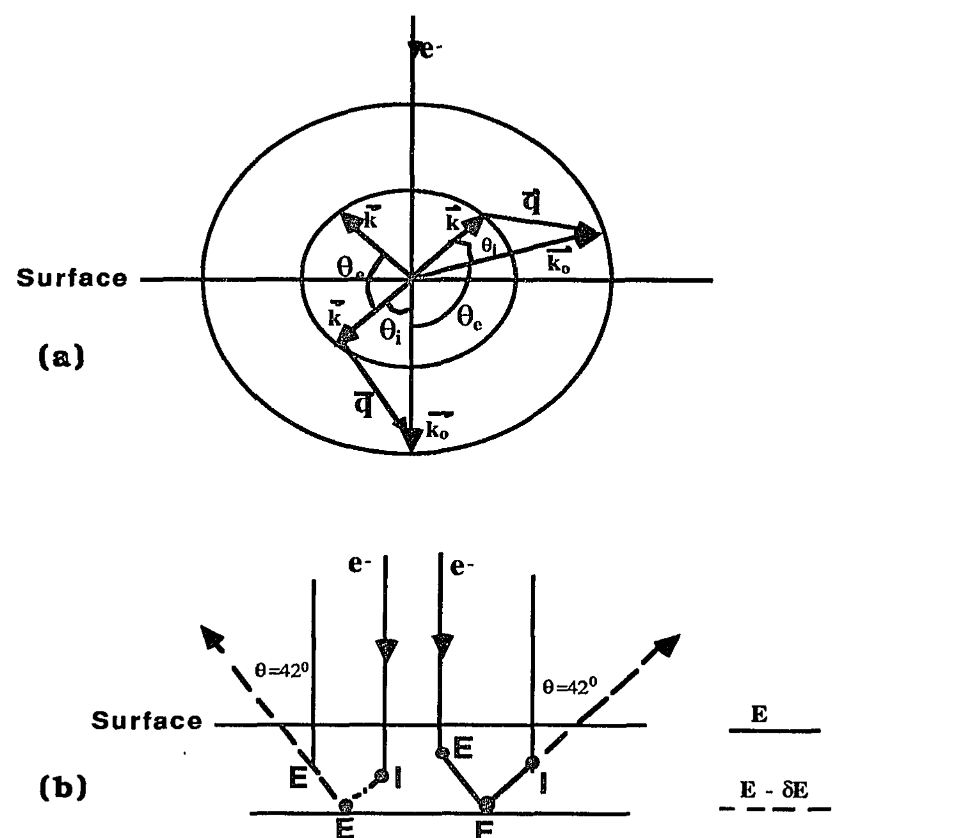

Figure 2.12 A typical diagram of a two-step [I-E, E-I] scattering process [Ref. 40].

Based on this idea, the maximum and minimum momentum transfer q can be calculated as follows:

$$q\,(\max) = \frac{\sqrt{2m\Delta E}}{\hbar}\ , \qquad 2.21$$

$$q\,(\min) = \frac{\sqrt{2m}}{\hbar}\left(\sqrt{E_0} - \sqrt{E_0 - \Delta E}\right)\ , \qquad 2.22$$

where ΔE is the energy loss, and E_0 is the primary energy. According to this relation, we plot the momentum transfer vs energy loss for three different primary energy beams in Figure 2.13. From Figure 2.13, we can see that at an energy loss smaller than 20 eV, the minimum momentum transfer is less than $0.5Å^{-1}$. Thus the dipole

approximation at a lower energy loss region is valid. For a large q, a higher order approximation should be considered. Evidences for slow EELS have been reported by many authors like C. Colavita, H. Araki, M. H. Mohammed, etc. [41-43]

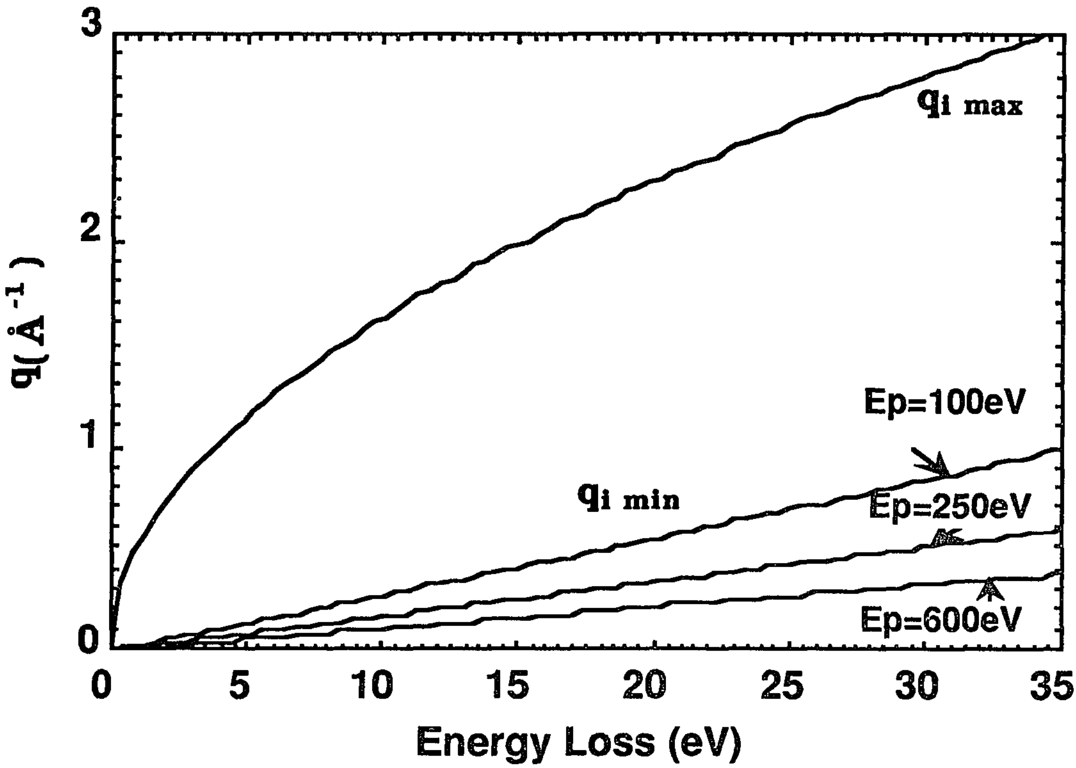

Figure 2.13 Maximum and minimum momentum transfer q at three different primary energies. At the small energy loss region, the long wavelength approximation is possible.

For the angle resolved SEELS, the detector has the freedom of focusing at those inelastic scattering electrons which are closed to the specular beam. If the scattering angle is very small, then the dipole approximation is valid.

(1) Free Electron: The long wavelength dielectric function $\varepsilon(\omega)$ of a free electron gas with damping and relaxation time τ is obtained from

the equation of motion of a free electron in an electric field E(x,t),

$$m\ddot{x} + \frac{m}{\tau}\dot{x} = - eE \ . \qquad 2.23$$

Let both x and E have a time dependence of exp(-iωt), then

$$-m\omega x - i\omega\frac{m}{\tau}x = - eE \ , \qquad 2.24$$

$$x = \frac{eE}{m\omega^2 + i\omega\frac{m}{\tau}} \ . \qquad 2.25$$

The dielectric function at frequency ω is

$$\varepsilon(\omega) = \frac{D(\omega)}{E(\omega)} = 1 + \frac{4\pi P(\omega)}{E(\omega)} \ , \qquad 2.26$$

where P(ω) is the polarization, and is defined as the dipole moment per unit volume. That is,

$$P = -nex \ . \qquad 2.27$$

Then it follows from Eqs. 2.25 - 2.27 that the dielectric function of free electrons is

$$\varepsilon(\omega) = 1 - \frac{4\pi ne^2}{m\omega^2 + i\omega\frac{m}{\tau}}$$

$$= 1 - \frac{4\pi ne^2/m}{\omega^2 + i\frac{\omega}{\tau}}$$

$$= 1 - \frac{\omega_p^2}{\omega^2 + i\frac{\omega}{\tau}} \ , \qquad 2.28$$

where $\omega_p{}^2 = 4\pi ne^2/m$ is defined as the plasmon frequency.
Since $\varepsilon = \varepsilon_1 + i\varepsilon_2$,

then

$$\varepsilon_1 = 1 - \frac{\omega_p^2}{\omega^2}\frac{1}{1+(\frac{1}{\omega\tau})^2} \qquad 2.29$$

$$\varepsilon_2 = \frac{1}{\omega\tau}\frac{\omega_p^2}{\omega^2}\frac{1}{1+(\frac{1}{\omega\tau})^2} \qquad 2.30$$

At $\varepsilon(\omega) = 0$, we obtain as a solution, $\omega = \omega_1 + i\omega_2$, where

$$\omega_1 = \omega_p[\ 1-\frac{1}{(2\omega_p\tau)^2}\ ]^{1/2} \qquad 2.31$$

$$\omega_2 = \frac{-1}{2\tau}\ . \qquad 2.32$$

If damping is neglected, for $\omega\tau >> 1$, we then have $\omega_1 = \omega_p$ and $\omega_2 = 0$.

By substituting the values of ε_1 and ε_2 from Eqs. 2.29 and 2.30, respectively, into the loss function

$$\mathrm{Im}(\frac{-1}{\varepsilon}) = \frac{\varepsilon_2}{\varepsilon_1+\varepsilon_2} = \frac{\omega_p^2\,\omega/\tau}{(\omega^2 - \omega_p^2)^2 + (\omega/\tau)^2}\ . \qquad 2.33$$

There is a maximum for small $1/\tau$ at ω_p in this Lorentz-like function, that is,

$$\mathrm{Im}(\frac{-1}{\varepsilon})_{max} = \frac{1}{\varepsilon''(\omega_p)} = \omega_p\tau\ . \qquad 2.34$$

In Figure 2.14, a schematic representation of ε_1, ε_2 and the loss function $\mathrm{Im}(-1/\varepsilon)$ are shown. A plasmon oscillation frequency is observed when ε_1 crosses the zero value and ε_2 is at a small value.

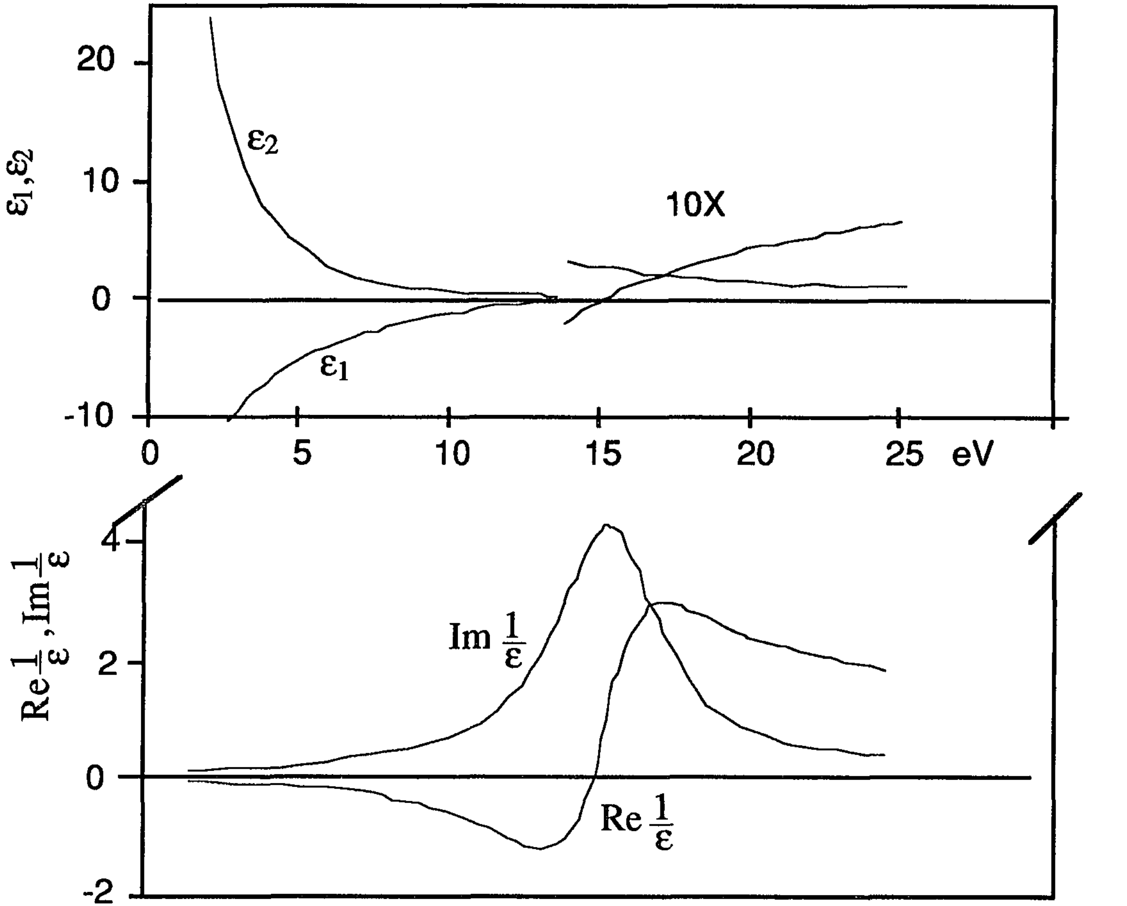

Figure 2.14 The dielectric function of ε_1, ε_2 and the loss function of a free electron gas at $\hbar\omega_p$ =15 eV [Ref. 32].

(2) Bound Electron: In the case of an electron bound by a harmonic force and acted upon by an electric field E(x,t), the dielectric function $\varepsilon(\omega)$ can be obtained in the same way as in the free-electron case, and that is by solving the equation of motion,

$$m\ddot{x} + \frac{m}{\tau}\dot{x} + m\omega_n^2 = - eE \qquad 2.35$$

where ω_n is the eigenfrequency of the bound electron.

$\varepsilon(\omega)$ is given by

$$\varepsilon(\omega) = 1 + \frac{4\pi ne^2}{m} \frac{1}{\omega_n^2 - \omega^2 + i\omega/\tau} . \qquad 2.36$$

where n is the number of electrons per unit volume. If n_f is the number of free electrons per unit volume, there will be n_b electrons in eigenfrequency ω_n. The dielectric function can be described in this way

$$\varepsilon(\omega) = 1 + \chi_f + \chi_b \qquad 2.37$$

with the contribution of free electrons

$$\chi_f = \frac{4\pi n_f e^2}{m} \frac{1}{-\omega^2 - i\omega/\tau} , \qquad 2.38$$

and the bound electrons

$$\chi_b = \frac{4\pi n_b e^2}{m} \frac{1}{\omega_n^2 - \omega^2 - i\omega/\tau} . \qquad 2.39$$

The eigenfrequency of plasmon excitation with $1/\tau = 0$ is the solution of $\varepsilon_1 = 0$:

$$\omega_b^2 = \frac{\omega_p^2}{1+\chi_b} , \qquad 2.40$$

where ω_b is the plasmon frequency under the perturbation of bound electron excitations. There are two different plasmon frequencies under the influences of the bound electron excitations :

(a) If ω_n lies at higher frequencies (see Figure 2.15)

$\omega < \omega_n$ and $\omega_p < \omega_n$, thus

$$\omega_b^2 = \omega_p^2 - \frac{4\pi n_b e^2}{m}\,\frac{\omega_p^2}{\omega_n^2} \quad , \qquad 2.41$$

This means that the plasmon energy $\hbar\omega_b$ is reduced when the plasmon frequency of n_f free electrons lies below the bound electrons.

(b) The reverse happens if the regarded frequencies ω are higher than the interband transition and with $\omega_n < \omega$. We then have

$$\omega_b^2 = \omega_p^2 + \frac{4\pi n_b e^2}{m} \quad . \qquad 2.42$$

So the plasmon energy $\hbar\omega_b$ shifts to the higher energy side. A simple picture showing the results is given in Figure 2.15.

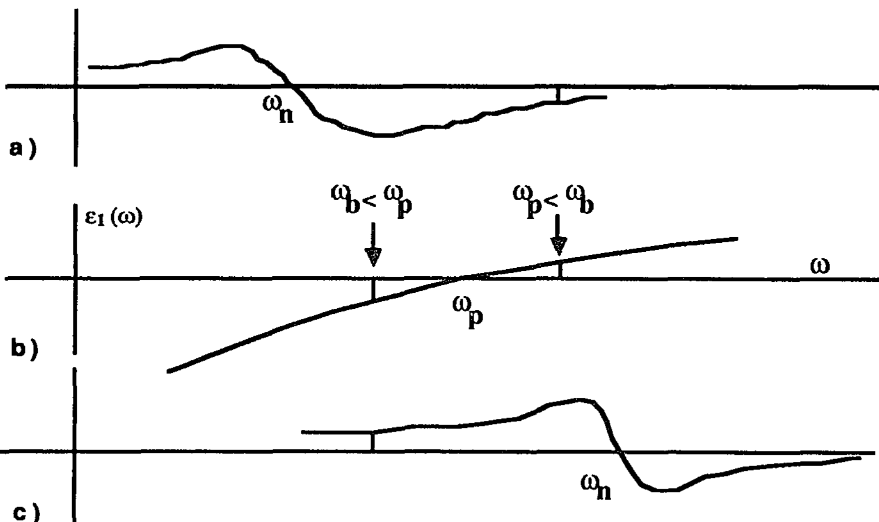

Figure 2.15 The influence of bound electrons in the dielectric function. (a) If the eigenfrequency of the bound electrons ω_n, lies below the plasmon frequency of the free electrons ω_p, the position of $\varepsilon_1(w) = 0$ will shift to higher values. (c) The reverse takes place if $\omega_n > \omega_p$ [Ref. 32].

(3) Dielectric function and interband transition: The basic connection between electron band structure and the dielectric constant[43] ε_2 can be expressed by:

$$\varepsilon_2 = \frac{4e^2\pi^2}{\omega^2 m^2} \sum_{v,c} \int_{BZ} \frac{2dk^3}{(2\pi)^3} |\hat{e}.M_{cv}(k)|^2 \, \delta(E_c(k) - E_v(k) - \hbar\omega), \qquad 2.43$$

where M_{cv} is the dipole transition matrix. This equation tells us that the imaginary part of the dielectric constant is determined by all possible interband transition between states of energy difference $\hbar\omega$ and the matrix element $\hat{e}.M_{cv}$ which depends on the wave function of both the initial and final state.

ε_1 can then be obtained through the Kramers - Kronig integral relation

$$\varepsilon_1 = 1 + \frac{2}{\pi} P \int_0^\infty \omega' \varepsilon_2(\omega') \frac{1}{\omega'^2 - \omega^2} d\omega' \quad . \qquad 2.44$$

Thus in principle, once the band structure is known, one can calculate all the dielectric constant ε_1, ε_2 through Eqs. 2.43 - 2.44.

Equation 2.43 can be transformed into a surface integral by using the δ function relation

$$\int_a^b h(x)\delta[f(x)]dx = \sum_{x_0} h(x_0) \left|\frac{df}{dx}\right|^{-1}_{x=x_0} \quad . \qquad 2.45$$

It then takes the form

$$\varepsilon_2(\omega) = \frac{e^2}{\pi\omega^2 m^2} \sum_{v,c} \int_s ds \frac{|\hat{e}.M_{cv}(k)|^2}{|\nabla_k(E_c - E_v)_{E_c - E_v = \hbar\omega}|} \quad . \qquad 2.46$$

The matrix element M_{cv} is always a smooth function of k except near special k vectors where $|\hat{e}.M_{cv}|$ vanishes because of symmetry. The kernel part of the integral

$$\sum_{v,c} \int_s \frac{ds}{|\nabla_k(E_c - E_v)_{E_c - E_v = \hbar\omega}|}$$

is always defined as the joint density of states (JDOS)

$$J_{CV} = \sum_{v,c} \int_s \frac{ds}{|\nabla_k(E_c - E_v)_{E_c - E_v = \hbar\omega}|} \quad . \qquad 2.47$$

The contribution to the dielectric function from a pair of bands is now proportional to $1/\omega^2$ and the quantity from JDOS. The JDOS shows a strong variation in the neighborhood of particular values of E:

$$\nabla_k E_c(K) = \nabla_k E_v(K) = 0 \ , \qquad 2.48$$

which are called critical point energies. These critical points defined by Eq. 2.48 and characterized by a set of values (ω,k) are the most important part in the discussion of optical spectra.

2.1.4 Surface Electron Energy Loss Fine Structure (SEELFS)

2.1.4.1 Introduction

SEELFS (Surface Electron Energy Loss Fine Structure) is a surface-sensitive, electron-induced spectroscopy. It also displays the oscillations above the threshold frequency, and bears information of interatomic distances. The study of SEELFS is a parallel development

to the photon induced EXAFS techniques.

It is well known that the x-ray absorption cross section will be modulated by the presence of other atoms close to the absorbing center. The photoelectron emitted in the absorption process will propagate as a spherical wave. The outgoing wave will be back scattered by the neighboring atoms (see Figure 2.16), thereby producing

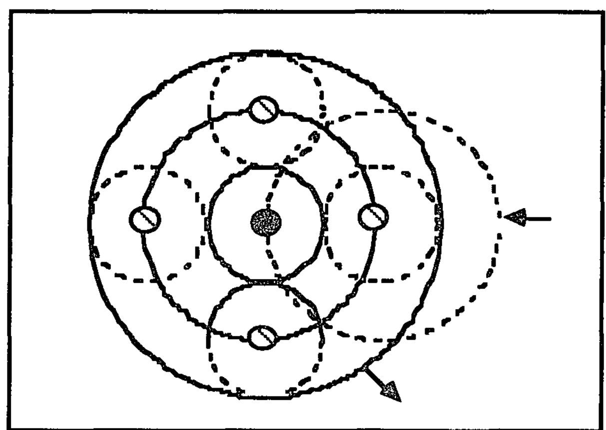

Figure 2.16 Schematic representation of the interferences of two different waves incoming and outgoing. The outgoing photoelectron (solid line) originated from the central atom (circle) propagates to the neighboring atoms (dashed lines circle). The back-scattered waves (dashed lines) interfere with the outgoing waves, and give rise to the EXAFS.

an incoming wave which will interfere either constructively or destructively with the outgoing wave. The final result is that the interference gives rise to an oscillatory variation in the absorption

cross section. It was shown that this oscillatory behavior contains information on the interatomic distances.[44]

2.1.4.2 EXAFS and SEELFS

Theoretically, the x-ray modulation of the absorption rate[45] in the Extended X-ray Absorption Fine Structure (EXAFS) (Figure 2.17) after normalized to back-ground absorptions (μ_0) can be described as:

$$\chi(E) = (\mu(E) - \mu_0(E))/\mu_0(E), \qquad 2.49$$

where the absorption rate μ described by the dipole approximation for the x-ray induce transition of an electron from an initial state $|\phi_i>$ to a final state $|\phi_f>$ has the form:

$$\mu = D|\langle\phi_f|\hat{\varepsilon}.\hat{r}|\phi_i\rangle|^2 , \qquad 2.50$$

where D is a constant.

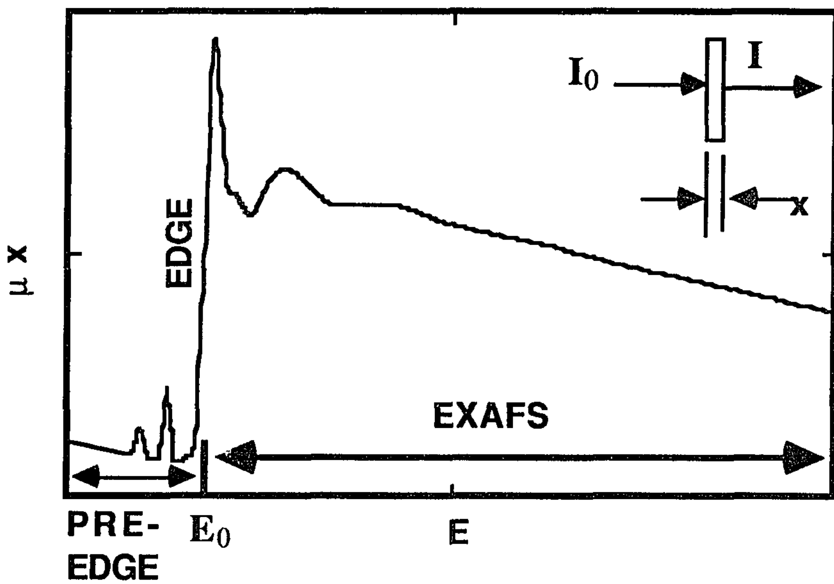

Figure 2.17 Typical X-ray absorption spectrum μx vs E (Ref. 46).

In the k space, $\chi(k)$ can be expressed, in more detail, in the structure parameters as:

$$\chi(k) = S_j A_j \sin(2kr_j + \theta_{ij}(k)) , \qquad 2.51$$

with $A_j = S_j N_j S_i(k) F_j(k) \exp(-2\sigma_j 2k^2) \exp(-2r_j/\lambda_j(k)) / kr_j^2$,

where N_j is the number of neighboring atoms of the jth shell, $S_i(k)$ a reduction factor, and $F_j(k)$ is the backscattering amplitude function. The term $\exp(-2\sigma_j 2k^2)$, is the Debye -Waller factor, taking into account the thermal vibration and static disorder of the atoms in the jth shell. The term $\exp(-2r_j/\lambda_j(k))$ is due to the photoelectron inelastic scattering with a mean free path of $\lambda_j(k)$. $\theta_{ij}(k)$ is the total phase shift experienced by the photoelectron. It is described by:

$$\theta_{ij}{}^{l}(k) = \theta_i{}^{l}(k) + \theta_j(k) - l\pi, \qquad 2.52$$

where $\theta_i{}^{l}(k)$ and $\theta_j(k)$ are the phase shift of the absorber and the backscatter, $l=1$ for K and L_I edges and $l=2$ or 0 for $L_{II,III}$. $\sin(2kr_j + \theta_{ij}(k))$ is the oscillation part due to the modulation from the presence of the other atoms in an EXAFS spectrum.

In Figure 2.18, a simplified model of the interaction of fast electrons with an atom is shown. When the inner shell electrons are excited by the inelastic scattering of fast electrons, the EELS spectrum can exhibit EXAFS - like oscillations. Such observations have been reported in recent literature.[47-48] In the EELS, the scattering cross section[27] (under the Born approximation) can be described as:

$$\frac{d^2\sigma}{d\Omega d\omega} \approx \frac{\left|\left\langle \phi_f \left| \sum_j \exp(i\vec{q}.\vec{r}_j) \right| \phi_i \right\rangle\right|^2}{a_0^2 q^4} \delta(E_i - E_f - h\omega) \,, \qquad 2.53$$

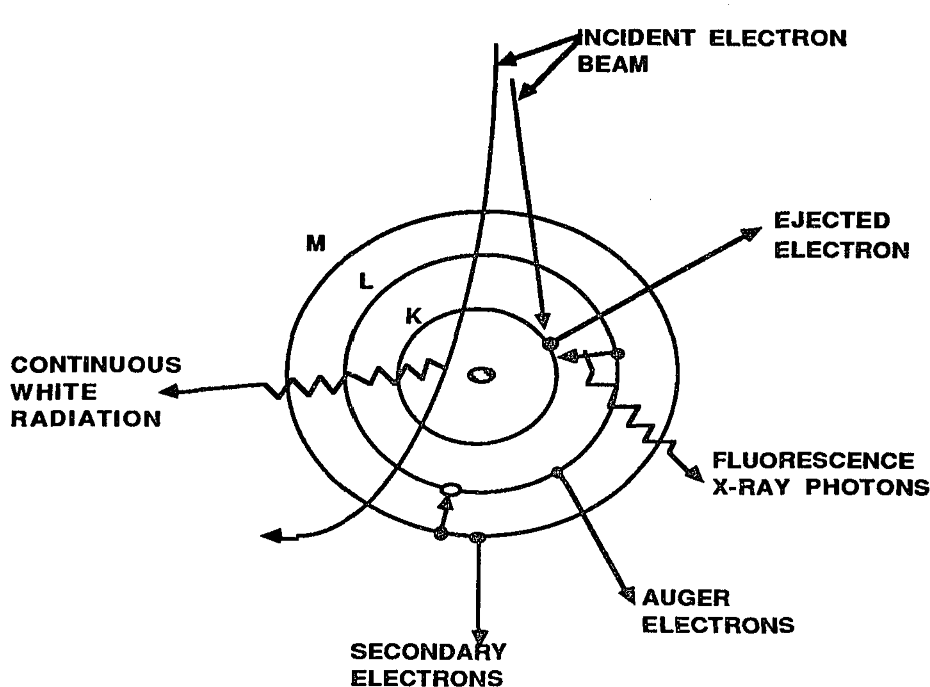

Figure 2.18 Interaction of fast electrons with an atom. Many different transitions may happen after an atom is ionized by an energetic incident electron. Continuous white radiation may be produced while the incident electron is decelerated in the field of the nucleus. [ref. 45]

where $\hbar\omega$ is the energy loss in an inelastic scattering, a_0 is the Bohr radius, and q is the momentum transfer. E_i and E_f are the initial and final state energies of the target, respectively. ψ_i and ψ_f are the corresponding many - electron determinantal wave functions. In the close shell initial states, the matrix element can be reduced to a single electron matrix element:[49]

$$\left|\langle\psi_f|\sum_j \exp(i\vec{q}.\vec{r}_j)|\psi_i\rangle\right|^2 = \sqrt{2}\left|\langle\phi_f|\exp(i\vec{q}.\vec{r}|\phi_i\rangle\right|^2. \qquad 2.54$$

For small $\vec{q}\cdot\vec{r}$ values, the single electron matrix element can be expressed by the dipole approximation:

$$\frac{d^2\sigma}{d\Omega d\omega} \approx \frac{\left|\langle\phi_f|\exp(i\hat{\varepsilon}_q.\vec{r}_j)|\phi_i\rangle\right|^2}{a_0^2 q^4}\delta(E_i-E_f-\bar{h}\omega)\ , \qquad 2.55$$

where $\hat{\varepsilon}_q$ is the unit vector of q. Comparing Eq. (2.50) with Eq. (2.55), the matrix element for inelastic electron scattering in SEELFS is similar to that for x-ray absorption. This equivalence shows that the oscillating fine structures detected above the core edge in the loss spectra of SEELFS should obey the EXAFS formula (Eq. 2.51) and indirectly give information about the radial atomic distribution function F(R) around the absorbing central atom.

In the reflection electron energy loss spectroscopy measured in the CMA, the scattering angle is very large if one considers only one inelastic scattering step process [Sec. 2.1.2.4]. The radius distance r for a core electron is smaller than 1Å, so that dipole approximation is possible. A comparison between the SEELFS and EXAFS techniques has been reported by M. De Crescenzi et al,[50] and their results made a very strong evidence that both SEELFS and EXAFS spectra have similar fine structures.

2.2 Rutherford Back Scattering and α particles on ^{16}O resonance Elastic Scattering

2.2.1 Introduction

Rutherford backscattering spectroscopy (RBS) is a useful technique to measure the concentration vs depth profiles of elements in the outermost layers of a solid. When using 2Mev He^+ ions, one can get a penetration depth of around 1 μm. Under special circumstances, the depth resolution might be 1 nm.[51] The RBS can provide fast and quantitative profiles that are nondestructive and reliable. Its major applications have been directed towards layered structures containing few elements.

The basic experimental arrangement of a Rutherford backscattering is shown in Figure (2.19).

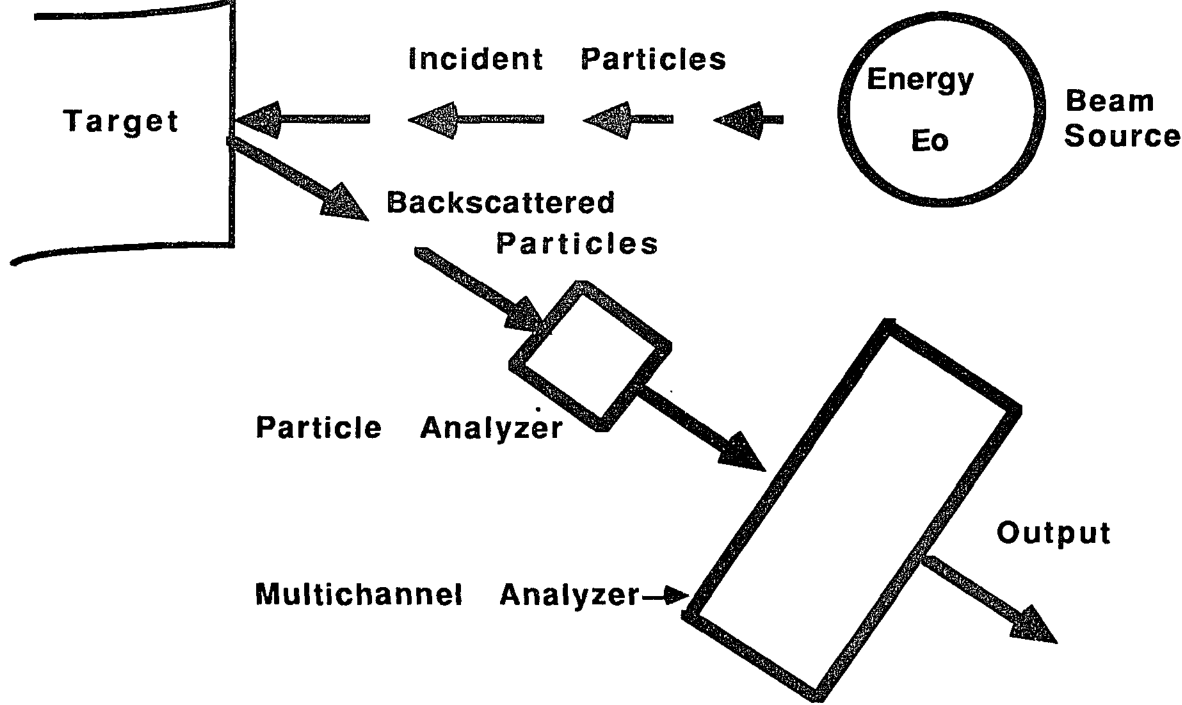

Figure 2.19 Schematic diagram of a typical backscattering experiment in use today.

The ion sources chosen for the probes are usually the light elements such like He^+ and H^+. The energy of acceleration is often kept below the threshold for nuclear reactions or resonance scattering. The probability that the ion particles experience a large angle scattering is about 10^{-5}.

The basic physical concepts of RBS. can be ascribed to the following three parts: (1) kinematic factor, (2) scattering cross section , and (3) energy loss.

2.2.2 Kinematic Factor (K) of Elastic Collision

In an elastic collision (like the RBS), the monoenergetic particles (He^+, H^+) hit a very heavy target nucleus. The target nucleus will remain stable and absorb only a little energy. The backscattering particles (He^+, H^+) will retain most of its incident energy. But, if the projectile particles (He^+, H^+) hit on a light target nucleus, the target will absorb most of the energy and leave the backscattered particles (He^+, H^+) with a low energy. The energy ratio of the projectile particles after and before scattering ($E_{after\ collision}/E_{before\ collision}$) is specified by the kinematic factor (K) ($E_{after\ collision}/E_{before\ collision}$). This factor can be calculated by using the momentum and energy conservation laws. The results of this calculation is :

$$K = \frac{E_{after\ collision}}{E_{before\ collision}} = \left[\frac{m\cos(\theta) + (M^2 - m^2\sin^2(\theta))^{1/2}}{m+M} \right]^2 , \qquad 2.56$$

where m, M is the mass of the projectile, target separately; θ is the scattering angle. From Eq. 2.56, we can find that the energy transfer will favor the light target.

2.2.3 Scattering Cross Section

Rutherford backscattering is totally due to coulomb forces, and can be accurately described by the Rutherford differential cross section formula[52]

$$\frac{d\sigma}{d\Omega} = \left(\frac{Z_1 Z_2}{4E}\right)^2 \frac{4}{\sin^4(\theta)} \frac{\{[1-((\frac{m}{M})\sin(\theta))^2]^{1/2}+\cos(\theta)\}^2}{[1-((\frac{m}{M})\sin(\theta))^2]^{1/2}}, \qquad 2.57$$

where Z_1 is the atomic number of the ion, (He^+, H^+) with mass m and Z_2 is the atomic number of the target with mass M. θ is the scattering angle in the laboratory frame. From Eq. 2.57, one finds that more scattering occurs for high atomic number target atoms and less from lower ones. Therefore this technique is more sensitive to small amounts of heavier elements than to light ones.

2.2.4 Energy Loss

When the ion pushes its way through the target, it will lose small amounts of energy due to the collisions with the dense electron sea of the target. This energy loss is almost continuous and passes through the final energy, providing information to the total depth length of the projectile in the target. This energy loss δE per unit length δx (normal to the target surface) depends on the density of the target, the velocity and the identity of the projectile. The relation between energy loss and penetration depth (x) can be specified by.[53]

$$\Delta E = [\varepsilon] N x \qquad 2.58$$

where ε is called the stopping cross section, N the atom density in the target and x the ion penetration depth.

2.2.5 Example

In Figure 2.20, a schematic representation of RBS is shown. From this figure, the large energy change of the projectile can be used to identify the atomic masses in the target from the simple correlation $E_{after\ collision}=KE_o$. One can also see that energy loss distributions are in a broad band. This is because of the small amount of energy losses due to the electron sea of the target. The ions scattering depth in the target give lower energy. So each broad peak gives the profile of the target element concentration versus depth.

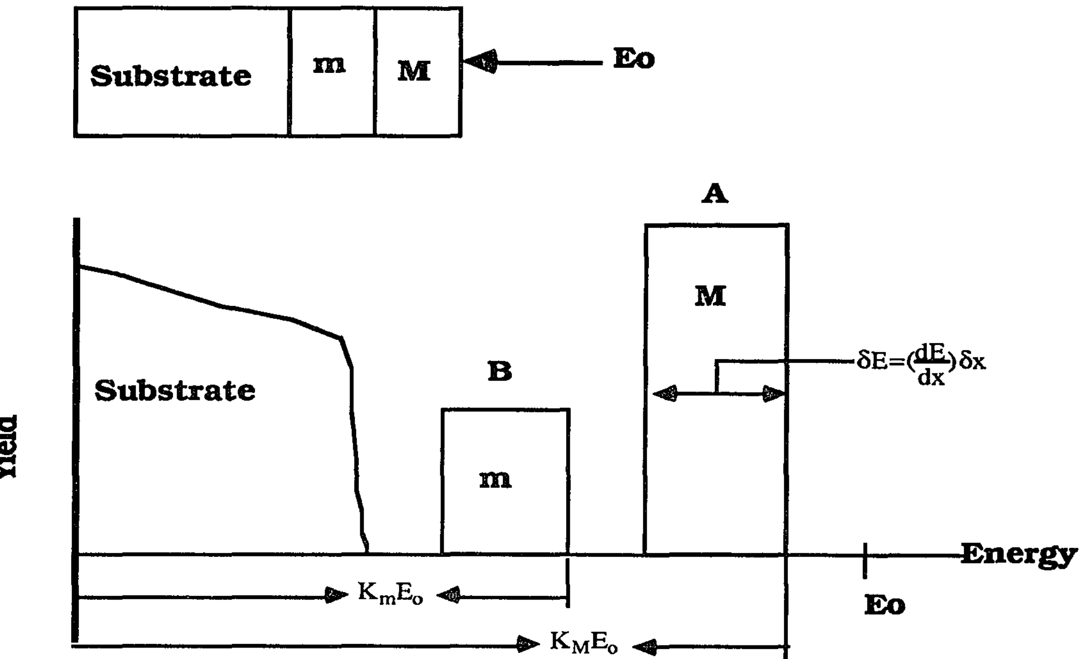

Figure 2.20 A typical backscattering spectrum of an ion at energy E_o. M represents the heaviest element, substrate is the lightest. The heavy mass (M) gives a signal at high energies side, then next m. The high energy edge of each peaks is equal to KE_0[ref. 53].

2.2.6 ^{16}O resonance elastic scattering

Small amounts of low atomic mass mixed in a target with higher atomic mass are very difficult to detect by RBS. However, if one chooses the scattering at the resonant scattering, the scattering cross section will be greater than the pure Rutherford backscattering many times. From reference,[54] we find that the scattering cross section for 3.05 Mev α-particles impinging on ^{16}O is very large compared to RBS. This provides a good way to detect the oxygen.

2.3 X-RAY Reflectivity

2.3.1 Introduction

X-ray has the property of long range penetration in the surface of a solid compared to low energy electron beams. With this characteristic, X-ray reflectivity at small angles is one of the best techniques for measuring the electron density in a solid. The electron density at the interface of the multilayers may be extracted from the parameters obtained by fitting to a theoretical formula. With the electron density information one can determine the composition of the sample. The basic theory is described as follows.

2.3.2 The Refractive Index of Matter for X-rays of Wavelength λ:

It is well known that the complex refractive index (n) obtained from optical measurements can be used to characterized the nonmetallic medium. For the metallic medium, at a certain wavelength of X-rays, the metallic medium is also characterized by its complex refractive index n. The refractive index of matter for X-rays

of wavelength λ is expressed as:

$$n=1-\delta+i\beta\ , \qquad 2.59$$

where

$$\delta=\frac{1}{2\pi}\left(\frac{e^2}{mc^2}\right)\left(\frac{N_o\rho}{A}\right)\left(Z+\Delta f'\right)\lambda^2, \qquad 2.60$$

$$\beta=\lambda\ \mu/(4\pi), \qquad 2.61$$

where $N_O\rho/A$ is number of atoms per unit volume. $Z+\Delta f$ is the real part of the scattering factor. μ is the linear absorption coefficient. ρ is the effective electron density. For low Z materials, ρ is just equal to the total electron density ρ_T. But for high Z materials, there is some fraction (f) of the electrons having binding energies which are greater than the incident x-ray energy, the density ρ should change to $\rho_T(1-f)$.

By ignoring β, we can have $n=1-\delta<1$. This complex refractive index (n) in matter is less than unity, therefore it is totally externally reflected from a surface at small glancing angle incidence. The condition for total external reflection is when :

$$\theta\leq\theta_c\approx\sqrt{2\delta}\approx\sqrt{\rho}\lambda \qquad 2.62$$

For a silicon substrate and λ=1.5405 Å, θ_c = 0.222^0 degree.

2.3.3 Reflectivity and Fresnel formula

(a) Thin Film

The reflectivity of X-rays from a flat, ideal surface can be calculated by using the classical Maxwell equations.[55] For a homogeneous thin film (Figure 2.21,) the Fresnel formula, for a non-magnetic media, $\mu=1$, can be expressed as:

$$r_{12} = \frac{n_1\cos(\theta_i) - n_2\cos(\theta_t)}{n_1\cos(\theta_i) + n_2\cos(\theta_t)} \qquad 2.63$$

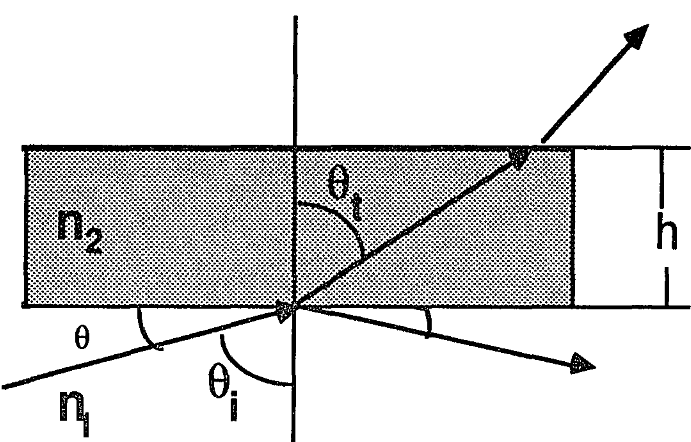

Figure 2.21 A schematic representation of the reflectivity at small angle.

where r_{12} is the reflectivity coefficient, n_1, n_2 are the complex refractive index of media 1 and 2. θ_i and θ_t are the incident and transmission angle with respect to the normal direction. Then the reflectivity is given by Eq. 2.63:

$$R = |r_{12}|^2 = \left| \frac{n_1\cos(\theta_i) - n_2\cos(\theta_t)}{n_1\cos(\theta_i) + n_2\cos(\theta_t)} \right|^2 . \qquad 2.64$$

At a small angle and by using Snell's law $[(n_1\sin(\theta_i) = n_2\sin(\theta_t)]$, the

reflectivity[56] can be modified as following:

$$R = \left| \frac{\theta - \left(\theta^2 - \theta_c^2 + i\beta\right)^{1/2}}{\theta + \left(\theta^2 - \theta_c^2 + i\beta\right)^{1/2}} \right|^2 , \qquad 2.65$$

where θ is defined as in Figure 2.22, θ_c is the total reflection critical angle. It is more convenient to express the reflectivity using the scattering vector by transforming

$$q = 4\pi \sin(\theta)/\lambda; \qquad q_c = 4\pi \sin(\theta c)/\lambda.$$

That is :

$$R_f = \left| \frac{q - \left(q^2 - q_c^2 + 2i/\mu\right)^{1/2}}{q + \left(q^2 - q_c^2 + 2i/\mu\right)^{1/2}} \right|^2 . \qquad 2.66$$

This form is valid for angles greater than about twice the critical angle, where refraction effects are negligible.

For the real surfaces, the interfaces are neither sharp nor flat. Roughness surfaces always exist between these interlayers. Thus the distributions of electron density will not behave like a step function. A common and well known method to take account of this effect is by multiplying by a Gaussian-like factor the R_f. That is:

$$R = R_f \exp(-\sigma^2 q^2). \qquad 2.67$$

where σ is the root mean-square average of the roughness of the surface. The presence of roughness modify the type of equations that are needed to analyze the reflectivity.

(b)Multilayer

The calculation of the reflectivity of a multilayered structure has been treated in many optical textbooks (for example, reference 56-57). One can calculate the multilayer performances either by the Matrix methods or by the iterative use of the single film formula. In the matrix method, each boundary (or each film) is characterized by a matrix (M_i) and the multilayer is characterized by the product Matrix (M):

$$M = M_1 * M_2 * \ldots\ldots\ldots M_n \; . \qquad 2.68$$

The reflectivity is expressed by the elements of the product matrix M:

$$R = \left| \frac{m_{21}}{m_{11}} \right|^2$$

In the iteration method, the reflectivity coefficient[58] is

$$r_{0..n}(q) = \frac{r_{0j} + r^{\dagger}_{j,j+1} \exp(2iq_j d_j)}{1 + r_{0j} r^{\dagger}_{j,j+1} \exp(2iq_j d_j)} \qquad 2.69$$

$$\left(r^{\dagger}_{j,j+1}(q) = \frac{r_{j,j+1} + r_{j+1,j+2} \exp(2iq_{j+1} d_{j+1})}{1 + r_{j,j+1} r_{j+1,j+2} \exp(2iq_{j+1} d_{j+1})} \right),$$

where $r^{\dagger}_{j,j+1}$ is the compound reflectivity amplitude arising at the j, j+1 interface, d_j is the thickness of the j layer.

From the above analysis, one can see that the reflectivity is a function of the refractive index n_i and the thickness d_i. Thus by fitting the data with the theoretical reflectivity formula, then the electron density at a different layer can be figured out. At the interface, if there is a change in chemical state, the electron density will be different from other layers, and it can be extracted from the

parameters after fitting. A successful determination of the oxide layers on thin solid film by measuring the X-ray reflectivity has been reported in reference [59]. The oxide layers usually produce an additional amplitude modulation in the reflectivity, which depends on the average thickness and the density of the oxide layers.

CHAPTER 3

EXPERIMENTAL DESCRIPTION AND SAMPLE PREPARATION

In this chapter, we will make a simple description of the surface science experimental set up.

3.1 Electron Spectroscopy Apparatus

The equipment used in this experiment are

(1) Two ultra high vacuum chamber systems (VSW, Perkin Elmer) which were equipped with

- a. a Cylindrical mirror analyzer (CMA) (in the Perkin Elmer vacuum chamber),
- b. a Hemispherical energy analyzer (in the VSW vacuum chamber),
- c. a High resolution electron gun (EM50) (in the VSW vacuum chamber),
- d. a Sputter ion gun,
- e. a Sample manipulator and holder,
- f. a Heater and thermocouple,

(2) Vacuum pump

(3) Pressure gauge

3.1.1 Cylindrical mirror analyzer equipment

In Figure 3.1, we show one of the set ups in the (Perkin Elmer) vacuum chamber.

The main constituent part of the electron spectroscopy system (AES, EELS, SEELFS) is the electron energy analyzer which is entirely contained inside the high vacuum chamber. In our laboratory,

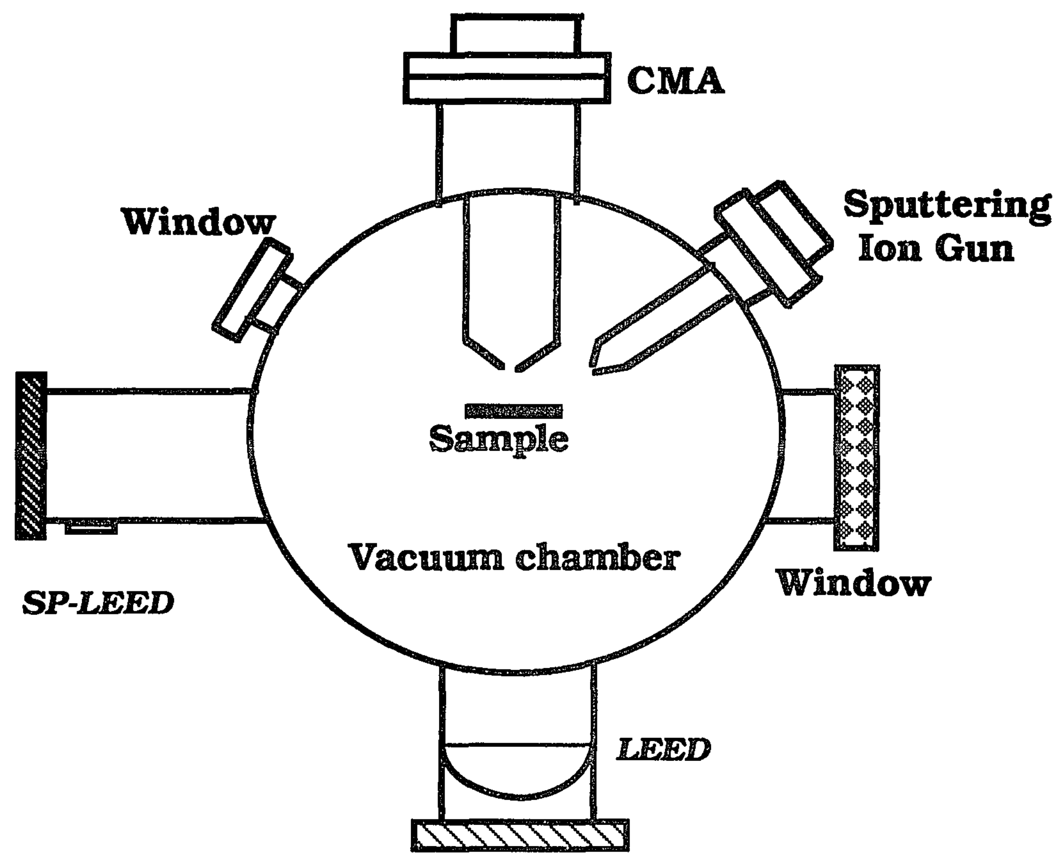

Figure 3.1 A schematic block diagram of experimental set up for the surface science research.

we have a cylindrical mirror analyzer and a concentric hemispherical analyzer(CHA). A schematic diagram of the CMA is shown in Figure 3.2. The schematic diagram for the CHA will be shown 3.1.2.

In Figure 3.2, the electron beam is generated from the electron gun which is mounted coaxially with two cylinders. The two cylinders have radius r_1(inner) and r_2 (outer). The inner cylinder is grounded with the analyzer and the outer cylinder is negative- biased through

terminal Vm. Electrons reflected from the sample pass through an aperture and then deflected by the electric field built up between these cylinders, and then directed through the exit aperture on the CMA to the electron multiplier. The relationship of the energy of electrons chosen to pass through the CMA and the applied voltage Vm is (in our CMA):

$$E_{pass} \sim 1.7 \text{ Vm} \qquad 3.1$$

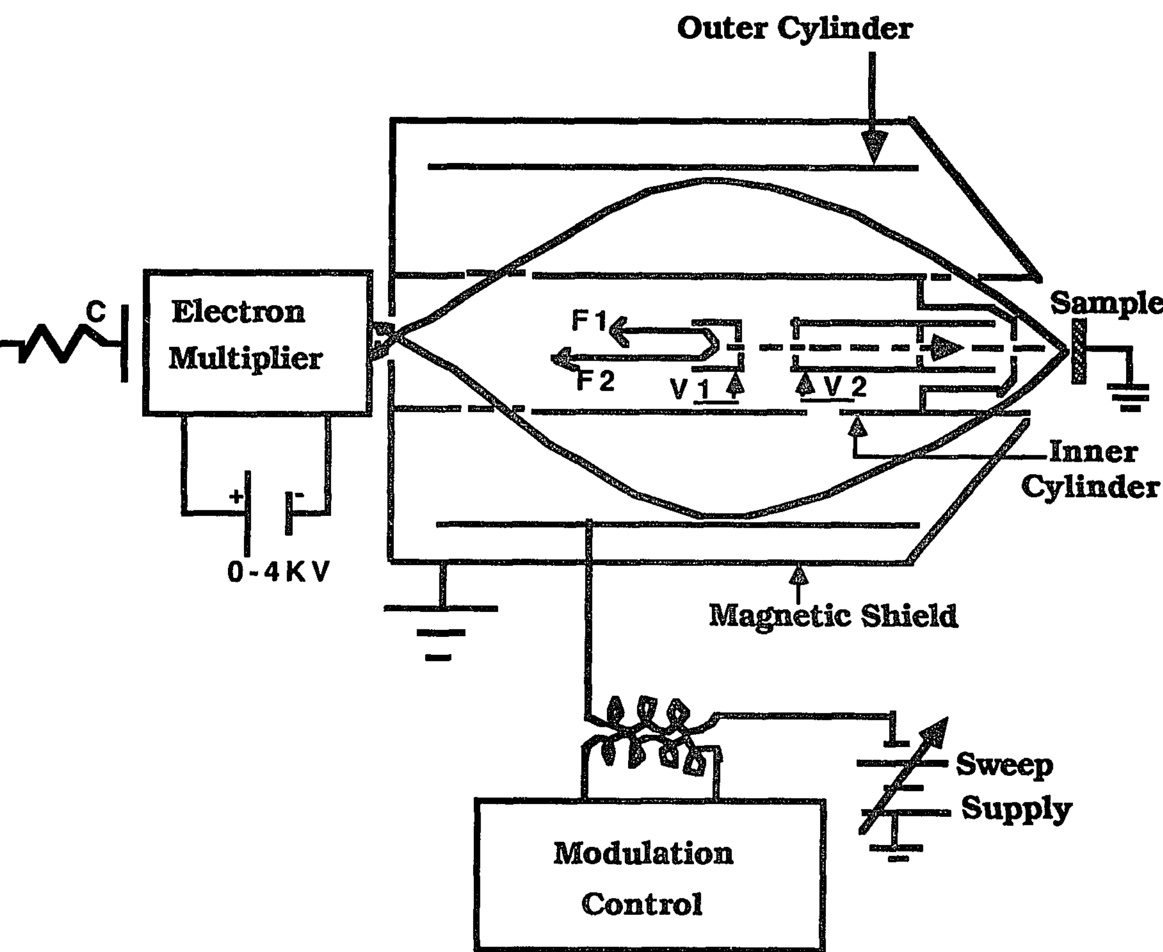

Figure 3.2 A typical Cylinder Mirror Analyzer.

where E_{pass} and Vm are in the unit of electron volts (eV). The constant 1.7 is determined from the analyzer geometry structure.

By changing the bias voltage Vm on the outer cylinder, and by measuring the resulting current simultaneously, the energy distribution function N(E) of the electrons reflecting from the target is produced. The Auger spectrum can be more emphasized if the derivative of the energy distribution is depicted rather than the energy distribution N(E) itself. One way to carry this out is to apply a small AC voltage component to the DC voltage applied to Vm. The amplitude of the applying AC voltage ranges from 0 -10 V. By detecting the first harmonic synchronous signal, by using an electron multiplier and a lock- in amplifier, the first derivative of the energy distribution is obtained. Surface constituents can then be identified. The second derivative mode also can be obtained by detecting the second harmonic synchronous signal.

3.1.2 Angle Resolved Spectroscopy Equipment

In Figure 3.3, we show a flow chart of the angle-resolved electron spectroscopy set up. The energy analyzer and the electron gun are installed in the VSW high vacuum chamber. The incident electron beam is generated from the electron monochromator, after scattering, the reflected electrons are detected and analyzed by the hemispherical analyzer. The detected signal is in the integrated mode.

In Figure 3.4, a schematic diagram of the concentric hemispherical analyzer(CHA) is shown. Two concentric hemisphere surfaces of inner radius R_1 and outer radius R_2 are mounted with the

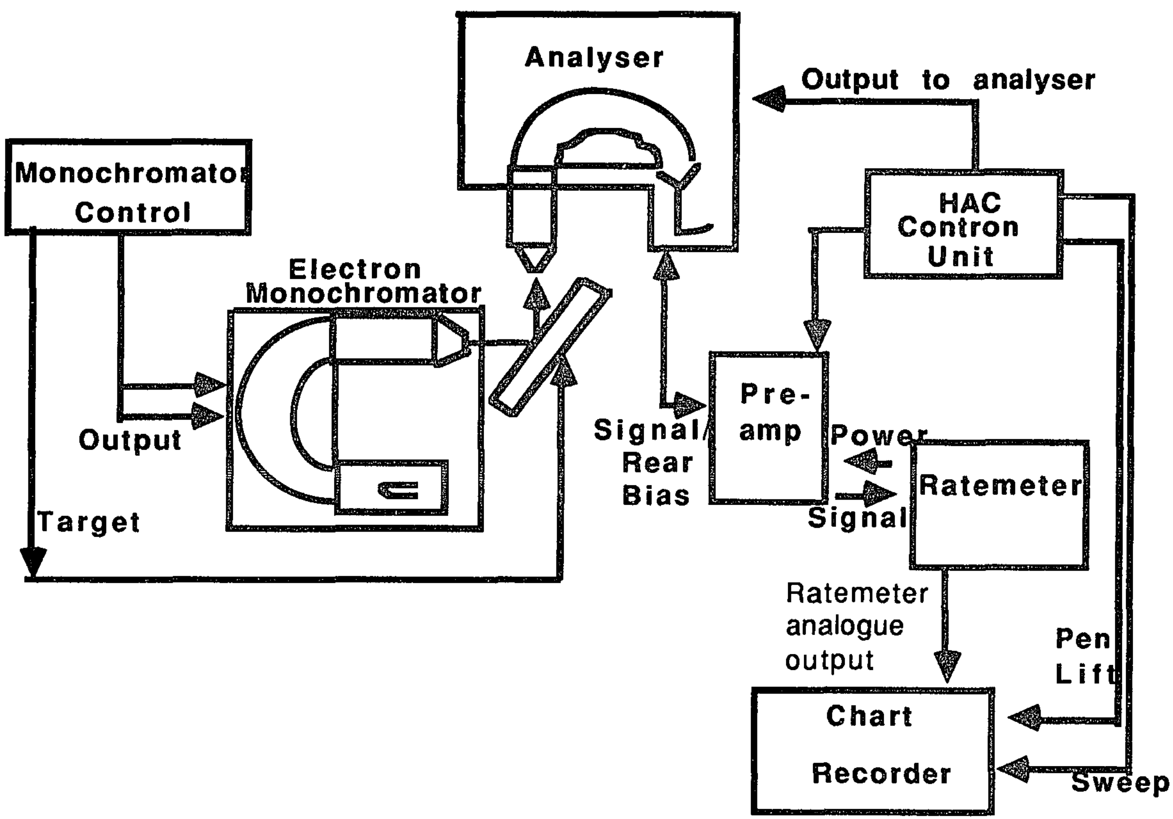

Figure3.3 Typical experimental arrangement using the electron monochromator (EM50) and VSW hemispherical analyzer.

common center of O. R_0 is the mean radius, the entrance and the exit slits are both centered on it. A potential V is applied between the surfaces so that the outer sphere is negative and the inner sphere is positive with respect V_{Ro}, which is the median equipotential surface between the hemispheres. The relationship between the kinetic energy E_{pass} of an electron traveling in an orbit of radius R_0 and applied voltage V is given by the expression:

$$E_{pass} = eV/(R_2/R_1 - R_1/R_2) \qquad 3.2$$

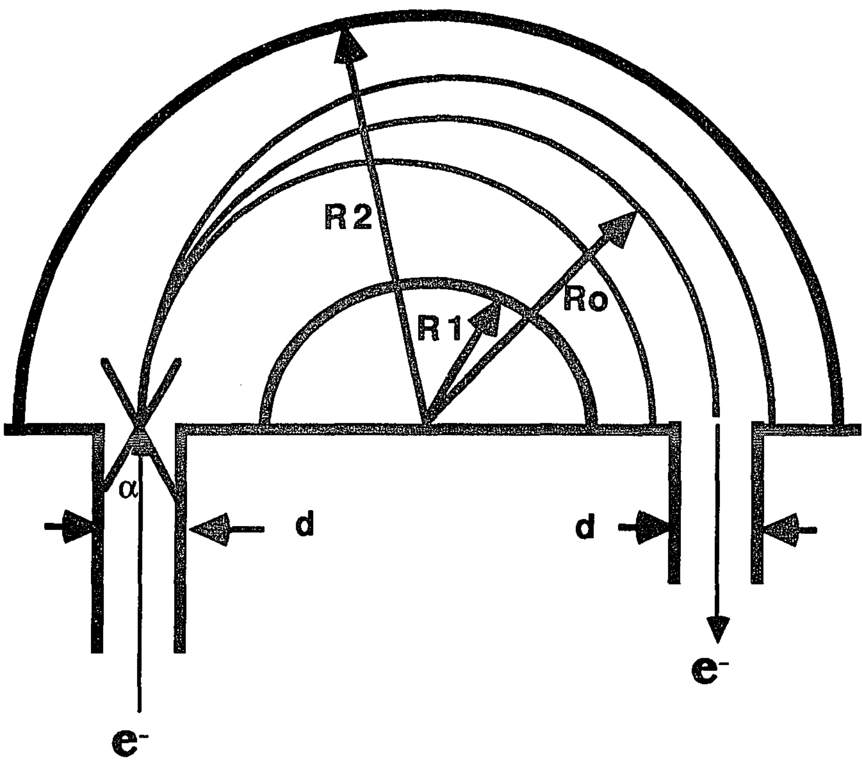

Figure 3.4 A schematic diagram of the Concentric Hemispherical Analyzer(CHA).

3.2 RBS equipment

The RBS equipment is using an already built up Dynamitron accelerator at Brooklyn College. A general set up for measuring the Rutherford Backscattering is shown in Figure 3.5. The accelerator consists of an ionization chamber for creation of the ions, followed by a column where the ions are accelerated. The acceleration high voltage is obtained from a series High Voltage multiplier which is supplied by a RF oscillator. This accelerator can support a maximum voltage around 3.7Mev. The pressure in the beam line is from 10^{-7} to 10^{-6}

Torr. An annular silicon surface barrier detector with resolution around 15KeV was used in all the measurements. Scattering angles were selected around 160^{0}.

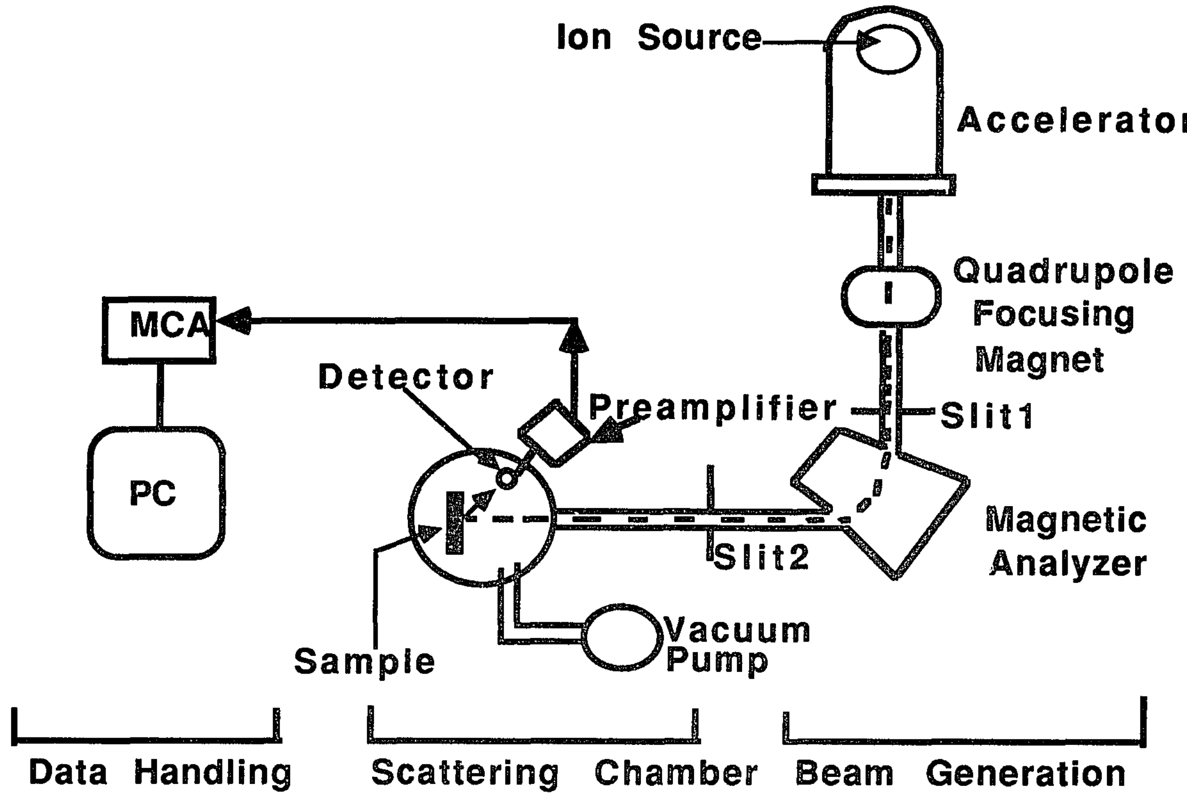

Figure 3.5 A typical schematic diagram of a Backscattering spectrometer system.

3.3 X-ray reflectivity equipment

The X-ray specular reflectivity measurements were performed at room temperature using beam line X-18B and X-6B at the Brookhaven National Synchrotron Light Source facility. Figure 3.6 shows a schematic of the X-ray reflectivity measurement set up. A Si(220) double crystal monochromator was used for selecting the synchrotron

radiation wavelength. The sample was mounted on a high precision goniometer attached to a two axes Huber diffractometer. The monochromatic X-ray beam passes through the beam monitor chamber which measures the intensity of incident beam I_o, then the beam strikes the sample. Reflected X-ray was detected by a NaI scintillation detector, and then digitized and collected using computer interfaces.

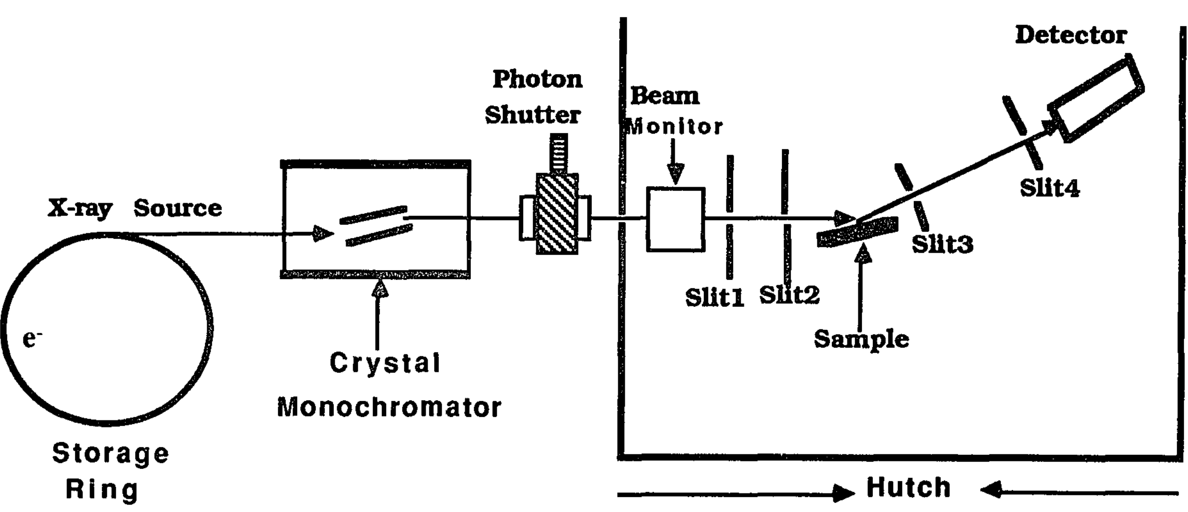

Figure 3.6 A typical X-ray reflectivity experimental set-up.

3.4 SAMPLE PREPARATION

3.4.1 W/C, Ti/C Multilayers[60]

The multilayers (W/C, Ti/C) were prepared using an argon plasma rf-sputter deposition system. The substrates were placed on a water cooled platform rotates below the carbon (reactor-grade ATJ graphite) or W/Ti (99.95%) targets. A shutter with a circular opening allows the preparation of several samples under almost identical conditions. The base pressures were $5x10^{-5}$ Pa and the argon pressure during deposition (~0.15Pa) was controlled using a capacitance manometer at argon gas flow rates of ~0.4cc/sec. Water vapor was gettered from the Ar sputtering gas by flowing it through a titanium gettering system.

The silicon single crystals [111] were micropolished by a combined chemical-mechanical process. Before deposition, the substrates were heat treated at 400^{0}C for 2 hours. The targets were pre-sputtered for ~2hours in order to clean surface contamination in the targets. The samples were characterized using Microcleave Transmission Electron Microscopy[61] and X-ray diffraction. The W/C sample modulations were between 11 to 30 Å. The W and C thicknesses were from 5.9 to 10 Å, and from 4.7 to 20 Å respectively. The number of periods was different in each sample, and the top layer was terminated by carbon. The Ti/C sample modulations were between 27 to 38 Å. The Ti and C thicknesses were from 14.7 to 25.7 Å, and from 11.5 to 12.1 Å respectively. The number of periods was in the average around 50, and the top layer was terminated by carbon.

3.4.2 Si/C Multilayers[62]

The silicon/carbon multilayers were prepared by magnetron sputtering of 5N silicon and 4N graphite targets. The substrates were placed on a water cooled platform rotating below the Si and C targets. The base pressure of the system was around 10^{-9} Torr. The substrates used for preparing the multilayers were α-Al_2O_3 (1120) and float glass, the substrate temperature during growth was maintained around 300 K. The samples were characterized by low and wide angle X-ray scattering using an in house facility. The total thickness of the samples were between 900 to about 2000 Å. The carbon layer thicknesses were between 10 to 35 Å, and the silicon layer between 5 to 35 Å thick. The modulation wavelength of the samples was determined to be from 14 to 62 Å.

CHAPTER 4
INTERFACE STRUCTURE AND STABILITY IN W/C MULTILAYERS

4.1 Introduction

Recent progress in sputtering deposition technologies have made possible the preparation of multilayers from refractory metals like tungsten. The interest in metallic multilayers arises from the possibility of producing new materials with novel properties. In recent years there has been great interest in the fabrication of W/C multilayers that can find applications as X-ray mirrors in the soft X-ray and UV range.[63-66] Tungsten-carbon compounds posses extraordinary material properties, from both a physical and a chemical point of view. The tungsten carbides (WC/W_2C) have high melting point, extreme hardness, and metal like thermal and electrical conductivities.[67] Tungsten-carbide can be used as a catalyst for a number of reactions which are readily catalyzed by platinum, but not by tungsten metal.[68,69] The tungsten carbides are chemically stable at room temperature, they oxidize in air only at very high temperatures.[70,71] In structural applications, the cemented tungsten-carbides are widely used as tips on drills, metal-cutting tools, wear- resistant, protective coating, etc. All these peculiar properties has stimulated our interest in studying the tungsten/carbon multilayers.

We report in this thesis a systematic study of W/C multilayers. Our main interest is the study of the metal-carbon bonds in the multilayers. A diverse number of experimental techniques were employed in the characterization of the sample, Auger spectroscopy,

electron energy loss spectroscopy (EELS), Rutherford back-scattering, resonance elastic scattering of α-particles by ^{16}O, X-ray diffraction etc. EEL spectroscopy is highly sensitive to variations in the electronic structure at the surface and bulk of the material. Several process contribute to the energy loss spectrum; optical inter/intra band transitions, collective excitation and core ionization and Auger processes[31,38,72,73]. We employed in our experiments the electron reflection geometry. We measure the evolution of the EEL spectra of the W/C multilayers at high temperatures. The objective was to investigate the electronic structure of the multilayers under such conditions, and to understand whether the artificially constructed structures offer an advantage over the naturally occurring crystalline structures in maintaining high-temperature stability in an oxygen containing environment. Our research was directed towards characterization of the W/C interfaces, and their possible role in determining the material properties of the multilayers.

4.2 Experimental

We employed a variety of techniques to study the interface structure. We used Rutherford Back Scattering (RBS), resonance elastic scattering of α-particles by ^{16}O, Auger spectroscopy (AS), electron energy loss spectroscopy, and surface electron energy loss fine structure (SEELFS) to characterize the sample.

The RBS measurements were performed using the Brooklyn College CUNY Dynamitron accelerator. Two different ion sources (p,

α) were employed as the probe in this investigation. We also used the oxygen elastic scattering resonance of α-particle at 3.05 MeV to detect the presence and distribution of oxygen within the sample. This technique was employed because of its great sensitivity to the presence of oxygen in the sample. If there is oxygen in the sample, then oxide inclusions will be present that will affect the mechanical properties of the multilayers.

For AS, EELS, and SEELFS measurements, the sample was mounted on a Molybdenum sample holder. A Chromel Alumel thermocouple was attached to the surface of the sample. The sample holder was hanging on a high precision manipulator with electron beam heating. The vacuum system used in these experiments has a base pressure around 1×10^{-10} Torr. The AS and EELS measurements were taken using a cylindrical mirror analyzer. The first derivative mode was used for AS and the second derivative for the EELS measurements, with a resolution $\Delta E/E = 0.6\%$. The modulation voltage used for the measurements was 1 eV p-p. The SEELFS measurements were carried out using an electron primary energy of 2200 eV and a modulation of 8 eV p-p.

The EEL spectra were measured at room temperature using different electron primary energies, from 100 to 1800 eV. The temperature dependence of the EEL spectra were measured between 293 K and 973 K. The oxidation of the multilayers were studied by exposing the material to 60 L ($L=10^{-6}$ Torr) of oxygen at 773 K. AS measurements were taken before and after exposure to oxygen.

The X-ray specular reflectivity measurements were carried out at

room temperature using beam line X-6B and X-18B at the National Synchrotron Light Source facility at Brookhaven National Laboratory. A Si(220) double crystal monochromator was used for selecting the synchrotron radiation wavelength. Horizontal and vertical slits were placed before the monochromator to define the beam size prior to monochromatization of the radiation. Inside the experimental hutch a second slit was placed for defining the monochromatic beam and a beam monitor was place after this slit to measure the photon flux before scattering from the sample. A third slit was placed after the beam monitor (ionization chamber) for trimming of the slit scattering, but causing no reduction in the collimated photon beam. The sample was mounted on a high precision goniometer attached to a two axes Huber diffractometer. After the sample a fourth slit was placed to cut down any scattering not originating in the sample. The last slit was placed before a NaI scintillation detector and was set wide enough to accept all the specularly reflected scattering. At very low angles the X-ray intensity is very large and this will saturate and damage the detector. To avoid this problem at very low angles we used a set of calibrated aluminum absorbers to reduce the beam intensity reaching the detector. In X-ray specular reflectivity measurements, one must determine the angle of incidence with great accuracy. The alignment of the sample and diffractometer was carried out using a methodology similar to that described in reference.[56] The energy of the X-ray used in this investigation was 9.988 KeV. The spectra from different beam lines for the same sample were totally reproducible.

Table 4.1 gives the list of samples studied in this work.

Table 4.1

W and C composition of the multilayers

W Thickness (Å)	C Thickness (Å)	No. of Periods
6	5	200
7	7	150
10	20	150
10	13	65

4.3 Results and Discussion

RBS and α-particles resonance scattering from ^{16}O were used to obtain a compositional profile of the multilayers. In Figure 4.1 we plotted the RBS spectra W/C=7Å/7Å corresponding to α-particles with energies of 3.065 to 3.04 MeV. One observes the dominant scattering by the high Z element, tungsten, and the silicon substrate contribution. We detected also the presence of small amounts of argon (which is incorporated in the samples during sputtering). Oxygen only appears at a beam energy of 3.05 MeV and with a very narrow peak. From reference [74] we know that 3.05 MeV is the energy for the resonance elastic scattering of α-particles by ^{16}O. At this energy the scattering cross-section is very large compared to Rutherford back scattering. We increased the beam energy, so that the resonance could occur not only on the sample surface but also in the bulk. The results were negative, indicating that the oxygen in the multilayer is present only on the surface. AS measurements show also the presence of surface oxygen.

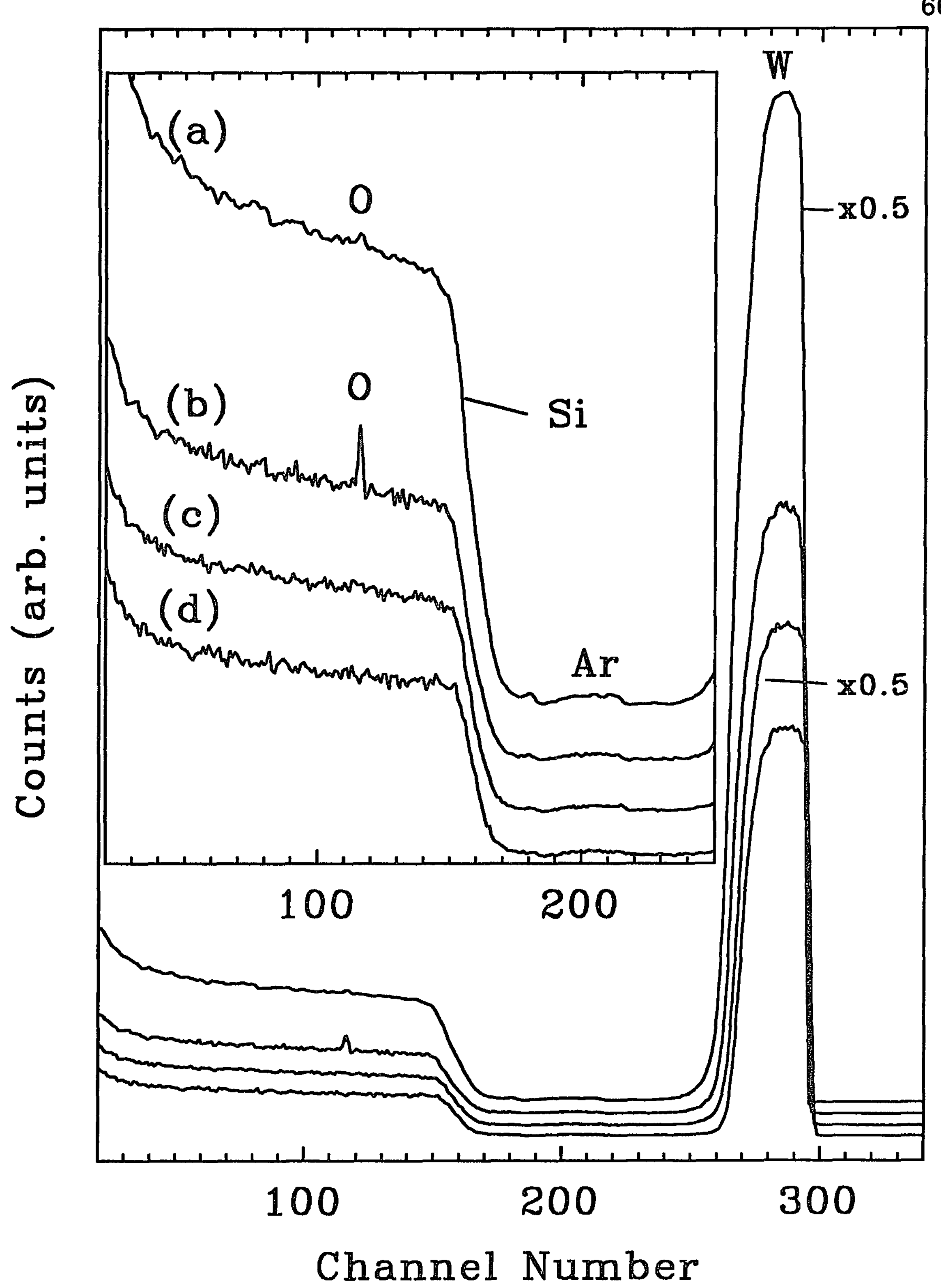

Figure 4.1. RBS spectra for a W/C multilayer (W/C= 7 Å/7 Å), α-particles at energies of (a)3.065, (b)3.05, (c)3.045, (d)3.04, MeV.

Figure 4.2. RBS spectrum for a W/C multilayer (W/C= 7 Å/7 Å) using protons at 3.0 MeV.

The carbon signal cannot be observed at this energy range (~3.05 MeV), because its cross-section is at the lowest value.[75] When we changed the ion source to protons and turned the energy to 3.0 MeV, then the carbon signal was easily detected, see Figure 4.2.

EELS is sensitive to the surface and bulk electronic properties of the material. One important aspect of this spectroscopic technique is the possibility of obtaining a non destructive composition depth profile of the material by changing the impinging electron energy. The inelastic scattering is proportional to Im $(-1/\varepsilon(q,\omega))$ for the bulk, where $\varepsilon(q,\omega)$ is the dielectric function of the crystal. The surface inelastic scattering is proportional $\mathrm{Im}(-1/(1+\varepsilon(q,\omega)))$. In EELS, the longitudinal part of the electric field is involved, while in optical processes the transverse field is involved. In our study we use as standards the loss functions calculated from optical measurements for graphite and tungsten[76,77,78]. Since up to now, there is not any optical measurements for the W/C multilayers. We try to construct the loss function in two different ways. The first way is to treat the dielectric constants of graphite and tungsten separately. The second way is to treat the two set of dielectric constants combined in a method analogous to capacitor in series. In Figure 4.3 we plot the bulk loss function for tungsten and graphite, and the surface loss function for graphite separately.

The volume and surface losses of graphite are very easy to observe in Figure 4.3. The peak around 6.7 eV is due to the bulk loss function $-\mathrm{Im}(1/\varepsilon)$, plasmon excitation of the π electrons[76], and at 25.3 eV by the π electrons plus σ electrons.[76] The surface plasmon

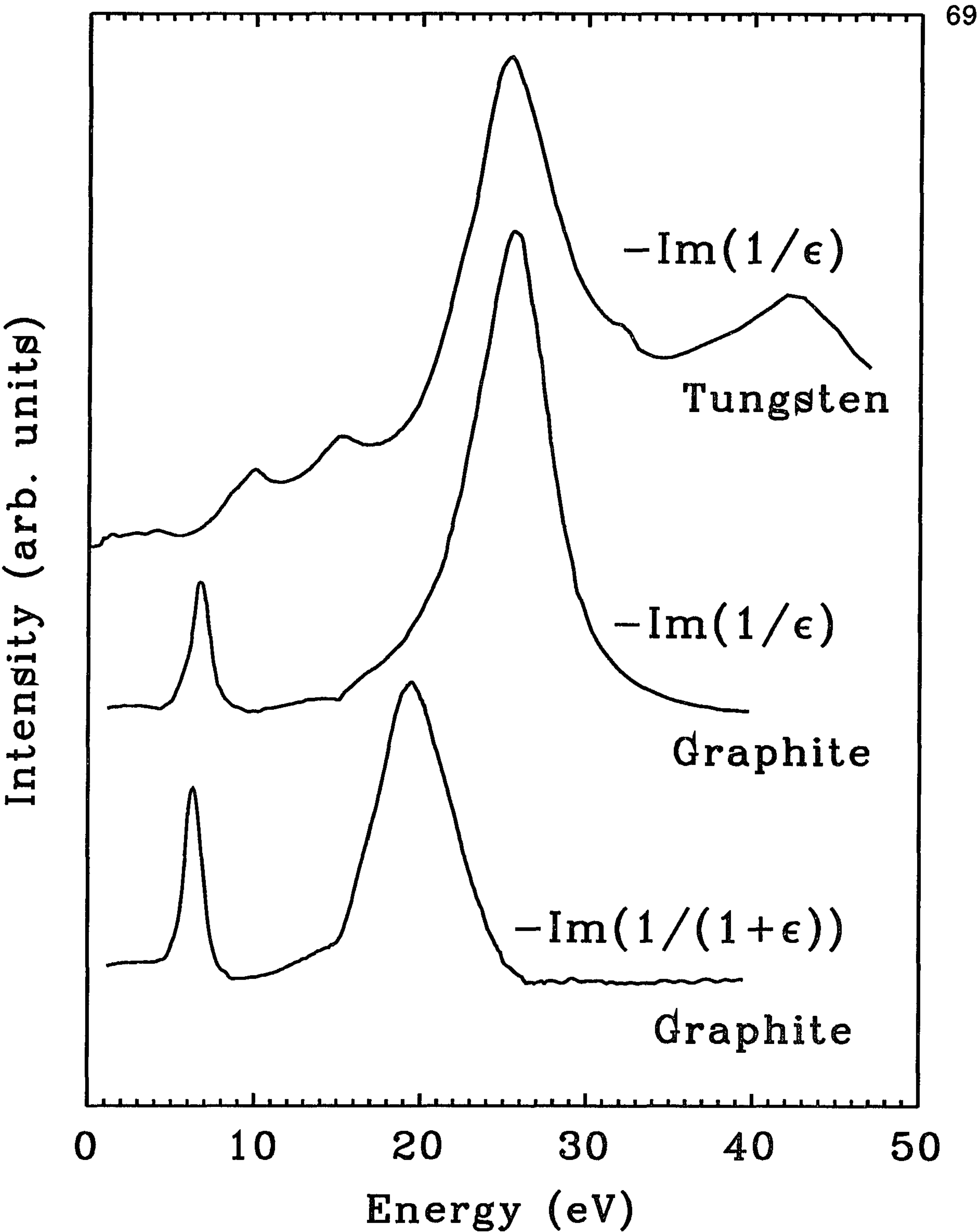

Figure 4.3. Optical dielectric loss function for graphite and tungsten.

produced by the π electrons is at about the same energy as the bulk plasmon, but the high energy surface plasmon (19.5 eV) is well separated from the bulk plasmon at 25.3 eV.

The loss peaks at energies of 10.0, 15.2, 25.3 eV for the bulk loss function of tungsten have been identified as bulk plasmons.[18] These bulk plasmons (except the one at 15.2 eV) also have been observed by Luscher[79] using EELS. The peak around 31.5 eV in tungsten is produced by the core (N_{VI}, N_{VII}) ionization.[80] The high energy broad peak observed at 43 eV in Figure 4.3 is due to the core ionization of O_{II}.[80]

In the combination method, we use the basic series-capacitor model to calculate the loss function from the two set of dielectric constants (dielectric constants of W and C). Since the (W/C) multilayers are fabricated layer by layer, the whole package looks like a condenser constructed by two different dielectric media. By using this method, the $1/(\varepsilon_{total})$ can be described as:

$$\frac{1}{\varepsilon_{total}} = \underbrace{\left(\frac{1}{\varepsilon_{c1}} + \frac{1}{\varepsilon_{w1}}\right)}_{\text{1st bilayer}} + \underbrace{\left(\frac{1}{\varepsilon_{c2}} + \frac{1}{\varepsilon_{w2}}\right)}_{\text{2nd bilayer}} + \ldots\ldots \underbrace{\left(\frac{1}{\varepsilon_{cN}} + \frac{1}{\varepsilon_{wN}}\right)}_{\text{Nth bilayer}} . \qquad 4.1$$

In the case of EELS measurements, because the inelastic scattering is very strong, it is more reasonable to introduce the mean free path factor into Eq. 4.1. By multiply a thickness (t) and mean free path (λ^{*1}) dependent factor $e^{-f(t,\lambda)}$ in each terms in Eq. 4.1, we can get the new $1/(\varepsilon_{total})$. The result is:

---

[1] $\lambda^* = A/E^2 + BE^{1/2}$ (Where E is the primary energy, A,and B are constants)[81]

$$\frac{1}{\varepsilon_{total}} = \left(e^{-f(t_{c1},\lambda)}\frac{1}{\varepsilon_{c1}} + e^{-f(t_{w1},\lambda)}\frac{1}{\varepsilon_{w1}} \right) + \left(e^{-f(t_{c2},\lambda)}\frac{1}{\varepsilon_{c2}} + e^{-f(t_{w2},\lambda)}\frac{1}{\varepsilon_{w2}} \right) +$$

$$\ldots \left(e^{-f(t_{cN},\lambda)}\frac{1}{\varepsilon_{cN}} + e^{-f(t_{wN},\lambda)}\frac{1}{\varepsilon_{wN}} \right)$$

$$= \mathrm{Re}\left(\frac{1}{\varepsilon_{total}}\right) + \mathrm{Im}\left(\frac{1}{\varepsilon_{total}}\right) \quad . \qquad 4.2$$

Then the loss function can be extracted from 4.2 using the relation:

$$-\mathrm{Im}\left(\frac{1}{\varepsilon}\right) = -\mathrm{Im}\left(\frac{1}{\varepsilon_{total}}\right) \quad .$$

In Figures 4.4a-4.4b, we plotted the combined dielectric loss function as a function of primary energies (E_p). The bilayer number (N) applied in Figures 4.4a and 4.4b is 4. The thickness of W/C in Figures 4.4a and 4.4b are 6Å/5Å and 6Å/2Å respectively. The aim for choosing different of W/C thickness is just for a comparison. From these two figures, we can see that the dominate peaks (at energy 7eV and 25eV) are from carbon, some small wriggles (at energy 10ev,15ev and 32eV) are from the tungsten. (The thinner C is, the clearer tungsten signal appears.) The characteristic transitions are obviously not as clear as those from Figure 4.3. In this model of expression, the loss function can only be shown up to 40eV, since the provided dielectric constant values are good only up to 40eV.

We measured the electron energy loss spectra at room temperature as a function of primary energies (from 100 to 1800 eV). The EELS spectra for the W/C= 6Å/5Å are shown in Figures 4.5 and 4.6. Similar spectra were obtained for the other samples. The inset

Figure 4.4(a) Combined optical dielectric loss function from graphite and tungsten with W/C=6Å/5Å and total bilayer (N)=4.

Figure 4.4(b) Combined optical dielectric loss function from graphite and tungsten with W/C=6Å/2Å and total bilayers(N)=4.

is an expansion of the spectra from 10 eV to 70 eV. The positions of the most prominent energy loss peaks are listed in Table 4.2 and have been labeled as a to i.

At primary energies of 100 and 150 eV, the EEL spectra have the characteristic losses of graphite. At these energies the primary beams can only penetrate a few angstroms, the carbon top layer. We

Table 4.2

Electron Energy Losses of W/C=6Å/5Å.

	LOSS PEAKS (eV)								
ENERGY [Ep (eV)]	a	b	c	d	e	f	g	h	i
100	3.6	6.1	13.6	20.7	26.6				
150	3.6	6.1	13.7	20.7	25.4				
200	4.4	7.5	13.7	20.8	25.7	35.0			
250		5.1	13.4	20.7	25.4	35.0		52.0	
300		6.0	13.7	20.9	25.3	34.9		54.2	
350		6.6	13.7	20.8	25.2	34.5	43.8	53.4	
400		7.4	14.3	21.4	25.3	34.6	43.8	53.4	
500		10.3	14.5		25.7	34.8	44.0	53.8	
800			15.3		25.3		43.9	53.7	
1000					24.6		44.2	53.7	80.6
1400					25.4			53.1	80.2
1600					25.5			52.9	80.0
1800					25.5			53.6	80.0

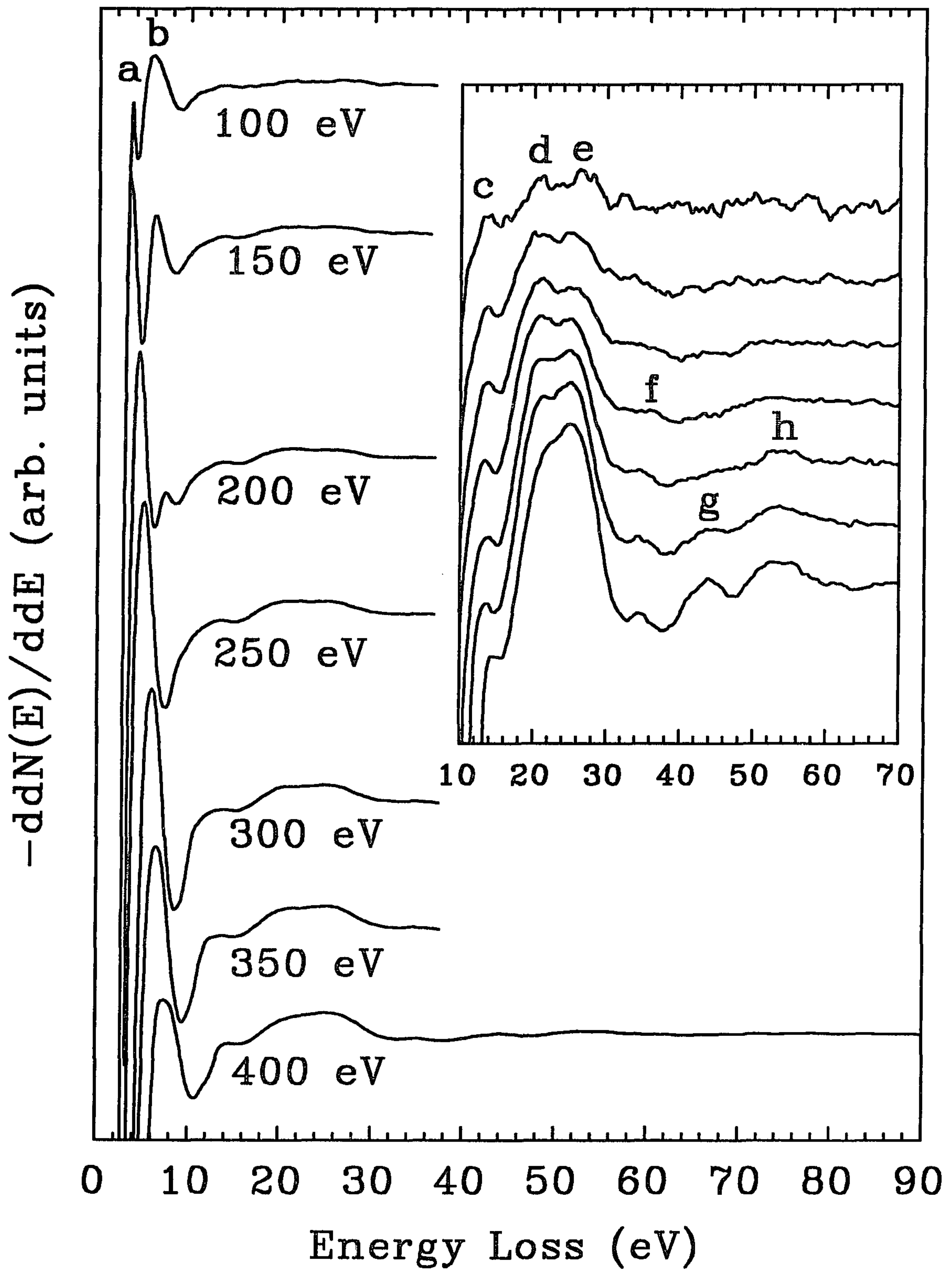

Figure 4.5. EEL spectra at room temperature before heating for a W/C multilayer (W/C= 6 Å/5 Å). The spectra were taken for primary energies from 100 to 400 eV.

Figure 4.6. EEL spectra at room temperature before heating for a W/C multilayer (W/C= 6 Å/5 Å). The spectra were taken for primary energies from 500 to 1800 eV.

obtained similar spectra for the other W/C multilayers when using the same electron primary energies. Peak a centered at 3.6 eV is far away from the π electrons bulk/surface plasmons of graphite. This peak is probably an inter/intra band transition of graphite. Peak c at 13.6 eV is assigned as an π->σ interband transition from p_3^- to p_3^+ in a single layer of graphite band structure calculated by Painter et al.[82] (see appendix B). The results of the unpolarized near normal reflectance measurements on natural graphite,[76] demonstrated a broad peak in the imaginary part of the dielectric constant at 14.5 ± 0.5 eV. Wills et al.[83] observed a peak at 13.5 eV in photoemission and secondary electron emission measurements. Therefore the assignment of peak c is in good agreement with band calculation and other experimental measurements. We assigned peak b as the combination of surface and bulk plasmon of the π electrons, peak d as a surface plasmon and e as the bulk plasmon of the π +σ electrons of the graphite layer.[76]

When the primary energy increases to 200 eV a slight shift in energies take place for peaks a and b. At higher energy losses, while peaks c, d, and e remain at the same positions, a new broad weak peak appears around 35 eV. This peak (f) is the (N_{VI}, N_{VII}) core ionization from tungsten. The emergence of this peak suggests that the beam had penetrated to the tungsten layer at this primary energy, as expected. At this primary energies the EELS measurements suggest that the interface W/C has not reacted in this sample. By contrast, we detect the presence of a pronounced electron energy loss peak around 9 eV in a multilayer with W/C= 7Å/7Å. The latter loss peak appears to

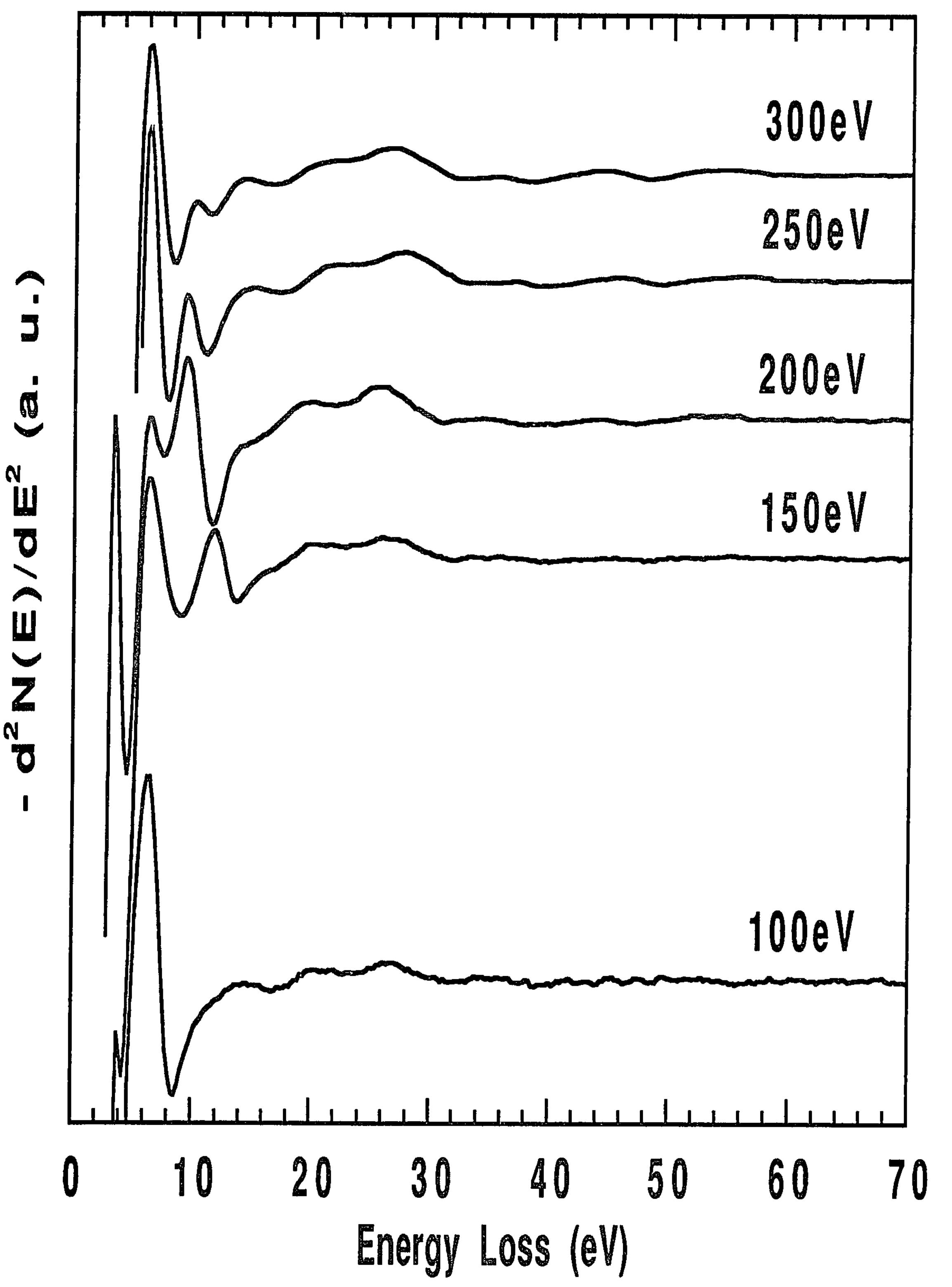

Figure 4.7. EEL spectra before heating for a multilayer with W/C=7Å/7 Å.

be characteristic of the interface for this particular sample, see Figure 4.7.

When the primary energies increases to 250, 300, and 350 eV the relative intensities of peak d and e start to change. We attribute this to the fact that the EEL spectra will show a larger contribution from the bulk of the multilayer. The intensity of peak f increases and peak g (the O_{II} core ionization of tungsten) is observable. Peak h is identified as due to bulk multiple plasmon losses. When the primary energy increases over 500 eV, the contribution of the energy losses at f and g diminishes. All the multilayer samples show similar spectra, with different threshold energies towards the appearance of the tungsten metal features in the EEL spectrum.

We measured the electron energy loss spectra of the samples as a function of temperature. Our objective was to use this technique to investigate the possible reactions taking place at the interface W-C. In Figures 4.8 and 4.9 we show the EEL spectra taken at different temperature for Ep=200 and 350 eV. We observe an irreversible phase transition at temperature between 873° K and 973° K. The EEL spectra at 973° K are very different from those spectra measured at lower temperature. The electron energy losses at 13.5 and 20.6 eV disappeared, see Table 4.3. A new peak(α_2) appears centered at 9.6 eV (10.8 eV for Ep = 350 eV). The peaks corresponding to the N_{VI} and N_{VII} core ionization of W located at 34 eV are now very well resolved. This spectrum has some of the characteristic losses of tungsten.[79] However some of the features of the EEL spectrum suggest the presence of a new compound. All the samples show a similar behavior at high temperatures. We were limited in our

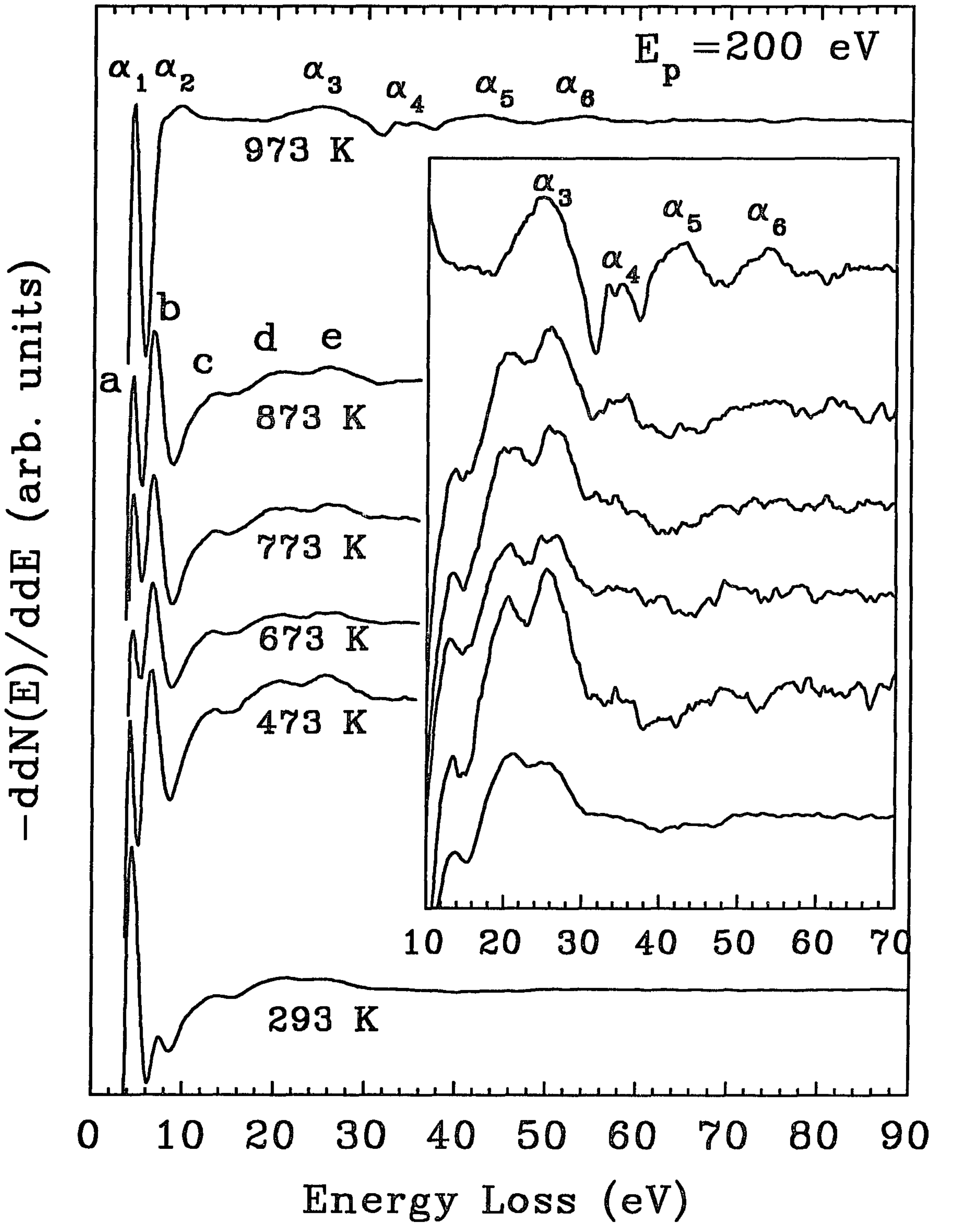

Figure 4.8. EEL spectra as a function of temperature for a 200 eV electron primary energy (W/C= 6 Å/ 5 Å).

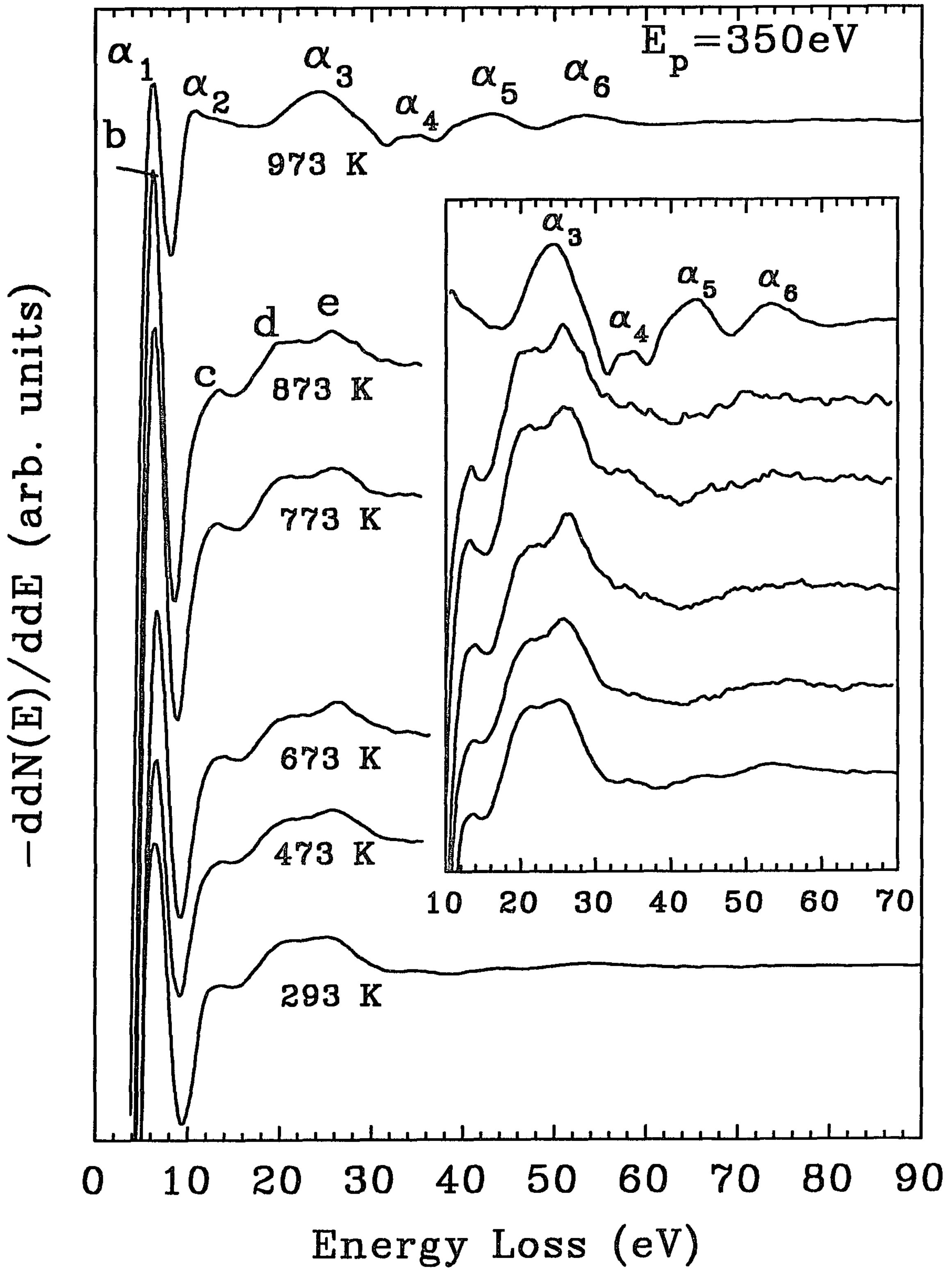

Figure 4.9. EEL spectra as a function of temperature for a 350 eV electron primary energy (W/C= 6 Å/ 5 Å).

our high temperature measurements to maximum of about 1000 K, due to the thermal properties of the silicon substrate used to grow the multilayers.

We measure the AS spectrum after heating the sample in UHV, see Figure 4.10 line (b). The tungsten signal has increased. This reflects the fact that some carbon migration into the W layer took place.

Table 4.3
Electron energy losses of W/C=6Å/5Å as a function of temperature (Ep=350 eV)

Temperature (K)	LOSS PEAKS (eV)								
	a	b	c	d	e	f	g	h	i
293		6.6	13.7	20.8	25.2	34.5	43.8	53.4	
473		6.5	13.7	21.1	25.7				
673		6.5	13.7	20.9	26.0				
773		6.5	13.3	20.8	26.4				
873		6.3	13.4	20.4	25.9				
	α1	α2			α3	α4		α5	α6
973	6.3	10.8			24.5	33.5-35.2		43.2	53.3

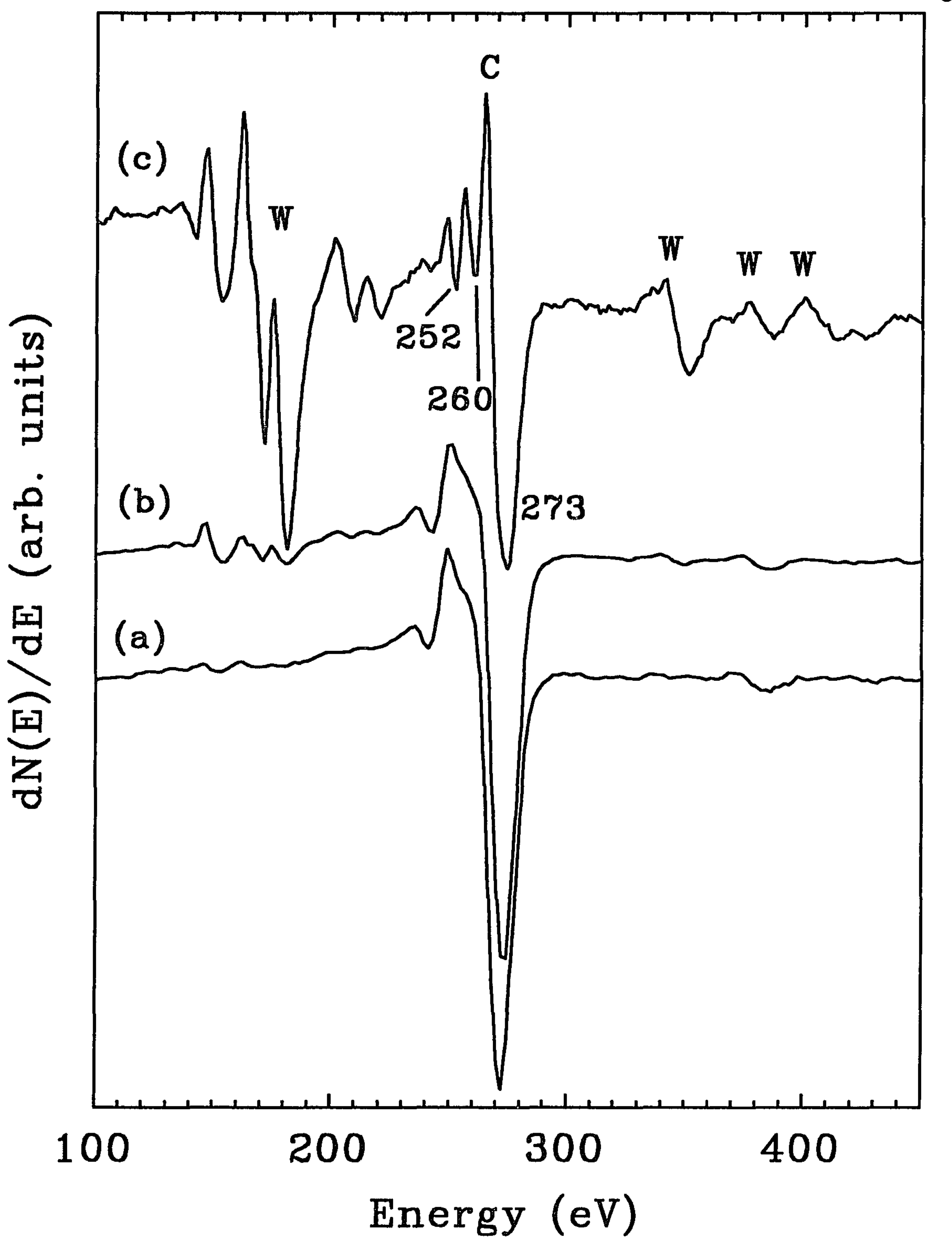

Figure 4.10. Auger spectra around the carbon signal for a W/C multilayer (W/C= 6 Å/5 Å): (a) before heating, (b) after heating and (c) after reaction with oxygen.

In order to verify this phenomenon, we exposed the sample to oxygen at 773° K for one minute. The AS spectrum taking after this reaction is very illuminating, Figure 4.10 line (c). The Auger spectrum of carbon ($KL_{2,3}L_{2,3}$ at 273 eV) after the reaction changes, and additional features at 260 eV and 252 eV appear. The Auger spectrum shows the characteristic structure of the formation of carbides. Figures 4.11 and 4.12 we show the EEL spectra before heating, at 973° K, and after reaction. The EELS spectra after heating and after reaction are very similar indicating that a carbide interface was formed during heating. The exposure to oxygen removes the graphitic top layer and expose the carbidic interface. The EEL spectra has energy losses from W and the carbide as well as from the other deeper layers (depending on the impinging energy). The carbides are very stable in an oxygen environment, at least up to 773 K.

Inner core shell electrons can be excited by the inelastic scattering of electrons and the EELS spectrum can exhibit EXAFS like oscillations.[44] We performed SEELFS measurements[47,48] at the carbon K-edge for the samples before, after heating and after reaction. The magnitude of the Fourier transforms (multiplied by the square of the momentum of the electron) for the SEELFS spectra are shown in Figure 4.13. The spectra are dominated by the carbide character of the interface. This provides further proof of the correct identification of the interface. The position of the C/C and C/W distance are indicated in the Figures. X-ray diffraction measurements gave further evidence of carbide formation. The type of carbide formed at the interface was identified as W_2C. A comparison of near-neighbor distances for the Carbon atoms in the W_2C and the experimental

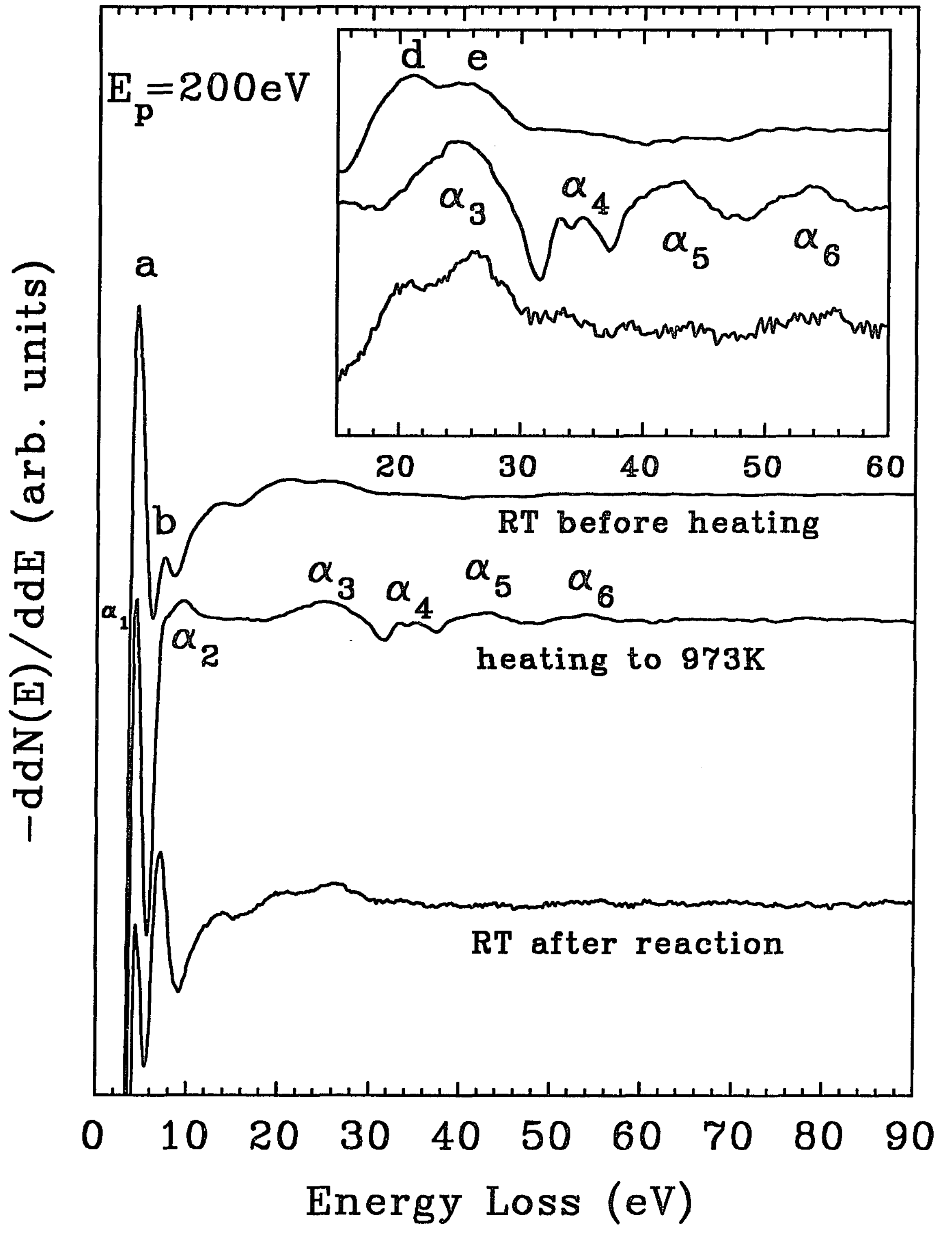

Figure 4.11. EEL spectra for W/C= 6Å/5 Å), 200 eV electron primary energy.

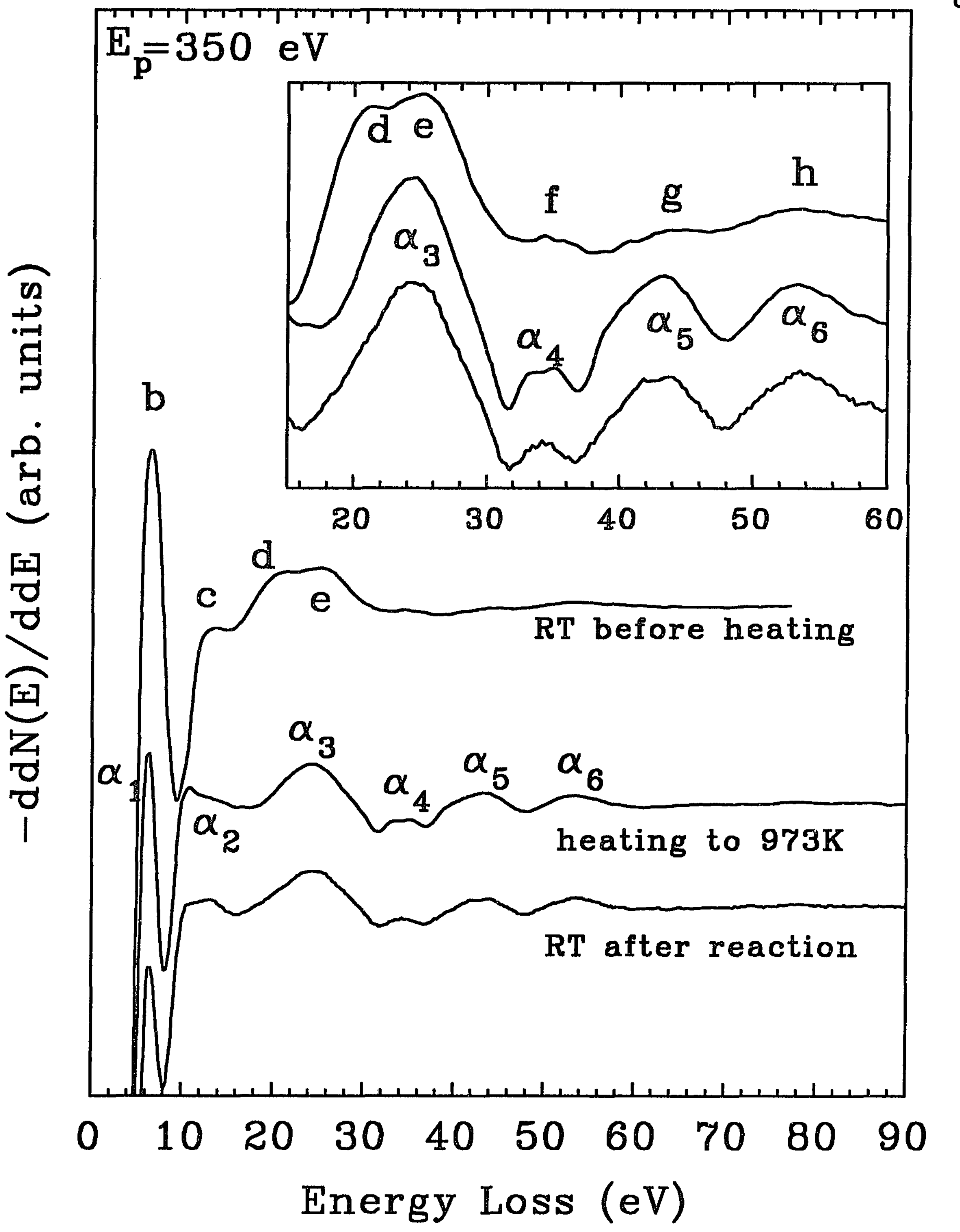

Figure 4.12. EEL spectra for W/C= 6Å/5 Å, 350 eV electron primary energy.

measurements (extracted from Figure 4.13b after heating) is listed in Table 4.4. The deviation between the true distance r and the peak position r', due to the phase shift θ_{ij} (k) can be roughly estimated using the linear approximation ($\theta_{ij}(k) = P_0+P_1k$). The oscillation part $\sin(2kr_j+\theta_{ij})$ in Eq. 2.51 is now rewritten as follows after introducing the linear phase function $\theta_{ij}(k)$:

$$\sin(2kr_j+\theta_{ij}) = \sin(2kr_j+P_0+P_1k)$$
$$= \sin(2k(r_j+\frac{p_1}{2})+p_0)$$
$$= \sin(2kr'_j+p_0). \qquad 4.3$$

The deviation $\Delta r = r_j - r_j'$ is approximately equal to $-0.5P_1$. P_1 can now be found out by fitting the theoretical phase shift data. In this analysis, we used the theoretical phase shift data listed (in appendix V) in ref.[45], and then performed a least square fit to the data. In this fitting, we limited the maximum k to 10Å^{-1}. This is because the maximum k value in the SEELFS is only about 10Å^{-1} (400eV in energy scale, see Figure 4.13a). After the fitting, the parameters of p_1 for C-C and C-W are about -0.7 and -0.6 respectively. The interatomic distances F(R) after the phase shift correction are listed in the Table 4.4. Some of the interatomic distances have 20% deviation from the standard crystal. This can be realized, since the peaks in Figure 4.13b (solid line) are not very separated from each other, and these peaks overlapping can prevent us to determinate the radius r_j' precisely. Our objective in this analysis is to have a semiquantitative evaluation of the parameters for a corroboration of the identity of the species present in the sample.

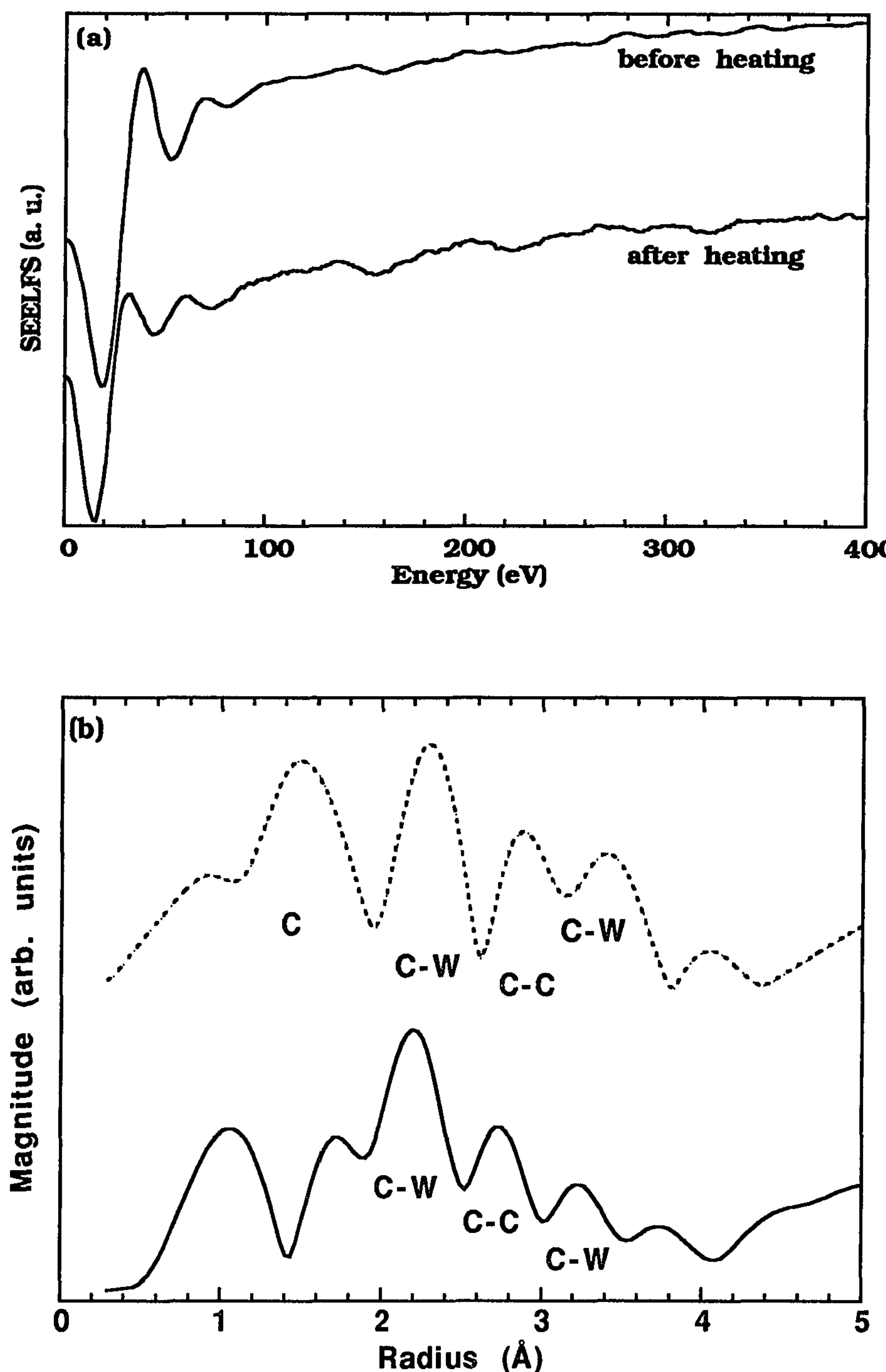

Figure 4.13. (a) SEELFS spectrum taken at C K-edge. (b) Magnitude of the Fourier transforms of the Carbon K-edge SEELFS spectrum, before heating (dot line) and after reaction (solid line).

Table 4.4
Comparison of near-neighbor distances for the Carbon atoms in the W_2C[ref. 84] and the experimental measurements (from the solid line in Figure 4.13).

Shell	HCP W_2C Bond Distances (Å)	Exp. *F'(R)* (Å)	After Phase Shift Correction F(R) (Å)
1	2.09 C-W	2.2	2.5
2	2.99 C-C	2.7	3.0
3	3.64 C-W	3.2	3.5

Shell	Graphite Bond Distances (Å)	Exp. *F'(R)* (Å)	After Phase Shift Correction F(R) (Å)
1	1.42 (C-C)	1.1	1.4
2	2.46 (C-C)	1.7	2.0

X-ray reflectivity

The basic theory for analyzing the X-ray reflectivity data has been discussed in chapter 2. In the following analysis, we will use the iteration method (Eq. 2.69) and a Gaussian type roughness at the interface to fit the experimental data. In this analysis of the data, the interface roughness, and the electron density of each layer are assumed to be constant throughout all the layers. Because of the large number of data points in each spectrum and the time consuming iteration calculation, most of the experimental data can only be analyzed in the main frame (CUNYVM) computer.

Figures 4.14, 16, 18, and 4.22(a) show part of the X-ray reflectivity measurements. Figure 4.14a shows the experimental data and the fit result of sample W/C= 6Å/5Å. In this figure, the upper line indicated fit(+1), is shift up by 1 in the log scale from the Y axis. There are three different modulations in this experimental data spectrum. One is from the the bilayer structure, one is from the interference of reflectivity waves between the substrate and the total thickness, and the remainder is from an unknown layer. From the width of the modulation, one can estimate that the thickness of this unknown layer is about 60Å. In the theoretical calculation, we assume that there is an extra layer with certain thickness embedded between the substrate and the first layer (tungsten). The result of the rough calculation shows that the medium frequency modulation is from a layer with thickness around 53Å and electron density at 2.8(6.022x10^{23} e/cm^3). The line shape of the fitting and the amplitude of the high frequency modulation are very similar to the experimental data.

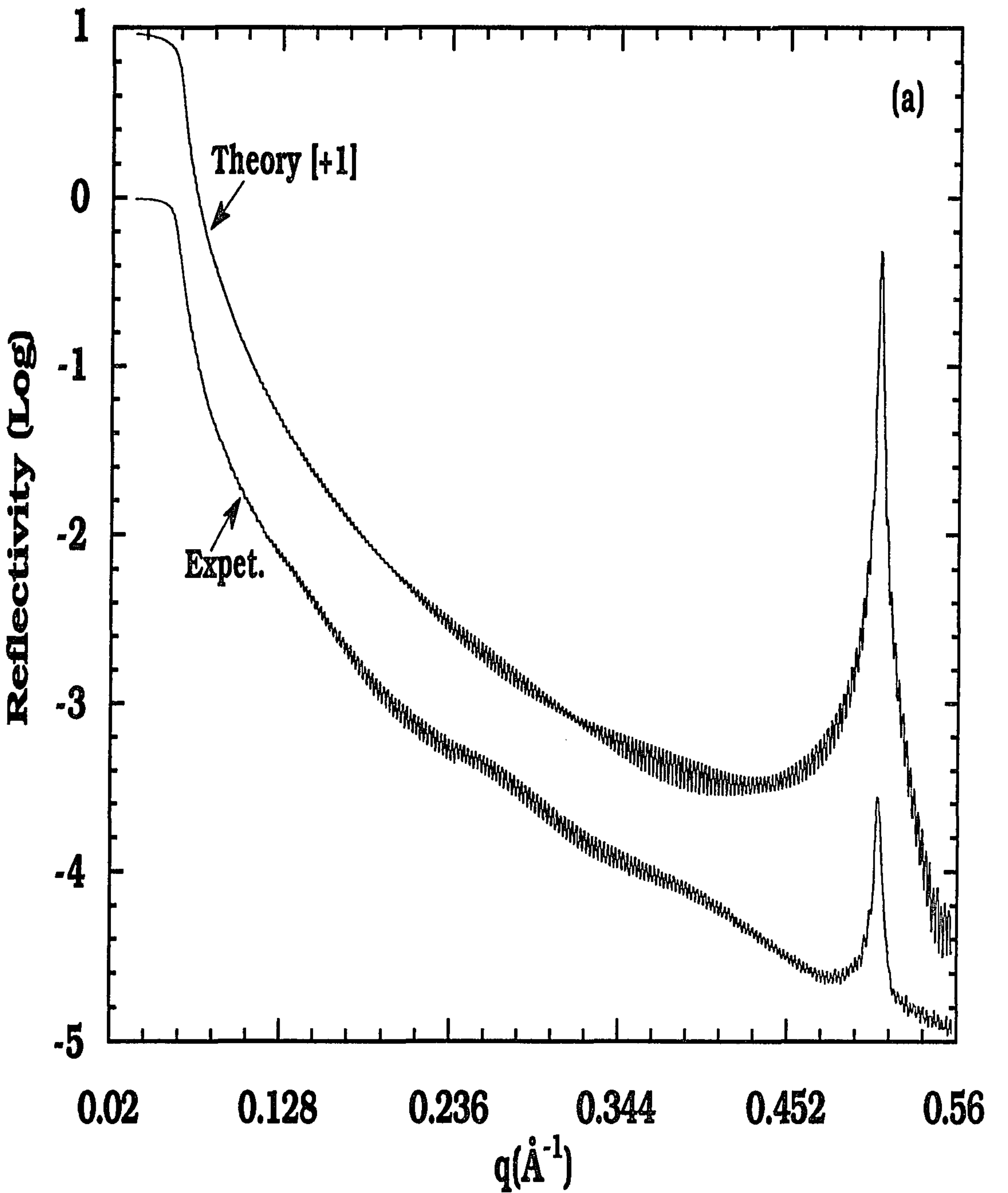

Figure 4.14a X-ray specular reflectivity of multilayer of W/C=6Å/5Å with 200 periods. The upper curve is the theoretical calculation and is shifted by 1 from the Y axis for illustration. The values of the fitting parameters are shown in Table 4.5 and Figure 4.15. The large modulation in this fitting curve is produced by assuming that there is an extra layer which is just embedded between the surface of the substrate and the multilayer with thickness of 53Å, electron density $2.8(6.022\times10^{23}\ e/cm^3)$. Figures 4.14b-4.14d are the expansions of Figure 4.14a.

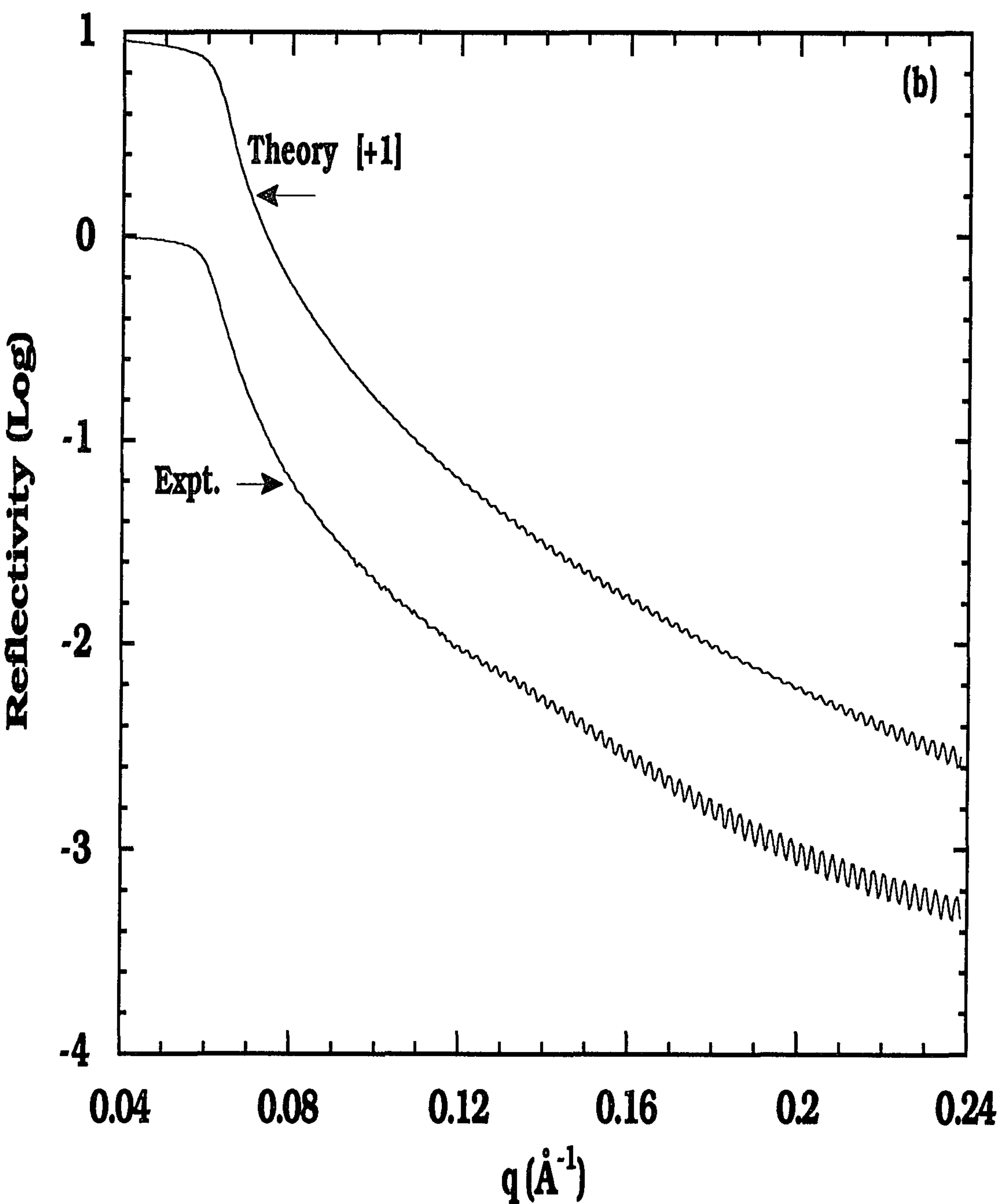
(b)
Theory [+1]
Expt.
Reflectivity (Log)
q (Å^{-1})
1
0
-1
-2
-3
-4
0.04
0.08
0.12
0.16
0.2
0.24

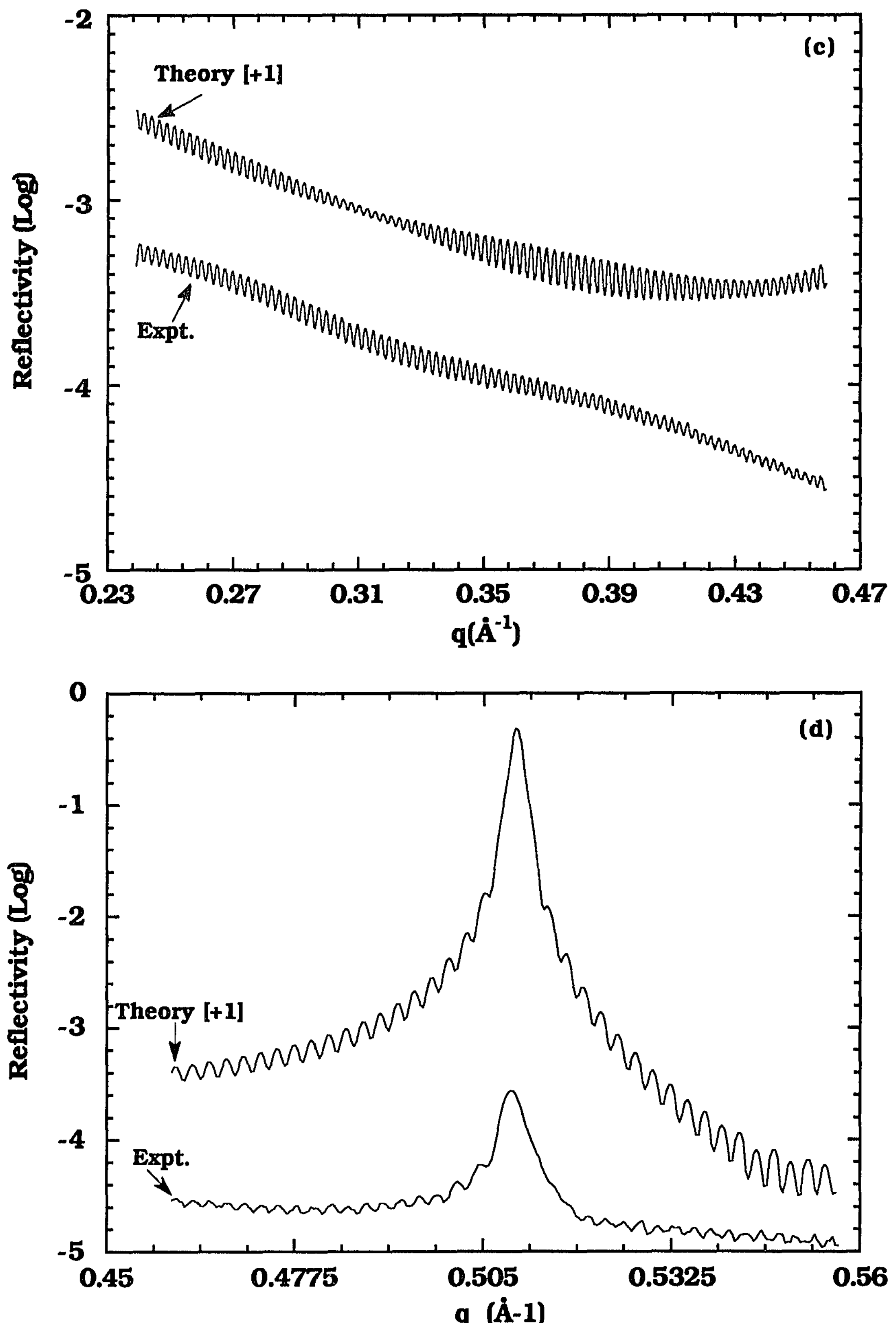
(c)
Theory [+1]
Expt.
Reflectivity (Log)
-2
-3
-4
-5
0.23
0.27
0.31
0.35
0.39
0.43
0.47
q(Å-1)
(d)
Theory [+1]
Expt.
Reflectivity (Log)
0
-1
-2
-3
-4
-5
0.45
0.4775
0.505
0.5325
0.56
q (Å-1)

Table 4.5

Parameters obtained from the fitting of the experimental data for the W/C=6Å/5Å multilayer.

Materials	Thickness	Interface-Roughness	
	d(Å)	σ(Å)	
Si(substrate)	∞	0.3	(Si - bottomlayer)
bottomlayer	52.5	0.8	(bottomlayer - W)
W	4.57	2.6	(W - W_2C)
W_2C	2.10	2.9	(W_2C - C)
C	3.65	3.8	(C - W_2)
		2.9	(W_2C - C)

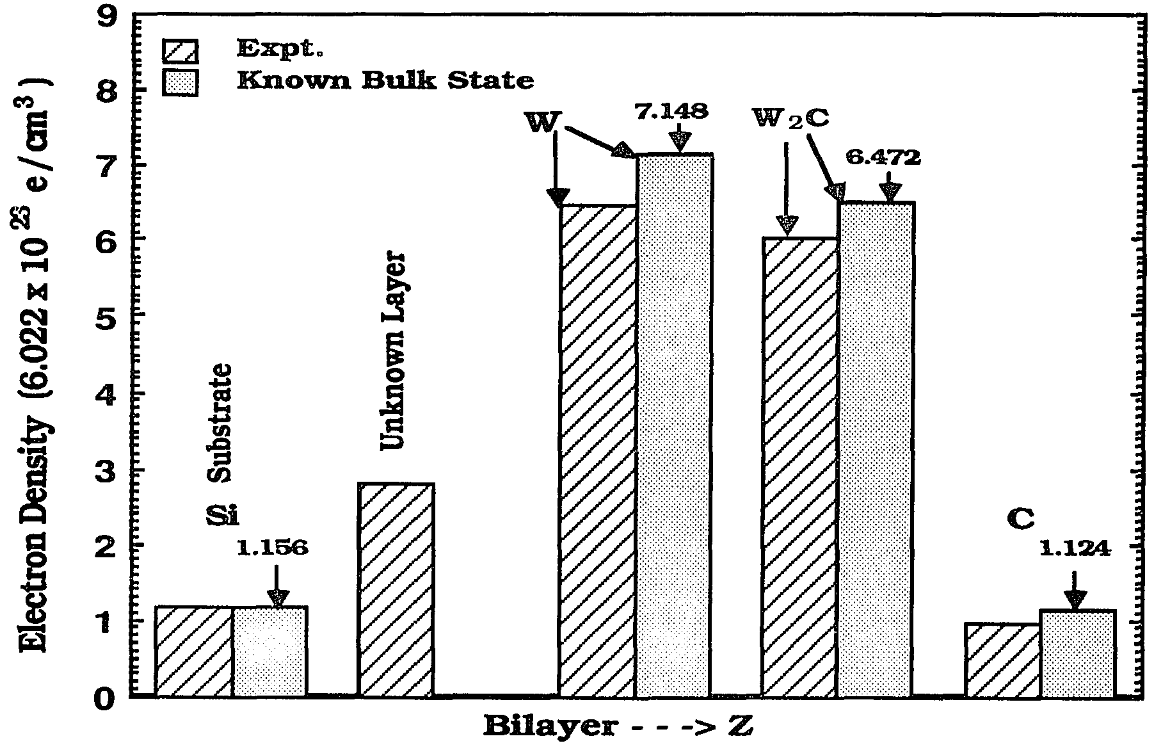

Figure 4.15 A comparison of electron density between the known bulk state and the experimental state. The experimental electron densities of W, W_2C and C are from the parameters used to obtain fit in Figure 4.14a. The electron densities of W, W_2C and C are about 10% , 7% and 14% less than the known bulk state respectively.

The fitting is not perfect but basically it tells us that the medium frequency modulation is built up from a thin layer with certain electron density. The thickness, electron density and the interface-roughness parameters of the individual layers are shown in Table 4.5 and Figure 4.15. Thin tungsten carbide W_2C layer was about 2Å at the interface.

Figure 4.16 is a spectrum measured from sample W/C=7Å/7Å before heating and Figure 4.18 from sample W/C=7Å/7Å after heating. Both figures are very similar. The position of the two peaks from the first Bragg peak in Figure 4.18 is slightly higher than the peaks from Figure 4.16. This indicated that the growing of the carbide at the interface may cause a contraction from the bilayer. It is very hard to expect a good fitting in these two figures because of the weak reflectivity at the first Bragg peak. In this analysis of the data, the following model is used. We assume that the two peaks at the first Bragg peak position were made up by two multilayers with very similar bilayer thickness. In Figure 4.16, we assume that the thickness (Λ_a) of the bilayer from peak (a) is about 13.2Å and with 23 periods (let us name this multilayer as M_a), the thickness from peak (b) is 3.5% least than peak (a) but with 127 periods (let us name this multilayer as M_b). The multilayer M_a is arranged on the top of the multilayer M_b. The thickness of the bilayers Λ_b and Λ_a is assumed to be linearly increasing from the direction of substrate layer to the top layer with $\Delta\Lambda/\Lambda \approx \pm$ 1% for peak b (±1.8% for peak a). The thickness ratios $d_W/d_{W_2C}/d_C$ are kept constant. For the case in Figure 4.18, we use the same model but the thickness of the bilayer of peak (b) is about 6.5% least than peak (a). The theoretical calculations are

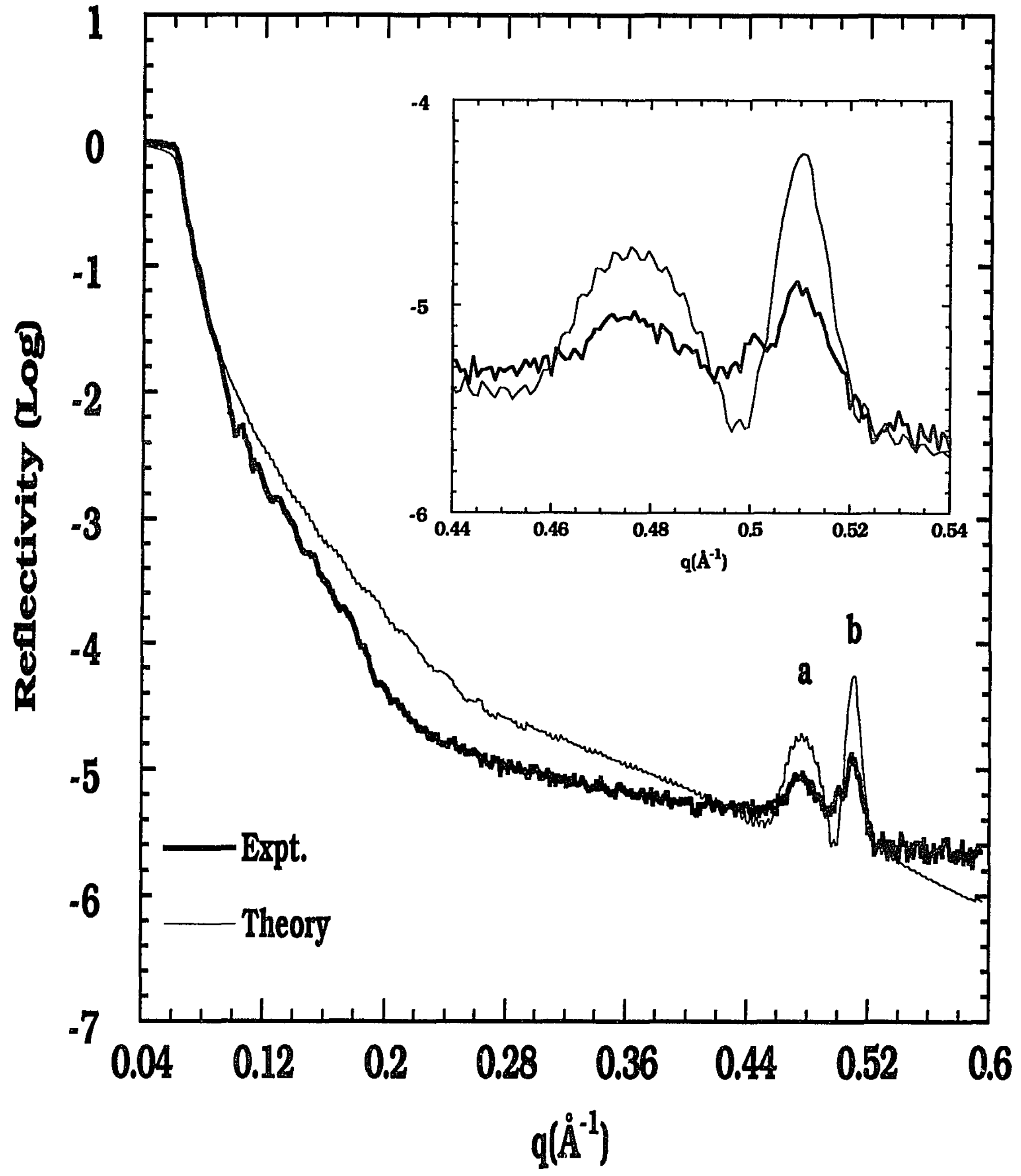

Figure 4.16 X-ray specular reflectivity of multilayer of W/C=7Å/7Å with 150 periods. The thin line curve is the theoretical calculation and the coarse line is the experimental data. The values of the fitting parameters are given in Table 4.6 and Figure 4.17. The two peaks at the first Bragg peak position were made up by two different thickness bilayer lattices. In Figure 4.16, we assume that the thickness (Λ) of the bilayer from peak (a) is about 13.18Å and with 23 periods, the thickness from peak (b) is 3.5% least than peak (a) but with 127 periods.

Table 4.6

Parameters obtained from the fitting of the experimental data for the W/C =7Å/7Å multilayer before heating.

Materials	Thickness	Interface-Roughness	
	d(Å)	σ(Å)	
Si(substrate)	∞	2.4	(Si - W)
W	4.4	5.6	(W - W_2C)
W_2C	2.3	6.8	(W_2C - C)
C	4.3	5.5	(C - W_2)
		5.3	(W_2C - W)

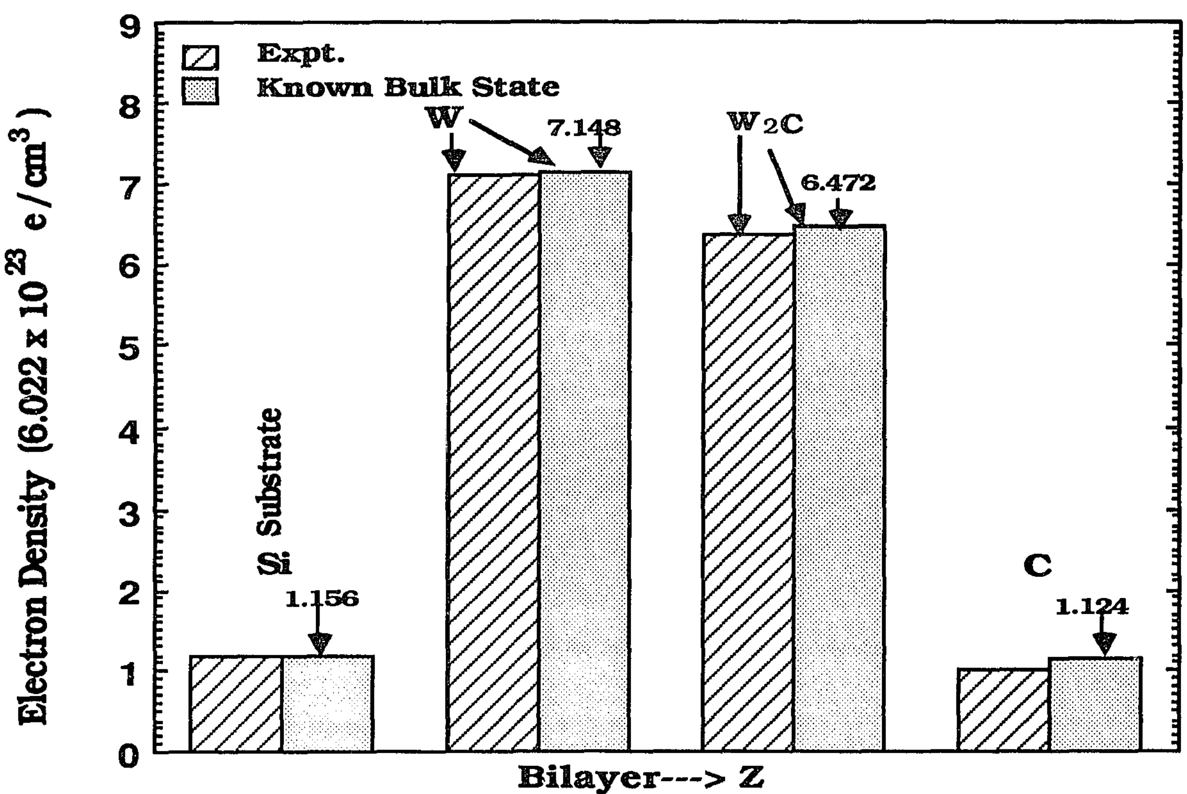

Figure 4.17 A comparison of electron density between the known bulk state and the experimental state. The experimental electron densities of W, W_2C and C are from the parameters used to obtain fit in Figure 4.16. The electron densities of W, W_2C and C are about 1% , 2% and 8% less than the known bulk state respectively.

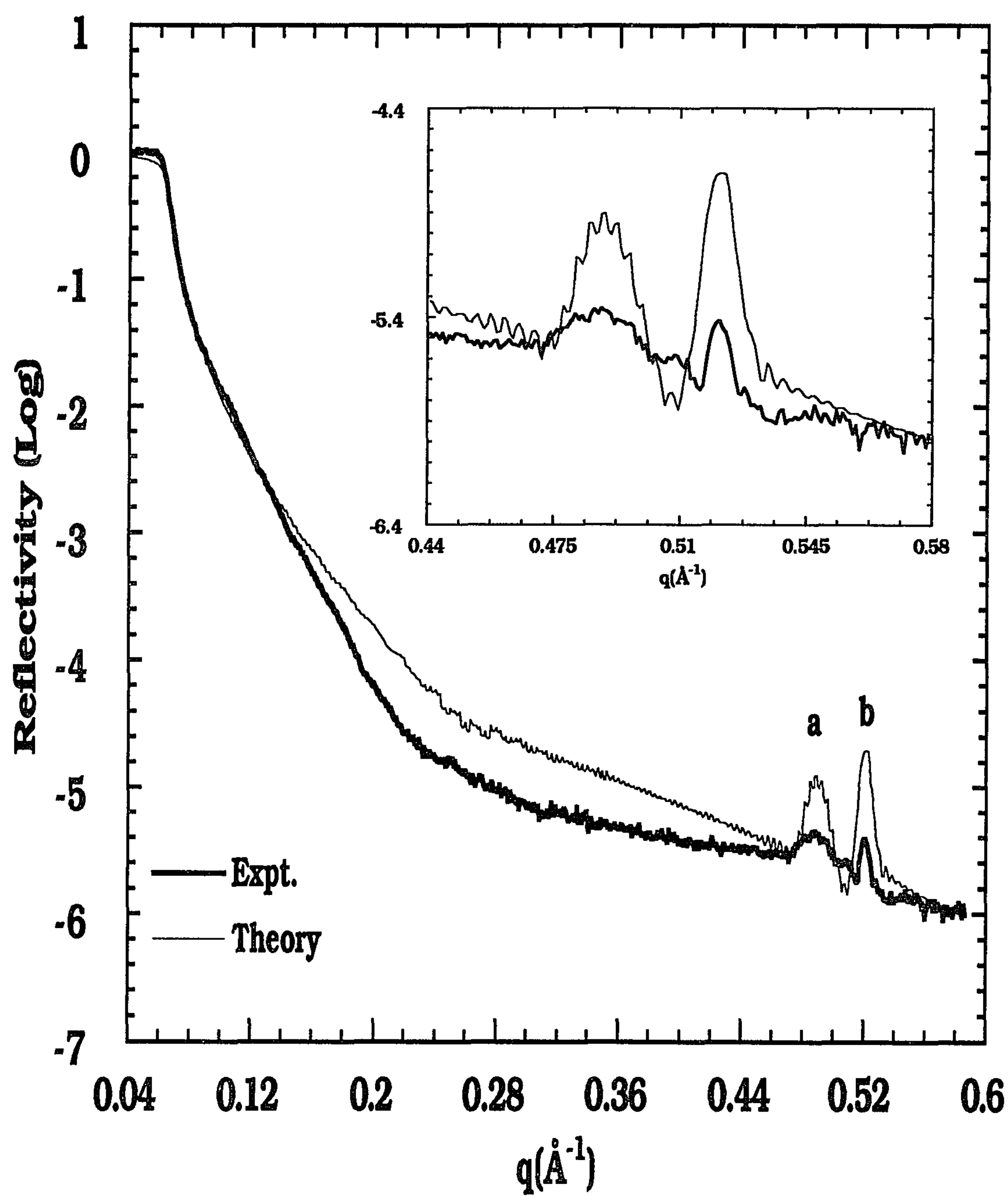

Figure 4.18 X-ray specular reflectivity of multilayer of W/C=7Å/7Å with 150 periods after heating. The thin line curve is the theoretical calculation and the coarse line is the experimental data. The values of the fitting parameters are shown in Table 4.7 and Figure 4.19. In the theoretical calculation, we used the same model as in Figure 4.16 but the thickness of the bilayer of peak (b) is about 6.5% least than peak (a).

Table 4.7

Parameters obtained from the fitting of the experimental data for the W/C=7Å/7Å multilayer after heating.

Materials	Thickness	Interface-Roughness	
	d(Å)	σ(Å)	
Si(substrate)	∞	2.4	(Si - W)
W	4.3	5.5	(W - W_2C)
W_2C	2.4	6.6	(W_2C - C)
C	3.9	5.7	(C - W_2)
		5.3	(W_2C - W)

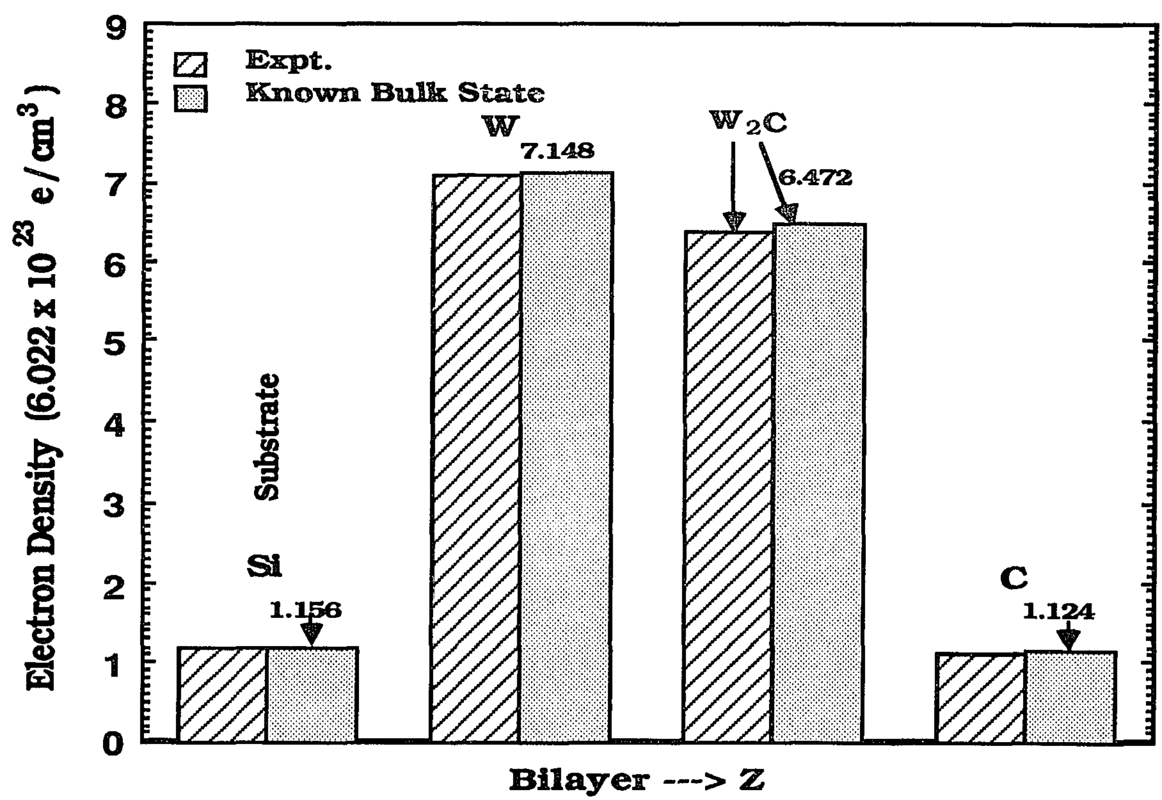

Figure 4.19 A comparison of electron density between the known bulk state and the experimental state. The experimental electron densities of W, W_2C and C are from the parameters used to obtain fit in Figure 4.18. The electron densities of W, W_2C and C are about 1% , 1% and 2% less than the known bulk state respectively.

shown in Table 4.6, Figure 4.17 and Table 4.7, Figure 4.19 respectively. The roughness at each interface is very large. We believe that the poor reflectivity at the diffraction peak is mainly caused by this roughness.

Figure 4.20 is a spectrum measured from sample W/C =10Å/20Å. We can not find the interference of the reflectivity waves between the substrate and the total thickness in this figure. The reason is that the wave width created from the interference of the 4800Å bilayers is much smaller than the resolution of the diffractometer. In the analysis of the data, the thickness of the bilayers Λ is found to be monotonically increasing from the substrate up to the top layer with $\Delta\Lambda/\Lambda \approx \pm 2.5\%$. The thickness and electron density parameters of the individual layers are shown in Table 4.8 and Figure 4.21.

Figure 4.22(a) is a spectrum measured from sample W/C =10Å/13Å. The interference of reflectivity waves between the substrate and the total thickness in this figure is very irregular. This is mainly caused by the influence of the thickness errors which are distributed in a randomize sequence. It can not be fit properly. So we use a simulation method to specify this spectrum. In this simulation, we assume that the thickness of the bilayers can be divided into several groups with different occupation numbers. The occupation number of the bilayer is assumed to have a Gaussian type distribution with respect to the thickness. The distribution is shown in Figure 4.23. The 150 bilayers are randomly arranged in a sequence in the way to form the multilayer. An X-ray reflectivity calculation is then performed. Figure 4.22(b) is one of the results by using the simulation method. From 4.22(b), we can find out the similarity of

the irregular interference which happened in Figure 4.22(a). It is indirectly proved that the thicknesses in this sample are randomly distributed. The thickness and electron density parameters of the individual layers are shown in Table 4.9 and Figure 4.24.

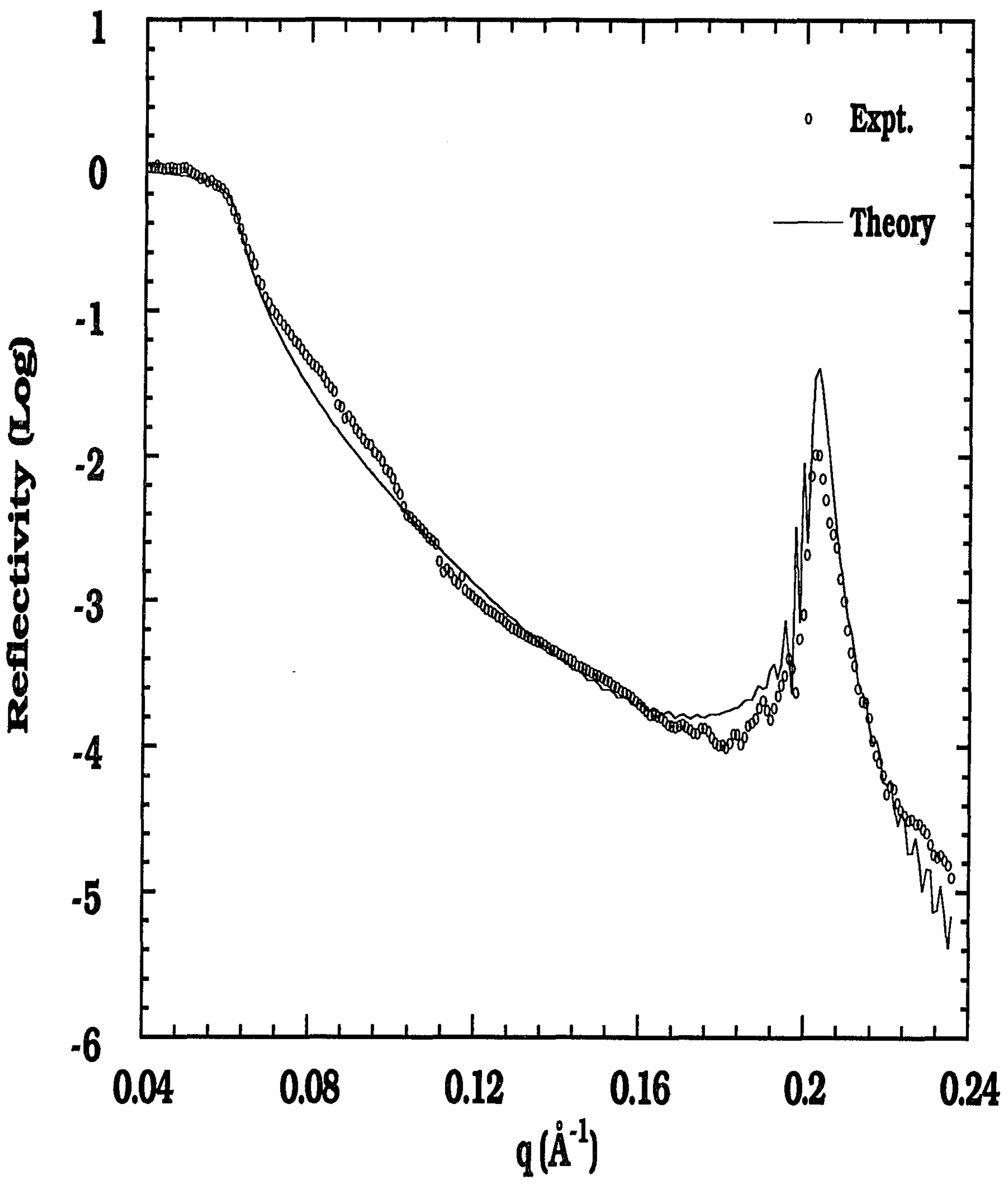

Figure 4.20 X-ray specular reflectivity of multilayer of W/C=10Å/20Å with 65 periods. The thin line curve is the theoretical calculation and the circle line is the experimental data. The values of the fitting parameters are shown in Table 4.8 and Figure 4.21.

Table 4.8

Parameters obtained from the fitting of the experimental data for the W/C=10Å/20Å multilayer.

Materials	Thickness	Interface-Roughness
	d(Å)	σ(Å)
Si(substrate)	∞	7.0 (Si - W)
W	8.4	9.0 (W - W_2C)
W_2C	7.7	11.0 (W_2C - C)
C	9.1	10.0 (C - W_2C)
		8.5 (W_2C - W)

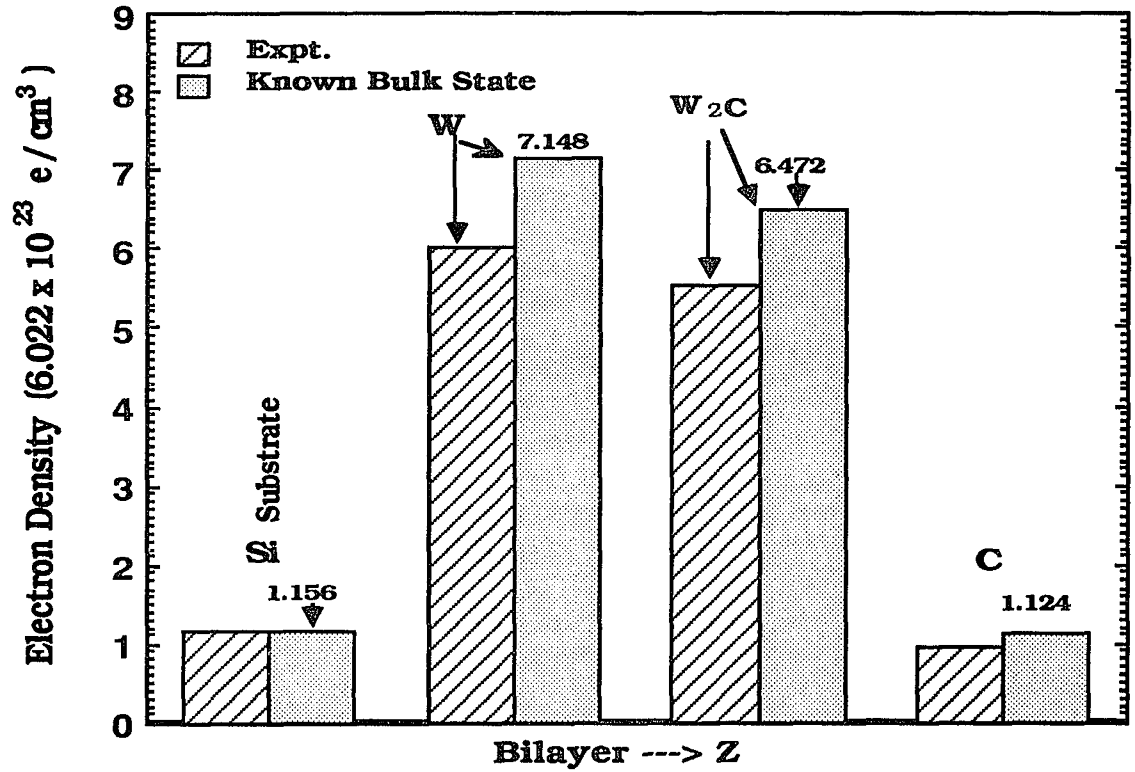

Figure 4.21 A comparison of electron density between the known bulk state and the experimental state. The experimental electron densities of W, W_2C and C are from the parameters used to obtain fit in Figure 4.20. The electron densities of W, W_2C and C are about 16% , 15% and 17% less than the known bulk state respectively.

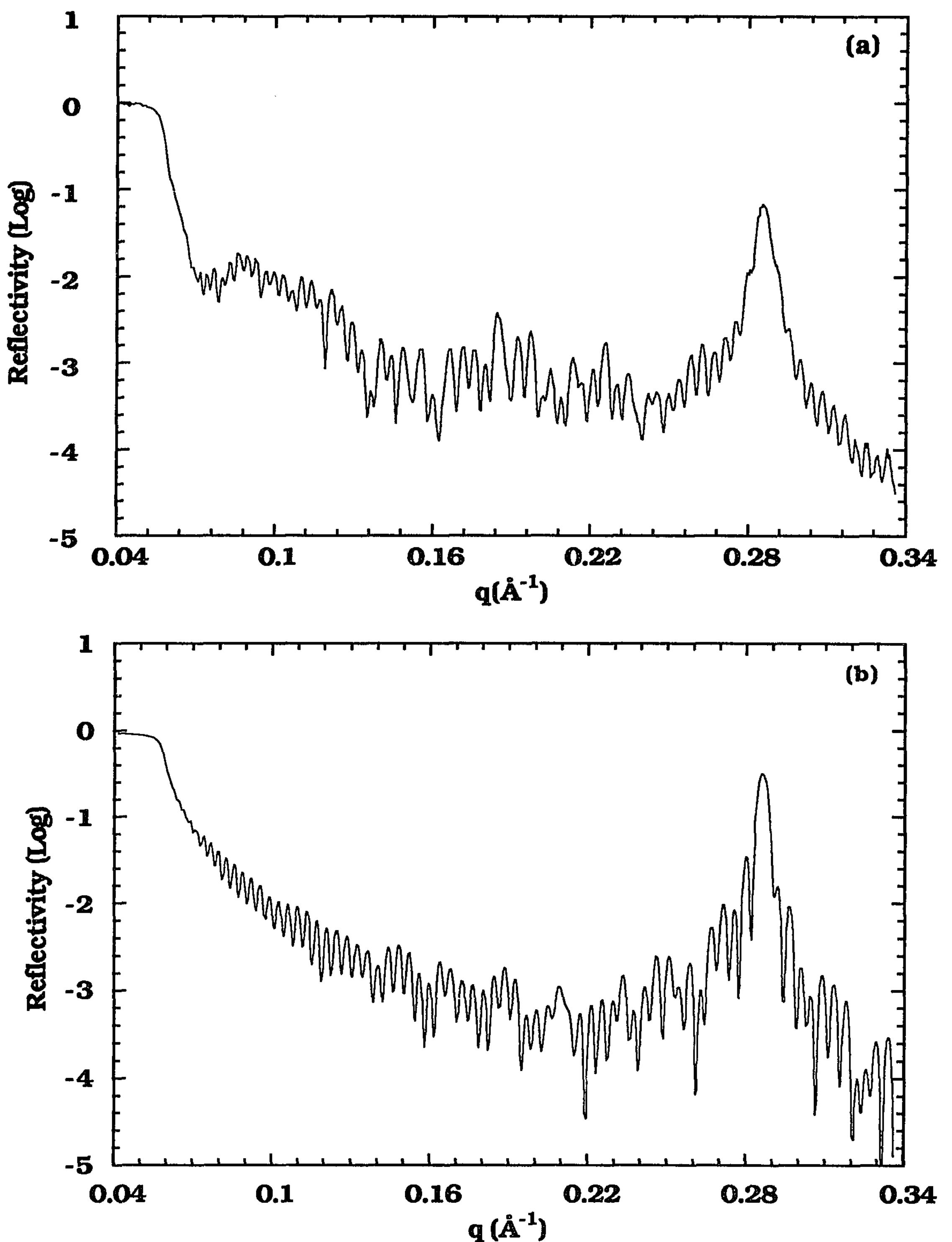

Figure 4.22 X-ray specular reflectivity of multilayer of W/C=10Å/13Å with 150 periods. The top one (a) is the experimental measurement and the lower one (b) is the theoretical calculation. The values of the simulation parameters are shown in Table 4.9 and Figure 4.24.

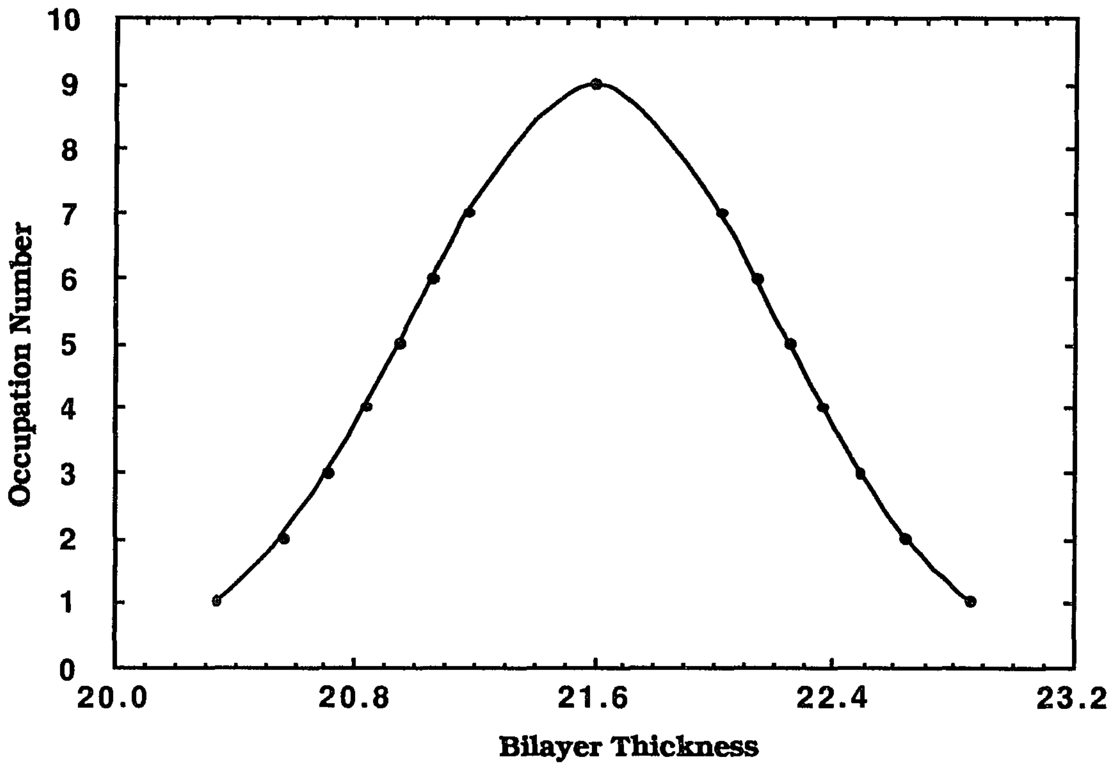

Figure 4.23 A Gaussian distribution of the occupation number versus bilayer thickness. The deviation σ used in this model is 1.2 Å.

Table 4.9

Parameters obtained from the fitting of the experimental data for the W/C=10Å/13Å multilayer.

Materials	Thickness	Interface Roughness	
	d(Å)	σ(Å)	
Si(substrate)	∞	4.5	(Si - W)
W	5.2	4.3	(W - W_2C)
W_2C	4.6	4.4	(W_2C - C)
C	8.1	4.4	(C - W_2)
		4.4	(W_2C - W)

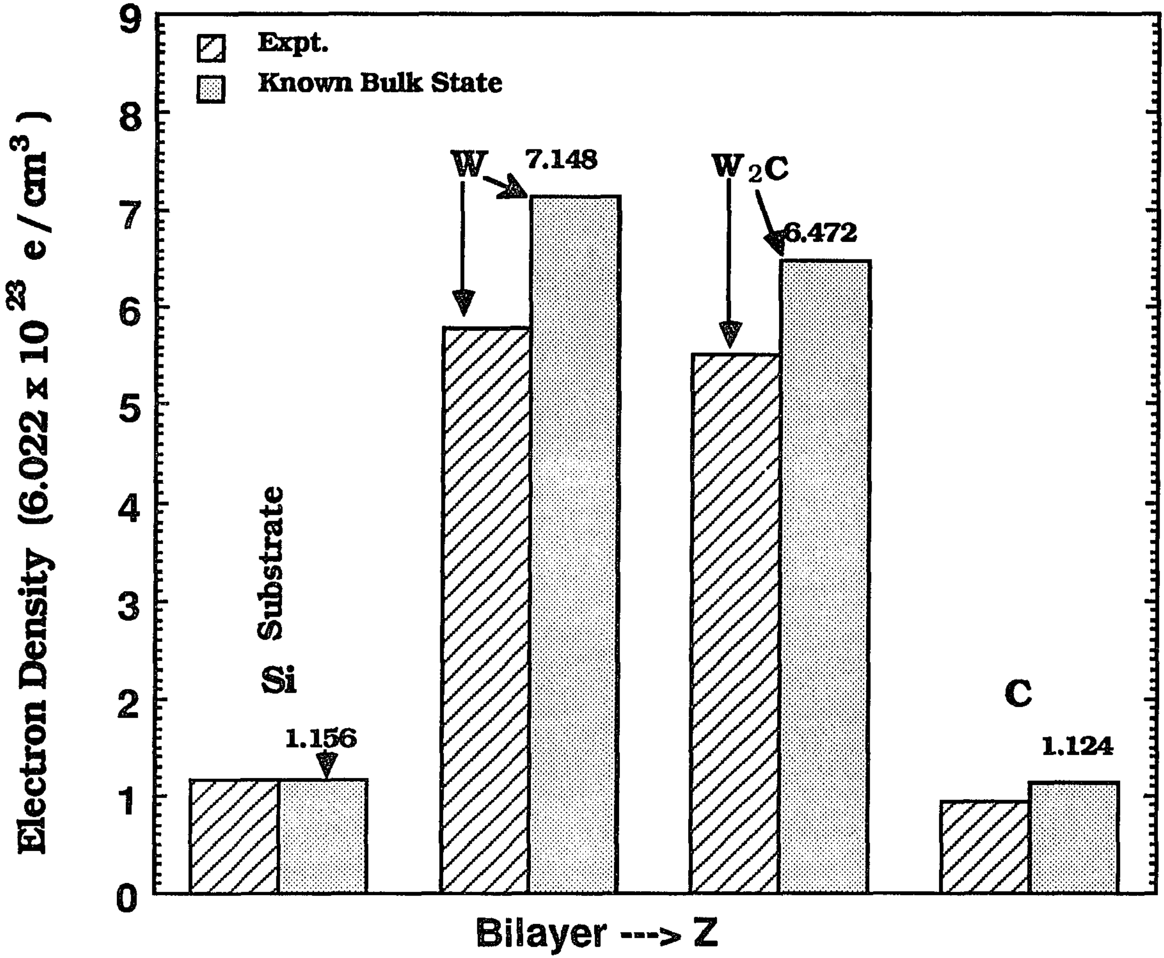

Figure 4.24 An illustration of electron density for the known bulk state and the experimental state. The experimental electron densities of W, W_2C and C are from the parameters used to obtain the simulation in Figure 4.22b. The electron densities of W, W_2C and C are about 19% , 15% and 17% less than the known bulk state respectively.

CHAPTER 5

SINGLE CRYSTAL TIC[111]

5.1 Introduction

Titanium carbide is an uncommon compound, it has a simple cubic rock-salt structure. It is similar to metals in its thermal conductivity and electrical resistivity. Its high melting points and hardness[11] make it widely used in cutting tools, wear resistant surfaces and high temperature materials. Some carbides posses superconducting properties at low temperatures.[11] These remarkable characteristics have stimulated continuous theoretical and experimental research of this compound. Titanium carbide is one of the most technologically important carbides. The TiC micro-hardness shows a curious temperature dependence when compared to other transition metal-carbides. The hardness decreases linearly from 3000 to 400 (kg/mm^2)[85] when the temperature increases from 300 K to 1073 K. Above this temperature it becomes rather ductile and deforms plastically. These physical properties should be to changes in electronic structure.

During the past two decades, there have been a number of TiC band calculations performed by different methods, tight binding approximation, EPM, LCAO, APW and MAPW,[1,86-93] to name a few. The results of these calculations are not always in full agreement. However, most of them show that the C-2p and Ti-3d states form the strongest bonding, and that the C-2s states are well separated from the lower level. More recent calculations are

considering not only pure covalent bonding but a mixture of covalent, metallic and ionic bonding between carbon and titanium.

Experimentally XPS and UPS have been used to investigate the band structure of titanium carbide.[91,94-98] The results of those measurements show that the C-2s band lies 10.0 -10.6 eV below the Fermi level, and the C-2p and Ti-3d hybridized band lie 2.9-3.6 eV below the Fermi level. The measurements are consistent with recent band structure calculations.

We present in this thesis an electron energy loss spectroscopy (EELS) study of TiC [111]. We also report in this manuscript the evolution of the EEL spectra at high temperatures. The objective was to investigate the electronic surface structure under such conditions. The reactivity of the TiC surface towards oxygen and ethylene was also investigated using the same techniques.

5.2 Experimental

The crystal studied was 8 x11 mm^2 and 2 mm thick. It was mounted on a Molybdenum sample holder. A Chromel Alumel thermocouple was attached to the surface of the sample. The crystal was mounted on a high precission manipulator with electron beam heating. A high power Yag Laser (200 W) was used for surface annealing of the sample. The vacuum system used in these experiments has a base pressure around $5X10^{-11}$ torr. The Auger spectroscopy (AS) and EELS measurements were taken using a cylindrical mirror analyzer. The first derivative mode was used for AS and the second derivative for the EELS measurements, with a

resolution $\Delta E/E = 0.6\%$. The modulation voltage used for the measurements was 1 eV p-p.

The AS spectrum of the sample showed the presence of oxygen and graphitic carbon on the surface. After many hours of annealing and many cycles of argon ion (at 2000 eV) sputtering we were able to obtain a clean sample as shown in Figure 5.1a. In order to monitor the cleanness of the surface, Auger spectra were recorded before each EELS measurement. Usually, it just needed a flash-heating for the removal of the residual oxygen.

We measured the EEL spectra in the N(E) and $-dN^2/d^2E$ modes for comparison purposes using electron primary energies from Ep=100 to 350 eV, see Figure 5.2. We observe in the figure that the N(E) mode has a strong background, and that can create difficulties in detecting small features in the EEL spectrum. By contrast, in the $-dN^2/d^2E$ mode, the background is suppressed, so that small features are easily detected. Because of this fact, we decided to used the second derivative mode in our studies. For comparison purpose we also measured the EEL spectrum of a Ti single crystal.

The TiC EEL spectra for the clean sample were measured at room temperature using seven different electron primary energies (Ep= 100, 150, 200, 250, 300, 350, 450 eV). The spectra are shown in Figure 5.3. The temperature dependence of the EELS spectra was measured in two different regions; between 128 K and 1073 K for Ep =150, 300 eV; and between 300 K and 1250 K for Ep=200 eV.

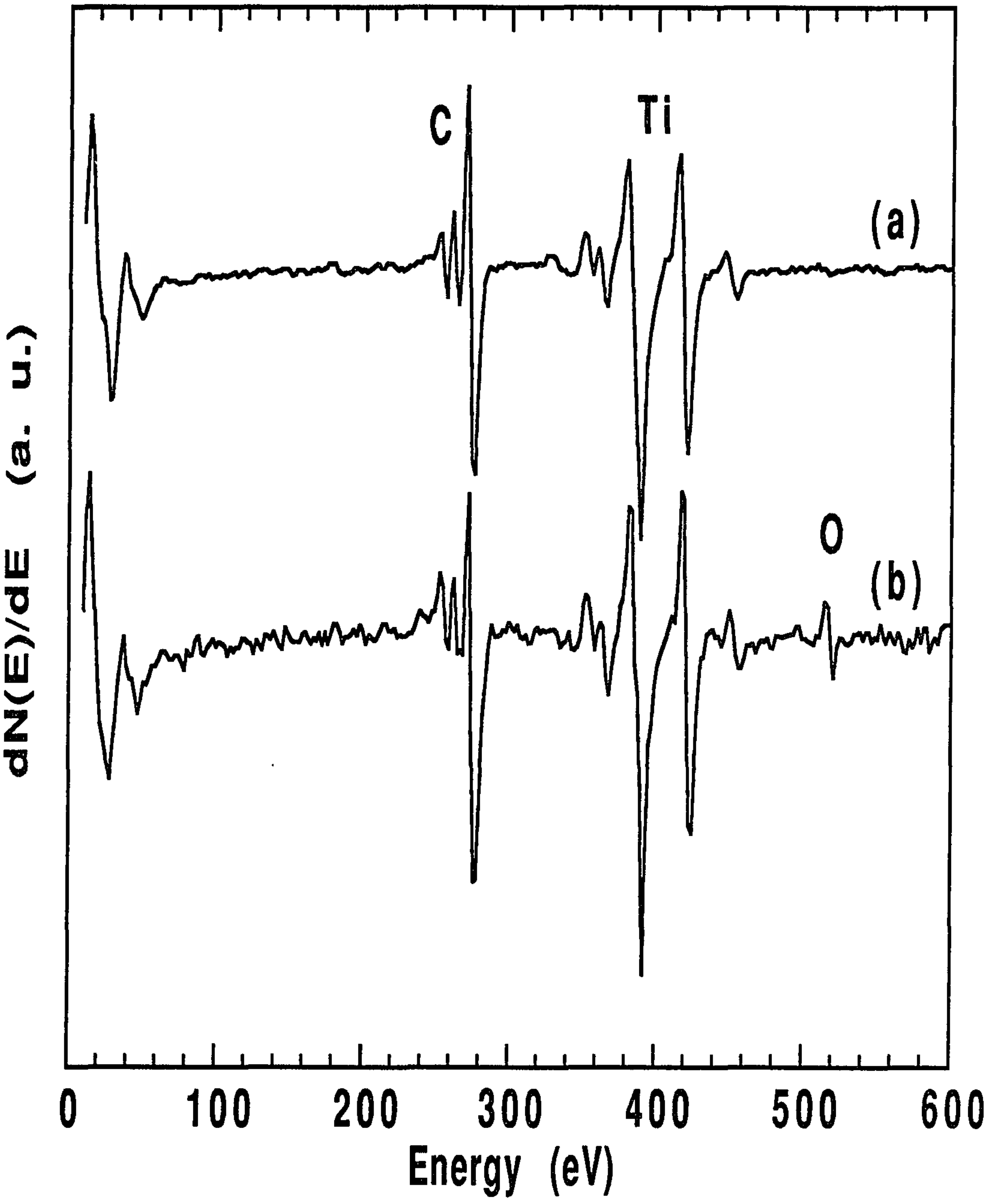

Figure 5.1 Auger spectra for (a) clean TiC (b) with Oxygen coverage.

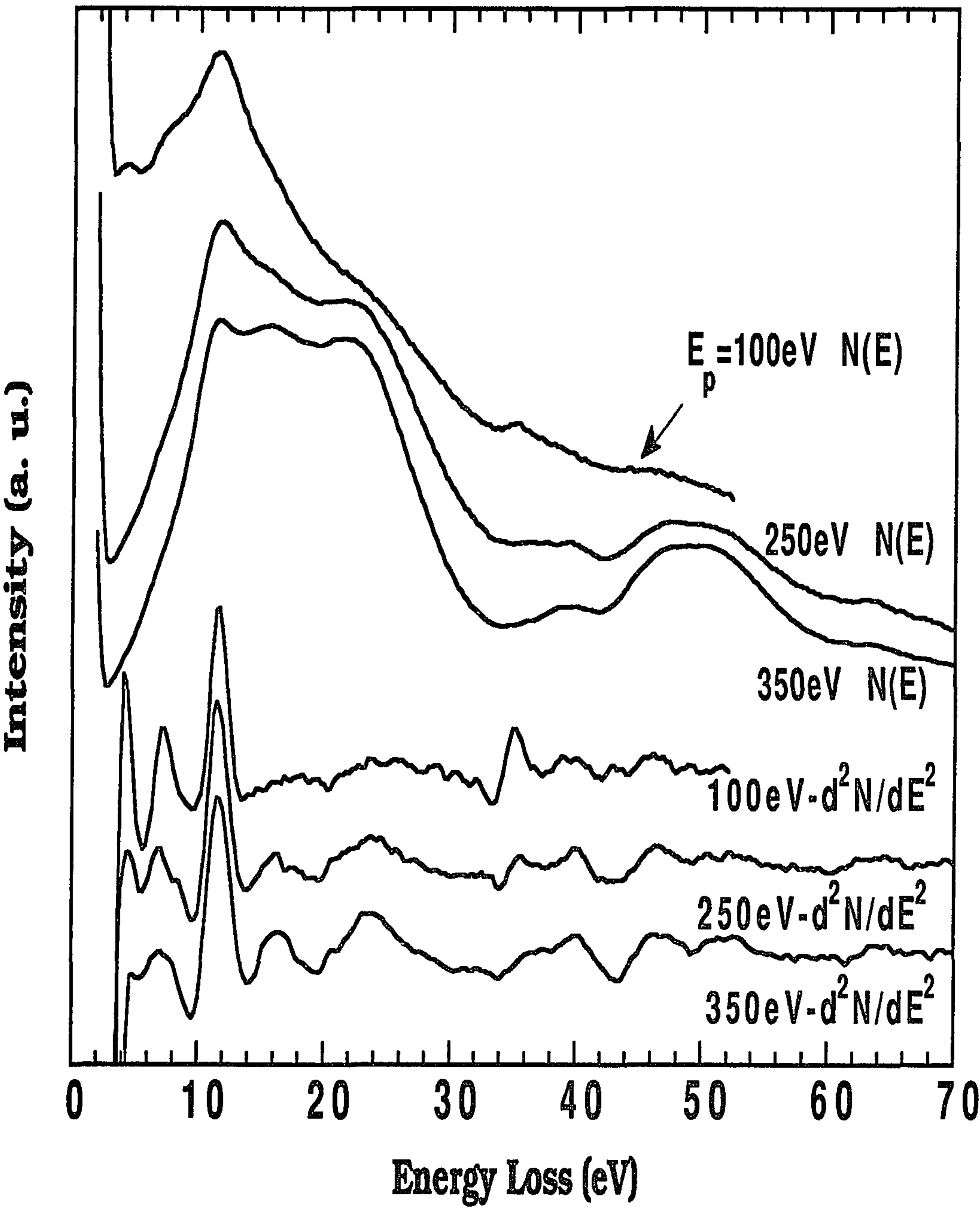

Figure 5.2 EELS spectra for N(E) and $-dN^2/d^2E$ mode as a function of primary electron energy (100 to 350 eV) at 300 ^oK.

The clean TiC sample was exposed to 240 L of ethylene at various temperatures 136 K to 700 K. Light exposures to oxygen were also performed on the clean samples to investigate the surface oxidation of the sample.

5.3 Results and Discussion

AS: The Auger spectra for the TiC sample with and without oxygen are shown in Figure 5.1. Figure 5.1a shows the spectrum of a clean TiC sample after ion sputtering and thermal annealing (including laser annealing). Figure 5.1b shows a typical spectrum of a TiC sample with small amount of oxygen on the surface.

EELS: The EEL spectra of clean TiC are shown in Figure 5.3. They were measured at room temperature using electron primary energies of Ep =100, 150, 200, 250, 300, 350, and 450 eV. The spectrum of Ti metal (E_p=150 eV) is also shown in Figure 5.3 for comparison purposes. The electron energy loss peaks of TiC are indicated in the Figure by the letters a to l. All electron energy loss spectra in Figure 5.3 have been normalized with respect to the elastic peak. The enegy loss peak positions are listed in Table 5.1. We also reproduce in Figure 5.4 the projected DOS calculations from Price and Cooper.[1] We will use this theoretical calculation for the interpretation of the EEL spectra.

Peak a at 4.4 eV appears at electron primary energies from 100 eV to 350 eV. This peak is not easily observed at 450 eV due to energy resolution limitations of the CMA. We assign this energy loss as an inter/intra band transition from the occupied valence states

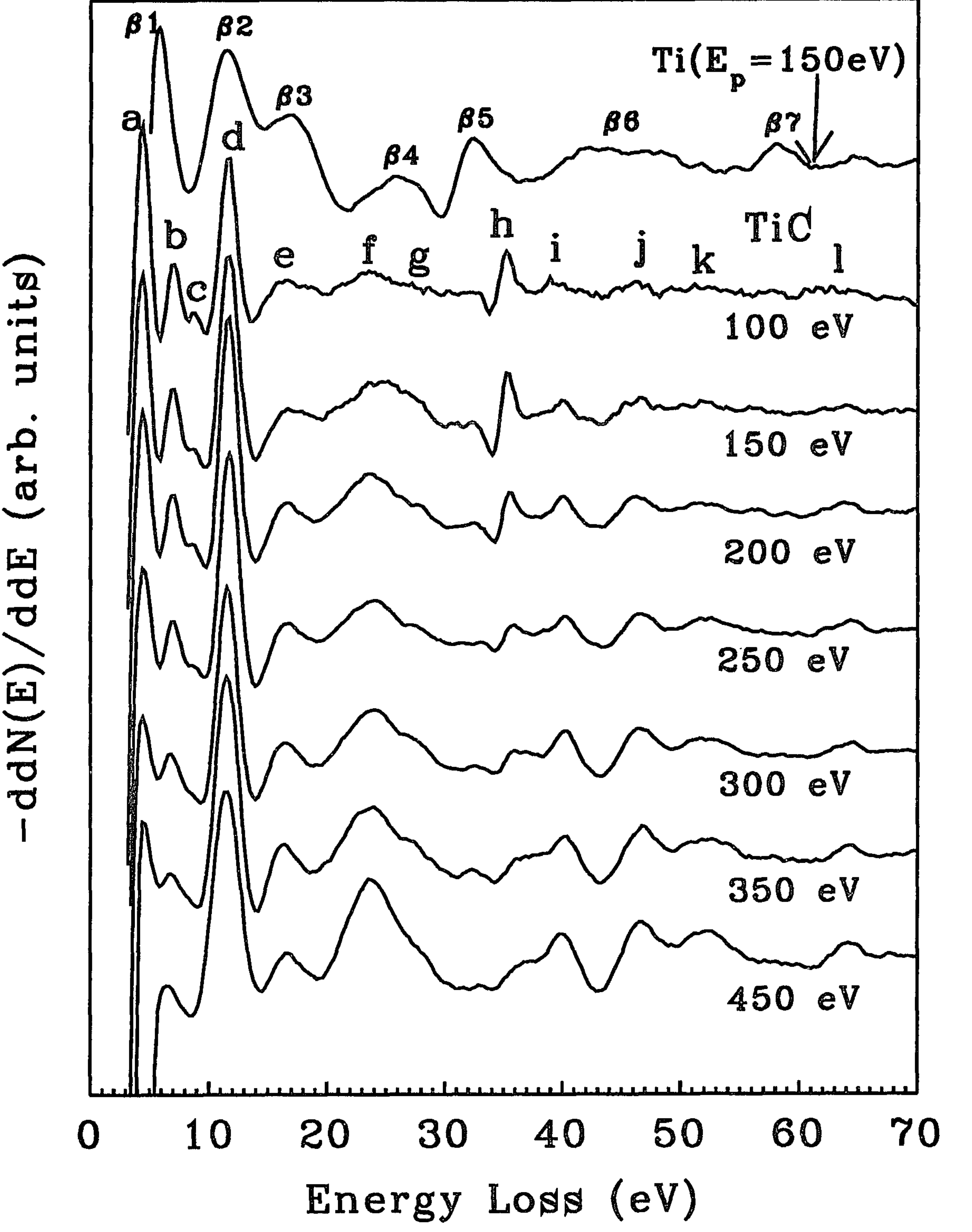

Figure 5.3 EELS spectra at 300 ^{0}K as a function of primary electron energy (100 to 450 eV).

Table 5.1.

Electron energy losses of TiC [111].

ENERGY (Ep)	Loss Peaks (eV)											
	a	**b**	**c**	**d**	**e**	**f**	**g**	**h**	**i**	**j**	**k**	**l**
100	4.4	6.8	8.8	11.6	16.4	23.5		35.2	39.6	46.2		
150	4.4	6.8	8.6	11.6	16.6	24.5	26.6	35.2	40.1	46.2	52.1	64.1
200	4.4	6.8	8.6	11.6	16.6	23.7	26.4	35.5	40.1	46.2	51.9	64.1
250	4.4	6.8	8.8	11.7	16.6	24.0	26.9	35.8	40.4	46.7	52.1	64.5
300	4.4	6.8	8.3	11.5	16.6	24.0	26.6	36.0	40.4	46.7	52.1	64.5
350	4.4	6.8		11.5	16.4	23.7	26.6	36.2	40.4	46.7	52.4	64.3
450		6.7		11.5	16.7	23.6	26.5	36.3	40.0	46.6	52.2	64.4
avg.	4.4	6.8	8.6	11.6	16.6	23.9	26.6	35.7	40.1	46.5	52.1	64.3

C-2p, Ti-3d to the Ti-3d empty states ($p_3 \rightarrow d_5$, $d_4 \rightarrow d_5$, see Figure 5.4 and Table 5.2). We assign this transition using the theoretical calculations given in Figure 5.4. The intensity of peak a shows a strong energy depence. It emerges as the strongest peak at Ep =100 eV, and then decreases gradually. This is strongly suggestive of surface states, at low electron primary energies only the top atomic layers of the sample are scanned. The inelastic mean free path at these energies is short enough to sense only the surface layers. According to Ion Scattering Spectroscopy (ISS) and angle dependent XPS measurements[99] the top layer of TiC [111] is favored by the titanium atoms. This nonneutral surface can be stabilized by charge redistribution accompanied by significant changes in the surface electronic structure. This means that the surface DOS is significantly different from the bulk. Fujimori et al.[100] have calculated the surface DOS for an eight atomic-layers film of TiC [111], Ti or C terminated. Their results show that for the Ti terminated surface the empty states are quite different from the bulk. All these observations are consistent with our interpretation of peak a as produced by surface states. Peak b located at 6.8 eV is identified as a transition from the occupied C-2p and Ti-3d states to empty states C-2p and Ti-3d (e.g. $p_1 \rightarrow d_6$, $p_1 \rightarrow d_5$, $d_2 \rightarrow d_7$, $d_2 \rightarrow d_5$, $d_3 \rightarrow p_4$, $d_3 \rightarrow d_7$, see Figure 5.4 and Table 5.2). This peak does not show a strong dependence on the electron primary energy.

Peak c is assigned as an inter band transition. This peak is narrow and weak when compared to the others. Peak d can be identified as an inter band transition from the occupied states C-2p,Ti-3d to empty states (e.g. $p_1 \rightarrow p_5$, $p_1 \rightarrow d_9$, $d_2 \rightarrow p_5$, $d_2 \rightarrow d_9$, see

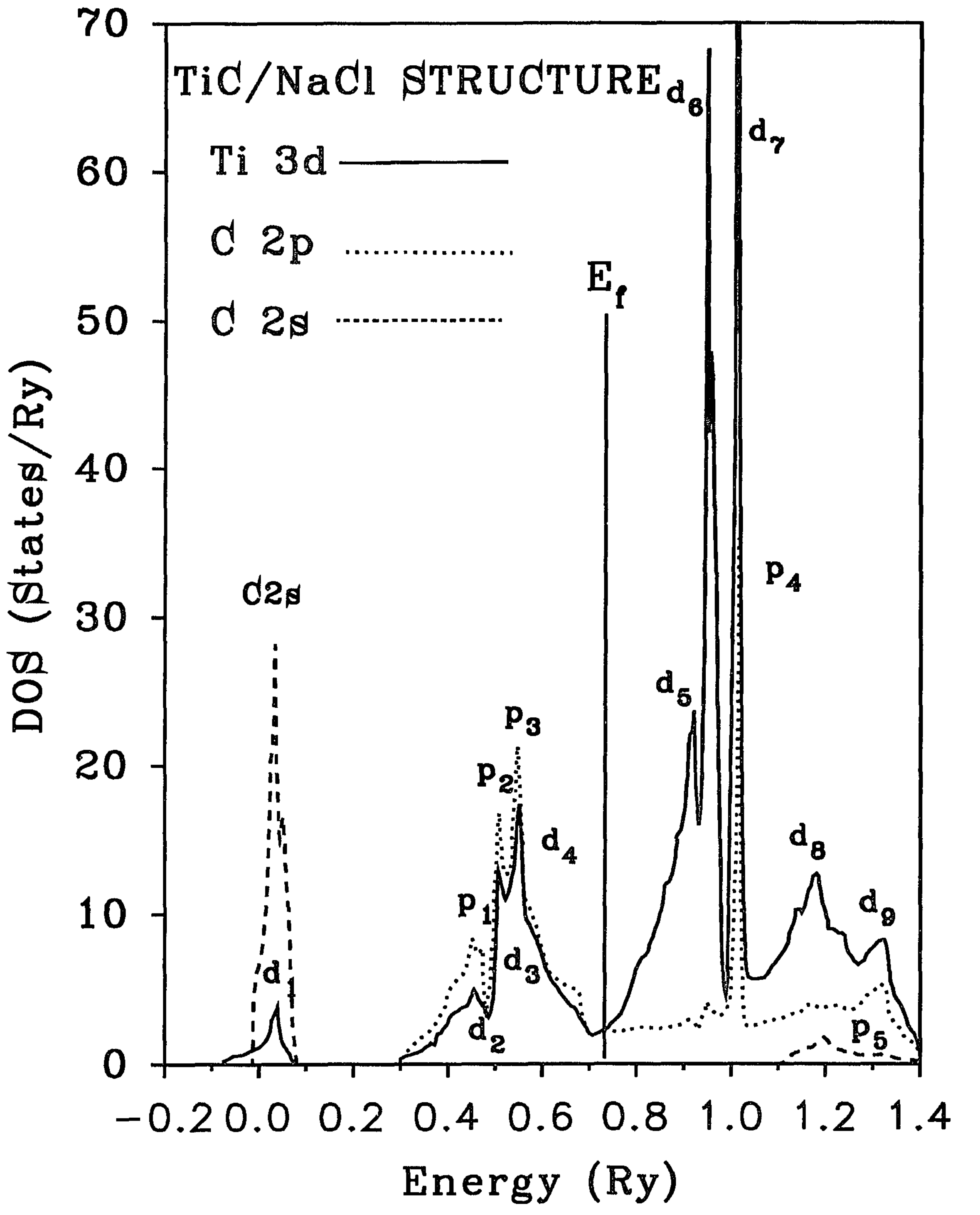

Figure 5.4 Partial density of states of TiC (from ref. 11); p_1-- p_5, d_1-- d_9 correspond to C-2p and Ti-3d states respectively.

Table 5.2

Electron energy loss peaks in Figure 5.3 and the corresponding transitions according to Figure 5.4.

loss peak	energy loss (eV)	Most probable transition path (Figure 5.4)
(a)	4.4	C-2p-> Ti-3d , Ti-3d-> Ti- 3d (p_3-->d_5, d_4-->d_5)
(b)	6.8	C-2p -> C-2p, Ti-3d -> Ti-3d (p_1-->d_6, p_1-->d_5, p_2-->d_7, p_2-->p_4 d_2-->d_6, d_2-->d_5, d_3-->p_4, d_3-->d_7)
(c)	8.8	C-2p -> Ti3d, Ti-3d ->Ti3d (p_3-->d_8, d_4-->d_8)
(d)	11.6	C-2p -> Ti-3d, Ti-3d -> Ti-3d (p_1-->p_5, p_1-->d_9, d_2-->p_5, d_2-->d_9)
(e)	16.6	C-2s-> C-2p, Ti-3d->C-2p, Ti-3d->Ti-3d (C-2s-->p_5, d_1-->p_5, d_1-->d_8, d_1-->d_9)

* All the p_i (i= 1 to 5), and d_i (i=1 to 9) refer the C-2p and Ti-3d states respectively.

Figure 5.4). Angle Resolved Photoemission was employed in reference [97] to study TiC, they observed a transition at 11.7 eV close to the position of peak d. They identified this peak as a transition from $L_{3'}$ to L_1. Those measurements seems to be in good agreement with reported theoretical band calculations. [86,88, 90,91,92]

The assignment of peak d is very different in our work to that of reference[87]. In reference[87], the optical loss function -Im(1/ ε) showed a strong peak at an energy around 11 eV, they identified this peak as a bulk plasmon. The range of the optical measurements was from 0.5 eV to 21 eV; they missed the range where the bulk plasmon will appear. We compare in Figure 5.5 our measurements (EELS at Ep=200 eV) to the loss function obtained in reference[87]. We use the same scale but shifted to lower energies by 0.5 eV. The dot line represents the loss function derived from optical measurements. We can observe in the figure that the positions of the two functions maxima appear at about the same energies. The major difference is the relative intensity of the peaks. This agreement can be taken as further evidence that the dipole approximation can be used to analyzed the EEL measurements

In Figure 5.6a, we plot peak d intensity vs primary electron energy, E_p. From the figure we can observe that the intensity increases rapidly at low energies, but after 200 eV, it starts to saturate. It does not show the characteristics energy dependence of bulk plasmons.

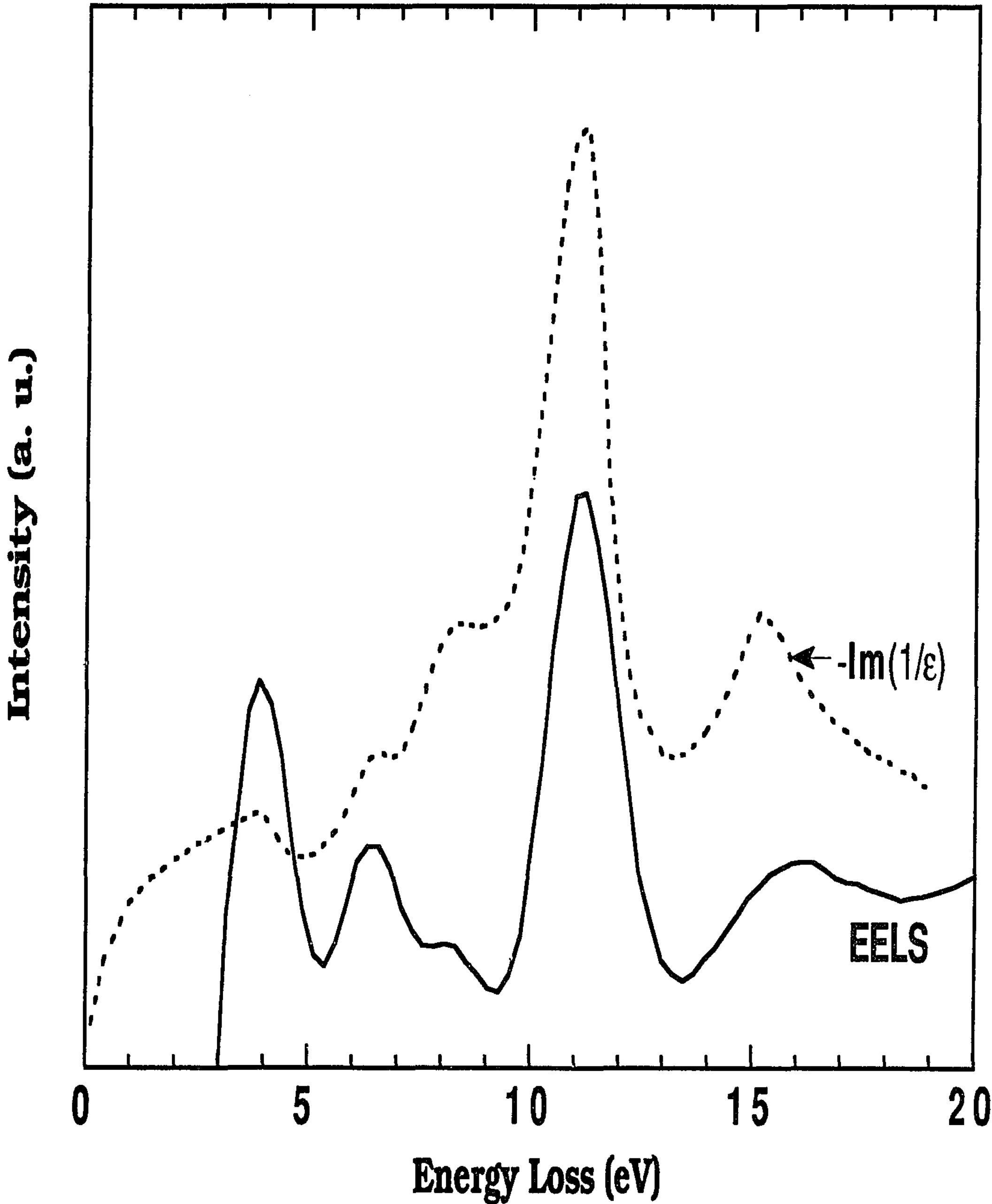

Figure 5.5 The dot line is the loss function from the optical measurement by Lye & Logothetis [87]. The solid line is the EEL spectrum measured at Ep=200 eV. (the solid line was shifted by 0.5 eV).

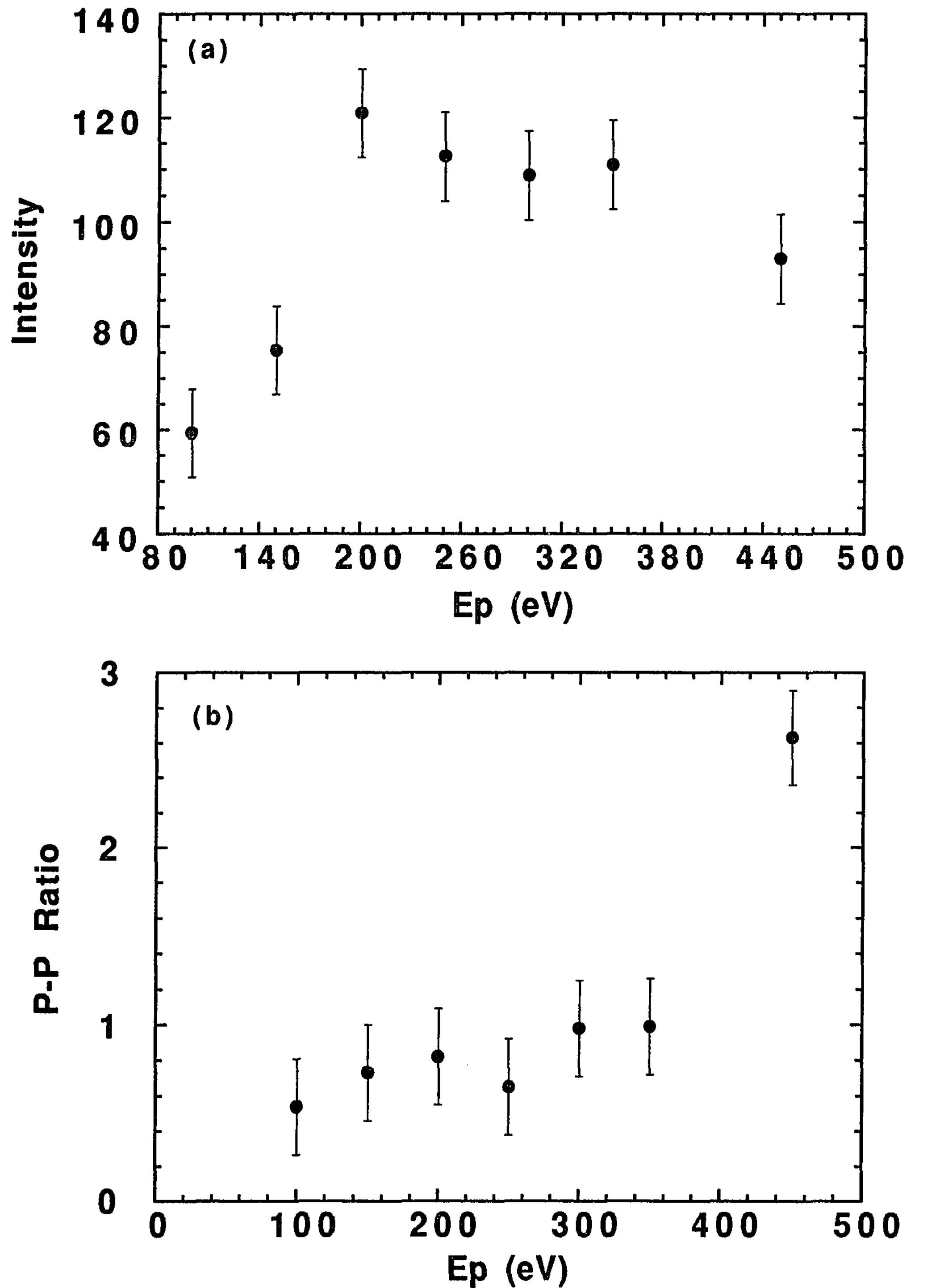

Figure 5.6 Peak intensity vs energy; (a) intensity of peak d vs primary energies; (b) the ratio of peak f with respect to peak e.

The energy loss values of peak e and f are 16.6 and 23.9 eV respectively. They are assigned as surface and bulk plasmon respectively. The assignments are according to (1) the dielectric constant theory[101] and (2) from the loss peaks functional dependence on incident primary energies. Generally, without considering the structure of the valence electrons; the free electron plasmon from the 8 valence electrons (4 from carbon, 4 from titanium) should be 23.3 eV. But from the (LMTO) calculation[1] and other band calculations,[86,88,90,91,92] there are two C-2s electrons deeply bound at the lowest level of all other bands. The plasmon energy should count only on 6 valence electrons, this will give a value of about 20.3 eV. From the dielectric constant theory[101], the frequency of the bulk plasmon under the influence of intra/inter band transitions can be expressed as:

$$\omega_p^{+2} = \frac{\omega_p^{*2}}{1 - \delta\varepsilon(\omega_p^{*2})_{fc}} \qquad \ldots\ldots (5.1)$$

Where $\omega_p^{*2} = n\, e^2/(m^* \varepsilon_o)$

{ m^* : electron effective mass over the Fermi surface for $k' - k = q \Rightarrow 0$.
ε_o : $(4\pi \times 9 \times 10^{11})^{-1}$ Coul. (Volt cm)$^{-1}$}

$\delta\varepsilon(\omega_p^*)_{fc}$ the contribution from the interband transition [from the conduction band (c) to the free band (f) above it]. The term $\delta\varepsilon(\omega_p^*)_{fc}$ in the dominator, is only a small correction. It is positive

when the inter band transitions occur at an energy below the free electron plasmon, and negative in the reverse case. Using the free electron approximation ($m^* = m$), we obtain $\hbar\omega_p^* = 20.3$ eV . In the energy loss spectra, we can observe inter band transitions in an energy range below the free electron plasmon value. Consequently. We expect that the true plasmon should shift to higher energy, this can explain why we do not measure the bulk plasmon at 20.3 eV, but at the energy of peak f 23.9 eV.

From the surface and bulk plasmon energy relation, we have:

$$\hbar\omega_s=\hbar\omega_p/\sqrt{(1+\varepsilon)} \quad \text{.........} \quad (5.2)$$

or $$\hbar\omega_s=\hbar\omega_p/\sqrt{2} \quad \text{.........} \quad (5.3) \qquad \text{(vacuum boundary)}$$

If we insert the bulk plasmon (23.9 eV) value into equation (3) we can find that $\hbar\omega_s = 16.9$ eV; very very close to the value of peak e. In Figure 5.6b, we plot the relative intensity of peak f to peak e vs electron beam energy. From the figure we can see that the ratio changes rapidly when Ep increases. This is related to the energies dependence of the electron mean free path. At low energies the probability of exciting surface plasmons is higher. We must add that from the DOS theoretical calculations[1] there is a possible contribution to peak e from interband transitions. According to the calculations in references[90] and[91] this transition can happen from the C-2p to

Ti-4s states. The results show that the energy level of Ti-4s is high above the fermi energy, the Ti-4s charge will diffuse to Ti-3d & C-2p to form the metal-metal, metal-carbon bonds, so the C-2p electrons still have a great probability to be excited to the partial empty Ti-4s states.

Peak g appears only at high primary energies as a small shoulder of peak f. This peak is not clearly resolved, and we have not given any assignment to it.

We assign peak h as a transition from the core level Ti-3p to the Ti-3d empty states[102]. The measured energy loss value is 35.7 eV. It is shifted by 3 eV in comparison to titanium metal. It shows a maximum intensity between 100 and 150 eV. The strong energy dependence is partially related to the core-ionization cross - section variation with primary electron energy. We have used Worthington and Tomlin's[103,104] calculations obtained from the modified Bethe's equation[105] to evaluate the energy dependence of the cross-section. The modified equation is given by:

$$\sigma_{nl}=C\frac{a_{nl}}{E_{nl}^{2}U_{nl}}\ln\left[\frac{4U_{nl}}{1.65+2.35\exp\left(1-U_{nl}\right)}\right]\frac{b_{nl}}{}\,cm^{2} \qquad \ldots\ldots \quad (5.4)$$

where a_{nl} is the number of electrons in that shell; $U_{nl}=E_p/E_{nl}$; C is a constant ($6.51X10^{-14}$); b_{nl} is a parameter (for the M shell

b_{nl}=0.25). The cross-section is only a function of U_{nl}, see Figure 5.7. The maximum in the cross-section occurs around U_{nl} =3, and decreases rapidly there after. For a binding energy of 35.7 eV, the maximum cross-section will be at a primary energy of 107 eV. This value is very close to that observed experimentally. There is also a strong contribution from transitions to the empty 3d surface states[101]. At these energy the penetration of the primary electrons in the sample is very sensitive to the electronic structure of the surface. These two factors dominate the behavior of peak h at low energies.

Peaks i, j, and k are not clearly observed at low primary energies, Ep =100 eV. Their intensities increase for E_p values above 150 eV. The energy loss values for the i , j and k peaks are 40.1, 46.5 and 52.1 eV respectively. We assign these peaks as autoionization electron emission corresponding to the Ti-3p - Ti-3d resonant transitions.[106-109] The processes can be described as :

$$3p^6 3d^N \rightarrow 3p^5 3d^{N+1} \quad \ldots\ldots\ldots \quad (5.5)$$

$$3p^5 3d^{N+1} \rightarrow 3p^6 3d^{N-1} + ef \quad \ldots\ldots\ldots \quad (5.6)$$

where ef is the electron emitted into a continuum state which is well above the vacuum level. Eq. (5.5) represents the Ti-3p-> Ti-3d resonance excitation. In eq. (5.6), the final state is followed by an Auger transition accompanied by a shake up process. There are many reports in the literature about the autoionization emission effect, especially for transition metals. Optical resonance effects measured on Titanium and Nitrides of Titanium also show this phenomenon. [108-110]

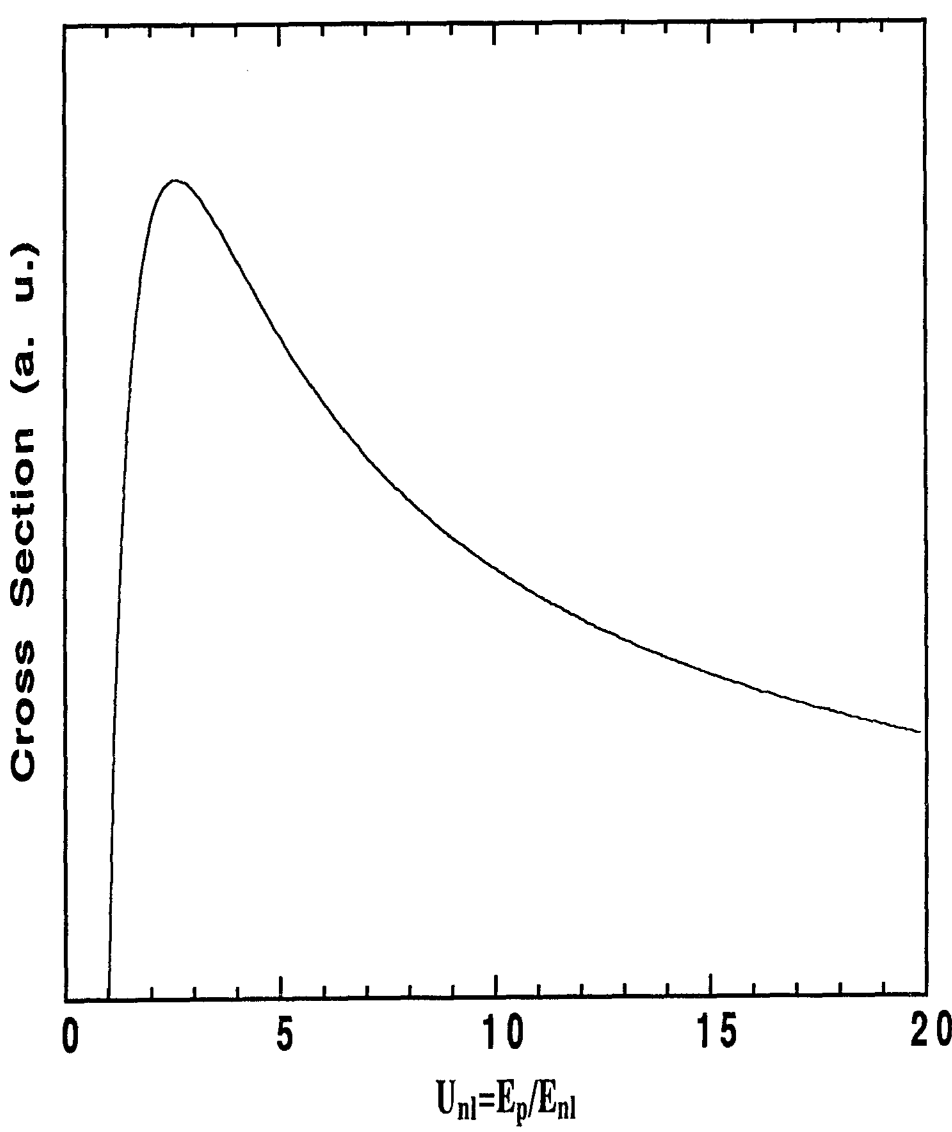

Figure 5.7 Ionization cross section vs U_{nl} for M shell electrons.

Peak 1 is assigned as a Ti-3s core-ionization. According to ref. [111], the binding energy of Ti-3s is 58.7 eV referred to the fermi level. The clean titanium metal EEL spectrum also displays a strong peak at 58.7 eV and a smaller one at 63.5 eV. In the carbide this transition appears at 64 eV, the shift in energy is attributed to the strong covalent bonding present in TiC.

Ti metal: In Table 5.3, we list the loss peaks of the clean metal. The most common interpretation of the energy losses found in the literature[102,112, 113] is the following :

(β_1) is the surface-plasma loss.

(β_2) is the volume-plasma loss.

(β_3) is a combination of surface-volume plasma losses.

(β_4) is due to the second harmonic of the volume plasmon.

(β_5) is the transition from the Ti 3p to empty 3d states (M core ionization).

(β_6) is attributed to the Ti 3p resonance(Ti 3p-3d threshold transition).

(β_7) is from the Ti 3s to empty 3d states transition(M core ionization).

Table 5.3.
Electron energy losses (in eV) of clean Ti(100) for Ep=150 eV.

Loss Peaks						
β_1	β_2	β_3	β_4	β_5	β_6	β_7
6.1	11.6	17.0	25.9	32.7	44.9	58.4

Bertel et al.[114] and Robins and Swan[115] identified the 17 eV loss as a volume plasmon, because from the well-known "Dielectric Theory",[116] the volume-plasma loss for free electron is

$$\Delta E_p = \hbar\omega_p = \hbar\sqrt{4\pi ne^2/m} = 17.7 \text{ eV}$$

while the surface -plasmon loss :

$$\Delta E_s = \hbar\omega_p/\sqrt{2} = 12.5 \text{ eV}.$$

Best,[117] however, assigned the 11.4 eV loss as an interband transition and the 25.1 eV loss as volume plasmon.

A comparison between titanium metal and the carbide shows great differences in the EEL spectra. This is associated with the variation in the electronic structures of the compounds, the bonding is metallic for the former and mainly covalent for the carbide.

Temperature Dependence

We show in Figures 5.8, 5.9, 5.10 and 5.11 the EEL spectra taken at different temperatures for three electron primary energies, Ep=150, 200, and 350 eV. The EEL spectra remained the same in the temperature range from 128 K to 673 K (Ep=150 eV). When the temperature increases to 1073 K one can observe a shift in peak e to 14 eV from 16.6 eV. This peak is also narrower. We can observe that peak a increases with temperature and the intensity of peak c decreases. We attribute these changes to partial surface

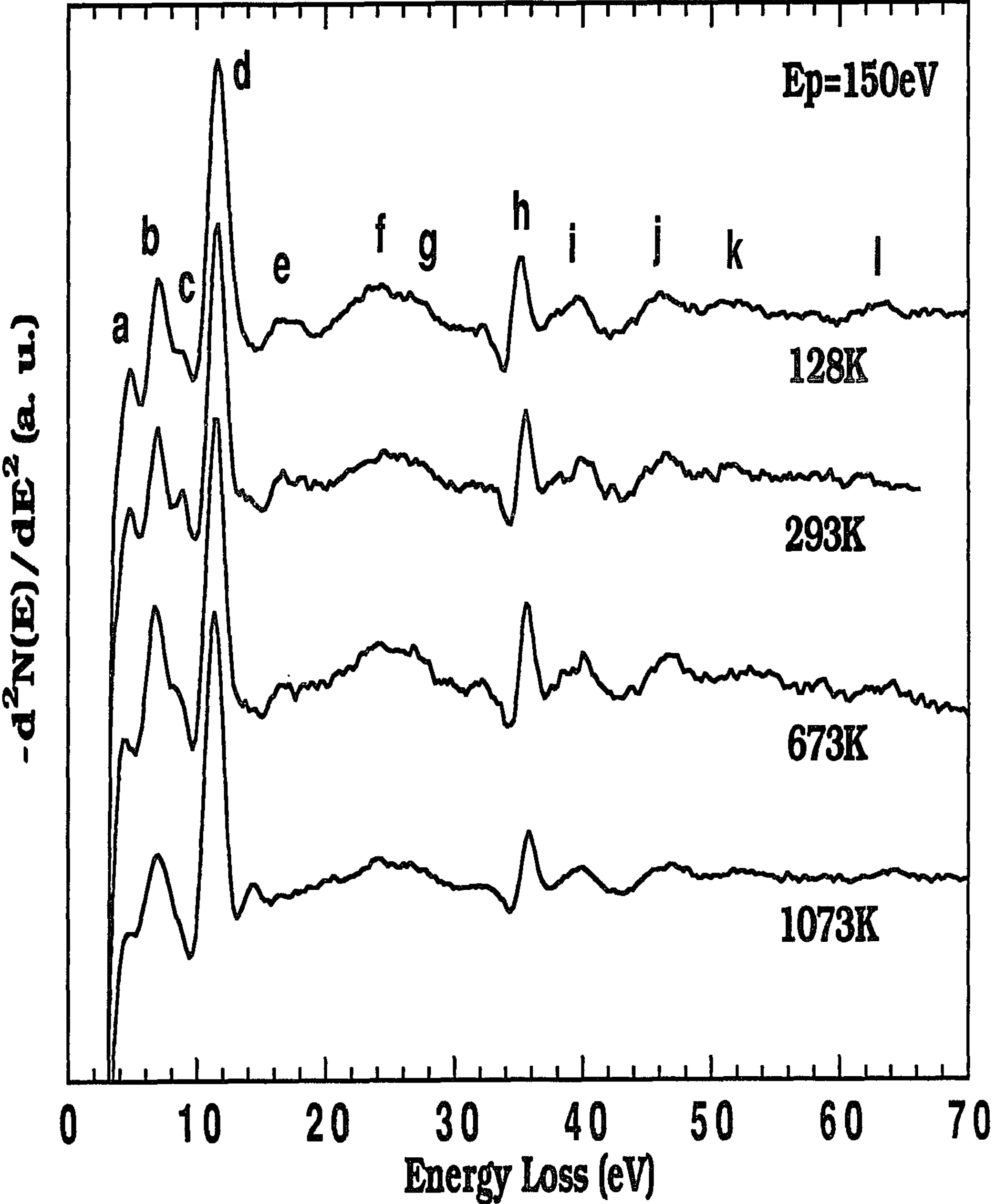

Figure 5.8 EELS spectra for Ep =150 eV as a function of temperature (128 °K to 1073 °K).

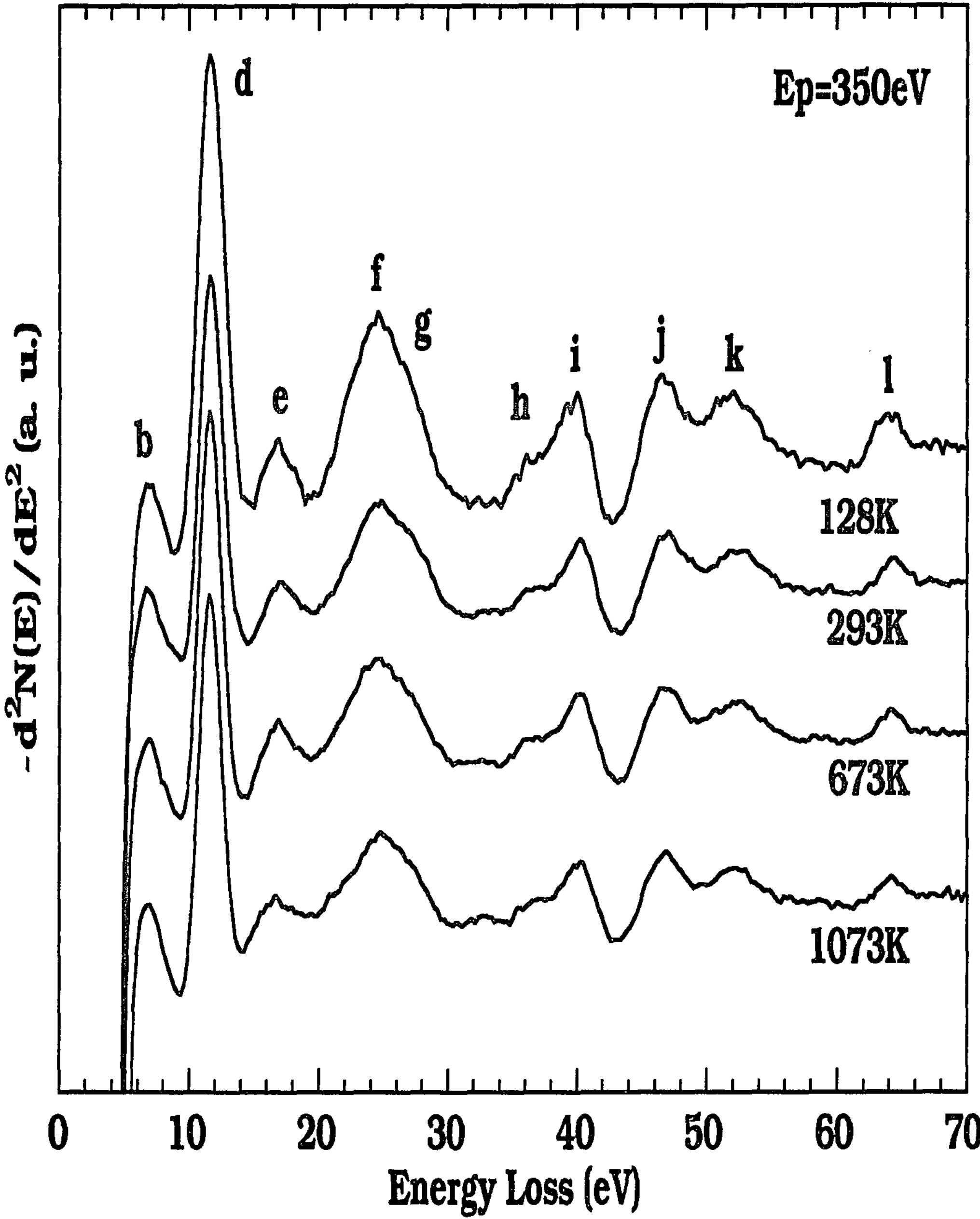

Figure 5.9 EELS spectra for Ep =350 eV as a function of temperature (128 °K to 1073 °K).

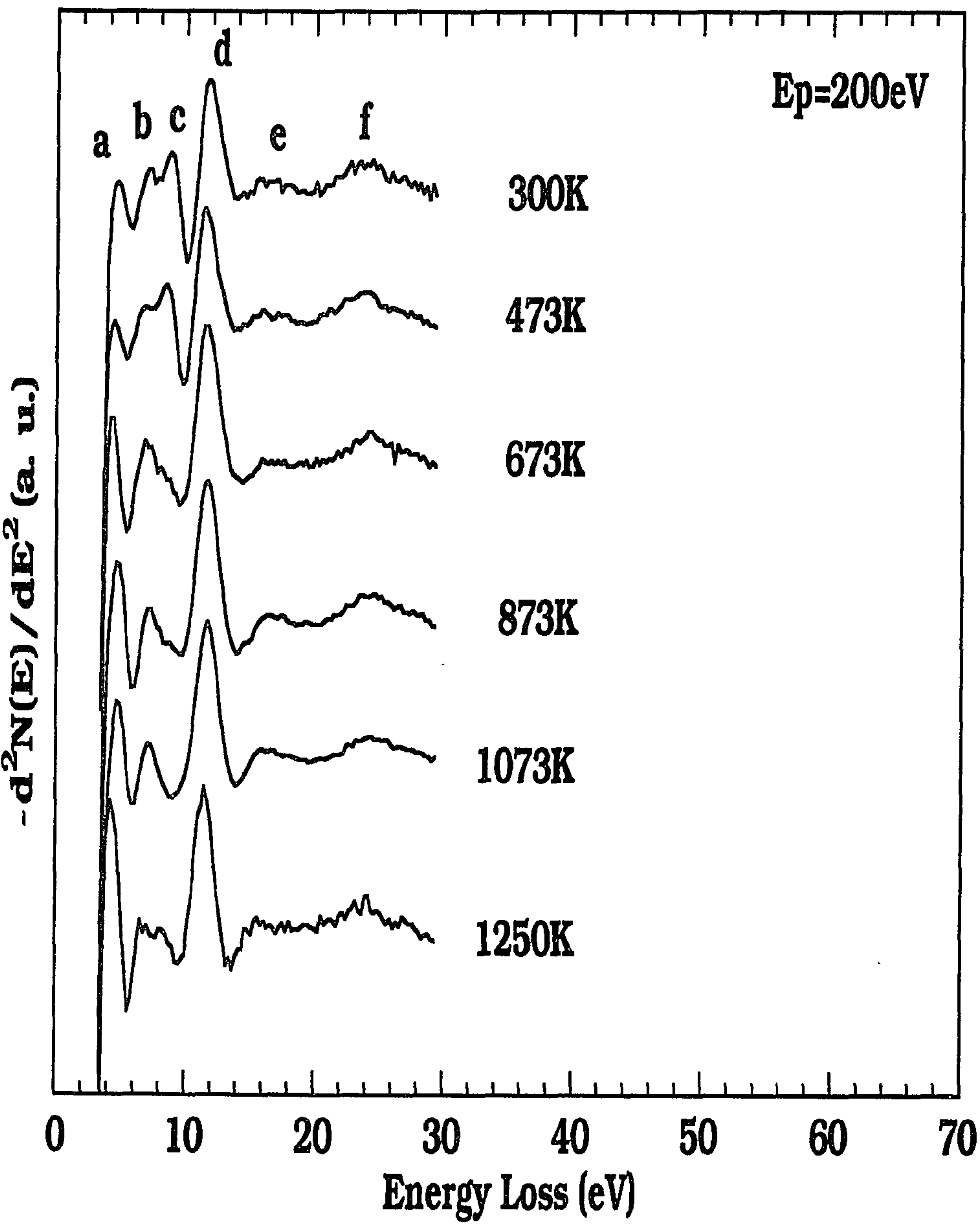

Figure 5.10 Lower range EELS spectra for Ep =200 eV as a function of temperature (300 °K to 1250 °K) with Oxygen coverage.

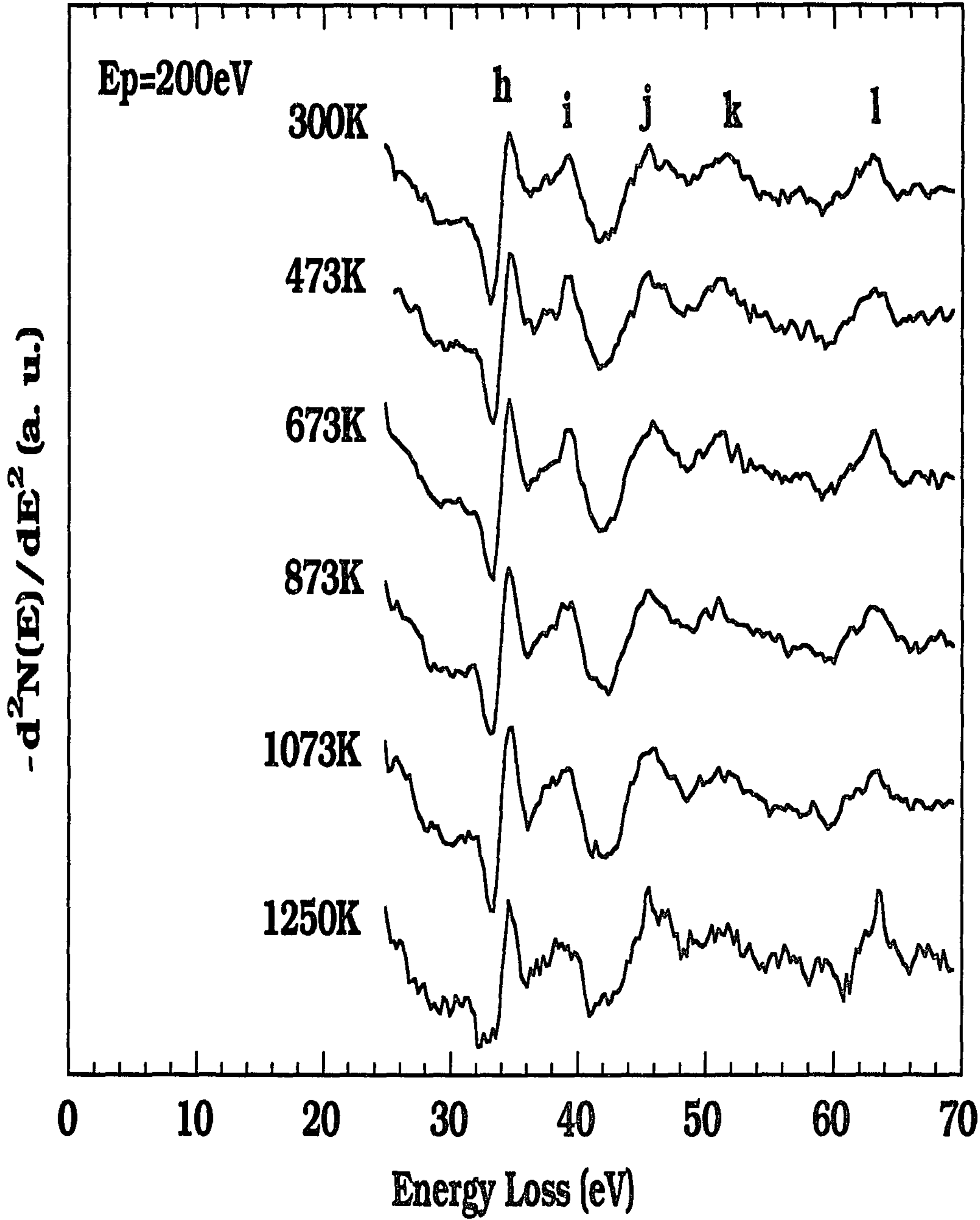

Figure 5.11 Higher range EELS spectra for Ep =200 eV as a function of temperature (300 °K to 1250 °K) with Oxygen coverage.

oxidation. The core level peaks, shown in Figure 5.7, are very stable through all the temperatures. For a primary electron energy of 350 eV, the EEL spectra remain the same as a function of temperature. This fact is taken as evidence that the bulk electronic structure remains unaltered as compared with the surface.

In Figure 5.12 the electron reflectivity is shown as a function of temperature for two different primary energies. At low energy (E_p=150 eV) there is a large decrease in reflectivity above 750 K. By contrast for a higher energy (E_p=1000 eV) there is a significant increase in reflectivity. This is probably indicative of the presence of defects on the surface at high temperature. The surface also shows the presence of a very small amount of oxygen. The changes in the surface electronic structure of the carbide can have important technological implications in bonding of the carbides to other surfaces. The [111] surface seems to show some temperature effects that can be detrimental towards the formation of stable interfaces in ceramic materials.

Ethylene Reaction With TiC [111]

Figure 5.13 shows the EEL spectra recorded after C_2H_4 adsorption at 136 K. Basically, the spectra are very similar to the spectra shown in Figure 5.3. The positions of the maxima are the same but the relative intensities are different. There is a peak denoted as (c) that appears and keeps its position and intensity even at higher primary energies. This peak is identified as a π^{b}- π^{*} transition from ethylene (7.6 eV gas phase).[117] This peak remains

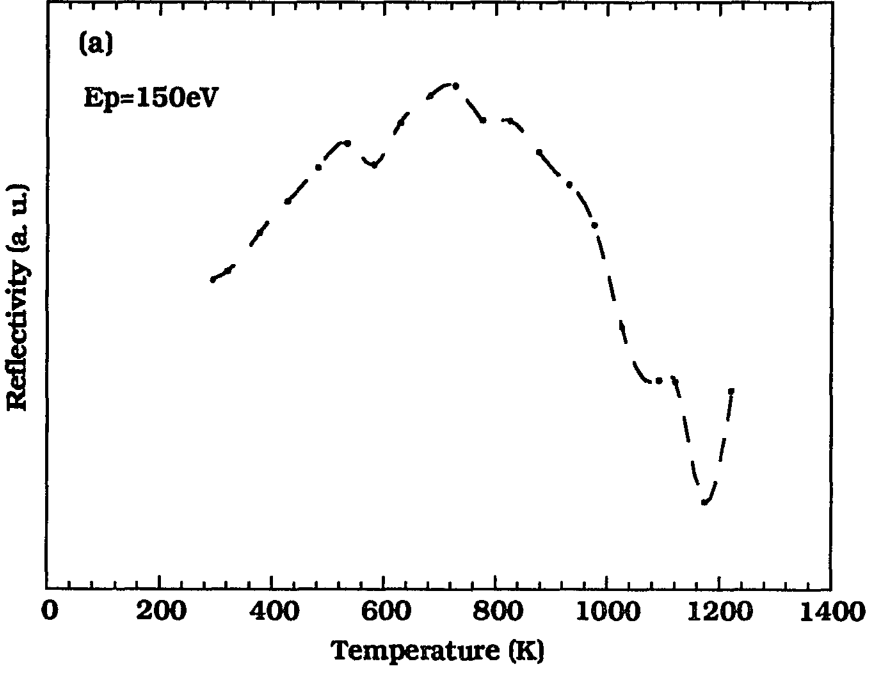

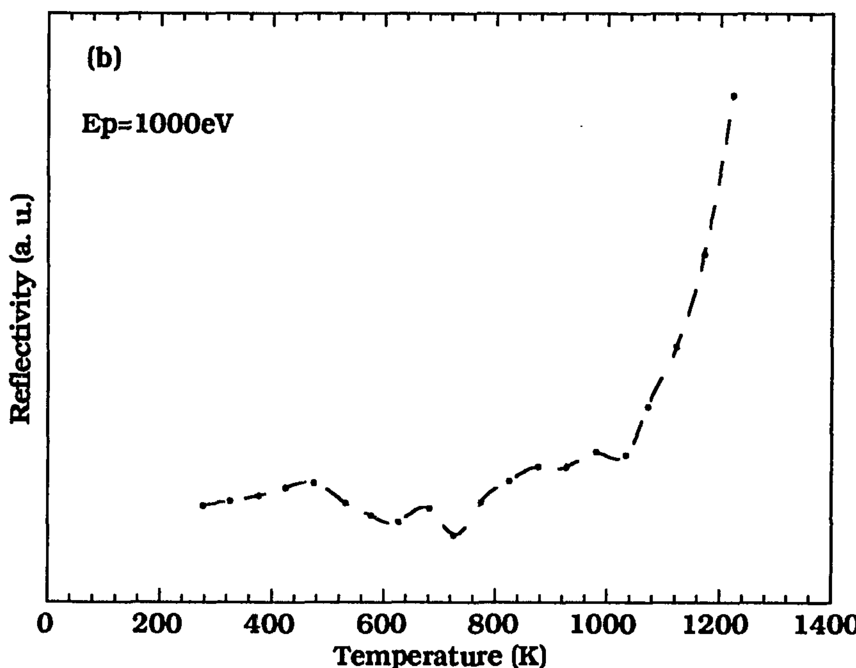

Figure 5.12 The reflectivity measurement vs temperature; (a) for Ep=150 eV; (b) for Ep=1000 eV.

even after the temperature is raised to 300 K. But after flash-heating the peak disappears. The EELS spectra returns back to that of clean TiC. This implies that the the bonding to the carbide surface is weak, ethylene bonding to the surface seems to be only physisorption.

Molecular Oxygen Reaction With TiC [111]

Figure 5.14 shows the EEL spectra after O_2 adsorption taken at room temperature. The Auger measurement showed that the oxygen coverage was 1.6ML. The intensity of peak a changes appreciable when compared to the clean sample and it fades rapidly after Ep=250 eV. This reveals that he electronic structure at the surface has been changed by the reaction with oxygen. However, the EEL spectra are different from those observed for titanium oxide.[118] Peak c is stronger than in the clean sample at the same Ep. At Ep=100eV we find an extra peak located at 13 eV, this peak is induced by the surface oxygen. It is attributed to an oxygen 2p ionization loss. For higher electron primary energies, we can not observe this peak. All other peaks show no significant changes with respect to the clean carbide.

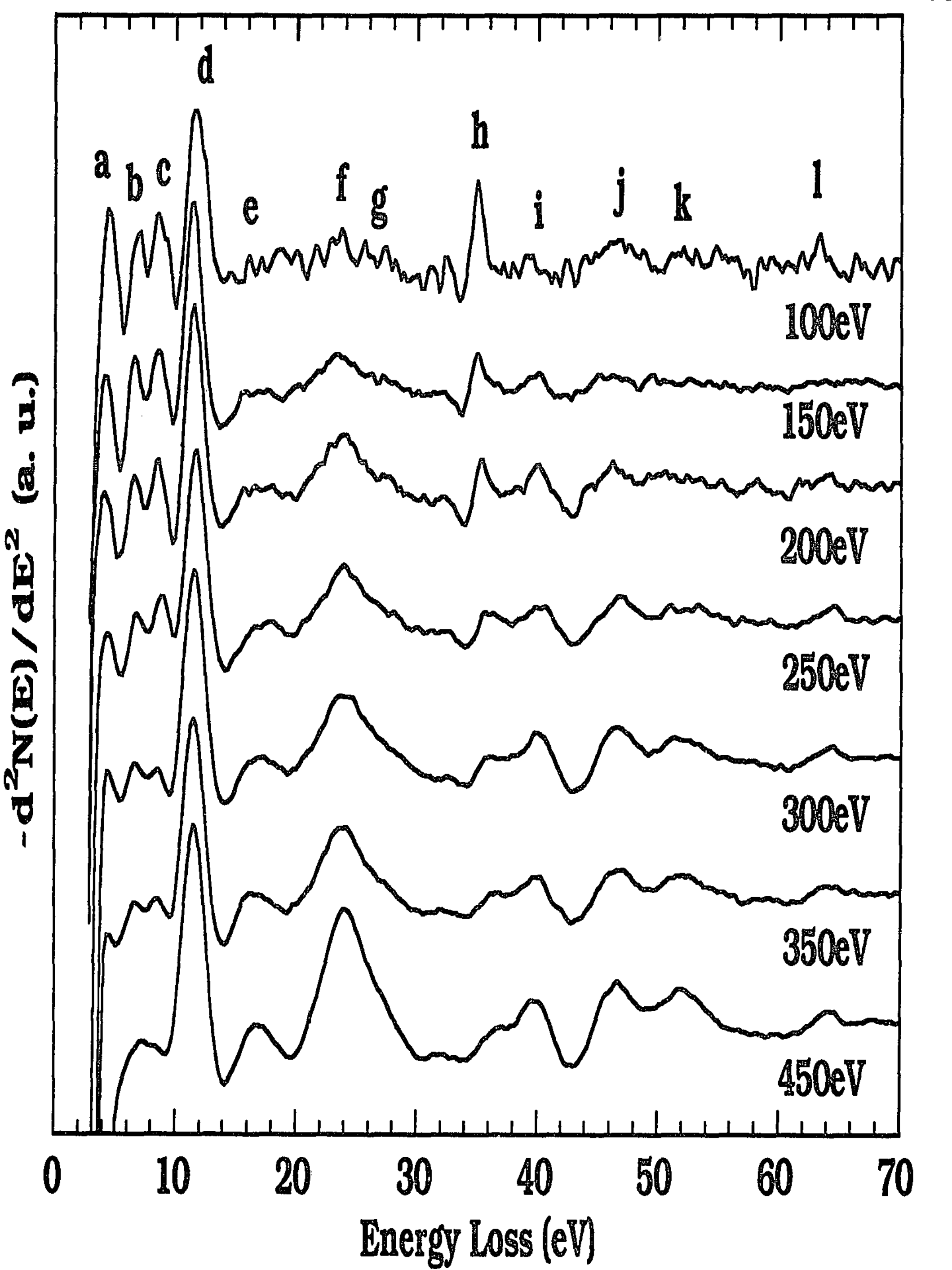

Figure 5.13 EELS spectra at 136 ^{o}k after Ethylene adsorption as a function of primary electron energy (100 to 450 eV).

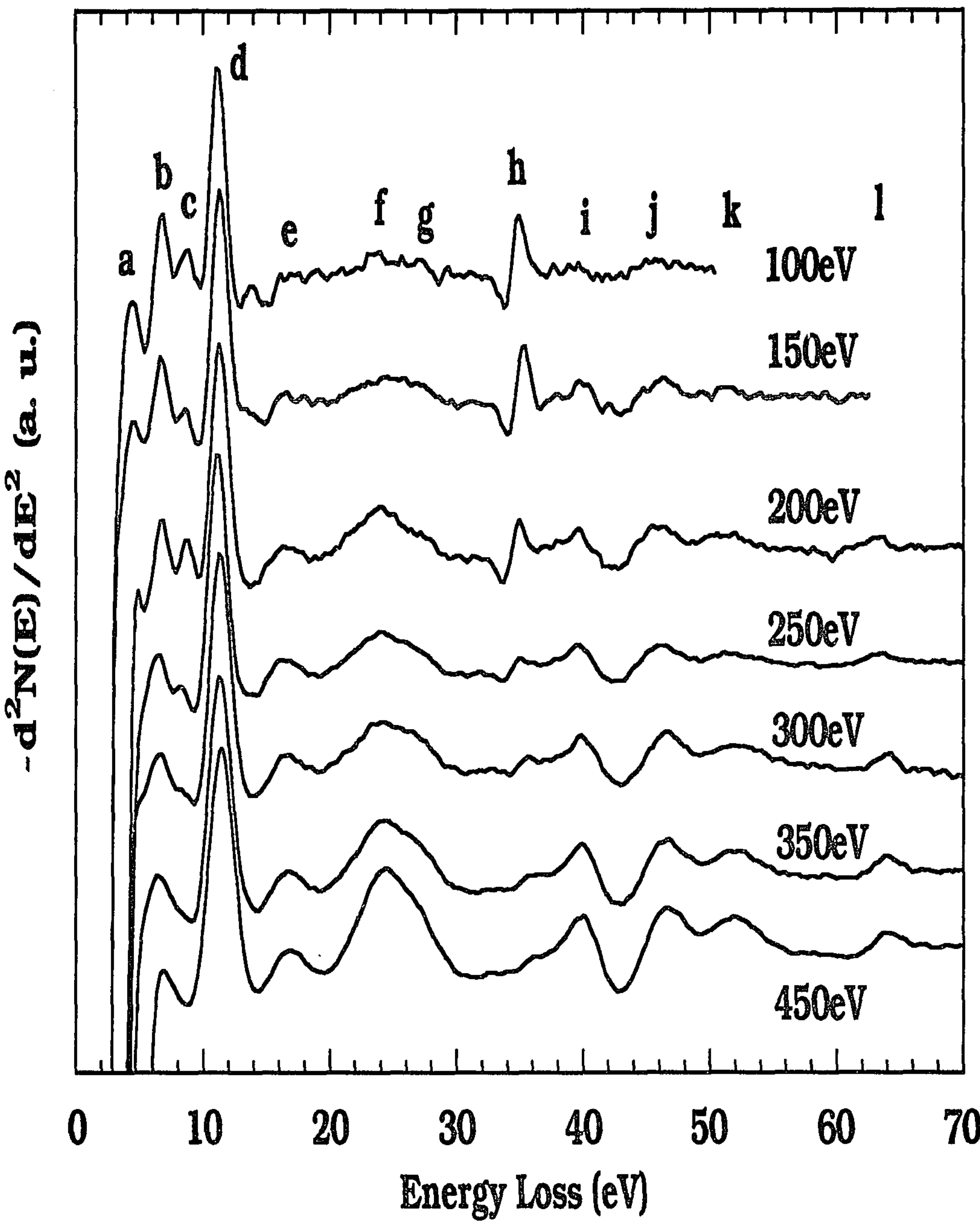

Figure 5.14 EELS spectra for Oxygen coverage on TiC (111) at 300 °K as a function of primary electron energy (100 to 450 eV).

CHAPTER 6

INTERFACE STRUCTURE AND STABILITY IN Ti/C MULTILAYERS

6.1 Previous work

Previous work on AES and EELS

In 1988, N. Thangprasent et al.[118] had studied the Ti/C multilayers by using surface sensitive techniques like AES and EELS. It was observed that the Ti/C interface is isolated by a thin Titanium oxide layer. The estimated thickness of TiO_2 layer is about 4-5Å.[119] The center of the Ti layer gives a typical EELS spectrum of Ti metal. The carbon shows a graphitic character. The results of these measurements have confirmed that the equilibrium structure is dominated by C-C bonding and they found that the interface has a graphite-like atomic arrangement rather than a carbide like arrangement. They further explored the interactions in this graphitic arrangement and found that the interface does not have a significant Ti-C bonding and that the interface most likely consists of simply a layer of graphite adjoining a titanium surface.[119] This carries important implications for the diffusion and bonding at the interface.

6.2 Introduction

It is well known that titanium carbide is one of the refractory metal monocarbides. Its hardness, high-temperature stability, good electrical conductivity and lightweight have made it extremely attractive in the aerospace industry. The interest in titanium carbon multilayers is based on the fact that it is possible to synthesize some

novel materials with character similar to titanium carbide but more ductile. Some artificial structures have shown remarkable elastic properties, so-called supermoduli had been discovered by W. M. C. Yang et al.,[6] J. E. Hillard,[7] D. Baral et al.,[8] and D. Wolf et al..[9] Multilayers are artificial structures that have drawn attention due to the possibility of tailoring material properties by appropriation of chemical elements and periodicity. Multilayer synthesized Ti/C is one way to control and modify the bonding between metal and carbon. If we can change the bonding length then we may succeed in controlling the mechanical properties of the multilayers, because covalent bonding typically supplies hardness, but at the price of brittleness, while metallic bonding supplies ductility. This is one way to explore the correlation between structure and bonding at the interface and mechanical properties of the multilayers.

In this chapter we used X-ray reflectivity at small angles and RBS to study the properties of Ti/C multilayers.

6.3 Experimental.

The multilayers studied in the present paper were prepared using a Perkin-Elmer argon plasma-rf-sputter deposition system. Table 6.1 gives the list of samples studied in this work.

Table 6.1

Ti and C composition of the multilayers

Ti (Å)	C (Å)	No. of Periods	
25.7Å	11.5Å	50	**(Sample 1)**
14.7Å	12.1Å	50	**(Sample 2)**

The X-ray specular reflectivity measurements were carried out at the National Synchrotron Light Source facility at Brookhaven National Laboratory using beam lines X-6B. The alignment of the sample and diffractometer was carried out using a methodology similar to that described in reference[56]. At very low angles, a set of calibrated aluminum absorbers was used to reduce the beam intensity before reaching the detector. All the measurements were carried out at room temperature. The energy of the X-ray used in this investigation was around 10.0 KeV.

We also used RBS to obtain the elemental composition of the samples as a function of depth. The RBS experiments were carried out at the Brooklyn College CUNY Dynamitron accelerator. Two different ion beams were employed in this investigation, protons and alpha particles. Resonance elastic scattering of α - particles by ^{16}O, were also used to detect the presentation of oxygen within the multilayers. Different energies of ion beam had been used in this study.

6.4 Results and Discussion

RBS

Figure 6.1 shows a typical RBS spectrum. In this measurement, we used He^+ as the ion source, and the accelerating energy at 2.2MeV. For all the samples we observed the presence of two peaks due to Ti and C as well as features due to the substrate Si. We also observed a small peak below the Ti that corresponds to Argon (which was embedded in the samples during sputtering). The most active

element - oxygen cannot be seen at this energy range (it did exist at the interface from the AES, EELS measurements[118]). In order to make sure of the presence of oxygen in the bulk of the sample or not, we used the elastic scattering resonance of alpha particles at 3.05 MeV. Figure 6.2 shows a typical spectrum at the resonance energy for alpha particles energy. Oxygen can be clearly observed at this energy stage. There is a strong dependence of the O peak on the alpha particles energy. A work of caution is necessary concerning the area of the peaks. Although O and C peaks seem to have similar areas, the amount of oxygen is very small. This is because resonance scattering is a nuclear force scattering. The scattering cross section is anomalously enlarged and it cannot be treated like RBS. This identification of the presence of oxygen within the sample is consistent with the AS and EELS measurement.[118] The total thickness (t) of oxygen at the interface can be calculated by using (Eq. 2.58)

$$\Delta E=[\varepsilon]Nt,$$

where ΔE = energy loss,

$[\varepsilon]$ = stopping cross section factor,

N = number of atoms (Oxygen in TiO_2) in cubic center meter.

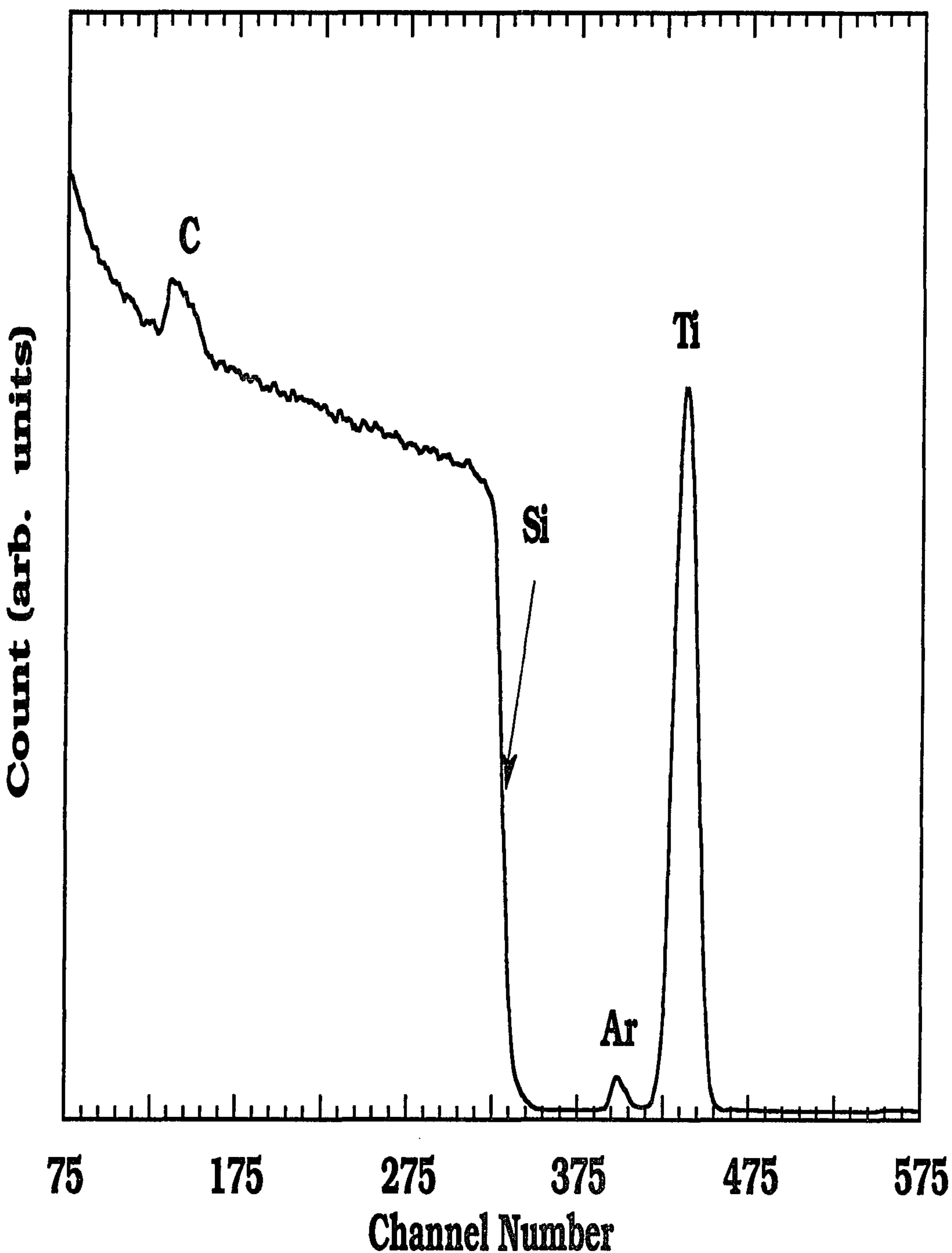

Figure 6.1 RBS spectrum for alpha particles at 2.2MeV.

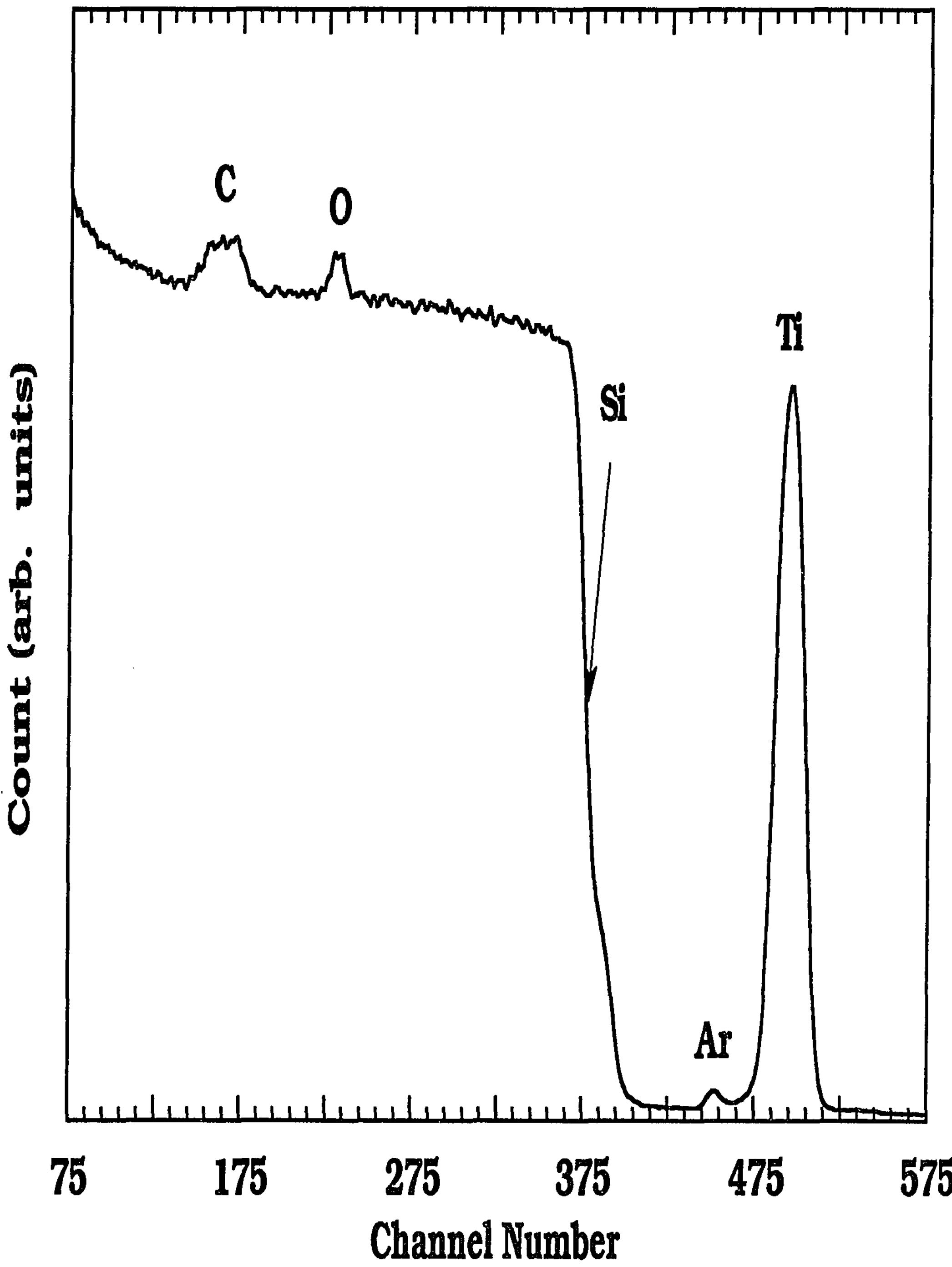

Figure 6.2 A typical RBS spectrum for alpha particles at 3.05 MeV.

By a rough calculation, one can obtain the total thickness t around 540Å ~ 670Å for energy losses at 20 keV and 25 keV. (This calculation is slightly larger than the AES, EELS measurements.) The average thickness of oxygen at each interfaces is about 5.4Å~6.7Å. This thin oxygen layer has been proved[118] that it comes from the titanium oxide layer which formed at the Ti/C interface.

RBS from the proton ion beam did not give significant results but it provided a better signal for the carbon.

X-ray reflectivity

The basic theory for analyzing the X-ray reflectivity data has been mentioned in chapter 2. In the following analysis, we will use the iteration method (Eq. 2.69) and a Gaussian type roughness at the interface to fit the experimental data. In this analysis of the data fitting, we do not consider the oxidation layer as an individual layer, because the electron densities of TiO_2 and Ti are almost the same. The electron density sensitive X-ray reflectivity can not make the discrimination between them.

Sample 1: The sample consists of 50 bilayers of [Ti(25Å)/C(12Å)] on Si. In this analysis of the data, the following model is used. The thickness of the bilayers Λ is assumed to be linearly increasing from the substrate layer to the top layer with $\Delta\Lambda/\Lambda \approx \pm 2.5\%$. The thickness ratio d_{Ti}/d_C is kept constant. The roughness between titanium and carbon, and the electron density of titanium and carbon are assumed to be constant throughout all the 50 layers. In order to have a good fit to the experimental data, the changing of thickness of each bilayer is necessary. A continuously, smoothly changing thickness can always

eliminate the strong interference happening around the Bragg peak.

Figure 6.3 shows the experimental data and its best fit. The data and the fit are represented by the closed circles and the bold solid line respectively. The spectrum of the data is quite complicated because there are three different modulations mixed together. One is from the bilayer structure, one is from the interference of reflectivity waves between the substrate and the total thickness, and the remainder is an unknown one. This unknown modulation is due to a layer with total thickness (Λ) about 320Å. Therefore, the possibility for a thin interface oxide layer creating this kind of modulation is very small. This layer can only exist in three different cases: (a) as a bottom layer, (b) as a submultilayer with different electron density in every 320 Å within the Ti/C multilayer, (c) as a topmost layer. We did try to fit the data for the three different cases. In case (a) and (b) we can not get a good fitting, only in case (c) can we obtain a good fitting like in Figure 6.3. In Figure 6.3, the fitting is very close to experimental data up to the first Bragg peak position (due to the bilayer structure near $q \approx 0.17Å^{-1}$). The secondary fringes, due to the interference of the reflected waves between the substrate and the total thickness of the multilayers match each other very well regarding angle (from $q \approx 0.065Å^{-1}$ to $0.18Å^{-1}$) and intensities. The position of the critical angle and Bragg peaks give information about the electron density contrast of the first few top layers, and modulation wavelength. Those are accurately determined by this fitting. An angle divergence $\Delta\theta \approx 0.009^0$ of the incident X-ray beam was taken into consideration.

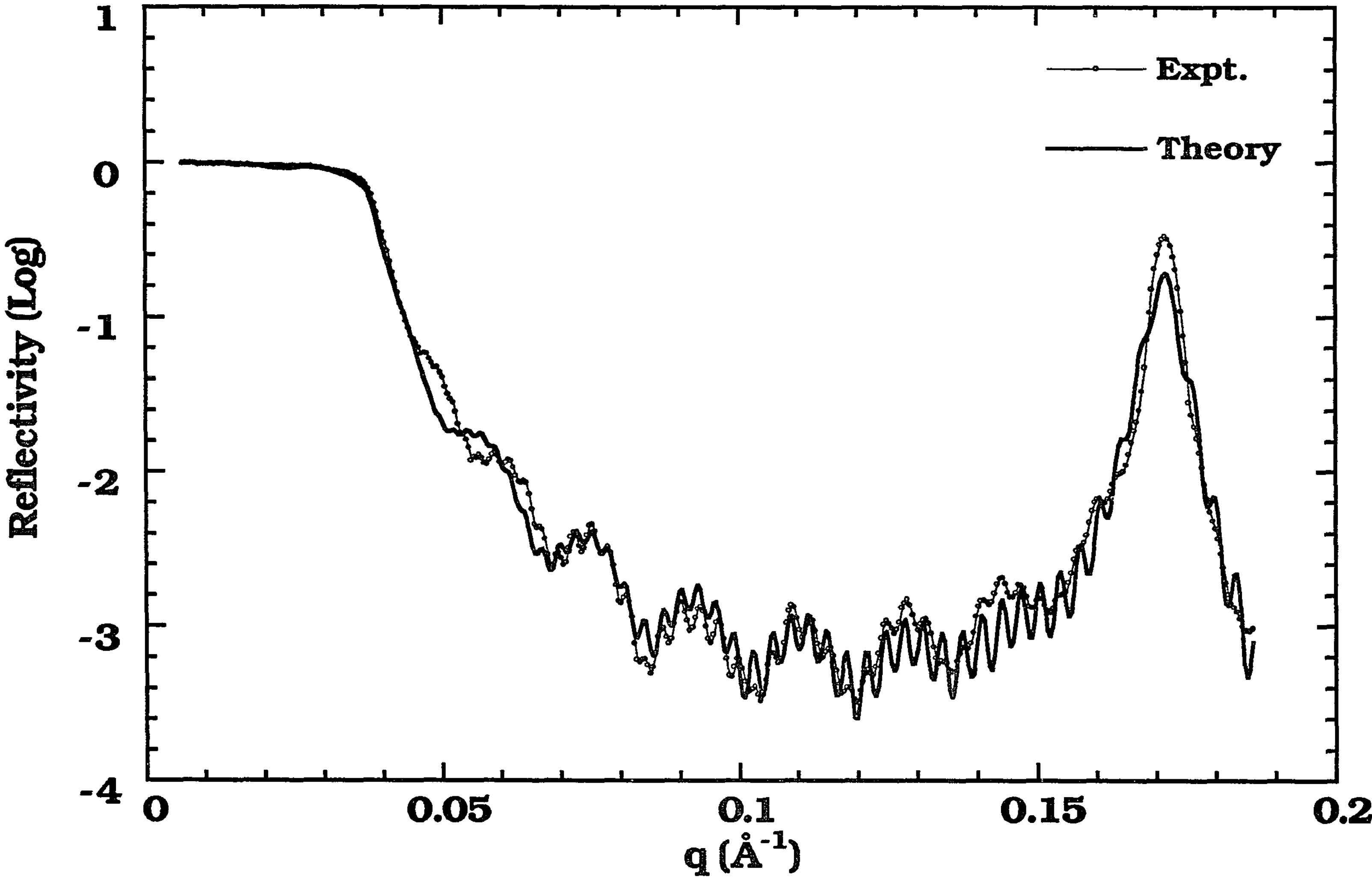

Figure 6.3 X-ray specular reflectivity of 50 bilayers of [Ti(26Å)/C(12Å)]. The bold solid line is the theoretical fit to the data.

The thickness and electron density parameters of the individual layers are shown in Table 6.2 and Figure 6.4. In this fitting, the known bulk electron density ~1.124($6.022 \times 10^{23} e/cm^3$) for carbon in graphitic state is used. The electron density of carbon is about 20% less than its nominal bulk value. The thickness of the topmost layer is 323Å and its electron density ~0.324($6.022 \times 10^{23} e/cm^3$). This layer may be formed by low electron density organic materials deposited on the the sample. Figure 6.5 illustrates the structure of Ti/C multilayer near the substrate with the interface roughness obtained from the fitting. Thin titanium dioxide layer was introduced in this schematic diagram in order to specify the configuration at the interface. The roughness at the TiO_2/C interface is only 1.2~1.3 Å.

Table 6.2

Parameters obtained from the fitting of the experimental data for the Ti(26Å)/C(12Å) multilayer.

Materials	Thickness d(Å)	Interface Roughness σ (Å)
Si(substrate)	∞	18.5.0
Ti	25.7	1.3
C	11.5	1.2
Topmost-layer	323.7	10.0

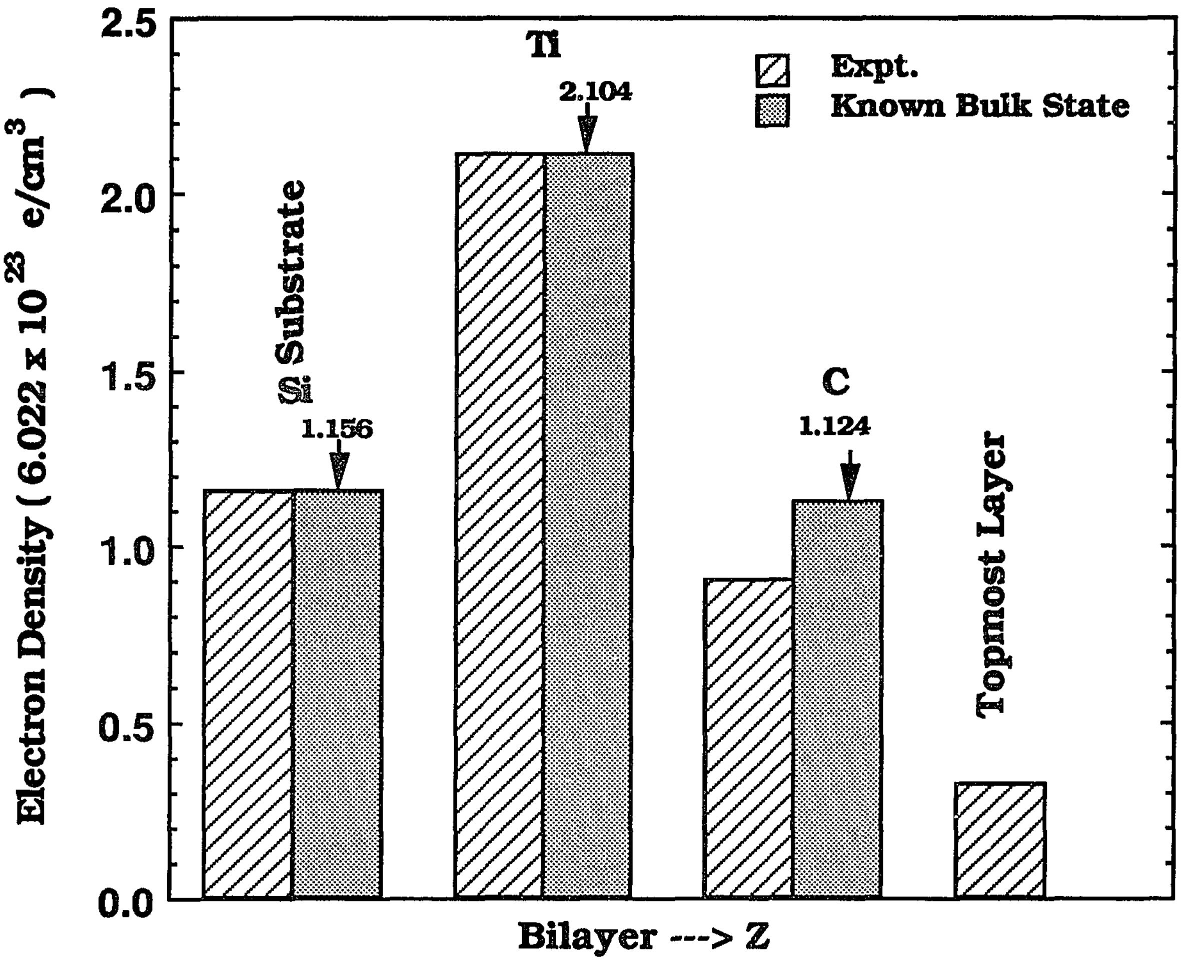

Figure 6.4 A comparison of electron density between the known bulk state and the experimental state. The experimental electron densities of Ti and C are from the parameters used to obtain fit in Figure 6.3. The electron densities of Ti and C have changed about 0% and -20% with respect to the known bulk state value.

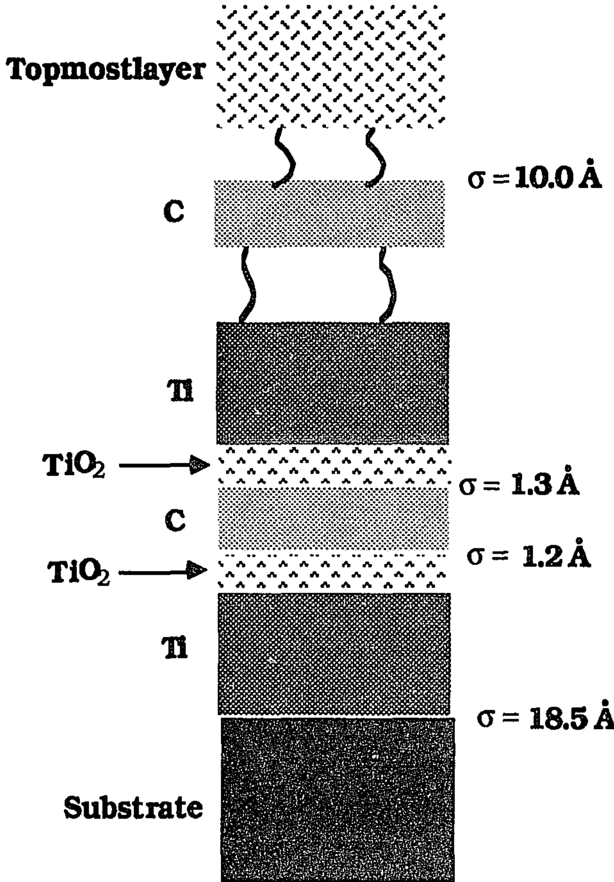

Figure 6.5 Schematic diagram of the [Ti(26Å)/C(12Å)] multilayer near the substrate with interface roughness values.

Sample 2: The second multilayer sample consisted of 50 bilayers of [Ti(15Å)/C(12Å)] on Si. In Figure 6.6 we show the X-ray reflectivity measurements for this sample. The plot in Figure 6.6 includes the first Bragg peak due to the multilayer spacing, the theoretical fit is also shown. In the analysis of the data the thickness of the bilayers Λ is found to be monotonically increasing from the substrate up to 19 layers with $\Delta\Lambda/\Lambda \approx 5.8\%$ and then decreasing slightly by 1% up to the

top layer. The thickness ratios were kept constant during the analysis. It was necessary to assume the presence of an extra layer of SiO_2 with thickness around 190 Å embedded between the bottom layer and the substrate. With this extra SiO_2 layer we can obtain a good fit of the medium frequency modulation.

Figure 6.6 shows the experimental data and its best fit. The data and the fit are represented by the closed circles and the bold solid line respectively. The fitting is very close to the experimental data from the angle $q \approx 0.095$Å^{-1} to 0.255Å^{-1} which is just before the first Bragg peak. The secondary fringes due to the interference of reflectivity waves between the substrate and the total thickness of the multilayers match each other very well regarding angle and intensities. In the region of $q \approx 0.035$Å^{-1} to 0.095Å^{-1}, there is a slight discrepancy between the data and the fit.

The thickness and electron density parameters of the individual layers are shown in Table 6.3 and Figure 6.7. The electron density of Ti and C are about 2% and 2% less than its nominal bulk value respectively. The thickness and electron density of the SiO_2 layer are 190.7Å and 1.380(6.022×10^{23}e/cm^3) respectively. This layer could be formed during substrate cleaning. Figure 6.6 illustrates the structure of Ti/C multilayer near the substrate with the interface roughness obtained from the fitting. Thin titanium dioxide layer was also introduced in this schematic diagram. The roughness at the TiO_2/ C interface is 8.0 Å. Compared with sample 1 this roughness is very large.

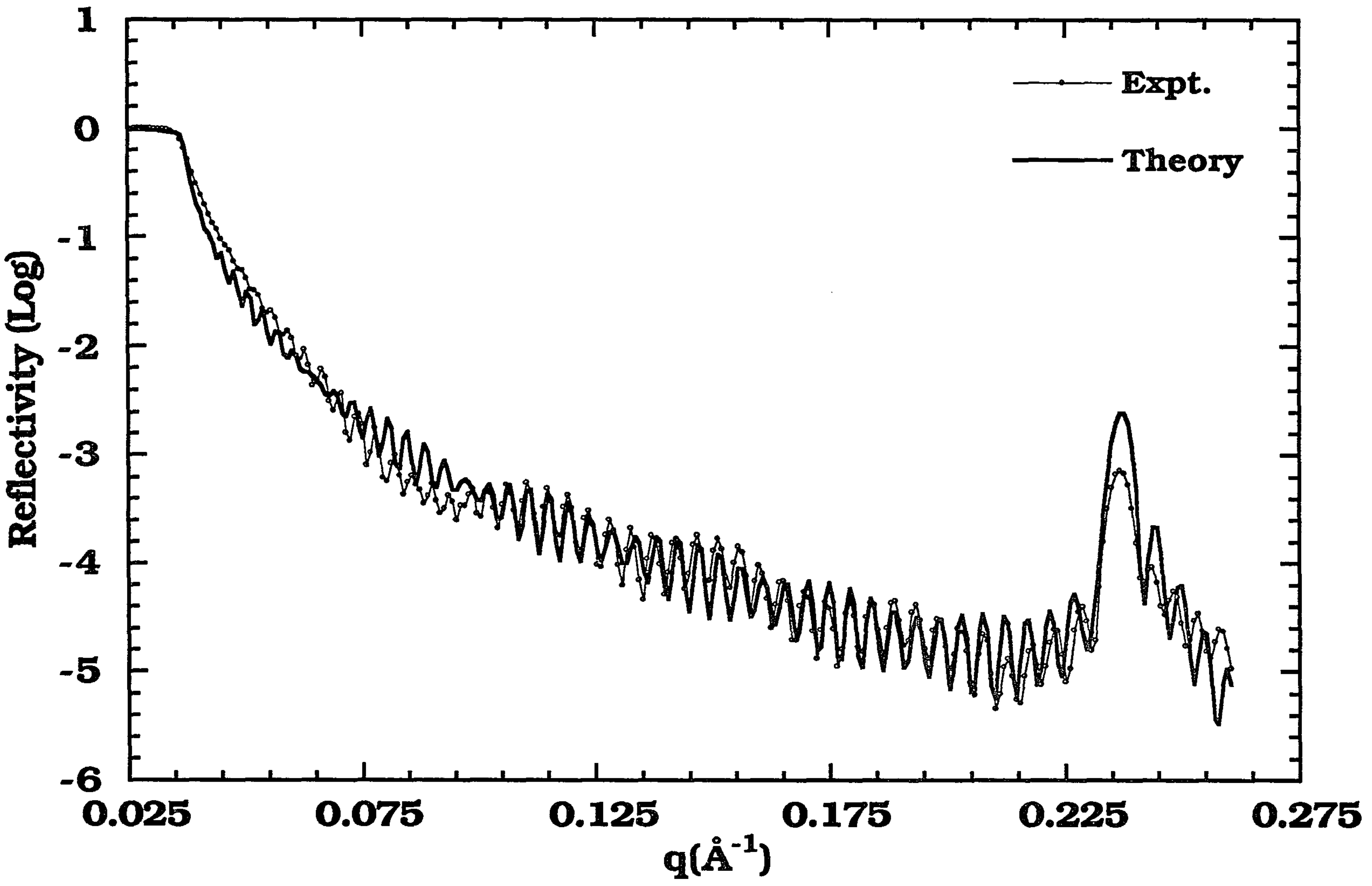

Figure 6.6 X-ray specular reflectivity of 50 bilayers of [Ti(15Å)/C(12Å)]. The bold solid line is the theoretical fit to the data.

Table 6.3

Parameters obtained from the fitting of the experimental data for the Ti(15Å)/C(12Å) multilayer.

Materials	Thickness d(Å)	Interface Roughness σ (Å)
Si(substrate)	∞	7.0
SiO_2	190.7	16.0
Ti	14.7	8.0
C	12.1	8.0

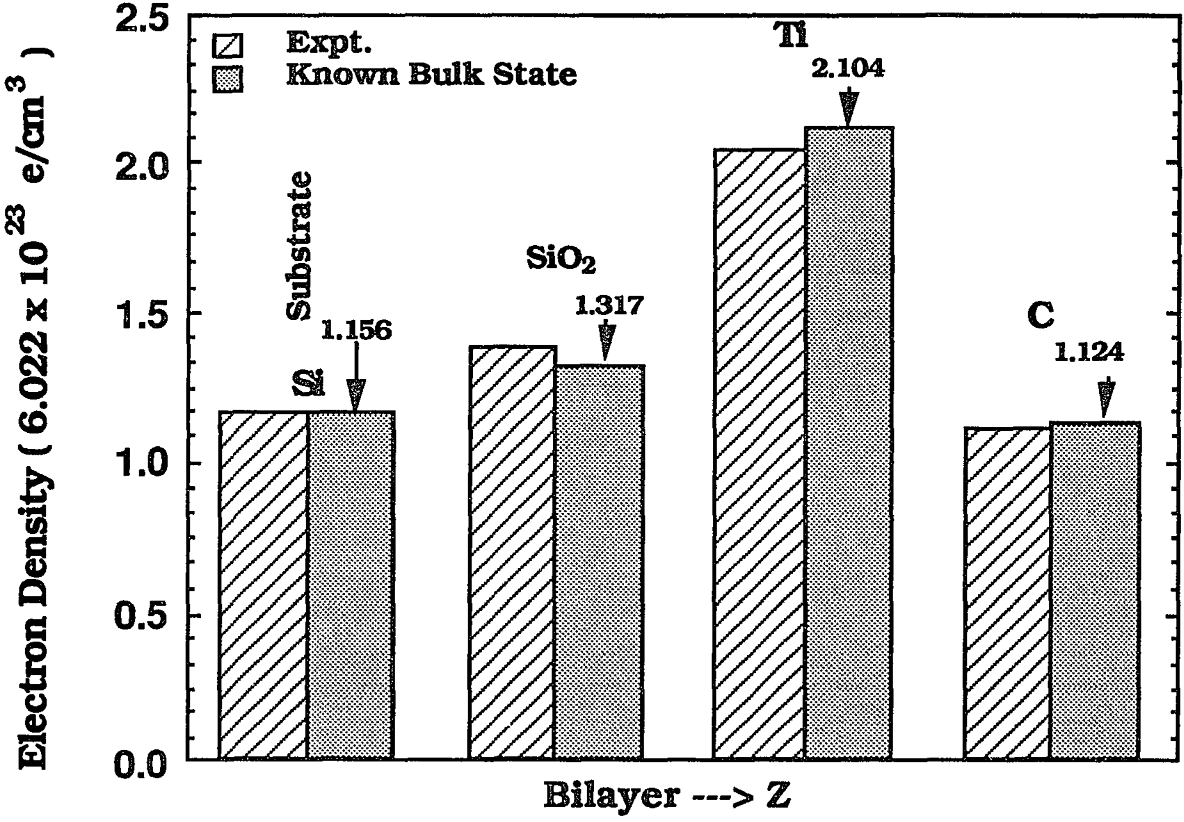

Figure 6.7 A comparison of electron density between the known bulk state and the experimental state. The experimental electron densities of SiO_2, Ti and C are from the parameters used to obtain fit in Figure 6.6. The electron densities of SiO_2, Ti and C have changed about +5% , -2% and -2% with respect to the known bulk state.

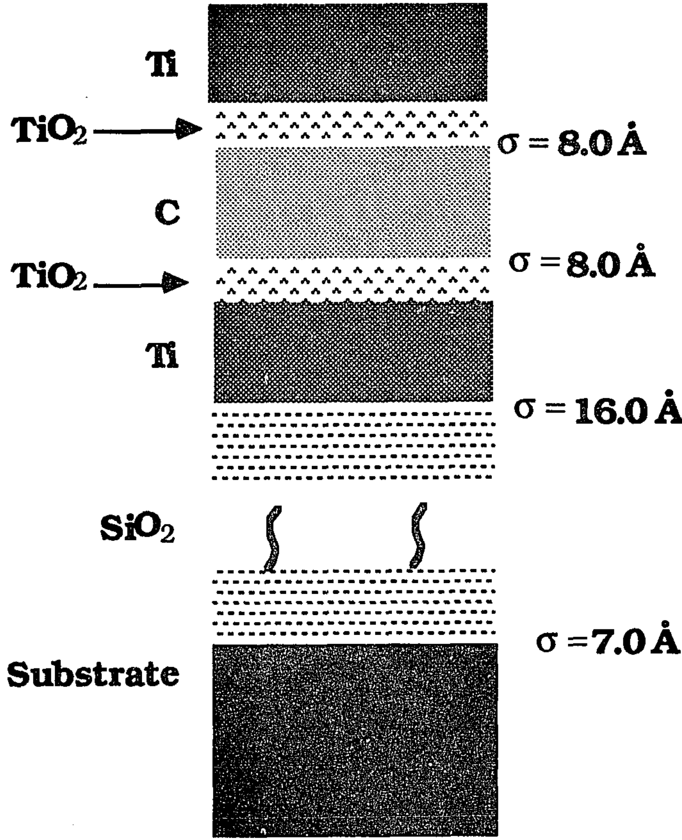

Figure 6.8 Schematic diagram of the [Ti(15Å)/C(12Å)] multilayer near the substrate with the values of the interface roughness.

CHAPTER 7

SURFACE STUDY OF SINGLE CRYSTAL of α-SiC-6H [0001] AT HIGH TEMPERATURES

7.1 Introduction.

Silicon carbide is a very important high temperature material that find wide industrial applications. SiC is a wide band gap semiconductor with good thermal conductivity and a small expansion coefficient.[120,121] These properties make this material very suitable for high temperature applications in electronic devices. Silicon carbide finds wide applications as a structural material. Self-bonded SiC was used as a cladding for nuclear fuels in gas cooled reactors.[122] It can be used in the aerospace industry for wear resistant parts, as a refractory material, for coatings, and reinforcement of materials exposed to high temperatures. SiC is one of the commonly used reinforcers in carbon and other composites.

SiC appears in many polytypes that differ from one another only in the stacking sequence of double layers of Si and C atoms.[124] Each double layer consists of a plane of close-packed (cp) Si atoms over a plane of cp C atoms; where one silicon atom lies directly over each carbon atom in a double layer. The most frequently encountered form of silicon carbide is hexagonal α-SiC, also known as 6H-SiC. The lattice parameters of α-SiC are a_0 =3.08065 Å and c_0=15.117384 Å. It sublimes at temperatures higher than 1800 C. Its physical stability if considered excellent below 1500 C. β-SiC is a cubic form of silicon

carbide (zinc blende structure) that has been studied in considerable detail in recent years.

There is considerable interest in the high temperature properties of silicon carbide. It has been reported that SiC evaporates with an excess of silicon in the vapor phase, free carbon being formed on the solid surface. It has been reported that the surface is completely covered with graphite in the high temperature region. Adachi et al[124] reported the evaporation of Si at high temperatures under UHV conditions. The surface depletion of silicon was also observed for β-SiC.[125] Great progress has been accomplished in recent years in understanding the surface properties of silicon carbide. In general the most common tool employed to study the silicon carbide surface has been Auger spectroscopy (AS). It is interesting to observe that the carbon AS signal is not significantly different from that observed for graphite. Electron energy loss spectroscopy (EELS) has not been widely applied to the study of the surface properties of silicon carbide.[126,127] We find this technique far superior to AS for surface characterization of silicon carbide.

We report in this thesis a series of high temperature measurements on hexagonal platelets of α-SiC, the platelets faces were perpendicular to the crystal c-axis <0001>. The initial surface face was carbon terminated. The surface measurements were performed under UHV conditions. We employed AS, EELS and surface electron energy loss fine structure (SEELFS) to characterize the variations in surface composition as a function of temperature and under oxidation conditions. Rutherford back scattering (RBS) and $^{16}O(\alpha,\alpha)^{16}O$ resonant

scattering were employed to study the elemental profile of the silicon carbide before and after reaction with oxygen.

7.2 Experimental.

The measurements were performed in an ultra high vacuum system with a vacuum better than 10^{-10} Torr. The samples were characterized by X-ray scattering prior to their use in the UHV system. The SiC sample was attached to a tungsten sample holder, and an electron beam heater was used to raise the sample temperature. The temperature was monitored and controlled using a proportional temperature controller. The chamber was equipped with a LEED system and a single pass cylindrical mirror analyzer(CMA) for AS and EELS measurements. The second derivative mode was used for the electron energy loss measurements using the CMA. The sample were exposed to oxygen using a needle valve, the sample temperature during oxygen exposures was varied between room temperature and 823 K. The angular resolved AS and EELS measurements were performed in a UHV system equipped with a 50 mm hemispherical analyzer with a position sensitive electron detector. A high resolution electron gun was employed for the angular resolved EELS (AREELS) measurements (15 meV resolution at 25 eV).

A very powerful tool to investigate the local atomic structure is SEELFS which has a similar fine structure as EXAFS. We have employed this techniques to study the variation in local structure around the carbon and silicon atoms. We used electron energy loss fine structure in our studies because of the low threshold energies of the carbon K-edge and silicon $L_{2,3}$-edge. The energy resolution for

the SEELFS measurements was about 8 eV. A modulating voltage of 8 volts was used in the measurements. This is necessary in order to obtain good signal to noise in the second derivative detection mode. The incident electron energy used in this experiment was 1500eV.

The RBS and $^{16}O(\alpha,\alpha)^{16}O$ elastic scattering resonance measurements were performed using the Brooklyn College dynamitron. This technique was used to determine the elemental composition profile on the silicon carbide samples before and after oxidation. We employed this technique to determine the oxygen content and depth profile in SiC. We also employed these tools to select our samples from different single crystal batches in order to have samples with no oxide inclusions.

7.3 Results and Discussion.

Auger Spectroscopy.

We employed AS for chemical characterization of the silicon carbide surface. Angular integrated AS did not show a high enough sensitivity to determine the type of carbon bonding at the surface or to distinguish between carbidic and graphitic carbon at high temperatures. Angular resolved AS was more sensitive for the identification of the surface composition. Figure 7.1 shows two AS spectra measured at two different angles of incidence, one at almost glancing angle (a) and the second at normal incidence (b). The spectra were collected in the count mode (no derivative of the spectrum was taken), one easily detects the presence of Si and C. One can clearly observe the presence of oxygen on the surface of the sample and its absence in the bulk. The oxygen peak disappears

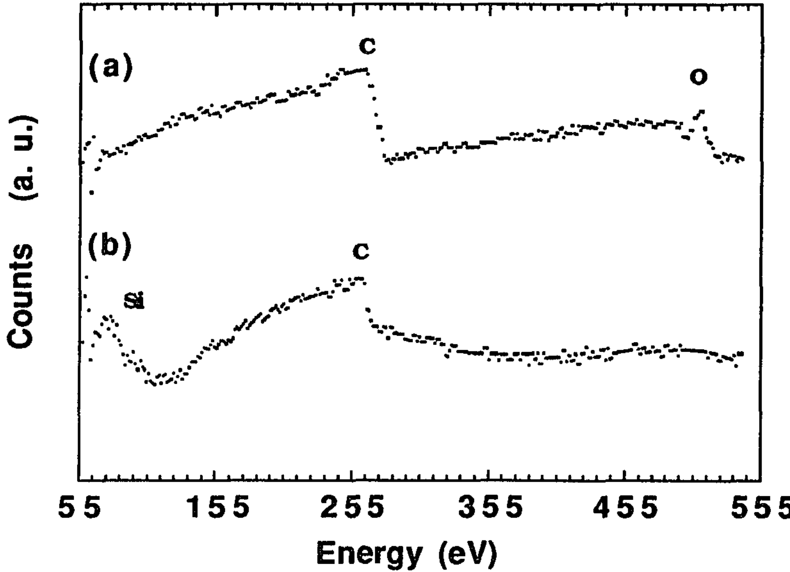

Figure 7.1 Angular resolved AS a) glancing angle of incidence. b) angle of incidence 70°.

after moderated heating of the sample. The angular resolved AS measurements did not give any further information at high temperatures.

Surface Energy Loss Structure Fine Structure.

It is well-known that the X-ray absorption cross section will be modulated by the presence of other atoms close to the absorbing center. Inner shell electrons can also be excited by the inelastic scattering of electrons and the EELS spectrum can exhibit EXAFS like oscillations. Such observations have been recently reported in the literature.[47,48] In the present work we used the same methodology reported in references.[47,48] We measured the K-edge of C and the $L_{2,3}$

edges of Si. In Figure 7.2 we show the SEELFS spectra for the Si L-edge before and after heating to 1273K. One can observe the good quality of the signal to noise in the data. The magnitude of the Fourier transforms of the data before and after heating are shown in Figures 7.3a and 7.3b respectively. It is noted that no appreciable change has occurred in the Si nearest neighbors environment. In marked contrast the carbon K-edge spectra show remarkable differences before and after heating. In Figures 7.4a and 7.4b one observes that the spectra are very different. We attribute this difference to the fact that a thick graphitic surface layer has formed on top of the SiC. A comparison of the near-neighbor distances for carbon atoms in α-SiC 6H and the experimental measurements (extracted from Figure 7.4a) is listed in Table 7.1. Table 7.2 is a comparison for carbon atoms in graphite and the experimental measurements (extracted from Figure 7.4b). The difference between the true distance r and the peak position r', $\Delta r = r - r'$ due to the phase shift θ_{ij} (k) in Eq. 2.52 can be roughly estimated using the linear approximation ($\theta_{ij}(k) = P_0 + P_1 k$). The deviation $\Delta r = r - r'$ is equal to $-0.5P_1$. P_1 can now be found out by fitting the theoretical phase shift data. In this analysis, we used the theoretical phase shift data listed (in appendix V) in ref.[45], and then performed a least square fit to the data. After the fitting, the parameters of p_1 for C-C and C-Si are about -0.7 and -0.48 respectively. The interatomic distances F(R) after the phase shift correction are listed in the Tables 7.1 and 7.2. Some of the interatomic distances have 16% deviation from the standard crystal. This can be understood, since the peaks in Figure 7.4a and 7.4b are

not very separated from each other, and these peaks overlapping can prevent us to determinate the real distance. Our objective in this analysis is to have a semiquantitative evaluation of the parameters for a corroboration of the identity of the species present in the sample.

A word caution is pertinent at this point. Great care must be taken in outgassing the electron source prior to carrying out any measurement at the carbon K-edge and to have excellent base vacuum. If one ignores these procedures the detected graphite could be the result of residual gases reacting with the electron beam. We took the appropriated precautions to avoid this problem.

Table 7.1.
Comparison of near-neighbor distances for the Carbon atoms in the α- SiC-6H[128,84] and the experimental measurements extracted from Figure 7.4a.

Shell	α- SiC-6H Bond Distances (Å)		Exp. *F'(R)* Fig7.4(a) (Å)	After Phase Shift Correction F(R) (Å)
1	1.89	C-Si	1.9	2.1
2	3.07	C-C	2.9	3.2
3	3.61	C-Si	4.0	4.2
4	4.75	C-Si	4.8	5.0

Table 7.2
Comparison of near-neighbor distances for the Carbon atoms in the graphite[84] and the experimental measurements extracted from Figure 7.4b.

Shell	Graphite Bond Distances (Å)	Exp. *F'(R)* Fig7.4(b) (Å)	After Phase Shift correction F(R) (Å)
1	1.42	1.5	1.8
2	2.46	2.4	2.7

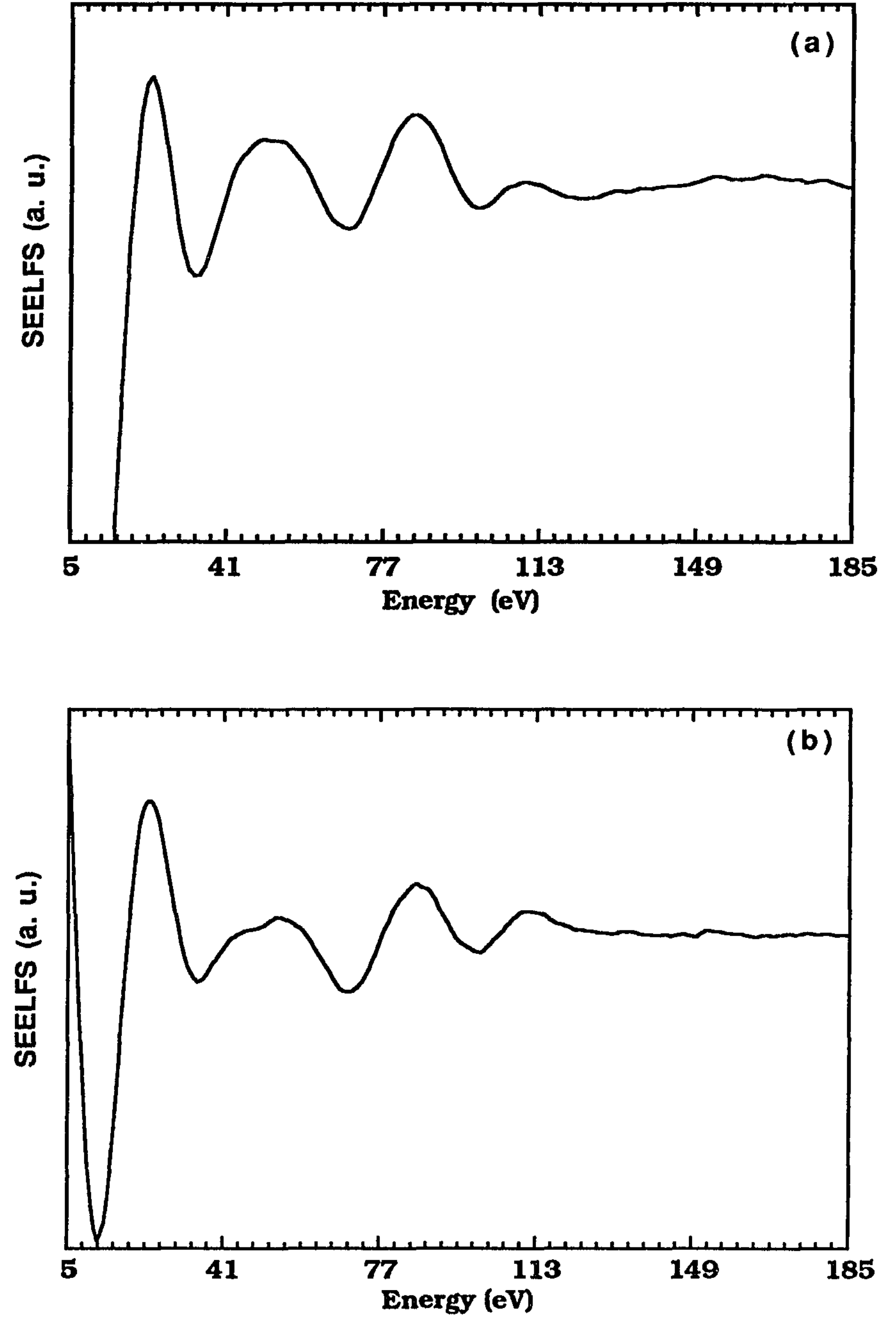

Figure 7.2 Top SEELFS spectrum at the Si L-edge before heating and bottom after heating.

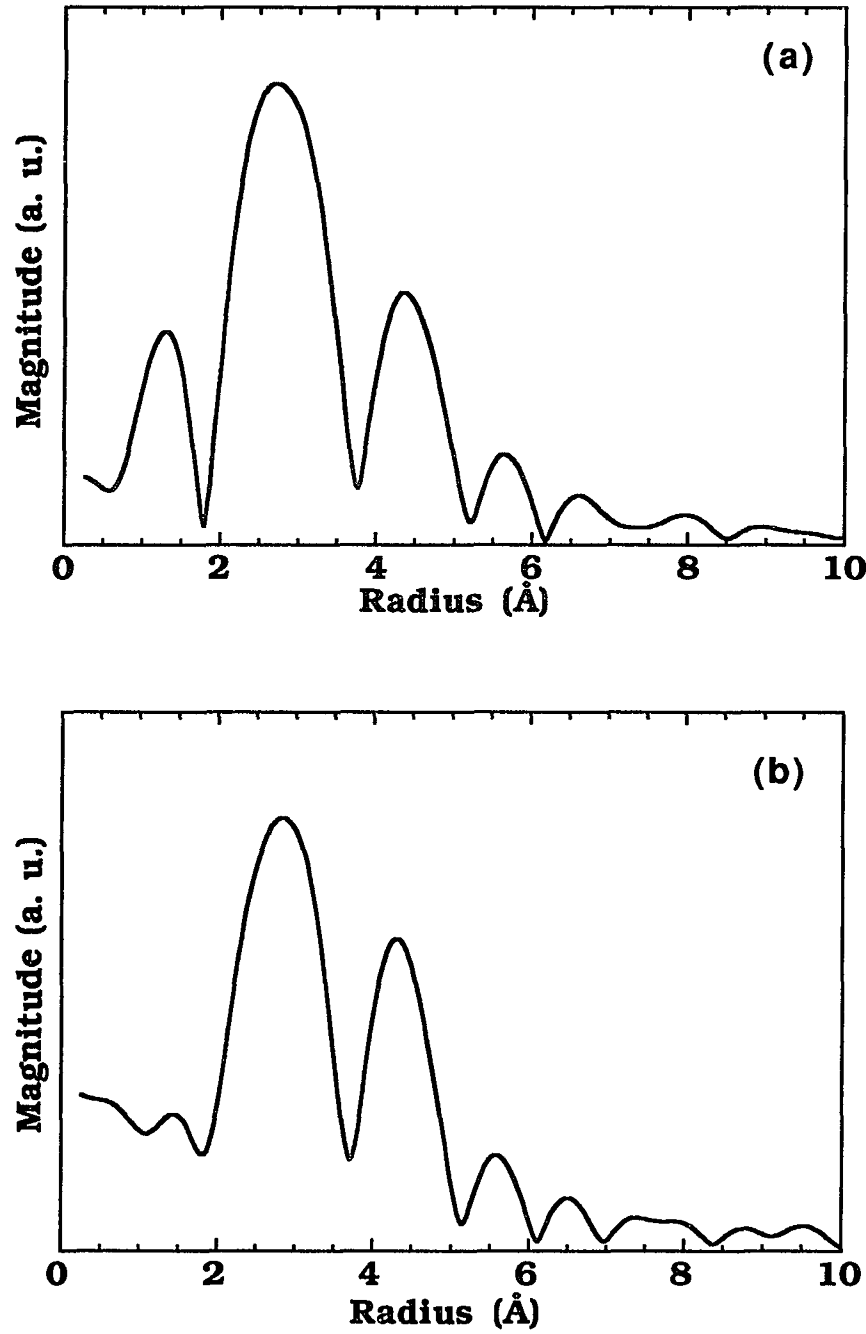

Figure 7.3 Magnitude of the Fourier transform of the SEELFS spectrum of Si: a) before heating; b) after heating.

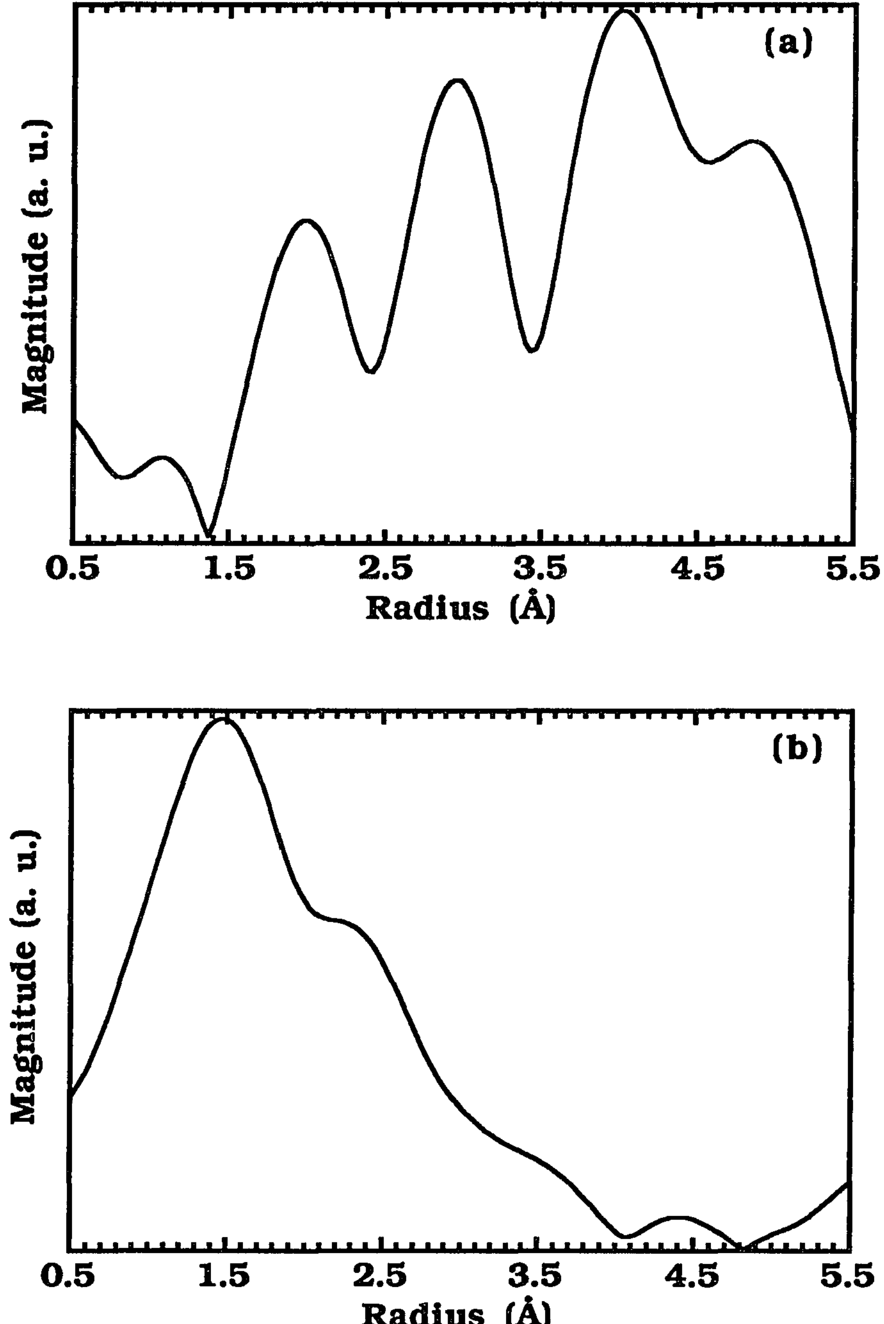

Figure 7.4 Magnitude of the Fourier transform of the SEELFS spectrum of C: a) before heating; b) after heating.

RBS and $^{16}O(\alpha,\alpha)^{16}O$ measurements.

The RBS measurements were used to study the purity of our samples prior to its selection for our studies. The elastic scattering resonance of a particles by ^{16}O were used to investigate the penetration of oxygen in the material. We observed for best samples that oxygen was confined to the surface at room temperature. There was evidence of rapid penetration of oxygen in the bulk for samples that were exposed at high temperatures to an oxygen environment. In some cases oxygen was detected at a depth of more than 300 Å. The reactions were carried rapidly, in a matter of seconds.

Electron Energy Loss measurements.

In our study we have calculated the dielectric functions for α-SiC and graphite. In Figure 7.5 we plotted the bulk and surface loss functions, as well as the second derivatives. One observes a broad peak around 22 eV that corresponds to the bulk plasmon, and a second peak at 17 eV corresponding to the surface plasmon. For graphite we obtain a bulk plasmon at 25 eV and the surface plasmon at about 19.5 eV.

The EEL spectra measured with the CMA using primary energies between 100 to 500 eV. The angular resolved EEL spectra were taken at various angles of reflection. One obtains great surface sensitivity with this technique, in particular for a glancing angle of detection with respect to the crystal face. The electron primary energy in the angular resolved measurements was varied between 50 to 300 eV.

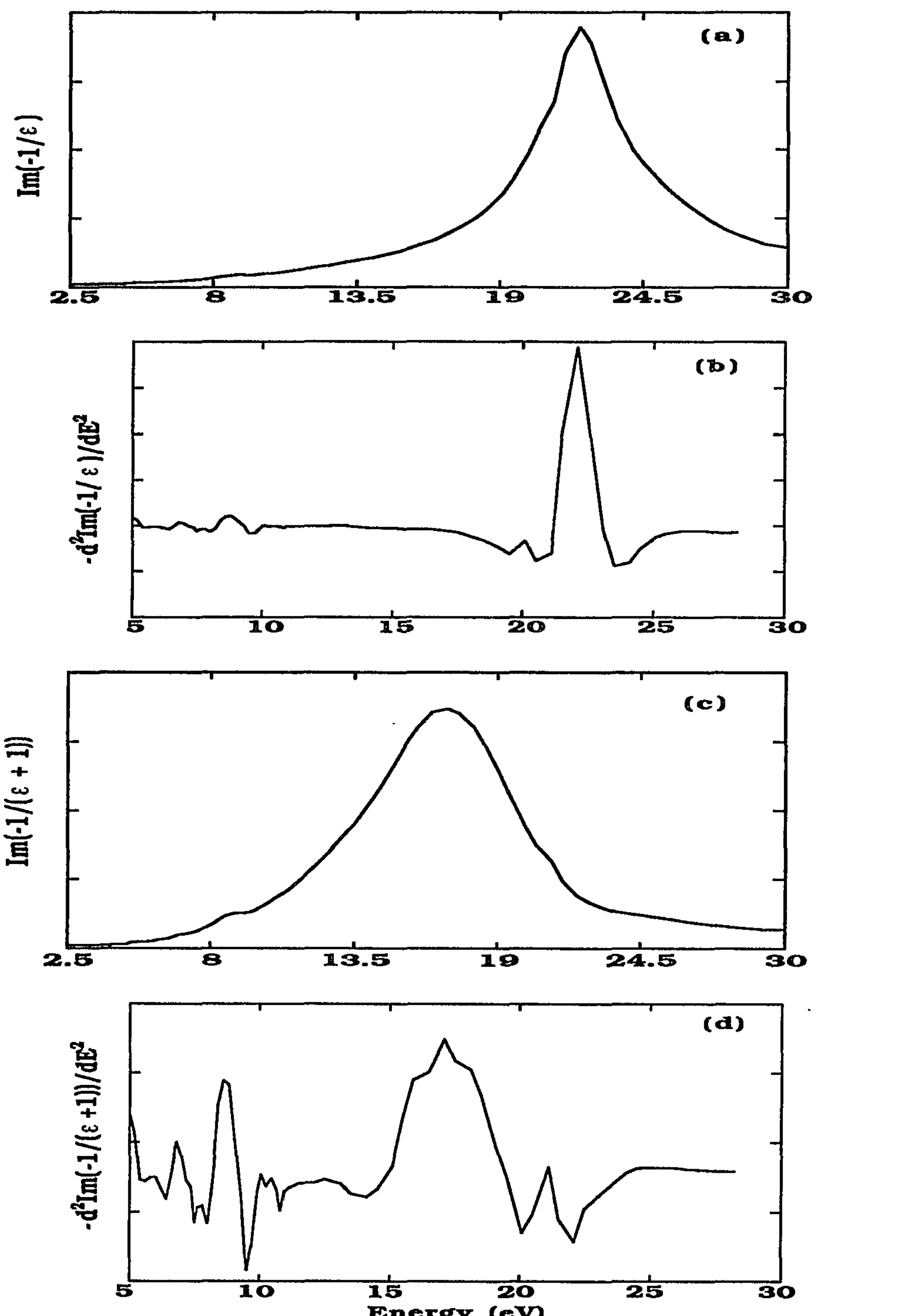

Figure 7.5 Energy loss functions and second derivatives for the surface and bulk of α-SiC.

In Figure 7.6 we show the EEL spectra (second derivative mode) as a function of primary electron energy (E_p) at normal incidence. The spectra correspond to the pristine single crystal, with the characteristic α-SiC plasmon losses at 22.2 and 18.6 eV. The bulk plasmon peak becomes more pronounced for high electron primary energies. The inelastic scattering mean free path for 500 eV electrons is about 22 Å. In the figure we have indicated with letters (a-f) the energy position of the electron losses (E_p=150eV): a=3.2 eV; b=6.0 eV; c=11.3 eV; d=13.6 eV; e=18.6 eV; f=22.3 eV. It is very significant that peak a is very close in value to the band gap in silicon carbide, we identify this peak as an exciton loss. The energy losses change slightly with increasing primary energy. There is considerable structure at low E_p due to surface states and excess carbon. Basically our EEL spectrum does differ much from the ones reported in the literature[127] for α-SiC (0001) and β-SiC (111).

In Figures 7.7 and 7.8 the EEL spectra are shown for temperatures between 300 K and 1273 K. A very significant change occurs between room temperature and 573 K, one observes that the plasmon losses has shifted significantly to higher values, about the same as measured for graphitic carbon. The low energy losses have not shifted significantly. In Figure 7.7(E_p=150eV) one can clearly see the formation of a graphitic layer on top of the sample. Two mechanism contribute to this phenomenon migration of carbon by creation of vacancies in the bulk and Si loss. The dramatic changes in all spectra occurs at rather low temperatures, where silicon evaporation is impossible. Consequently surface migration of carbon

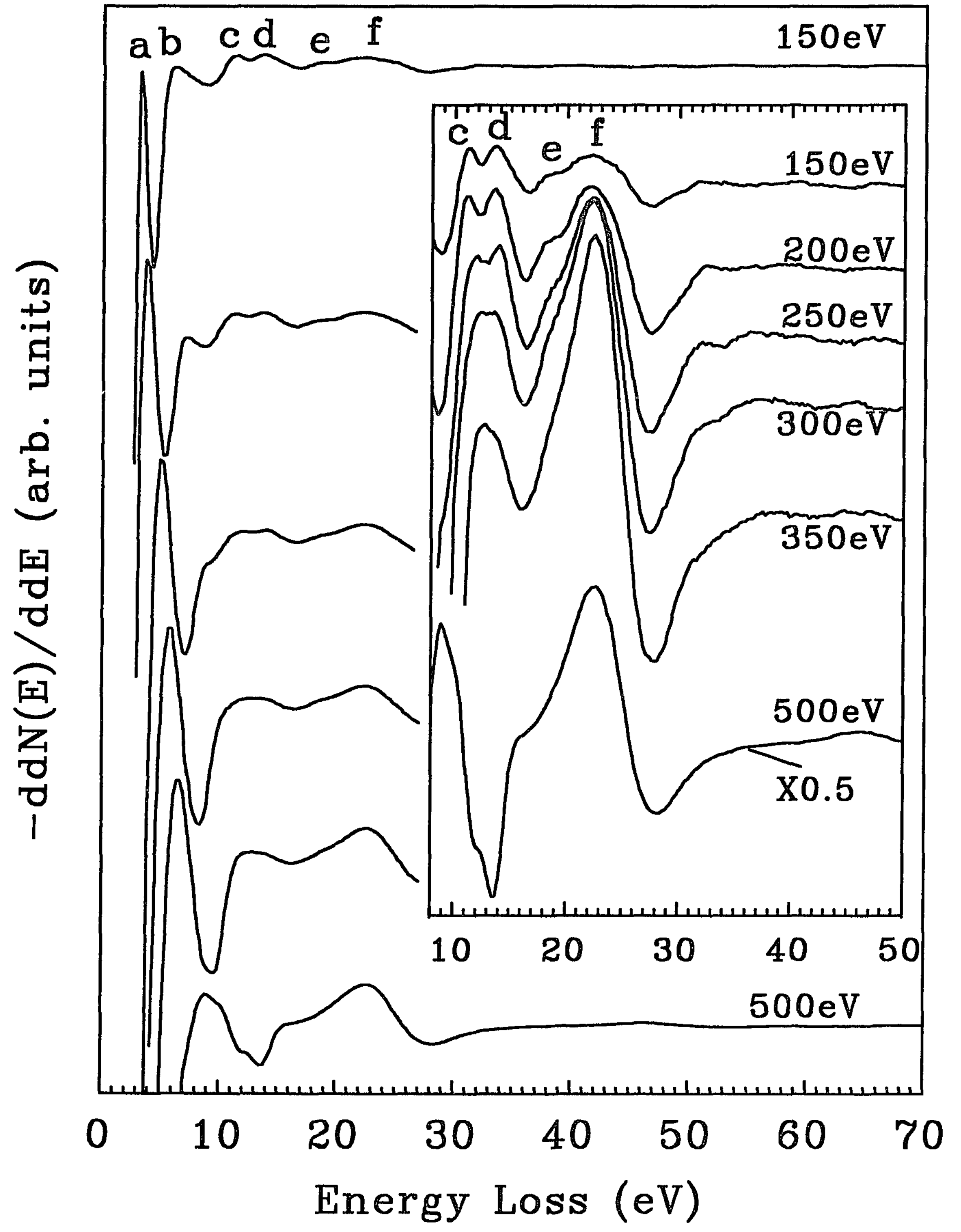

Figure 7.6 EEL spectra of α-SiC taken at room temperature as a function of electron primary energies. The insert is the expanded spectra of the most important energy loss region.

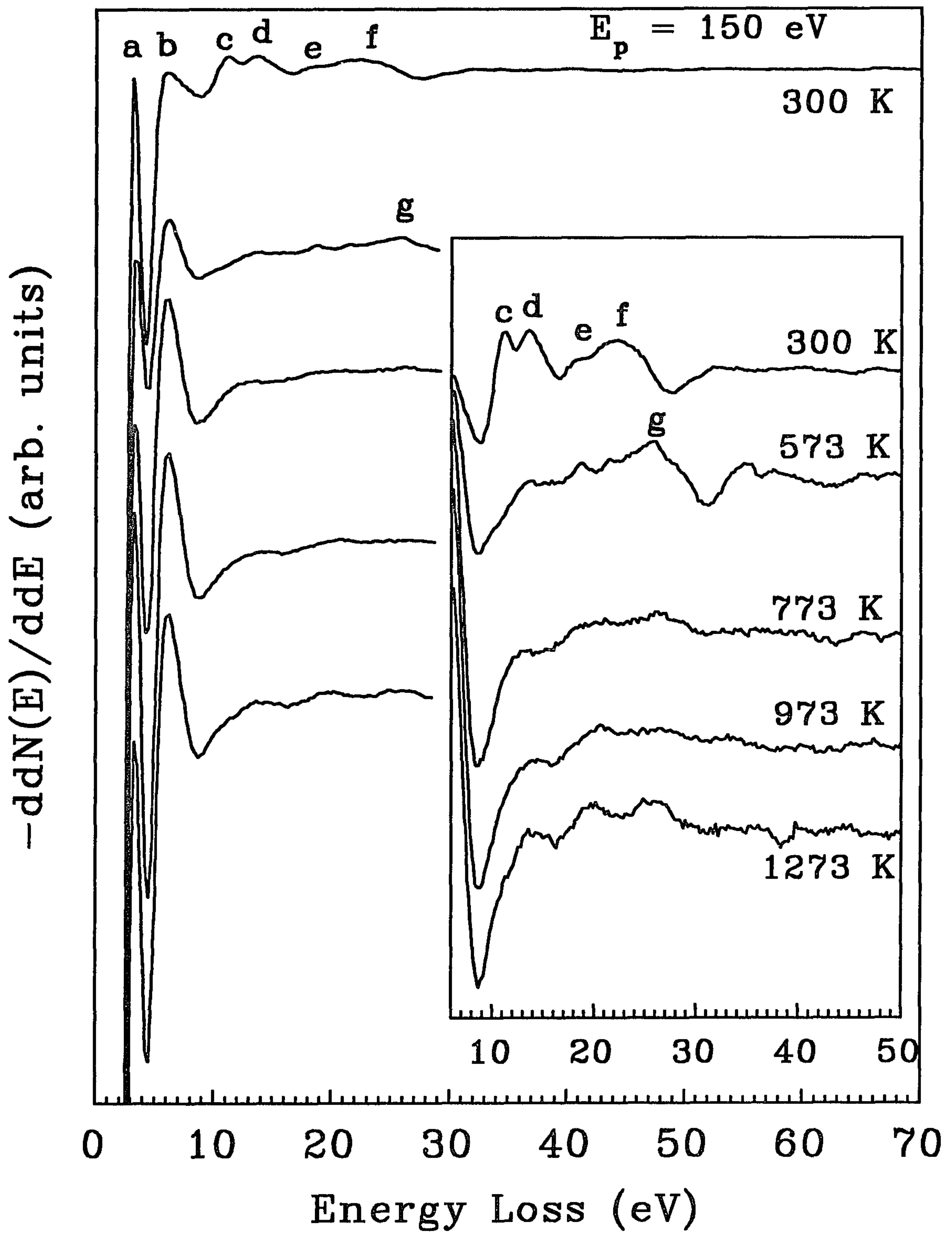

Figure 7.7 EEL spectra plotted as a function of temperature for E_p=150 eV.

Figure 7.8 EEL spectra plotted as a function of temperature for E_p=500 eV.

remains the only mechanism that can explain the observed phenomenon. This surface is rather resistant towards oxidation at low temperatures. The structural integrity of the carbide could be affected by the presence of the carbon vacancies, which could facilitate internal oxidation if the surface has porosity towards oxygen. In Figures 7.9 and 7.10 we show the spectra (E_p=150 and 500 eV) before, after heating, and after reaction with oxygen at 823 K. It is noted that the spectra at E_p=150 eV after heating and after reaction with oxygen are practically identical. However, the spectrum for E_p=500 eV shows small differences that suggests the presence of a third species within the bulk of the sample. These observations were corroborated by the alpha scattering measurements from ^{16}O.

We used AREELS to study the angular dependence of the α-SiC energy losses and facilitate their correct identification. We were concerned that the presence of carbon on the surface which could confuse some of our electron energy loss assignments. In these experiments we were able to detect signals coming from the top two Å from those from the bulk. We studied the pristine sample, after heating and after sputtering. In these measurements we employed the counting mode of detection and not the second derivative method. We have very high energy resolution in this system, the observed width of the energy losses are intrinsic to the transitions and not instrumental. Typical AREEL spectra are shown in Figure 7.11 for an angle of incidence of 35^0 with respect to the crystal face normal, and E_p=300 eV, the spectra were taken for different angles of detection. One clearly observes the bulk plasmon peak of α-SiC, and at glancing

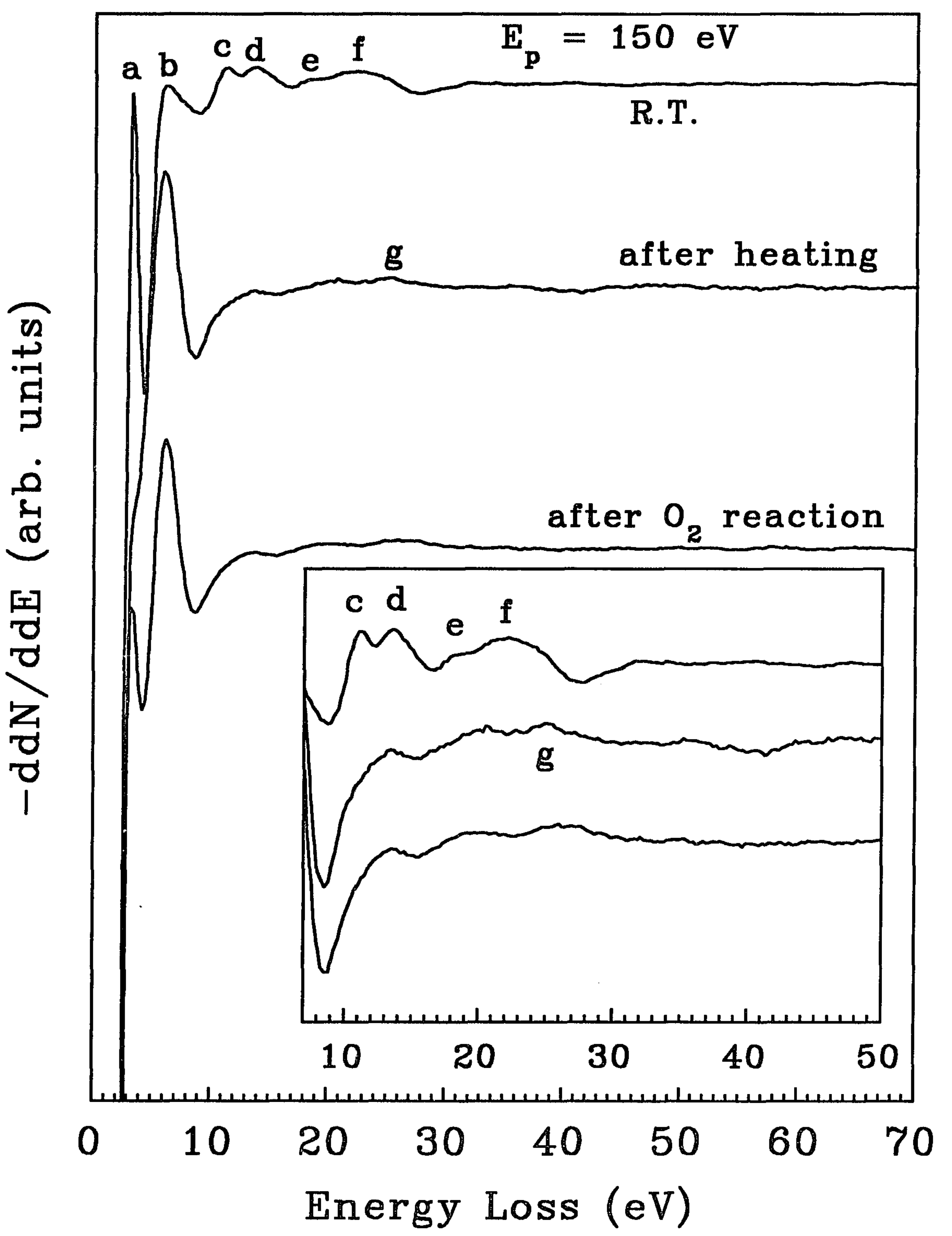

Figure 7.9 EEL spectra plotted at room temperature, after heating and after reaction with oxygen for E_p=150 eV.

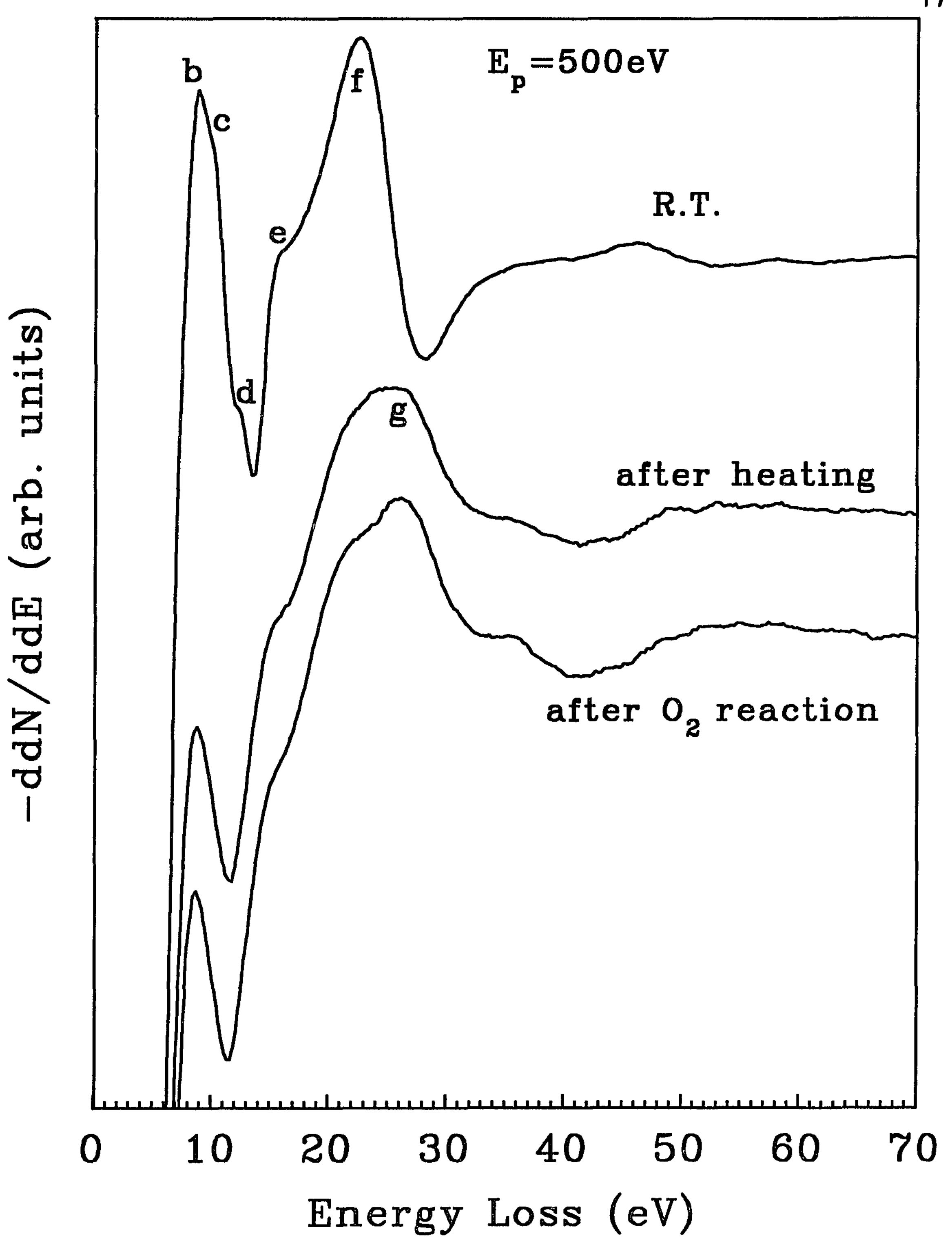

Figure 7.10 EEL spectra plotted at room temperature, after heating and after reaction with oxygen for E_p=500 eV.

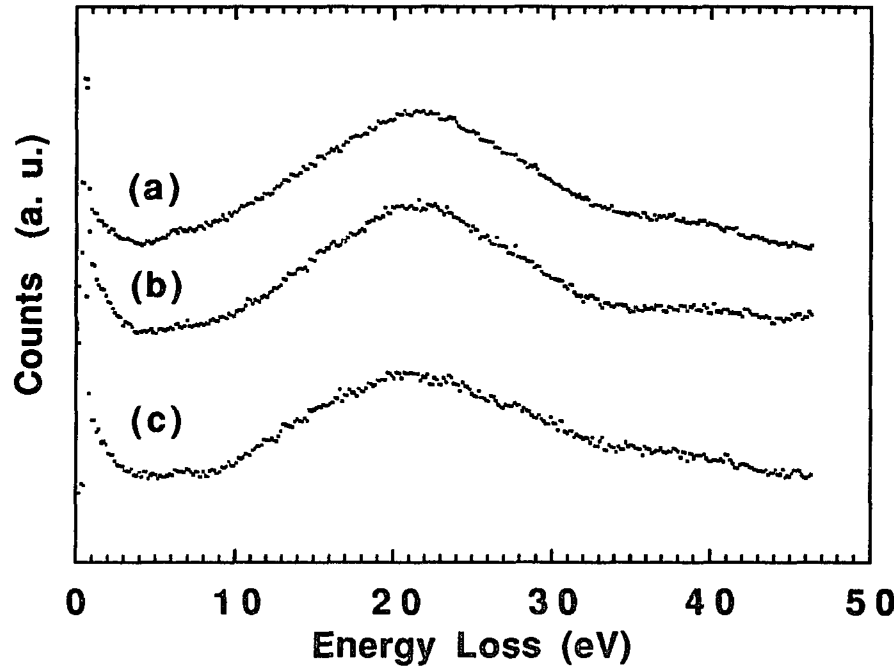

Figure 7.11 Angular resolved EEL spectra taken at room temperature for an angle of incidence of 35^0 and angles of reflection of a) 55^0, b)70^0, c) 85^0. All the angles are measured with respect to the normal to crystal face.

detection angle the surface plasmon can be seen as a shoulder of the main plasmon peak. For a primary energy of 50 eV the surface plasmon peak dominates the spectrum at a glancing angle of detection. We clearly observe the formation of a graphitic layer on the surface after heating the sample. Figure 7.12 is an AES spectrum taken after sputtering. This figure clearly shows a strong carbon peak but no oxygen and silicon. The AREELS measurements are in good agreement with our measurements using the CMA second derivative method. Finally, we want to point out that a mild sputtering of the surface with argon ions produces a significant change in the AREELS results. We observed Si enrichment of the surface that is easily detectable from the characteristic energy losses. Figure 7.13 is an EELS spectrum measured after sputtering at E_p=200eV. The incident angle is about 35^0, and the detecting angle is about 72^0 with respect to the normal direction.

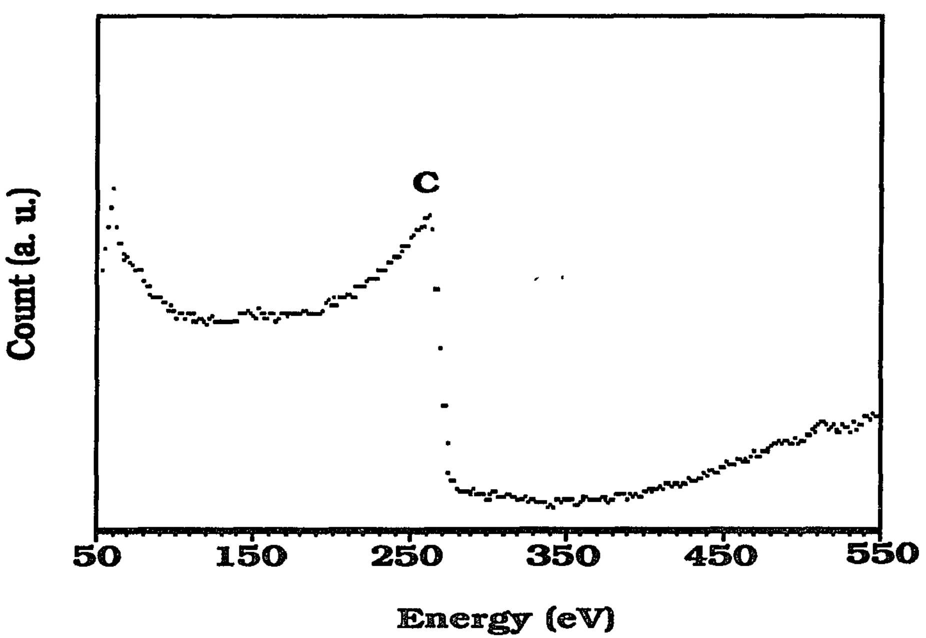

Figure 7.12 This AES spectrum was taken at glancing angle after sputtering($\theta_{in}=72^0$, $\theta_{out}=35^0$). This figure clearly shows a strong carbon peak but no oxygen and silicon.

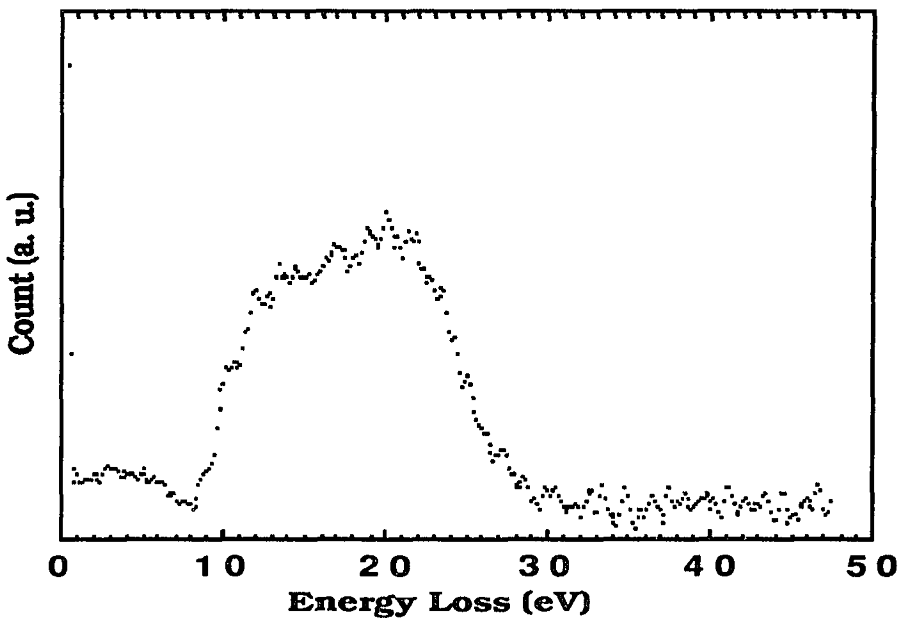

Figure 7.13 This is an EELS spectrum measured after sputtering at E_p=200eV. The incident angle is about 35^0, and the detecting angle is about 72^0 with respect to the normal direction.

Chapter 8

INTERFACE STRUCTURE AND STABILITY IN Si/C MULTILAYERS

8.1 Introduction

Metal-carbon multilayers are artificial structures that have found applications in soft X-ray optics[129,130]. Multilayers of Si/C are very attractive for high temperature applications, in particular if the interface Si-C has carbidic character. These systems have potential applications as low weight structural components. They also can be used as models for high temperature structural materials to investigate the bonding and thermal stability of the carbon-silicon carbide interfaces of such materials. A powerful tool to determine the interface structure is X-ray specular reflectivity. The non-destructive character of this technique permits the characterization of interfaces in such materials.

We report in this thesis the first electron energy loss study of silicon-carbon multilayers. We measured a diverse number of multilayers of variable thicknesses and grown on two different substrates, sapphire and float glass (SiO_2). The measurements were performed under UHV conditions. We employed Auger spectroscopy (AS) and EELS to characterize the samples and the variations in composition as a function of depth. The stability of the interfaces was measured as a function of temperature for all the samples.

We also employed the X-ray specular reflectivity measurements to characterize the silicon-carbon multilayers. We measured a number of multilayers of variable thicknesses and modulation wavelengths.

8.2 Experimental.

The Auger spectroscopy and electron energy loss spectroscopy measurements were performed in an ultra high vacuum system with a vacuum better than 10^{-10} Torr. The Si/C multilayers were mounted on a tungsten sample holder, and electron beam heater was used to change the sample temperature. The temperature was monitored and controlled using a proportional temperature controller. The sample temperature was varied between room temperature and 1073K (for multilayers grown on a sapphire substrate). The chamber was equipped with a single pass cylindrical mirror analyzer(CMA) for AS and EELS measurements. The second derivative mode was used for the electron energy loss measurements using the CMA. The electron primary energies was varied between 20 eV (using a high resolution gun) to 2600 eV. This large range of values for the primary electron beam allows to obtain depth sensitivity in the EELS measurements. The angular resolved AS and EELS measurements were performed in a UHV system equipped with a 50 mm hemispherical analyzer mounted on a goniometer with a position sensitive electron detector for rapid data acquisition.

The X-ray specular reflectivity measurements were carried out at room temperature using beam line X-18B at the National Synchrotron Light Source facility at Brookhaven National Laboratory. A Si(220) double crystal monochromator was used for selecting the synchrotron radiation wavelength. X-ray beam monochromatization is the same as described in chapter 2. The sample was mounted on a high precision goniometer attached to a two axes Huber diffractometer, and a NaI

scintillation detector was used in this measurement. At very low angle, we used a set of calibrated aluminum absorbers to reduce the X-ray beam intensity before reaching the detector. The alignment of the sample and diffractometer was carried out using a methodology similar to that described in reference[56]. All the measurements were carried out at room temperature. Table 8.1 gives the list of samples studied in this work.

Table 8.1
Si and C composition of the multilayers

Si Thickness (Å)	C Thickness (Å)	No. of Periods	
10Å	19Å	30	**(sample 1)**
25Å	25Å	30	**(sample 2)**
29Å	14Å	30	**(sample 3)**

8.3 Results and Discussion.

AREELS, AES, EELS

The AREEL spectra were measured with primary energies between 450 to 2600 eV and are shown in Figures 8.1a, 8.1b and 8.2a, 8.2b. The angular resolved EEL spectra were taken at an angle of incidence of 40^0 and equal to the angle of reflection(the angles are measured with respect to the sample normal). Figures 8.1a, and 8.1b show the measured spectrum using the angular resolved system for a Si/C multilayer with Si=25 Å and C=25 Å (sample 2), 30 periods thick. We observe a significant variation in peak positions as the energy of the impinging electron increases. In Figures 8.2a, and 8.2b we show

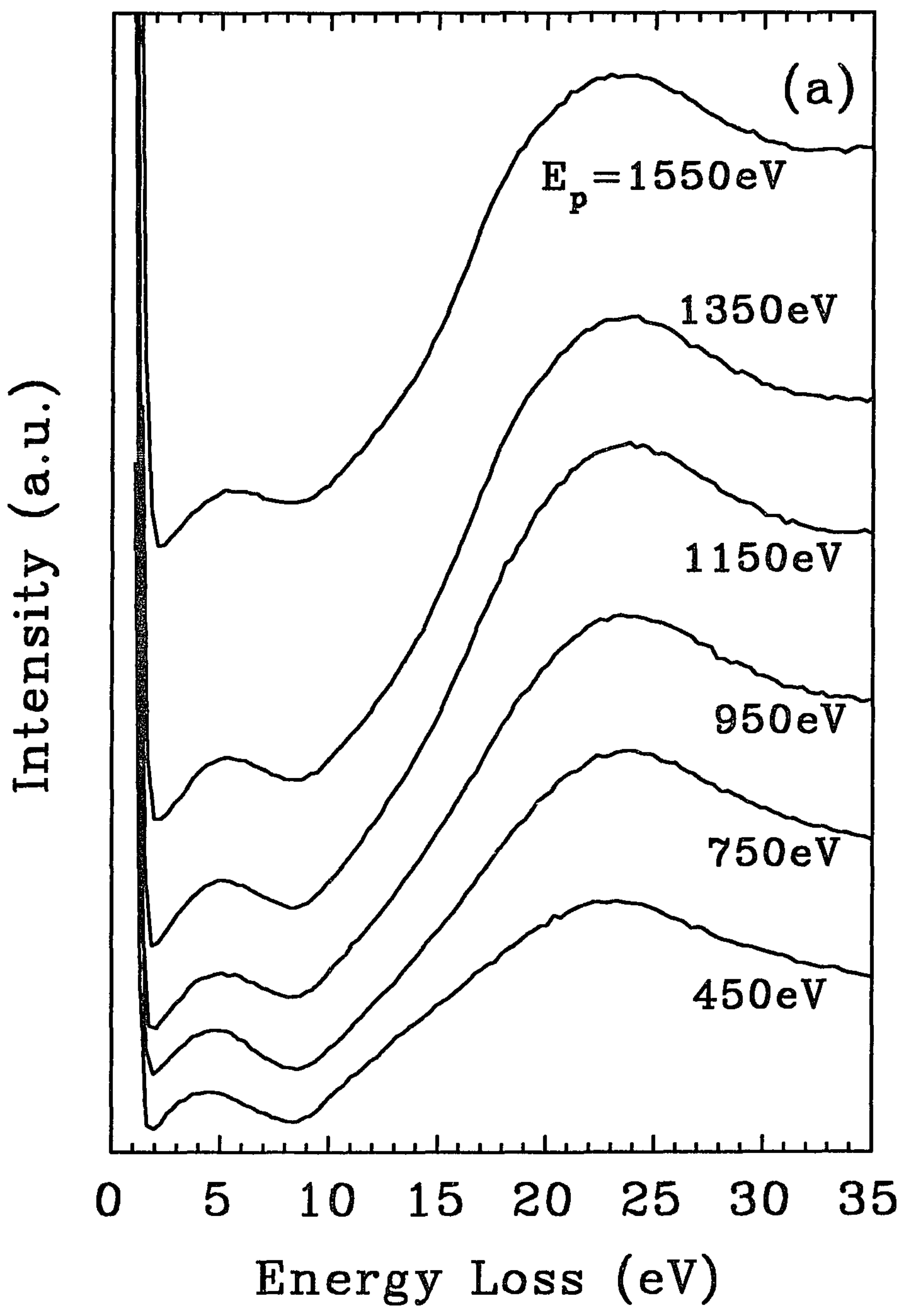

Figure 8.1(a) Angular resolved EEL spectrum as a function of electron primary energy for Si(25Å)/C(25Å) at Ep=450-1550eV, the angle of incidence is equal to the angle of reflection=40°.

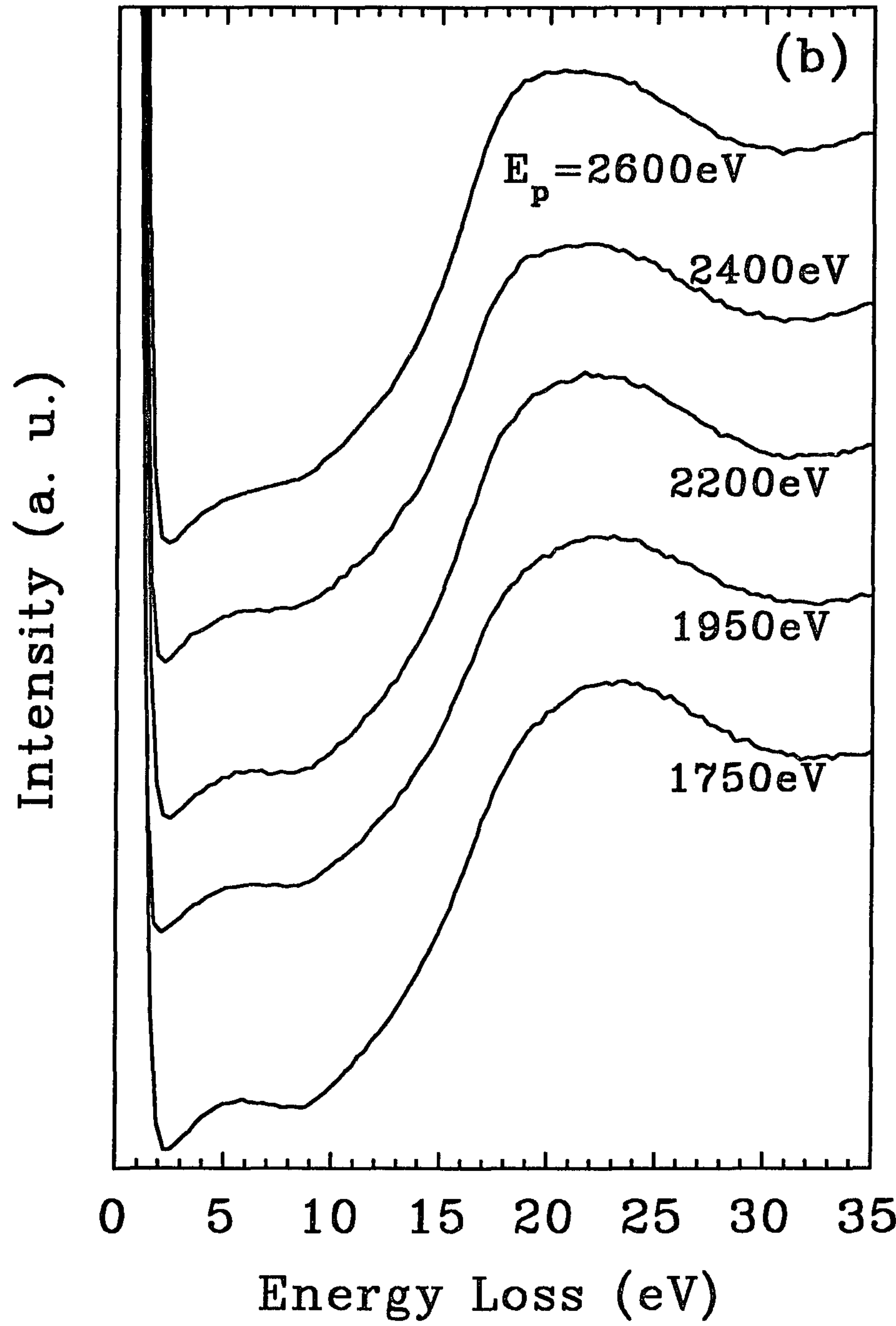

Figure 8.1(b) Angular resolved EEL spectrum as a function of electron primary energy for Si(25Å)/C(25Å) at Ep=1750 - 2600eV, the angle of incidence is equal to the angle of reflection=40^0.

the second derivative of the spectra given in Figures 8.1a, and 8.1b. This figures give a more detailed picture of the variations in peak positions as a function of primary electron energies.

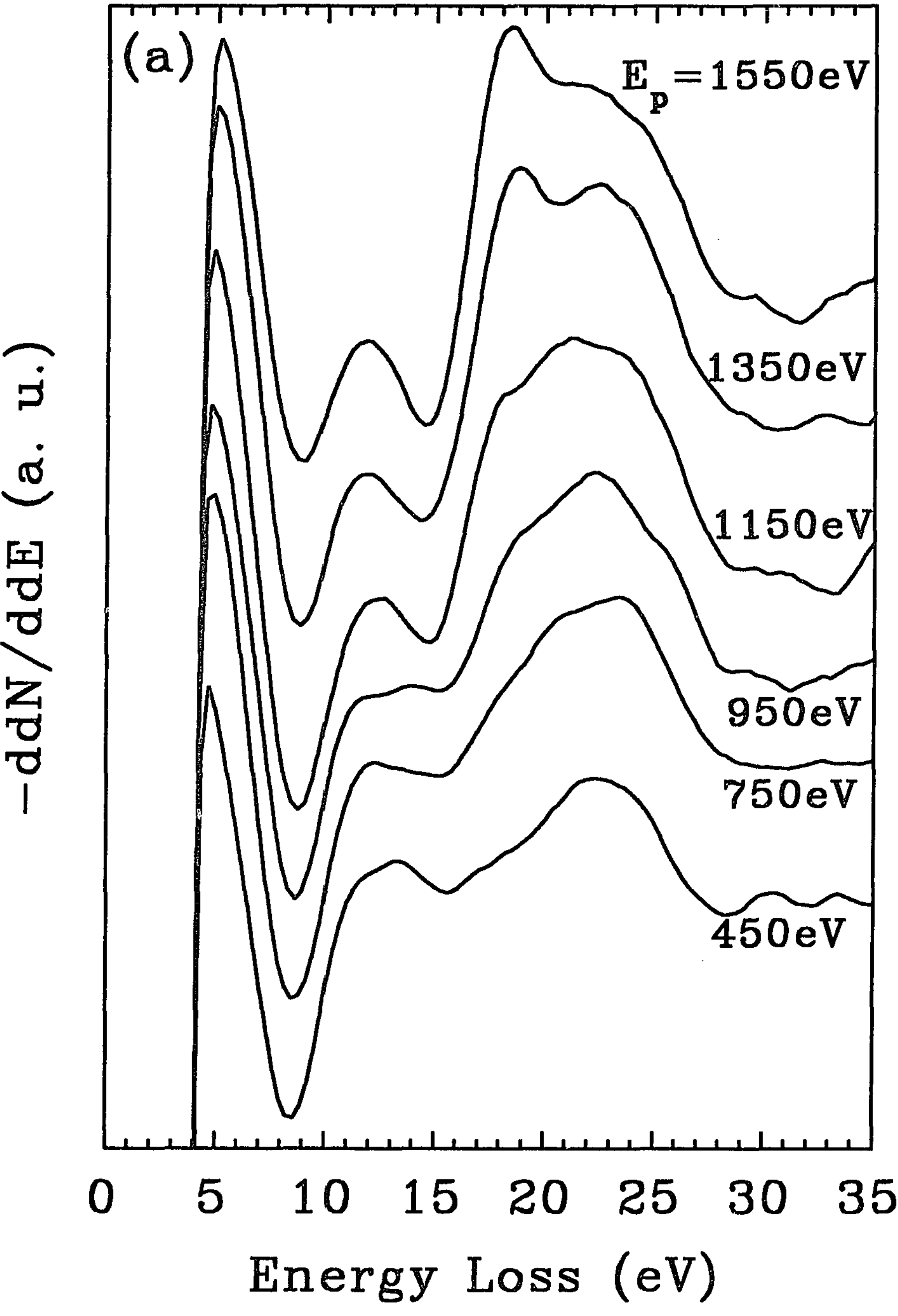

Figure 8.2(a) Angular resolved EEL spectrum (second derivative) as a function of electron primary energy for Si(25Å)/C(25Å) at Ep=450 - 1550eV, the angle of incidence is equal to the angle of reflection $=40^0$.

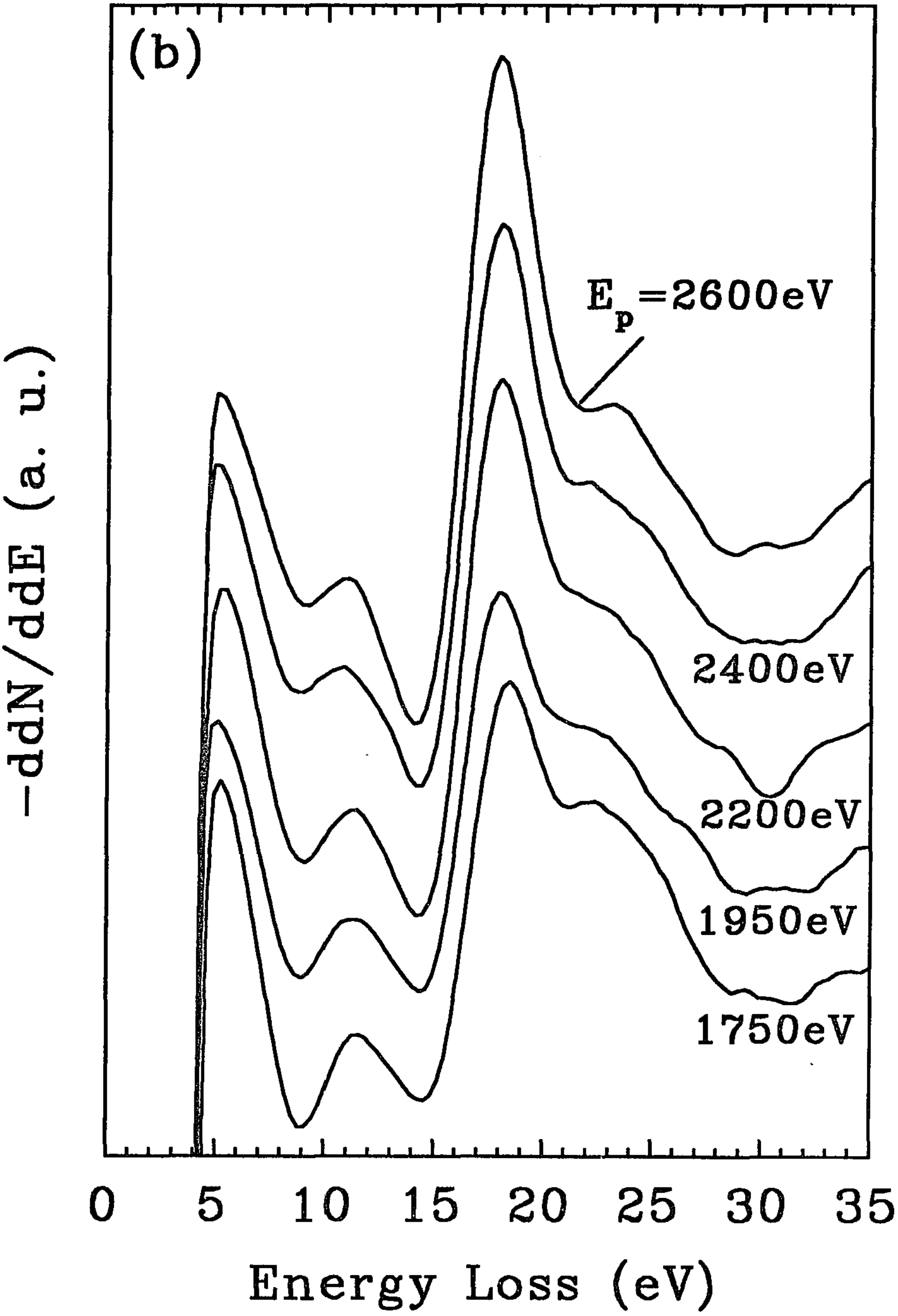

Figure 8.2(b) Angular resolved EEL spectrum (second derivative) as a function of electron primary energy for Si(25Å)/C(25Å) at Ep=1750 - 2600eV, the angle of incidence is equal to the angle of reflection =40^{0}.

The top layer of the sample is made of carbon, we detect at low energies a strong energy loss around 23-24 eV, a value slightly smaller than for pure graphite. This result is not totally surprising since the carbon crystallographic form in this type of multilayer is not well understood, and is a subject of considerable interest and controversy. These experimental observations are in good agreement with the angular resolved AS measurements, see Figure 8.3. In the AS

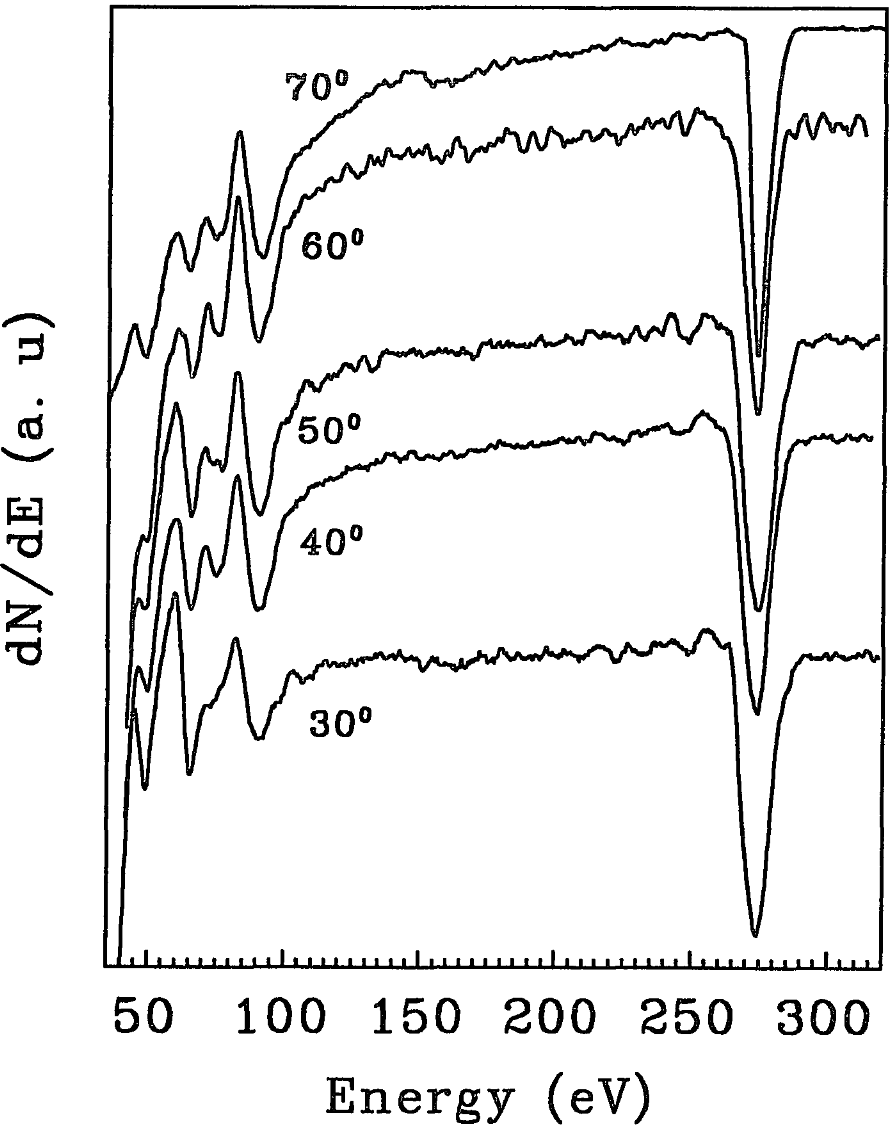

Figure 8.3 Angular resolved AS spectrum as a function of electron primary energy for Si(25Å)/C(25Å), the angle of incidence is equal to the angle of reflection=30°, 40°, 50°, 60°, and 70°.

measurements the carbon signal shape is significantly different from that of graphitic or carbidic carbon. When the electron primary energy increases one observes what appears to be a contribution from the interface Si/C, a loss peak near 21 eV. Eventually a pronounced energy loss peak appears around 18 eV. The latter peak is typical of the Si bulk plasmon. One obtains great surface sensitivity with the AREELS technique, in particular for a glancing angle of detection with respect to the crystal face. In Figures 8.4a, 8.4b, 8.4c, 8.4d, and 8.4e the AREELS spectra are shown as a function of angle of incidence and reflection, Ep=2400 eV. We observe the same behavior of the electron energy loss peaks, at angles close to normal the Si plasmon peak is very pronounced. At glancing angles the carbon top layer and the interface contribution are very pronounced. When the sample temperature increases the EELS spectra becomes more like those of graphitic carbon (see Figures 8.5a, 8.5b, and 8.5c). The effect of temperature is to anneal the carbon and form more crystalline graphite layers. This result is also corroborated by the change in the shape of the carbon Auger signal.

In Figure 8.6 we show the AREEL spectra (second derivative mode) for a multilayer with Si=29 Å and C=14 Å as a function of primary electron energy (Ep), this sample was prepared on SiO_2 substrate. The angle of incidence of the electrons is equal to the angle of reflection, 40^0. The bulk plasmon peak of Si becomes more pronounced at lower electron primary energies, than in the Si(25Å)/C(25Å) multilayer case. Such results are indicative that our interpretation of the EEL measurements is correct. It is noted in Figure 8.6a, 8.6b that the interface contribution can be seen at

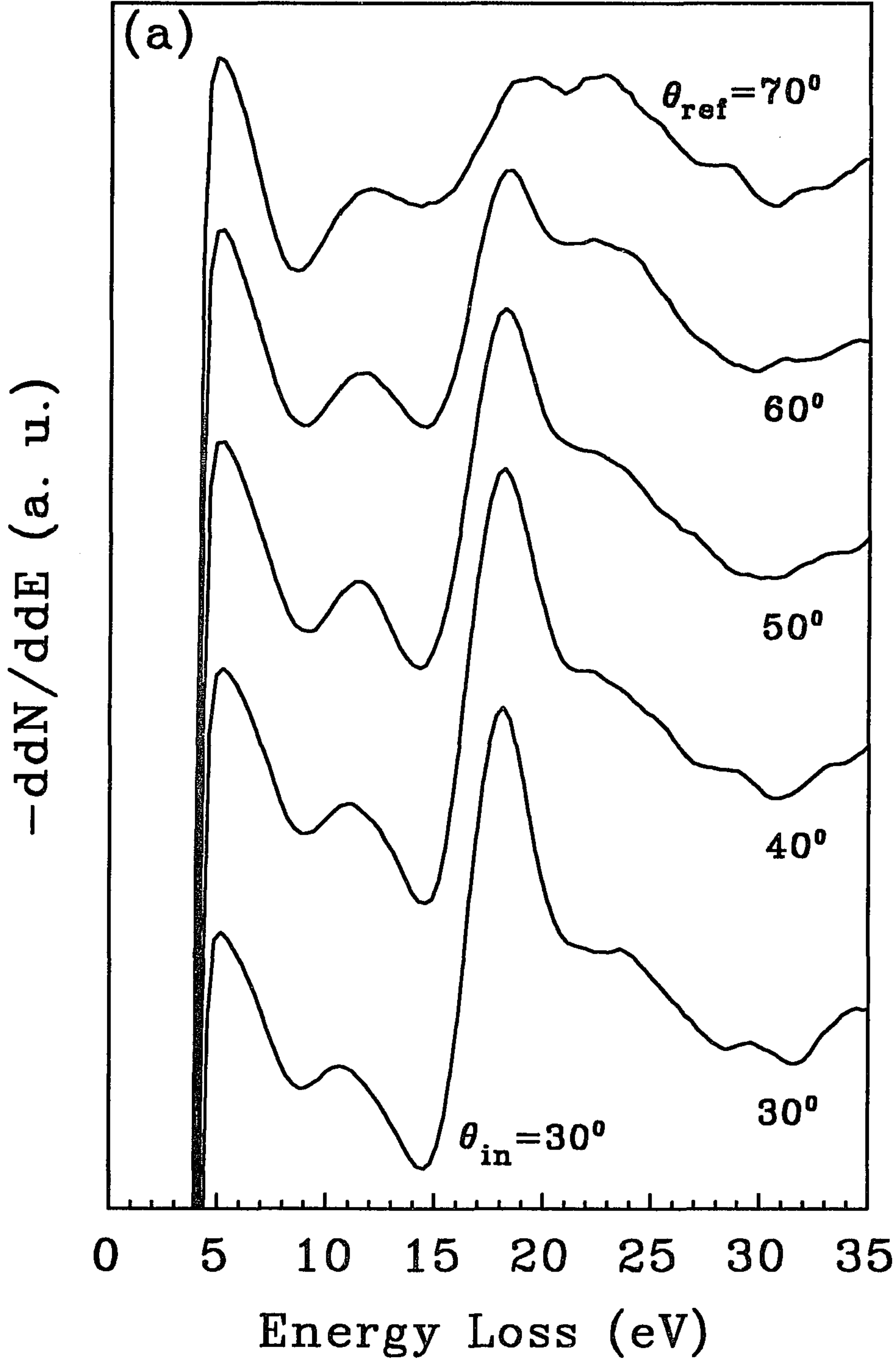

Figure 8.4 (a) Angular resolved EEL spectrum as a function of the angle of reflection for Si(25Å)/C(25Å) at incidence angle 30^0.

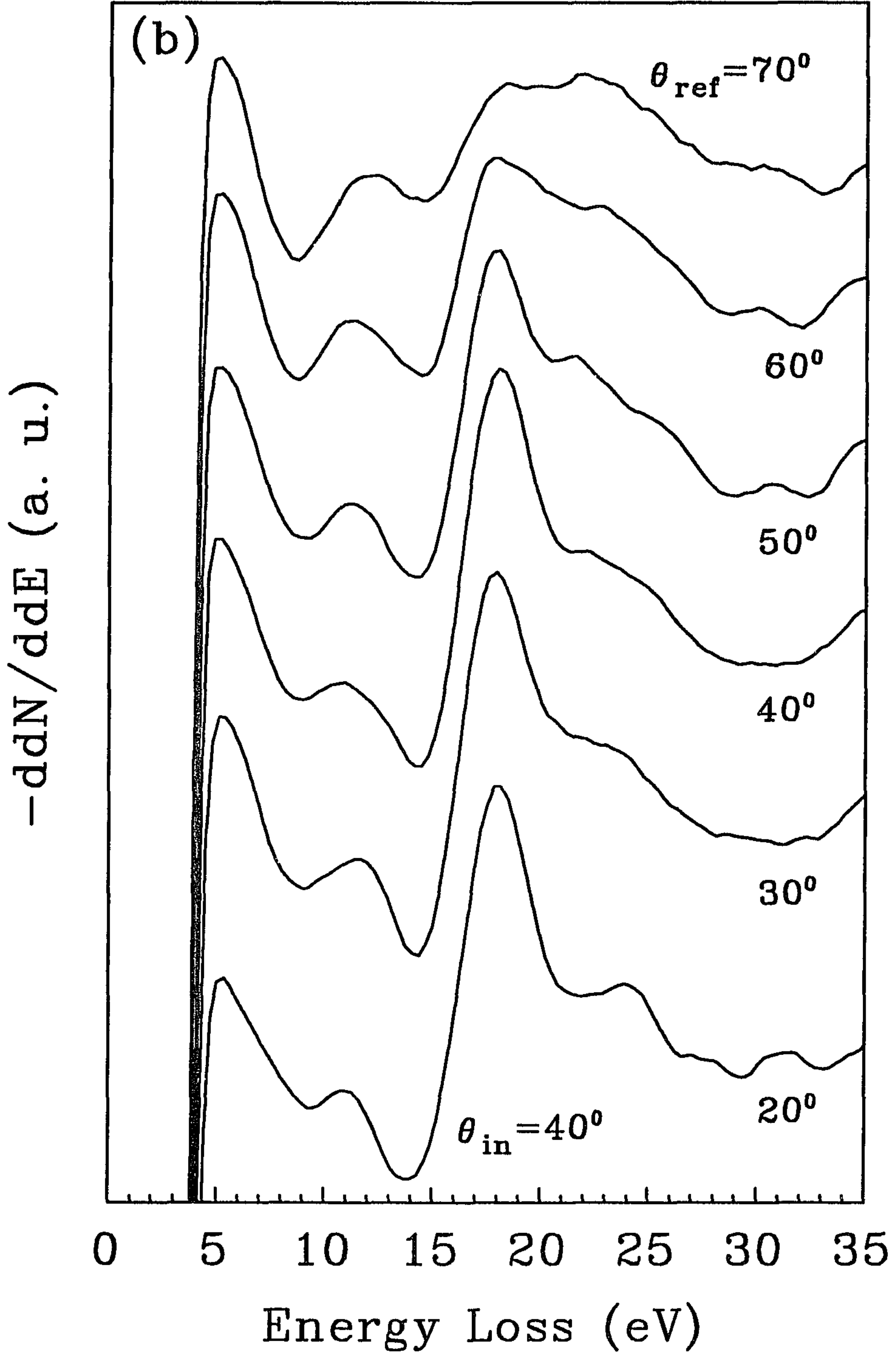

Figure 8.4 (b) Angular resolved EEL spectrum as a function of the angle of reflection for Si(25Å)/C(25Å) at incidence angle 40^0.

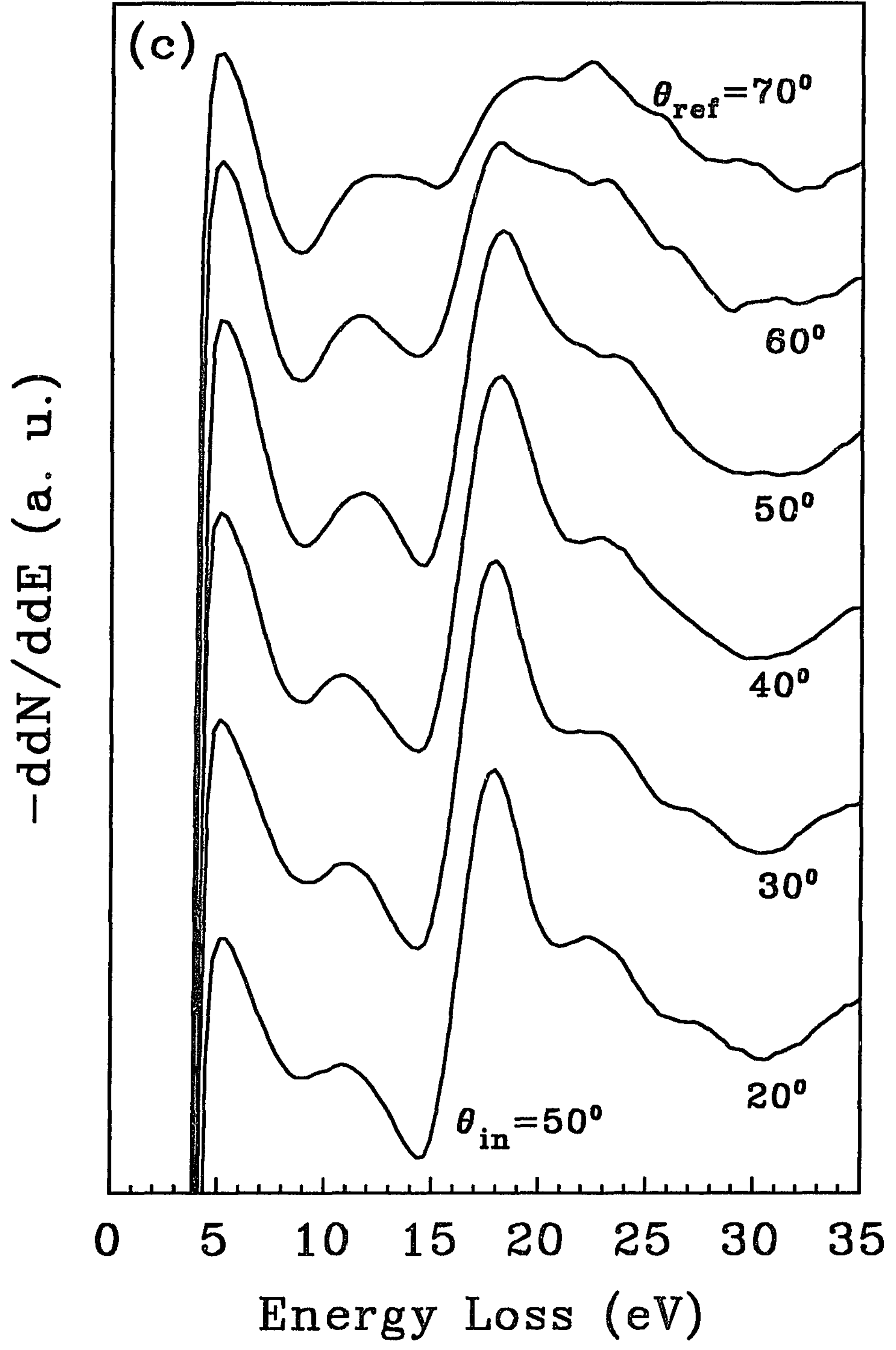

Figure 8.4 (c) Angular resolved EEL spectrum as a function of the angle of reflection for Si(25Å)/C(25Å) at incidence angle 50^0.

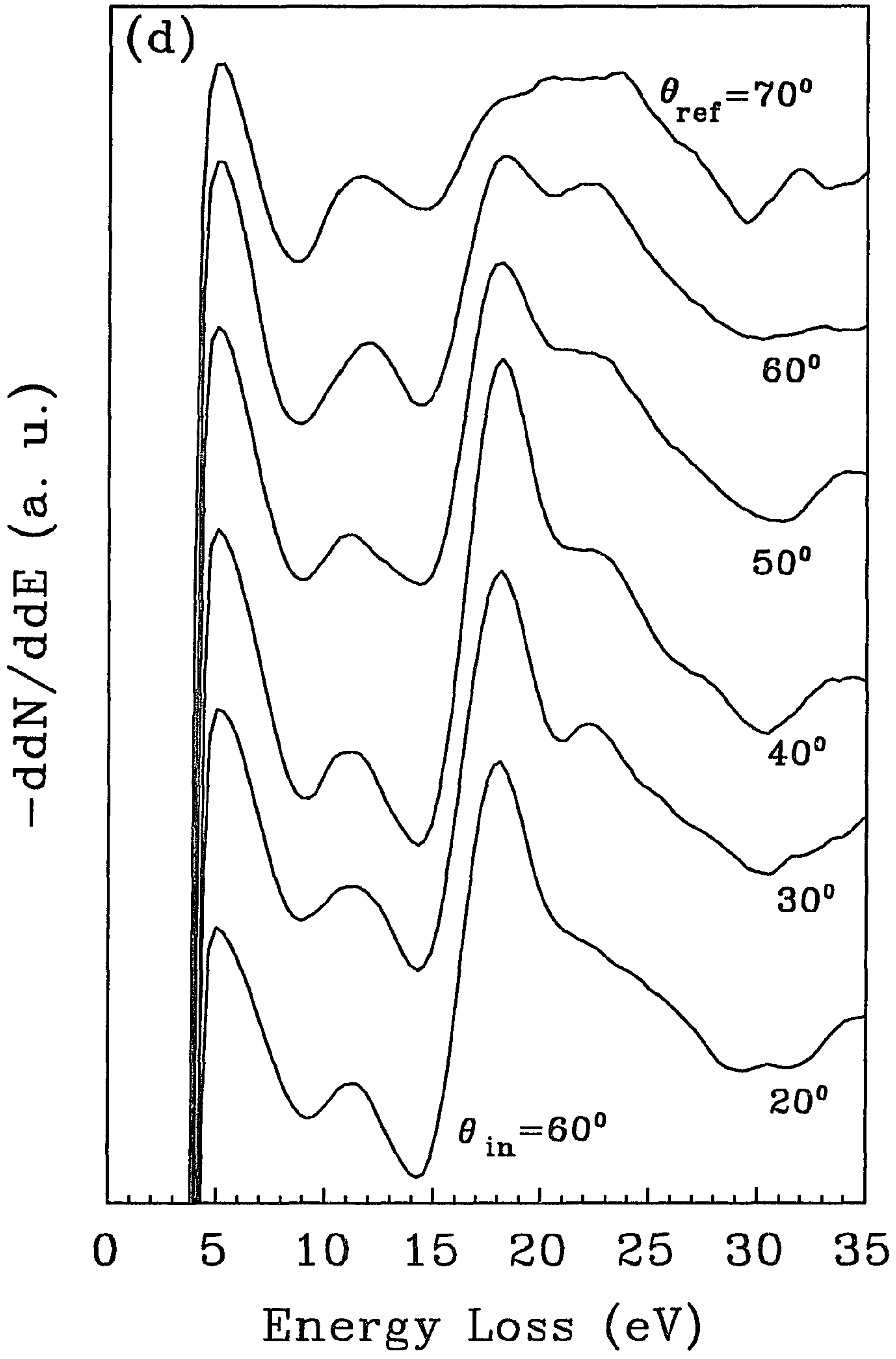

Figure 8.4 (d) Angular resolved EEL spectrum as a function of the angle of reflection for Si(25Å)/C(25Å) at incidence angle 60^0.

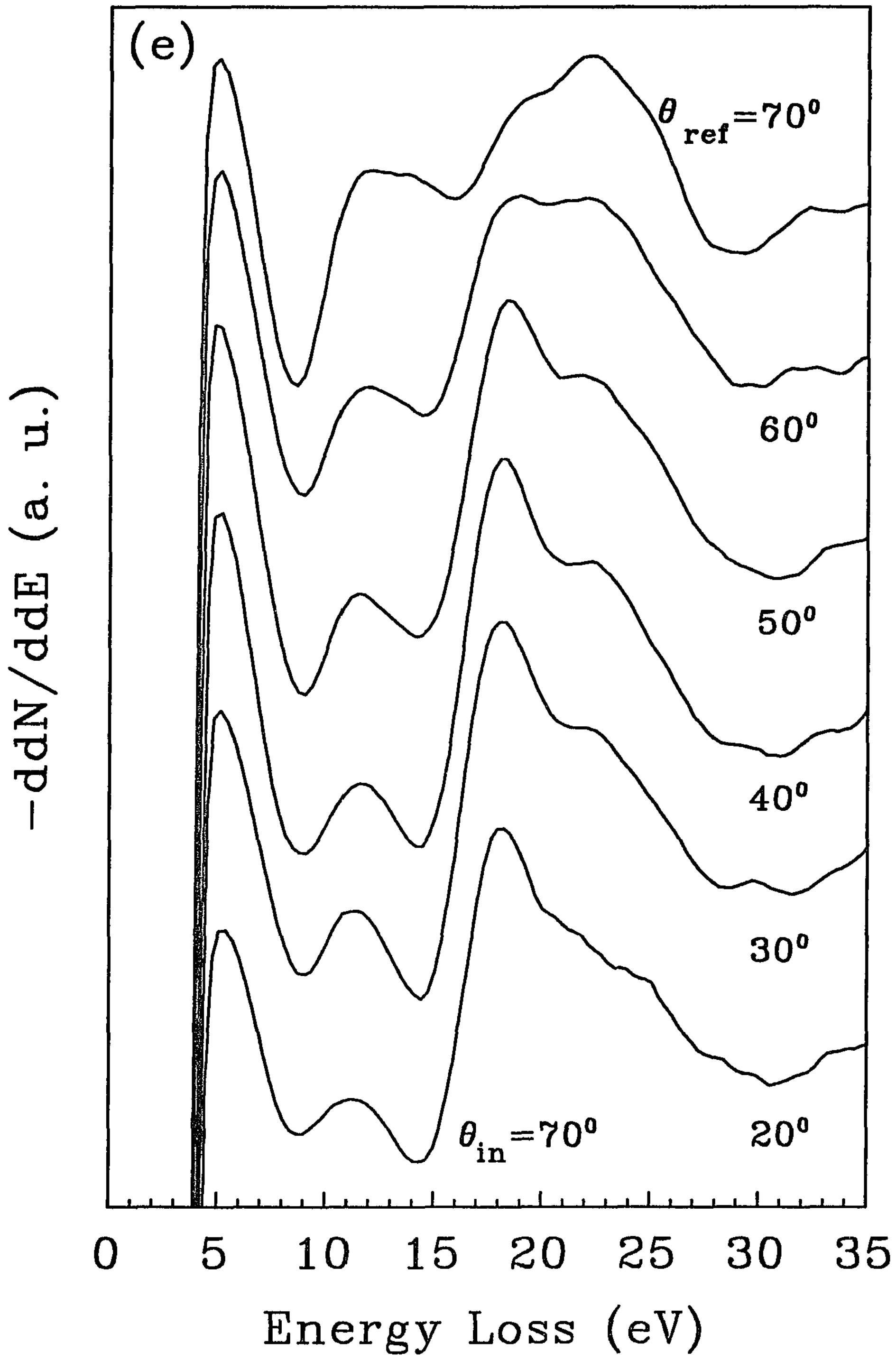

Figure 8.4 (e) Angular resolved EEL spectrum as a function of the angle of reflection for Si(25Å)/C(25Å) at incidence angle 70^0.

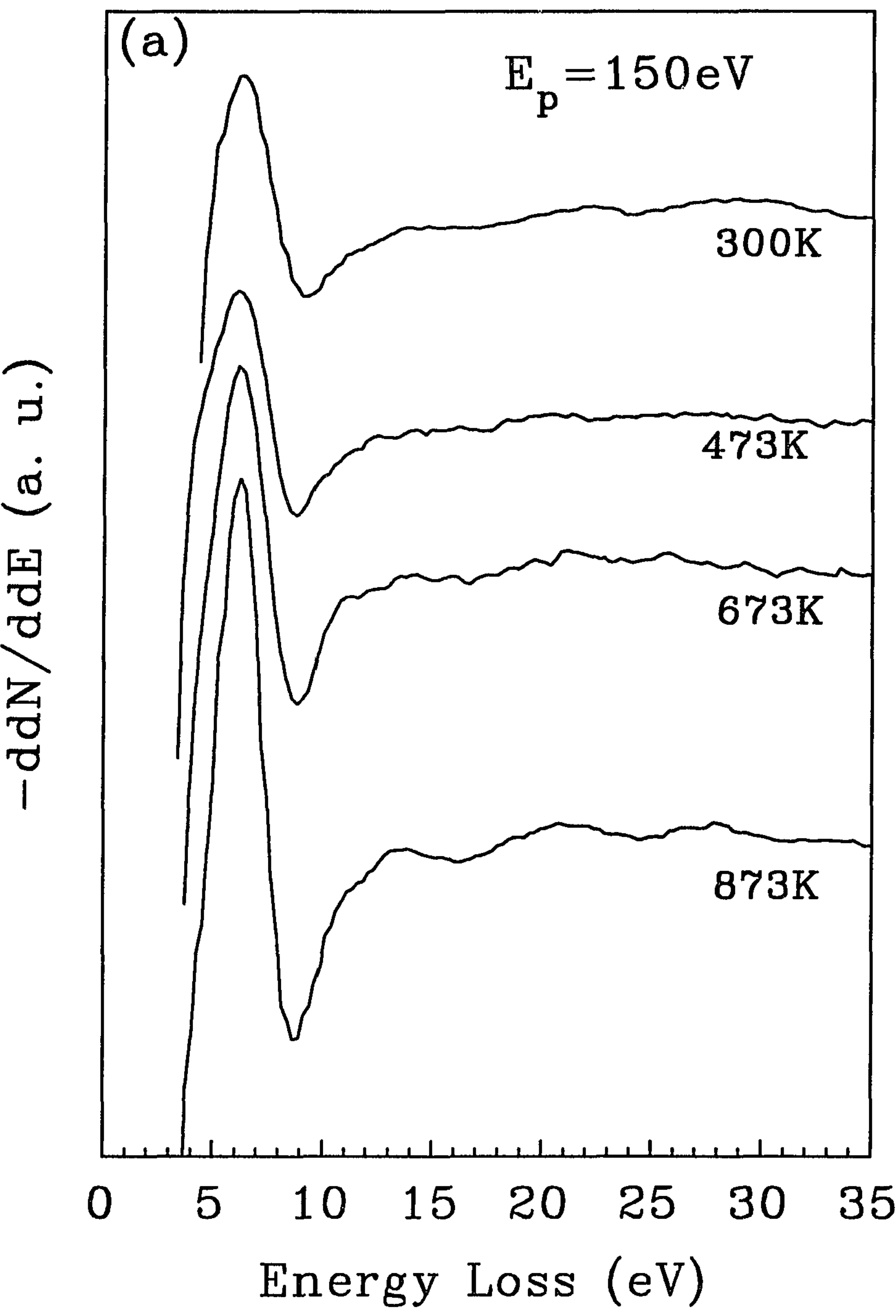

Figure 8.5(a) EEL spectrum as a function of temperature for Si(25Å)/C(25Å) multilayer, at Ep=150 eV.

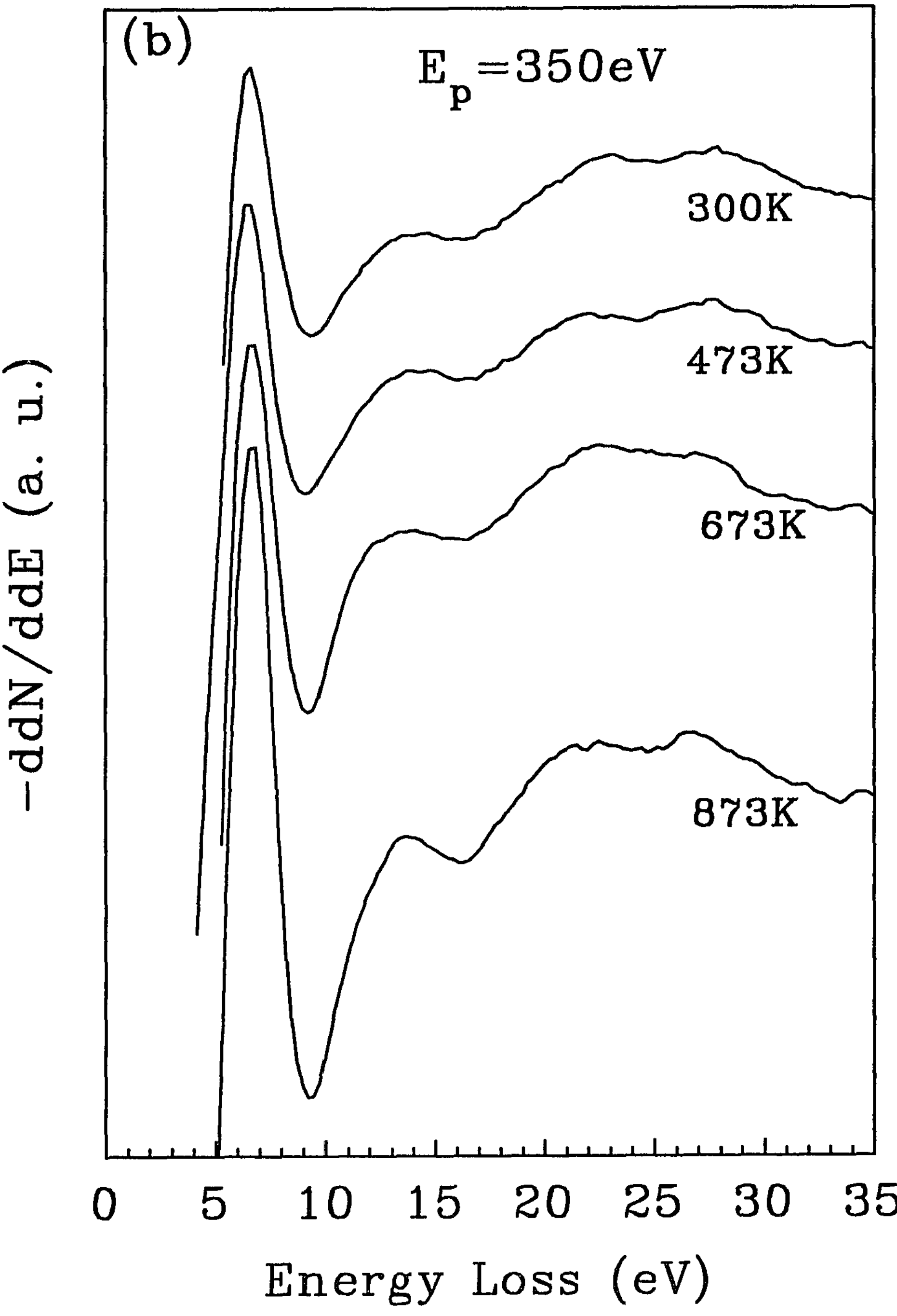

Figure 8.5(b) EEL spectrum as a function of temperature for Si(25Å)/C(25Å) multilayer, at Ep=350 eV.

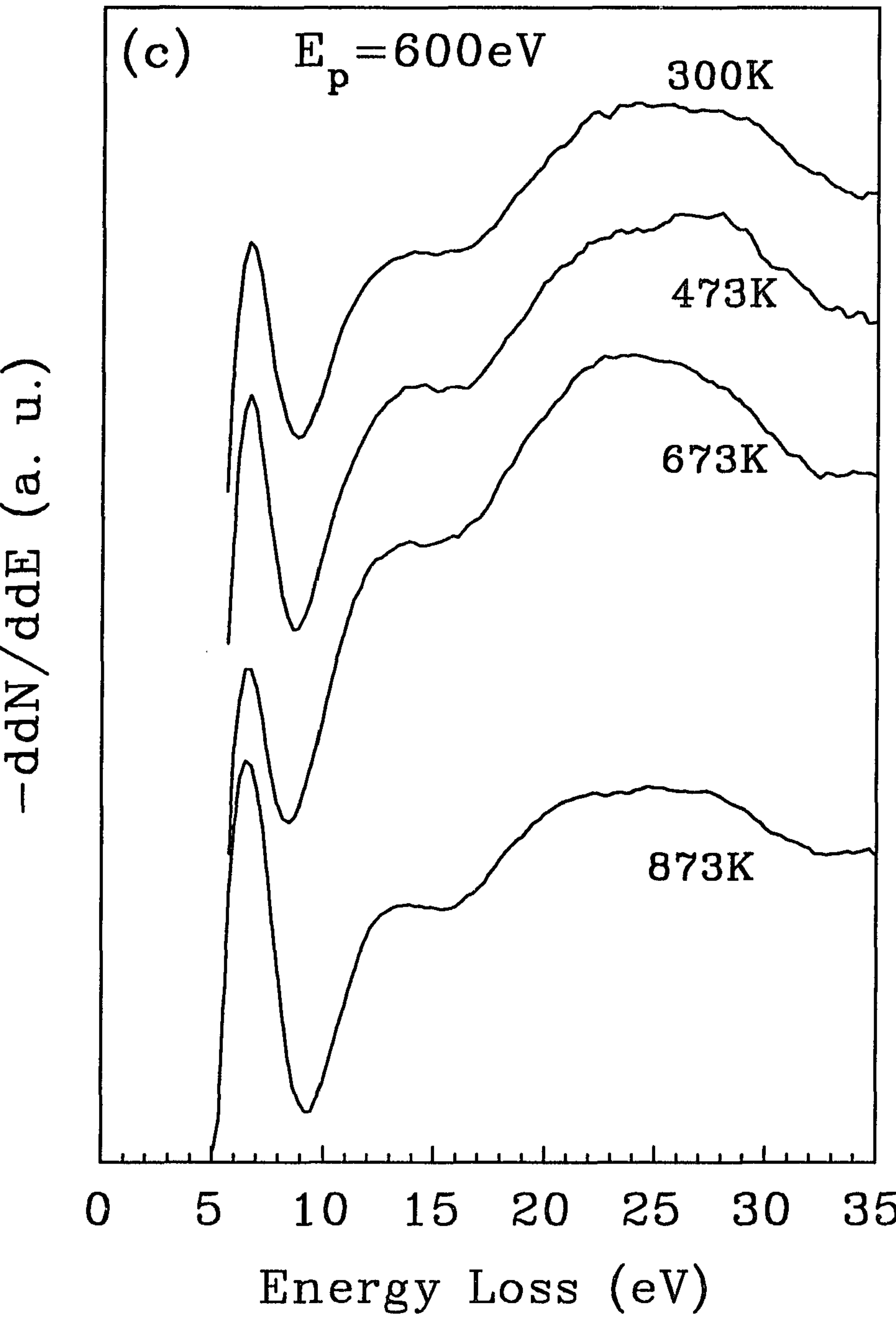

Figure 8.5(c) EEL spectrum as a function of temperature for Si(25Å)/C(25Å) multilayer, at Ep=600 eV.

electron primary energies between 750 to 1150 eV. The silicon carbide plasmon peak is detected at these electron impinging energies.

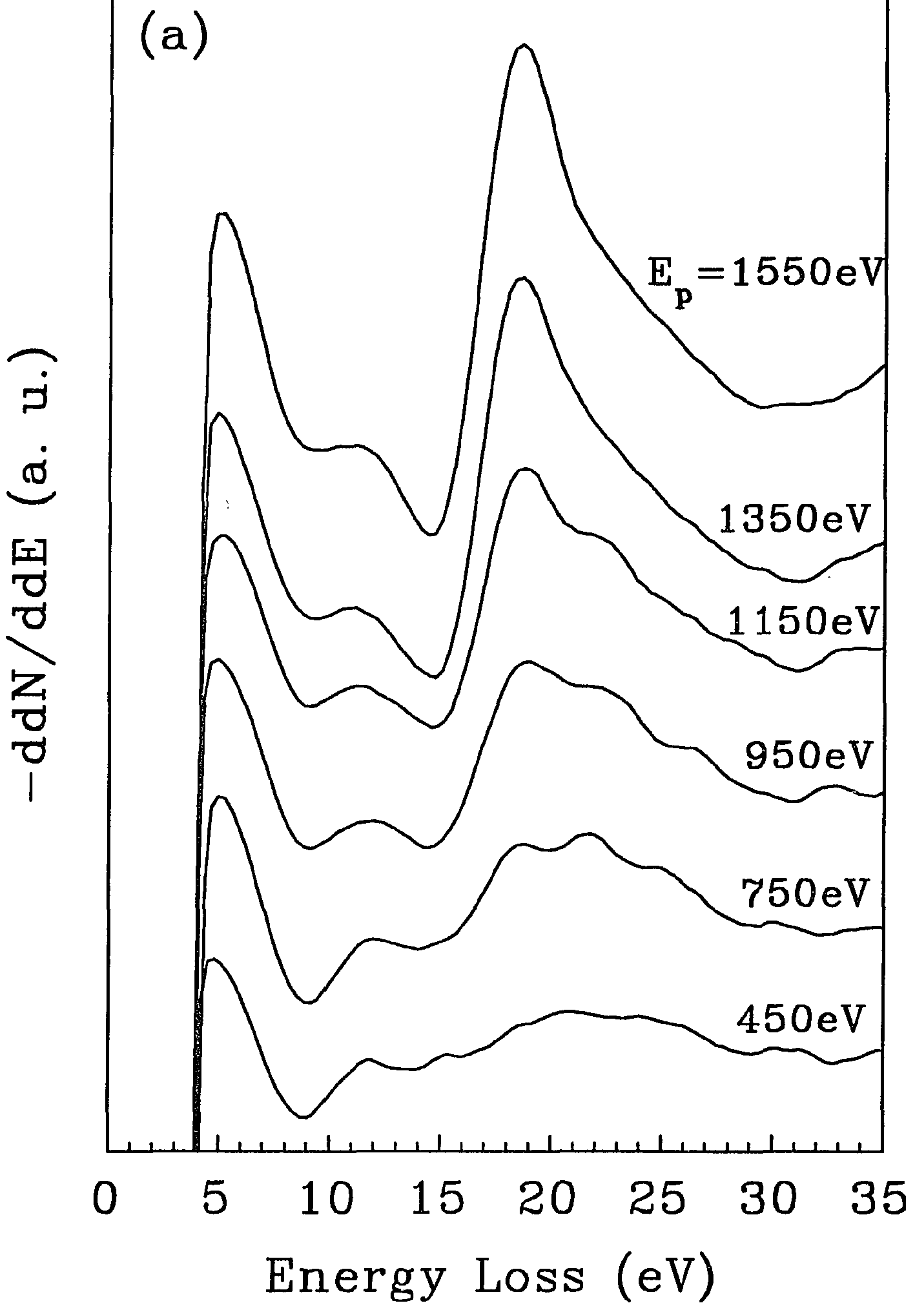

Figure 8.6(a) Angular resolved EEL spectrum as a function of electron primary energy for Si(29Å)/C(14Å) at Ep=450-1550eV, the angle of incidence is equal to the angle of reflection=40^0.

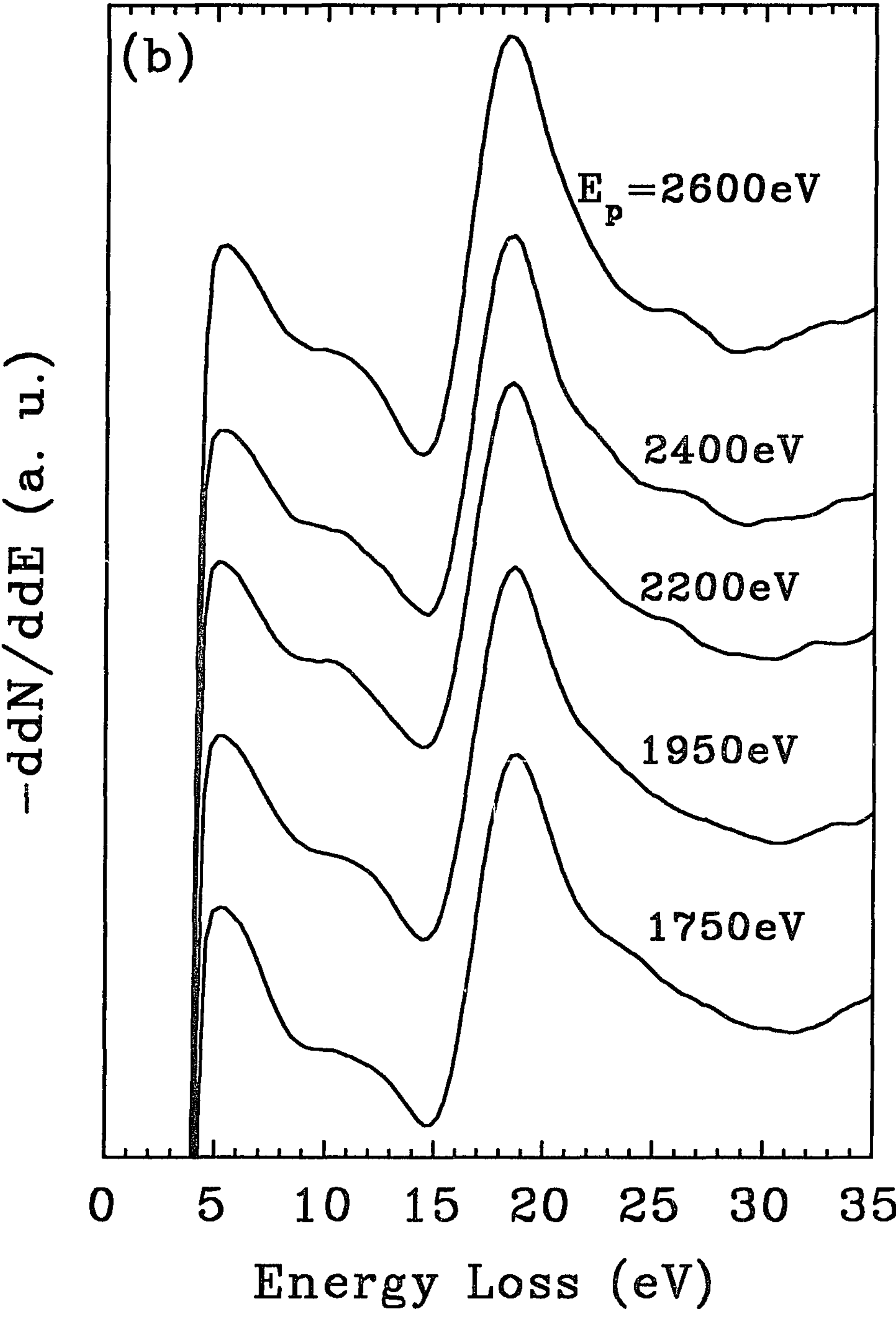

Figure 8.6(b) Angular resolved EEL spectrum as a function of electron primary energy for Si(29Å)/C(14Å) at Ep=1750-2650eV, the angle of incidence is equal to the angle of reflection=40^0.

In Figure 8.7 we show the AREELS spectra for very low primary electron energies. We observe two energy losses that are typical of carbon electronic transitions, one at 4.4 eV, the second at 6.5 eV. The lower peak (at energy 4.4 eV) is assigned as the interband transitions at Q^{-}_{2g}-- Q^{-}_{2u} in the graphite band structure calculated by Painter et al.[82] (see appendix B). This transition had also been observed from the photoemission and secondary electron electron emission measurements.[83] From optical reflectance measurements[76,131] of the graphite, a peak which corresponded to interband transition in the imaginary part of the dielectric constant at energy 4.5eV had been found. Greenaway et al.[132] observed a peak in optical reflectivity for polarization $E \perp C$ at photon energy about 4.6 eV, which they assigned as Q^{-}_{2g}-- Q^{-}_{2u} transitions. The peak at 6.5eV is referred to the combination of surface and bulk plasmon of the π electrons from graphitic carbon.[76] The major effect of heating the sample to moderate temperatures (due to the silicon substrate melting point) is to make the carbon layers more graphitic and probably to help in the formation of a carbidic interface.

The EEL spectra for the other samples reflect the variations in relative thicknesses of the Si and C layers. For a thinner carbon layer the silicon loss peak appears at lower primary electron energies. The low energy losses have not shifted significantly in all the measurements and reflect the graphitic character of the carbonaceous top layer. In the case of samples prepared on a silicon oxide substrate there is clear evidence that the Si/C interfaces are rougher. The most significant change that occurs at high temperatures are the

crystallization of the carbon layers, and probably an increase in the carbidic interface thickness.

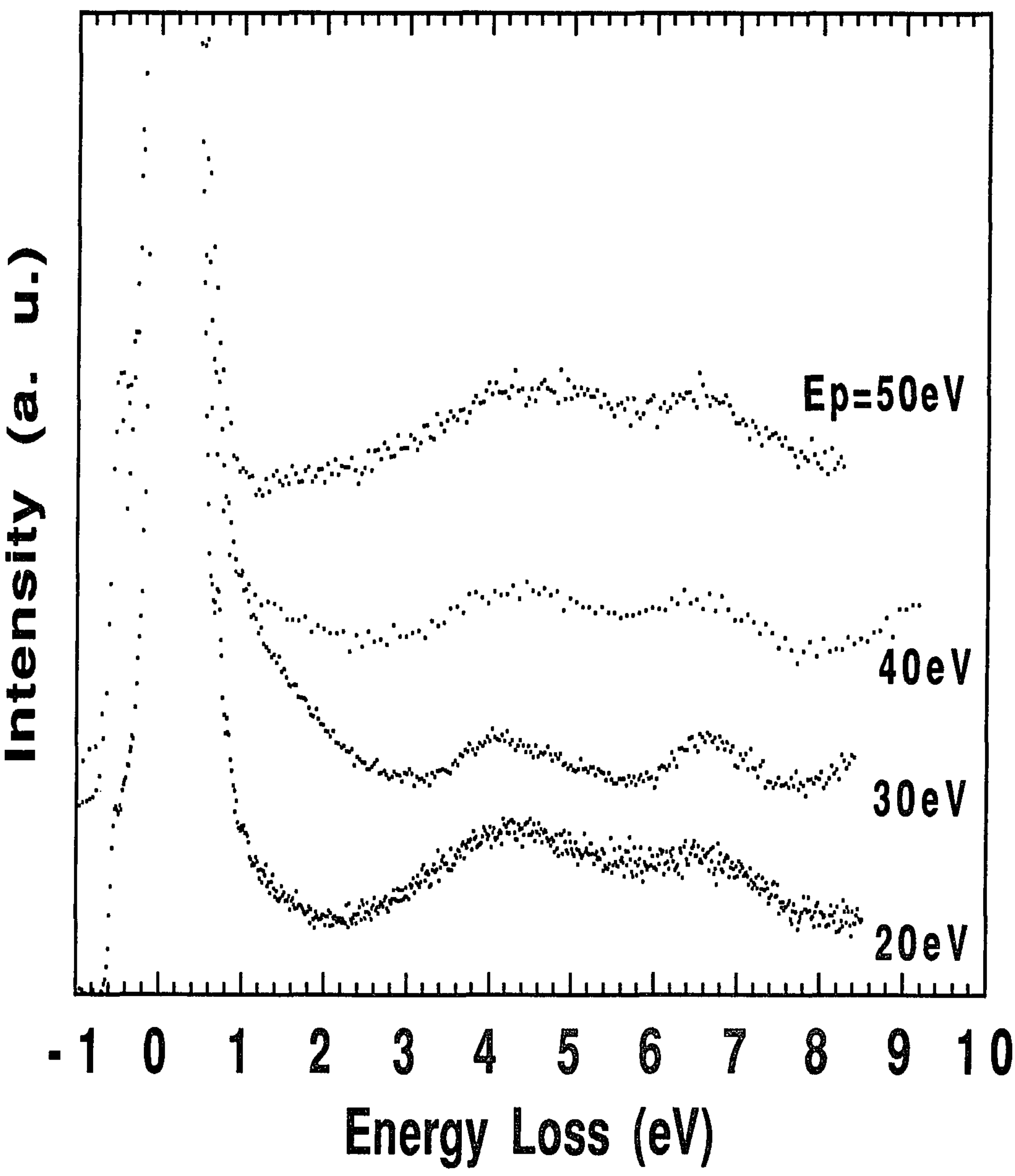

Figure 8.7 Angular resolved EEL spectrum as a function of low electron primary energies for Si(29Å)/C(14Å), the angle of incidence is equal to the angle of reflection=45°.

X-ray reflectivity results and discussions.

Measurements of the specular X-ray reflectivity give information on the electron density profile of the multilayers.[133] This information can be used to determine the composition profile of the sample. In our analysis we employed the method developed by Vidal and Vincent[133] to fit the reflectivity data, in this case we assume a Gaussian type of roughness at the interface. The theoretical reflectivity is fitted to the experimental data to obtain information on the electron density composition of the layers and the normal roughness at the interfaces. We assume that the Si/C interface roughness is the same for all the layers. The C/Si interface is another parameter in the fit in particular for the sample heated to 873 K under UHV conditions. The top and substrate roughness are assumed to be independent parameters. Since the samples are exposed to ambient conditions during the measurements the top most layer will have a significantly different electron density.

The theoretical fit is valid over all angles since we are solving the full dynamical problem, no kinematic approximation was taken. In our measurements we select an X-ray energy of 24.5 keV in order to neglect absorption effects.

In Figure 8.8 we show the X-ray specular reflectivity for **sample 1** which consists of 30 bilayers of [Si(10Å)/C(19Å)] on α- Al_2O_3. In the analysis of the data, the thickness of the bilayers Λ is assumed to be linearly decreasing from the substrate to the top layer with $\Delta\Lambda/\Lambda \approx \pm$ 7% and the thickness ratio d_{Si}/d_C is kept as a constant. This was found to give the best fit to the experimental data. The roughness

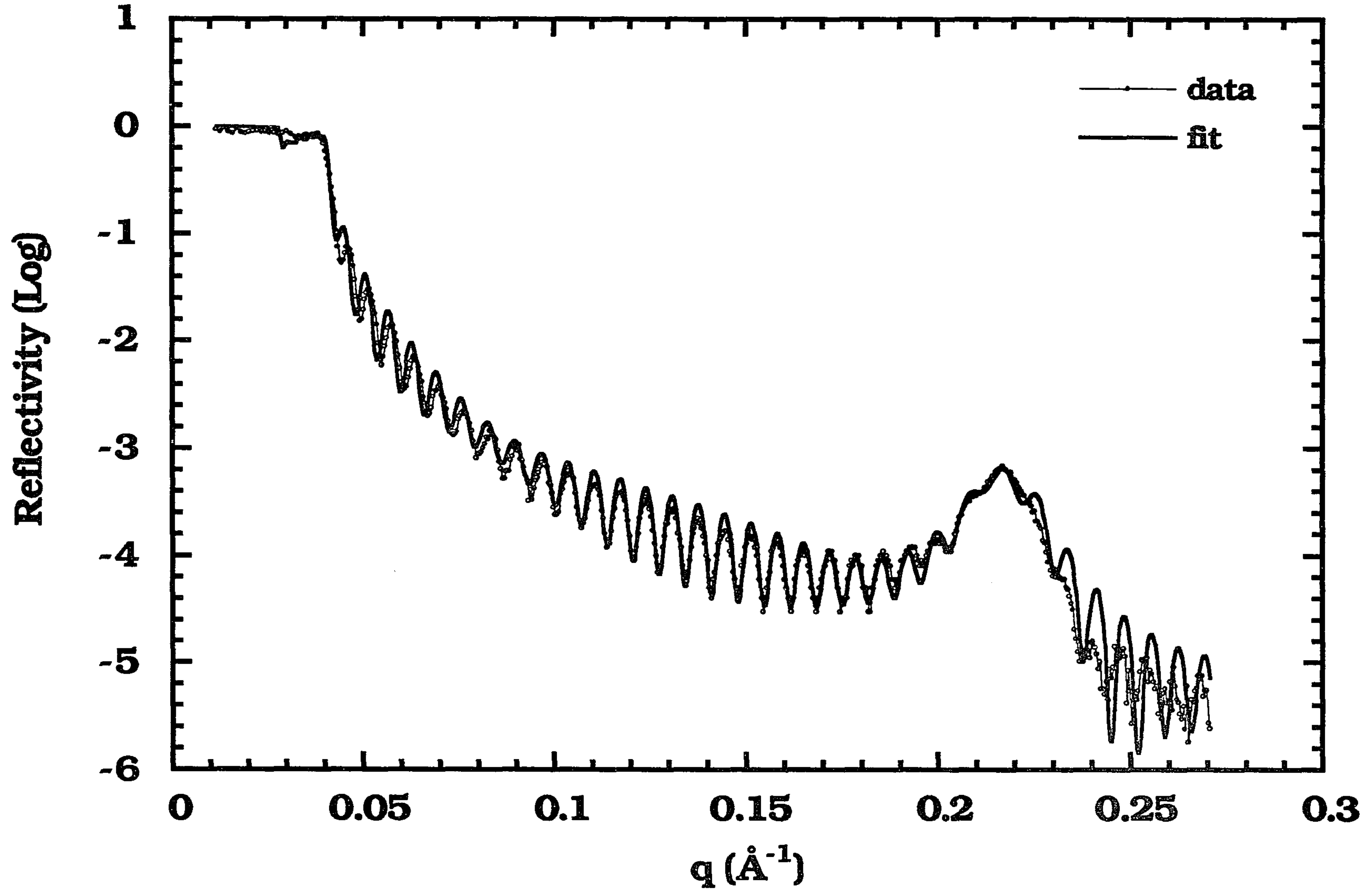

Figure 8.8 X-ray specular reflectivity for the Si(10Å)/C(19Å). The full line is the theoretical fit to the data.

between silicon and carbon, and the electron density of silicon and carbon are assumed to be as a constant throughout all the 30 layers. It was necessary to add an extra topmost thin layer with very low electron density to achieve a good fitting to the data. By introducing the top layer, one can also reproduce a weak node in the reflectivity spectrum $q=0.075Å^{-1}$ in Figure 8.8. Figure 8.8 shows the experimental data and the best fit. The thickness of the topmost layer is in 35.0 Å and its electron density is $0.46(6.022x10^{23}$ e/cm$^3)$. The data and the fit are represented by the closed circles and the solid line respectively. Fitting is almost perfect up to the first Bragg peak position due to the modulation structure near $q \approx 0.21Å^{-1}$. The secondary fringes due to the interference of reflectivity waves between the substrate and the total thickness of the multilayers match very well, regarding both angle and intensities. The position of the critical angle and Bragg peaks give information of electron density contrast of the first few top layers, and modulation wavelength respectively. Those are accurately determined by this fitting. The node shape at $q=0.075Å^{-1}$ can also be recovered in this fitting curve. Attempts to fit the data without a low electron density top layer gave a poor fit to the data. Divergence of the incident X-ray beam was found to be $\Delta\theta \approx 0.005^0$ and was taken into consideration in the analysis of the data. The variation in the total thickness was introduced in the analysis of the data by assuming a Gaussian function with standard deviation σ_D. The relation used in the analysis was $R_T(\Theta) = \int g(D)R(\Theta,D)dD$, where g(D) is a gaussian function, R(Θ,D) is the reflectivity at an angle of incidence Θ, and D is the total thickness of the multilayer. This relation

take into consideration the variation in total thickness of the sample and the best fit was accomplished with σ_D =10 Å.

The parameters of thickness and electron density in individual layers are shown in Table 8.2 and Figure 8.9. Figure 8.10 illustrate the structure of multilayer near the substrate with the interface roughness obtained from the fit. The electron density of silicon and carbon are about 3% and 15% less than its nominal bulk value respectively. The roughness at the silicon interface is only 0.5Å indicating a very sharp interface in the Si/C multilayers, partly because of amorphous nature of Si and C. Such a multilayer with a small interface roughness is an important physical systems. It is an ideal model for study the nature of interface bonding and roughness. It has important implications in terms of the mechanism of thin film growth.

Table 8.2

Parameters obtained from the fitting of the experimental data for the Si(10Å)/C(19Å) multilayer.

Materials	Thickness d(Å)	Interface Roughness σ (Å)
α-Al_2O_3	∞	0.8
Si	10.0	0.5
C	19.4	0.5
Topmost	35.0	4.0

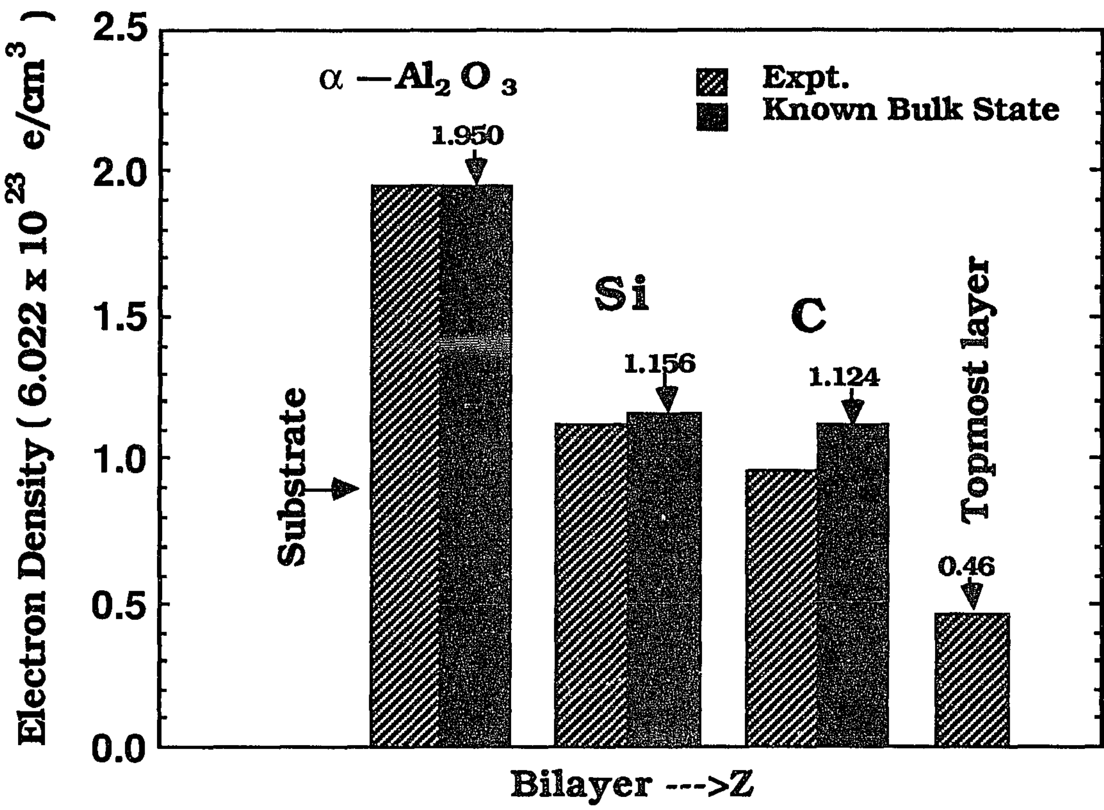

Figure 8.9 A comparison of electron density between the known bulk state and the experimental state. The experimental electron densities of Si, C and topmost layer are from the parameters used to obtain fit in Figure 8.8. The electron densities of Si, and C are about 3%, and 15% less than the known bulk state respectively.

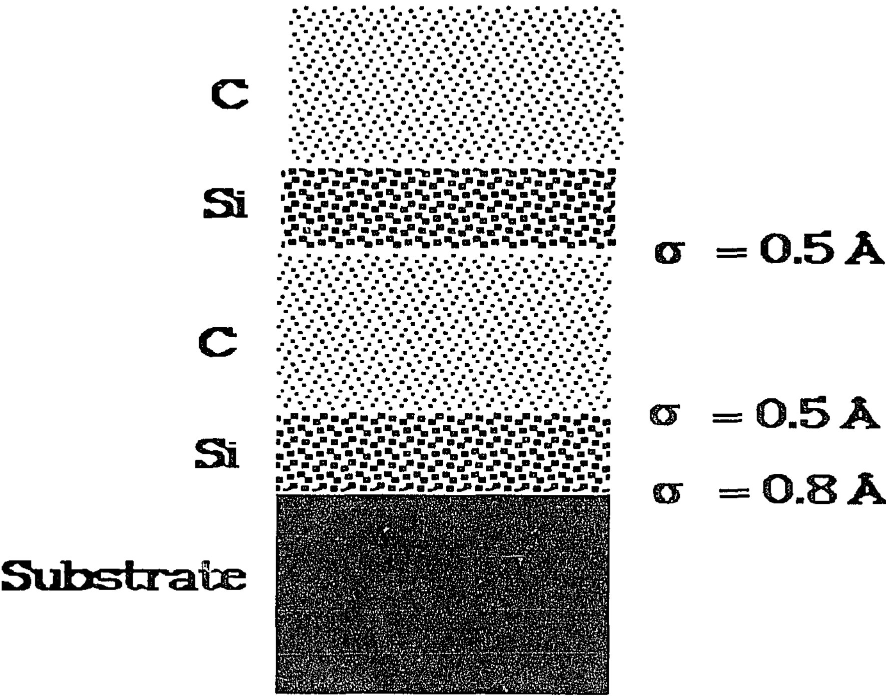

Figure 8.10 Schematic diagram of the Si(10Å)/C(19Å) multilayer near the substrate with interface roughness values.

The second multilayer (**sample 2**) originally consisted of 30 bilayers of Si(25Å)/C(25Å) on the α-Al_2O_3 that was heated up to 873 K under UHV conditions. In the analysis of the data the thickness of the bilayers Λ is found to be monotonically increasing from the substrate up to two third of the total thickness, about $\Delta\Lambda/\Lambda \approx 13\%$ and then decreasing slightly by 0.5% up to the top layer. The thickness

ratios were kept constant during the analysis. The total thickness standard deviation obtained was σ_D=15 Å, we employed the same methodology in this analysis as in sample #1.

In Figure 8.11 we show the X-ray reflectivity measurements for this sample. The plot in Figure 8.10 includes the first Bragg peak due to the multilayer spacing, the theoretical fit is also shown. In this case it was absolutely impossible to fit the data without the presence of a silicon carbide interface. This observation was independently corroborated by electron energy loss spectroscopy.

SiC layers were formed as the result of an interface reaction during heating of the sample. The structure now consists of 30 bilayers of [Si(12Å/SiC(10Å)/C(13Å/SiC(10Å)]. The interface roughness between Si and SiC, between SiC and C are kept constants respectively throughout the film in the fit of the data. The electron densities of Si and C are also kept constants for all the layers. Figure 8.11 shows the experimental data and its best fit. The data and the fit are represented by the closed circles and the solid line respectively. Fitting is almost perfect from the region of critical angle $q \approx 0.04Å^{-1}$ to $0.12Å^{-1}$, which is just before the first Bragg peak. A good agreement is observed between theory and the experiment for the secondary fringes due to the interference of the reflected waves from the substrate and the total thickness of the multilayers. In the region of $q \approx 0.12Å^{-1}$ to $0.15Å^{-1}$ there is slightly discrepancy between the data and the fit. Beyond the Bragg position, the good fit recovered again. A surprising result is that in spite of the chemical reaction result at interface the modulation structure is well preserved with larger roughness between Si and SiC.

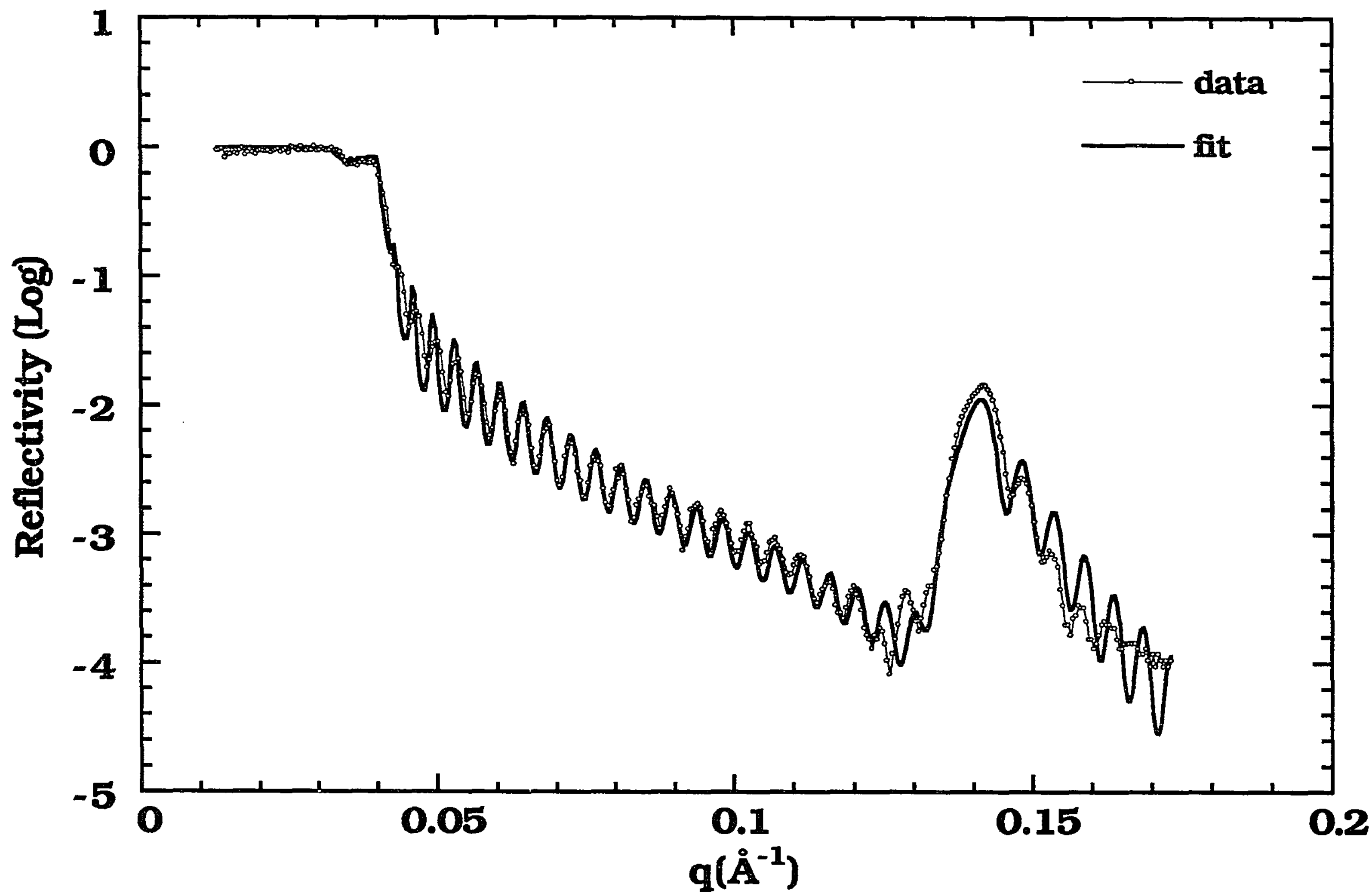

Figure 8.11 X-ray specular reflectivity of 30 bilayers of [Si(12Å/SiC(10Å)/C(13Å)/SiC(10Å)] on α-Al_2O_3. The solid line is the theoretical fit to the data.

The thickness and electron density parameters for the individual layers are shown in Table 8.3 and Figure8.12. Figure 8.13 illustrates the structure of Si/C multilayer near the substrate with the interface roughness values obtained from the fit. The electron density of Si, SiC and C are about 2%, 3% and 15% less than their nominal bulk values. The roughness at the Si/SiC interface is σ =5.0 Å. On the other hand the roughness at the SiC/C interface is only 0.5Å. This result suggests that Si is more reactive than the C at such temperatures. The roughness between Si and substrate, α-Al_2O_3 is also very large (13.0Å), this is due to the large chemical reactivity at the substrate interface during heating of the sample. We did not observed the presence of a low density top layer on this sample. This is attributed to the sample heat treatment to 873 K under UHV conditions, probably the desorbing the surface contaminants.

Table 8.3

Parameters obtained from the fitting of the experimental data for the Si(25Å)/C(25Å) multilayer after reaction at 873 K.

Materials	Thickness d(Å)	Interface Roughness σ (Å)
α-Al_2O_3	∞	13.0
Si	12.1	5.0
SiC	10.1	0.5
C	13.1	0.5

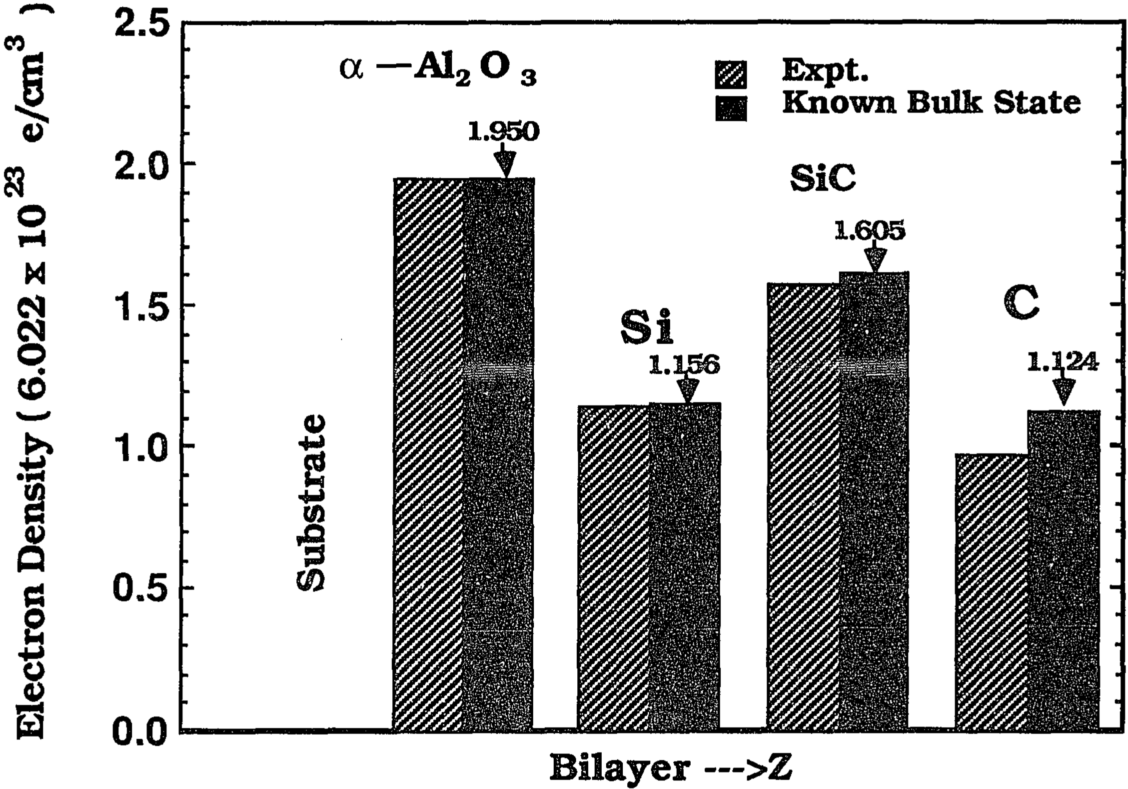

Figure 8.12 A comparison of electron density between the known bulk state and the experimental state. The experimental electron densities of Si, SiC and C are from the parameters used to obtain fit in Figure 8.11. The electron densities of Si, SiC and C are about 2%, 3% and 15% less than the known bulk state respectively.

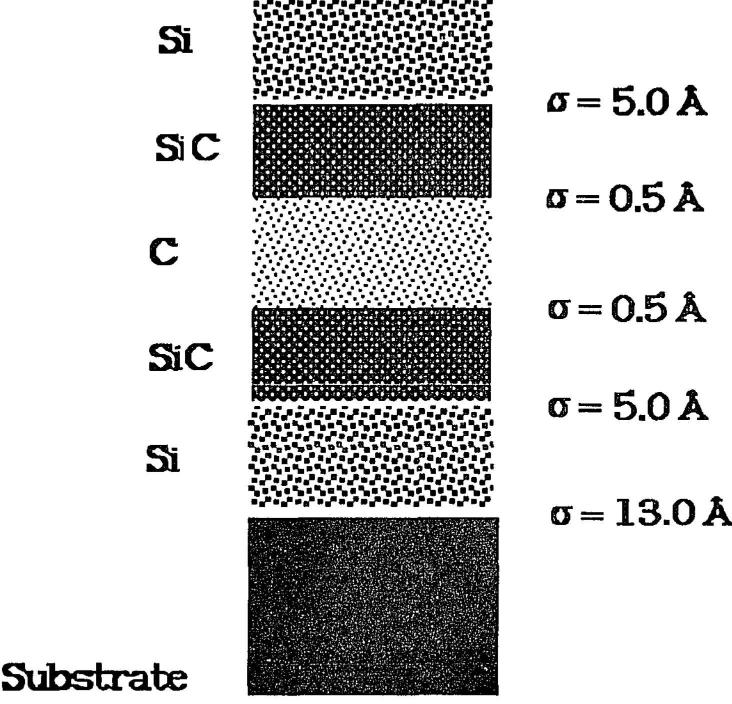

Figure 8.13 Schematic diagram of the Si(25Å)/C(25Å) multilayer near the substrate with the values of the interface roughness.

The third sample consists of 30 bilayers of [Si(29Å)/C(14Å)] on SiO_2. In this fitting, the thickness of the bilayers Λ is assumed to be linearly decreasing from the substrate and then linearly increasing until to the top layer. The variation of the$\Delta\Lambda/\Lambda$ is ± 7%. The rougnhess

between silicon and carbon, and the electron density of silicon and carbon are assumed to be as a constant throughout all the 30 layers.

Figure 8.14 shows the experimental data and its best fit with angle divergence around 0.0125^0 and the standard total thickness deviation σ_D about 60 Å. The data and the fit are represented by the closed circles and the solid line respectively. The secondary fringes due to the interference of reflectivity waves between the substrate and the total thickness of the multilayers can not be observed in this sample.

The parameters of thickness and electron density in individual layers are shown in Table 8.4 and Figure 8.15. Figure 8.16 illustrates the structure of Si/C multilayer near the substrate with the interface roughness obtained from the fitting. The electron density of silicon and carbon are about 2% and 9% less than its nominal bulk value respectively. The roughness at the interface is very large compared with sample 2, and 3. The sample prepared on a float glass substrate shows X-ray specular reflectivity characteristic of samples with considerable mixing at the interface. Although they can be fitted with our theoretical dynamical models the information on the interface composition is not as definite as in the case of the multilayers grown on sapphire.

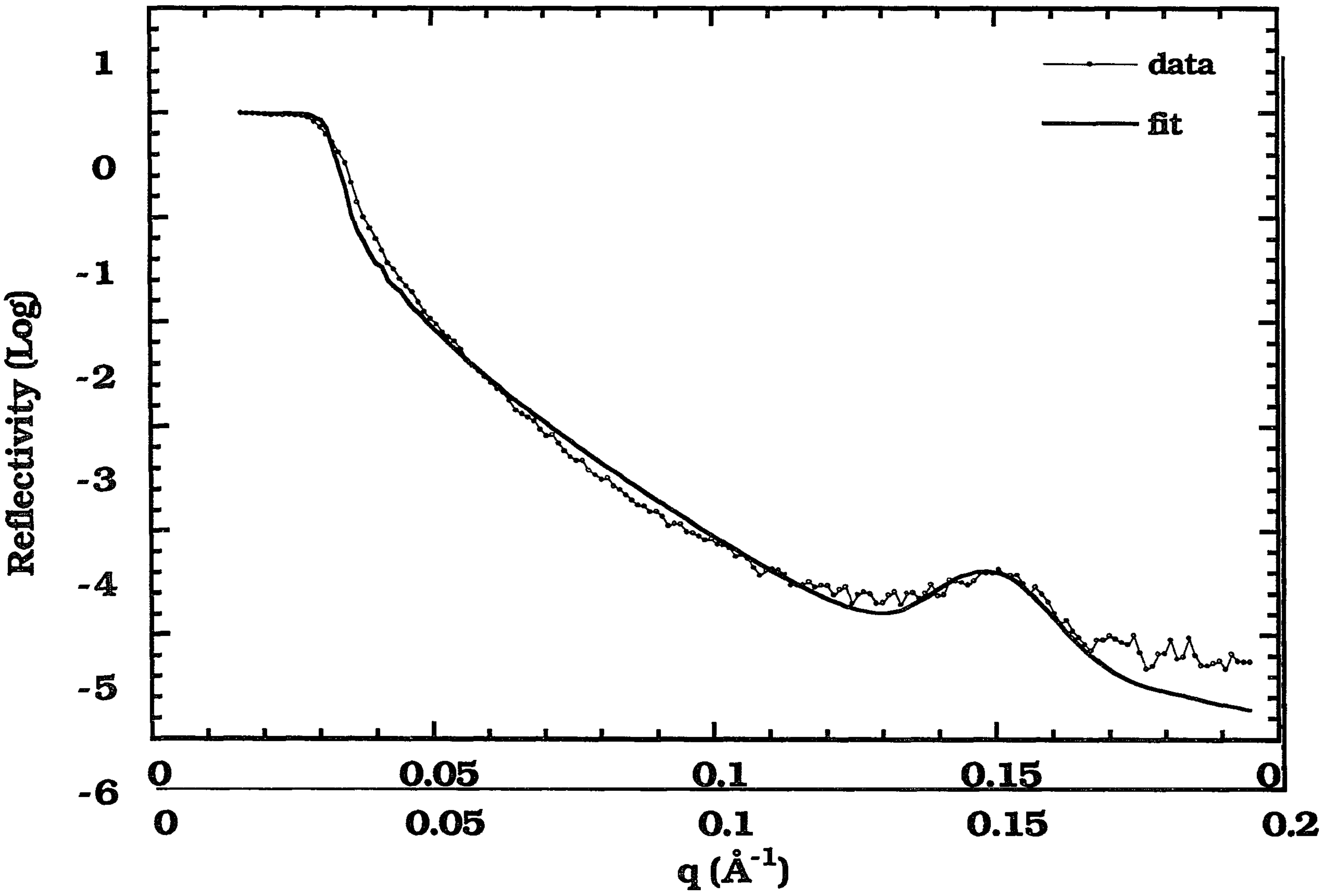

Figure 8.14 Low angle X-ray specular reflectivity of 30 bilayers of a [Si(29Å)/C(14Å)] on float glass. The solid line is the theoretical fit to the data.

Table 8.4.

Parameters obtained from the fitting of the experimental data for the Si(29Å)/C(14Å) multilayer.

Materials	Thickness d(Å)	Interface Roughness σ (Å)
SiO_2	∞	0.3
Si	28.53	12.3
C	13.99	10.3

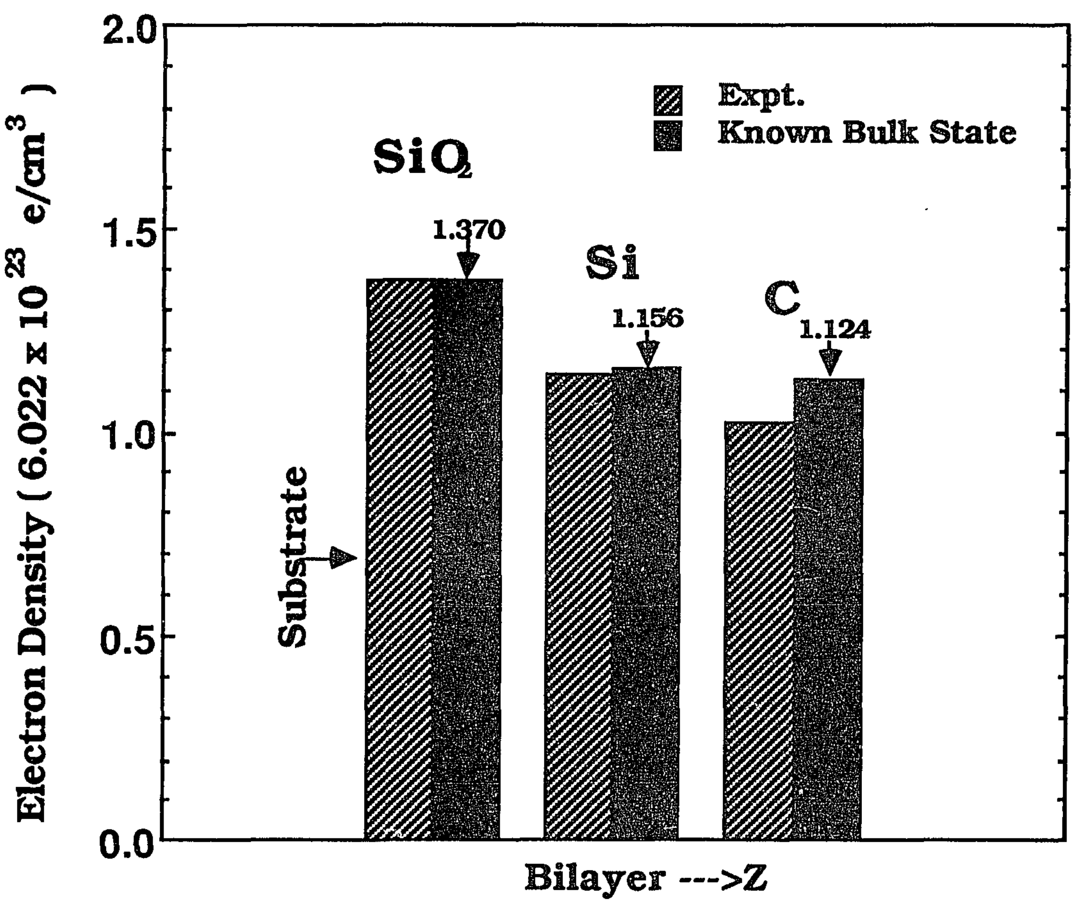

Figure 8.15 A comparison of electron density between the known bulk state and the experimental state. The experimental electron densities of Si, and C are from the parameters used to obtain fit in Figure 8.14. The electron densities of Si, and C are about 2%, and 9% less than the known bulk state respectively.

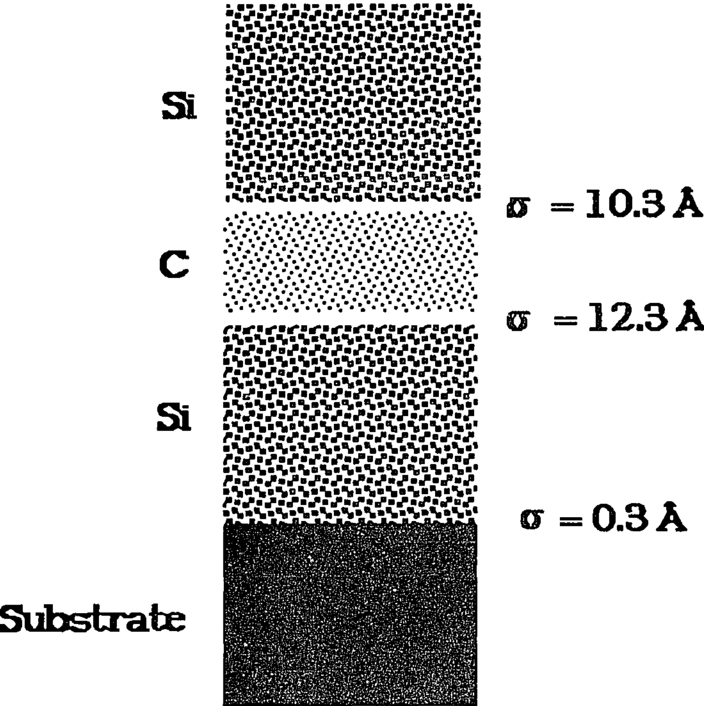

Figure 8.16 Schematic diagram of the Si(29Å)/C(14Å) multilayers near the substrate with the values of the interface roughness.

CHAPTER 9

CONCLUSIONS

9.1 W/C Multilayers

We have studied the interface structure of W/C multilayers using a number of diverse techniques. We were able to identify all the major electron energy losses in the multilayers. The W/C multilayers show the presence of a carbidic interface. The interface thickness grew in an irreversible fashion above 873° K. After the oxygen reaction, the graphitic layers are strongly reduced, and the carbidic phase are dominates in the AS and the EEL spectra. The carbidic interface was identified as W_2C. This interface and the multilayer structure shows good thermally stability in the presence of oxygen up to 773 K.

9.2 Single crystal TiC[111]

The observed EEL spectra in this work are in good agreement with the optical loss function. The EEL spectra for TiC [111] have been analyzed using the [LMTO] density-of states calculations. The theoretical DOS was used to identify the most probable intra/inter band transitions. The major electron energy loss peaks were identified as interband transition, (surface, bulk) plasmon excitations and core resonance - excitations. The temperature dependence of the energy losses show evidence of a variation in the surface electronic structure compared to the bulk of the material. The surface structure of the material shows evidence of the formation of defects at high temperatures. Ethylene bonding to the clean TiC surface was found to be very weak. The reaction with small amounts of oxygen leads to the formation of an intermediate surface oxide.

9.3 Ti/C Multilayers

We have used X-ray specular reflectivity and RBS to study the compositional profile and interfaces of the Ti/C multilayers. We have experimentally observed that there is a small amount of oxygen within the sample. The strongly alpha particles energy dependence specified that the oxygen distributed deeply inside the sample. The great affinity of titanium towards oxygen made us believe that oxygen could only exist with a titanium-oxide state in the carbon-titanium interface. This conclusion is consistent with the AES and EELS measurement.[118 212] Due to the similarity in electron densities, we cannot detect this oxidation using the X-ray reflectivity. From the X-ray reflectivity analysis, we can infer that the titanium layers have a bulk metal character, the carbon layers show a graphitic behavior. The interface does not have significant Ti-C bonding but has a graphite like atomic arrangement rather than a carbide like arrangement.

9.4 α-SiC-6H[0001]

We have used a diverse number of techniques to study the surface composition of α-SiC at high temperatures. We were able to identify all major electron energy losses in the spectra of silicon carbide. There was clear evidence of carbon migration to the surface during heating of the sample under UHV conditions. This phenomenon occurs at rather low temperatures, around 573 K. Consequently, the formation of carbon vacancies in the bulk occurs at low temperatures. At such temperatures Si evaporation is not probable. We also found evidence that oxygen can migrate into the

bulk and form oxide inclusions. We think that carbon vacancies in conjunction with surface porosity can promote such an oxidation. It is noted that in our experiments the oxidation characteristics are dependent on the history of the sample (purity, presence of protecting surface oxide, etc).

9.5 Si/C Multilayers

We have prepared Si/C multilayers of various thicknesses. Samples grown on sapphire substrates show smoother interfaces than those prepared on SiO_2. We have used AS, EELS and AREELS to study the variation in electronic structure of the Si/C multilayers. We were able to identify all major electron energy losses in the spectra of the multilayers. The values of the electron energy losses were estimated from the dielectric functions calculations for graphite, silicon and alpha-silicon carbide. There is evidence from our measurements that an interface of silicon carbide is formed in the multilayers. This phenomenon probably occurs during preparation of the multilayers and/or during heating.

We have studied the interfaces of Si/C multilayers grown on α-Al_2O_3. The samples grown on sapphire substrates show very smooth interfaces. We have used X-ray specular reflectivity to study the compositional profile of the Si/C multilayers. We were able to identify the structure of the multilayers interface. We also found the formation of silicon carbide at the interface silicon-carbon after the multilayer is heated in UHV to 873 K. The silicon carbide is formed in the multilayer during heating by interdiffusion of carbon and silicon. These observations are in good agreement with electron energy loss

measurements in the same systems. There is evidence that the Si layer is more reactive than the carbon layer since it also reacted with sapphire substrate.

Appendix A

Structure Factor and Dielectric Function

Image that the electrons system of the sample is perturbed by an external electrostatic potential which couples to the electron charge density through the interaction

$$H' = \int \rho(r)\phi_{ext}(r,t)d^3r \,. \qquad \text{........ A.1}$$

The electrostatic potential could be produced by the injecting electrons. The induced electron density can be calculated by using Kubo's[134] perturbation and response function theory. The results is

$$\rho_{ind}(r,\omega) = \frac{1}{2\pi}\int_{-\infty}^{\infty} \exp(i\omega t)\rho_{ind}(r,t)dt$$

$$= \int F(r,r',\omega)\phi_{ext}(r',\omega)d^3r' \,, \qquad \text{........ A.2}$$

where $F(r,r',\omega)$ is the response function and is described by

$$F(r,r'\omega) = -i\int_0^{\infty} \exp(i(\omega+i\delta t)\langle[\rho(r,t),\rho(r'0)]\rangle dt \,\cdot \qquad \text{........ A.3}$$

The Fourier transformation of Eq. A.2 yields

$$\rho_{ind}(q,\omega) = F(q,\omega)\phi_{ext}(q,\omega) \qquad \text{........ A.4}$$

where

$$F(q,\omega) = -i\int_0^{\infty} \exp(i(\omega+i\delta t)\langle[\rho_q(t),\rho_{-q}(0)]\rangle dt \,\cdot \qquad \text{........ A.5}$$

It is well known that the $\phi_{ind}(r,\omega)$ can be expressed as follows:

$$\phi_{ind}(r,\omega)=\int\frac{\rho_{ind}(r,\omega)}{|r-r'|}d^3r' \;. \qquad \text{A.6}$$

By using Eq. A.2, the Fourier transformation in momentum space of Eq. A.6 is given by:

$$\phi_{ind}(q,\omega)=\frac{4\pi}{q^2}F(q,\omega)\phi_{ext}(q,\omega) \;. \qquad \text{A.7}$$

From the definition of the dielectric function and a little mathematical arrangement, we can have

$$\frac{1}{\varepsilon(q,\omega)}=\frac{E(q,\omega)}{D(q,\omega)}=\frac{\phi_{total}(q,\omega)}{\phi_{ext}(q,\omega)} \;. \qquad \text{A.8}$$

By using Eq. A.7 and $\phi_{total}=\phi_{ind}+\phi_{ext}$, the dielectric function in the q space is given by:

$$\frac{1}{\varepsilon(q,\omega)}=1+\frac{4\pi}{q^2}F(q,\omega) \;. \qquad \text{A.9}$$

In Eq. A.9, the imaginary part of $1/\varepsilon(q,\omega)$ should equal the imaginary part of $F(q,\omega)$, then we can have the relation between the response function and the dielectric function:

$$-\mathrm{Im}(F(q,\omega)=\frac{q^2}{4\pi}\mathrm{Im}\left(\frac{-1}{\varepsilon}\right) \;. \qquad \text{A.10}$$

In order to find out the relation between $S(q,\omega)$ and $Im(-1/\varepsilon)$, we derive the relation between $S(q,\omega)$ and $F(q,\omega)$.

Suppose that we have a complete set of states for an interacting system in thermal equilibrium. $S(q,w)$ can be described in terms of these system and their energies

$$S(q,\omega) = \frac{1}{2\pi\hbar}\int_{\infty}^{\infty} e^{i\omega t}\, S(q,t)dt$$

$$= \sum_{l_o,\,l} \frac{1}{2\pi\hbar}\int_{-\infty}^{\infty} e^{i\omega t}\, e^{-\beta E_{lo}} \langle l_o| n_q | l\rangle e^{i(E_{lo} - E_l)t/\hbar} \langle l | n_{-q} | l_o\rangle\, dt$$

$$= \sum_{l_o,\,l} \frac{1}{\hbar}\, e^{-\beta E_{lo}} |\langle l_o| n_q | l\rangle|^2\, \delta(\omega + \frac{E_{lo} - E_l}{\hbar}) \;. \qquad \text{........ A.11}$$

{where $\beta = 1/kT$}

The correlation function can be expressed in a similar way

$$T(q,\omega) = \frac{1}{2\pi\hbar}\int_{\infty}^{\infty} e^{i\omega t}\, T(q,t)dt$$

$$\equiv \frac{1}{2\pi\hbar}\int_{-\infty}^{\infty} e^{i\omega t}\, e^{-\beta E_{lo}} \langle n_{-q}(0)\, n_q(t) \rangle\, d$$

$$= \sum_{l_o,\,l} \frac{1}{\hbar}\, e^{-\beta E_{lo}} |\langle l_o| n_{-q} | l\rangle|^2\, \delta(\omega + \frac{E_l - E_{lo}}{\hbar}) \;. \qquad \text{........ A.12}$$

When interchanging the dummy indices l and l_o, we have

$$T(q,\omega) = e^{-\beta h\omega}\, S(q,\omega) \qquad \text{........ A.13}$$

With this relation (Eq. A13) and the Eq. A.5, we can determine the

relation between response function $F(q,\omega)$ to the structure factor $S(q,\omega)$. The result is :

$$F(q,\omega) = -ie^2\int_0^{\infty} e^{i(\omega + i\delta)t}\left\langle [n_q(t),\ n_{-q}(0)] \right\rangle dt$$

$$= -ie^2\int_0^{\infty} e^{i(\omega + i\delta)t}\ (S(q,t)\ -\ T(q,t))dt$$

$$= -ie^2\int_0^{\infty} e^{i(\omega + i\delta)t}\int_{-\infty}^{\infty} e^{i\omega' t}(S(q,\omega')-T(q,\omega'))dt\ d\omega'\ .$$

.... A.14

After the time integral, the response function $F(q,\omega)$ is given by:

$$F(q,\omega)= e^2\int_{-\infty}^{\infty} \frac{S(q,\omega')-T(q,\omega')}{\omega - \omega' +i\delta}d\omega'$$

$$= e^2\int_{-\infty}^{\infty} \frac{(1-e^{-\beta\omega'})S(q,\omega')}{\omega - \omega' +i\delta}d\omega'$$

$$= e^2 S(q,\omega)i\pi(1-\ e^{-\beta\omega})\ .$$

.... A.15

And $S(q,\omega)$ can then be expressed:

$$S(q,\omega) = \frac{-Im(F(q,\omega))}{e^2\pi(1-\ e^{-\beta\ \hbar\omega}\ )}\ .$$

.... A.16

For the special case, when $\beta\hbar\omega>>1$, the structure factor is given by:

$$S(q,\omega) = \frac{-Im(F(q,\omega))}{e^2\pi}\ .$$

.... A.17

Finally, by combining Eqs. A.10 and A.17, the relation between

structure factor $S(q, \omega)$ and the dielectric function $Im(-1/\varepsilon)$ is given by

$$S(q,\omega) = \frac{q^2}{4e^2\pi^2} Im\left(\frac{-1}{\varepsilon(q,\omega)}\right) . \qquad \text{......... A.18}$$

Appendix B

Energy- band structure of a single two dimensional layer of graphite calculated by Painter and Ellis, Ref. [82].

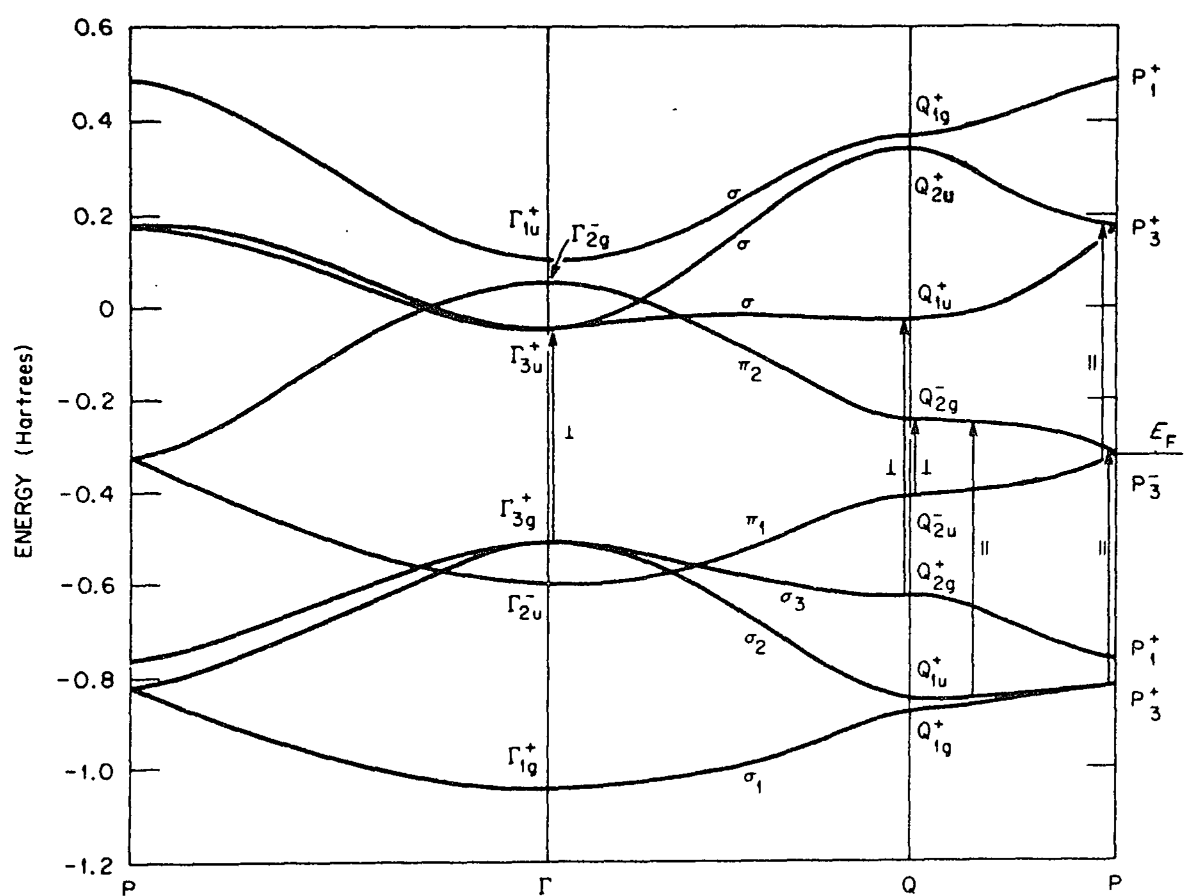

BIBLIOGRAPHY

1. David L. Price and Bernard R. Cooper, Phys. Rev. B39, No. 8, 4945(15, Mar. 1988).

2. J. H. Underwood, T. W. Barbee Nature 294, 429(1981).

3. I. Lovas, W. Santy, E.Spiller, R. Tibbetts, J. Wilczynsk, Proc. SPIE, 316, 90(1980); E. Spiller in Scanned Image Microscopy, E. Ash, ed., Academic, New York (1980), Page 365.

4. R.- P. Haelbich in Scanned Image Microscopy E. Ash, ed., Academic, New York (1980), page 413.

5. R. Acosta, R. Rippstein, et al. National Synchrotron Light source Annual Report, p103(1988).

6. W. M. C. Yang, T. Tsakalakos and J. E. Hillard, J. of Appl. Phys. Vol. 48, No.3, 876(1977).

7. J. E. Hillard, AIP Conf. Proc (USA) No. 53, P407 16(1979).

8. D. Baral, J. B. Kettersin, and J. E. Hilliar, J. of Appl. Phys. 57(4), 1076(1985).

9. D. Wolf and J. F. Lutsko, Phys. Rev. Lett. 60, 1170(1988).

10. B. J. Thaler, J.B.Ketterson, J. E. Hillard Phys. Rev. Let. Nov., 41, No.5, P335-9 (31 July 1979).

11. "Transition Metal Carbides and Nitrides", by Louis E. Toth, Academic Press, New York, (1971).

12. "Int. Conference on Silicon- Carbide 1973", University of South Carolina.

13. R. W. Conn Sci. Am. 249(4), 60 (1983).

14. M. Kaminsky, R. Nileson, and P. Zschack, J. Vac. Sci. Technol. 20, 1304(1982).

15. G. E. Mc Guire, "Auger Electron Spectroscopy Reference Manual", Plenum Press. New York and London (1979).

16. C. C. Chang, Surface Sci. 25, 53(1971).

17. J. C. Riviere, Contemp. Phys. 14, 513(1973).

18. R. H. Williams, Contemp. Phys. 19, 389(1978).

19. C. C. Chang, Surface Sci. 23, 283(1970).

20. H. Raether: In "Solid State Excitation by Electrons", Springer Tracts in Modern Physics, Vol.38, P.85 (Springer-Berlin 1965).

21. J. Geiger, Elektronen und Festkorper, Vol. 128 (Sammlung Vieweg, Braunshweig).

22. H. Boersch, H. Missner, W. Raith, Z. Phys. 168, 404(1962).

23. M. Creuzburg and H. Raether, Solid State Comm. Vol. 2 No. 11, 235-247(June, 1964).

24. R. Leapman, L. Grunes, and P. Fejes, Phys. Rev. B26, 614(19-81).

25. J.M. Ziman, "Principles pf the Theory of solids", Second Edition, Cambridge University Press, p163 (1986).

26. Ritche, R. H. Phys. Rev. 106, 874(1957).

27. S. E. Schnatterly, "Inelastic Electron Scattering Spectro-scopy", in solid state Physics Vol. 34, p275(1979).

28. P. M. Platzman and P. A. Wolf "Waves and Interactions in Solid State Plasmons", Supplement 13, Solid State Physics, Academic Press New York, 1973.

29. Stephen Gascorowicz, "Quantum Physics", John Wiley &Son, Inc. 1974, P.350.

30. J. E. Rowe and H. Ibach, Phys. Rev. Lett. 31 102(1973).

31. H.Ibach and J.E. Rowe, Phys. Rev. B9(4), 1951(1974).

32. H. Raether, "Excitation of Plasmons and Interband transition by Electrons", Springer Tracts in Modern Physics, Vol. 88, Springer, Berlin, (1980).

33. R. Ludeke and L. Esaki, Surf. Sci. 47, 132(1975).

34. D. F. Cox and G.B. Hoflund, Surf. Sci. 151, 202(1985).

35. E. Sickafus, Phys. Rev. B Vol. 6 No.10, 3714(15 Nov., 1972).

36. R. Ludeke and L. Esaki, Phys. Rev. Lett. 33, 653(1974).

37. E. Bauer, Z. Phys. 224, 19(1969).

38. N. R. Avery, surface science 111, 358-380(1981).

39. For more detail about the two steps process scattering picture, see: A.G. Nassiopoulos, and J. Cazaux, Surface Science 149, 313-325(1985); Surface Science 165, 203-220(1985).

40. C. Colavita, Phys. Rev. B. Vol. 25 No.4, 2490(15 Feb. 1982).

41. H. Araki, Phys. Rev. B Vol. 33 No.12, 8164(15 June, 1986).

42. Mohammed H. Mohammed, Phys. Rev. B Vol. 37 No.14, 8417(15 May, 1988).

43. F. Bassani, G. Pastori, and R.A.Ballinger "Electronic States and Optical Transitions in solids", Pergamon Press, Pg154.

44. D. E. Sayers, E. A. Stern, and F. W. Lytle, Phys. Rev. Lett. 27, 1204 (1971).

45. Boon K. Teo, "EXAFS: Basic Principles and Data Analysis", Springer-Verlag, Berlin Heidelberg New York, (1986).

46. Boon K. Teo: "EXAFS Spectroscopy", Plenum press, 1981.

47. M. DeCrescenzi, L. Papagno, G. Chiarello, R. Scarmozzino, E. Colavita and R. Rosei, Solid State Comm. 40, 613 (1981).

48. A. P. Hitchcock and C. H. Teng, Surface Science 149, 558 (1985).

49. S. H. Lin, Proc. R. Soc. London Ser. A 335, 51 (1973).

50. M. DeCrescenzi, G. Chiarello, E. Colavita, and R. Memeo, Phy. Rev. B, Vol. 29, No. 6, 3730(13 Mar. 1984).

51. Y. Taming a, M. F. C. Willemsen, F. H. P. Habraken and A. E. T. Kuiper, Nucl. Instr. and Mech. , 200, 499(1982).

52. Goldstein, H. "classical Mechanics" Addison Wesley, Reading, Massachusetts. 1959.

53. Wei-Kan Chu, James W. Mayer,Marc-A. Nicolet " Backscattering spectrometry", Academic Press, New York 1978.

54. John R. Cameron, Phys. Rev. Vol. 90, No. 5, 839(1, Jun,-1953).

55. Max Born, Emil Wolf, “Princiles of Optics”, Pergamon Press, 1959.

56. I. M. Tidswell, B. M. Ocko, P. S. Pershan, S. R. Wasserman, G. M. Whitesides, and J. D. Axe, Phys. Rev. B41, 1111 (1990).

57. Heavens, P. S. “Optical Properties of Thin Film”, Dover, New York, 1965.

58. J. P. Hannon, N. V. Hung, G. T. Trammell, E. Gerdau, M. Mueller, R. R ü ffer, Phys. Rev. B. Vol.32, 5068(15, Oct 1985).

59. R. Rohlsberger, Surface roughness and oxide layers of sputtered polycrystalline filmes, SPIE Vol. 1160 X-ray/EUV Optics for Astronomy and Microscopy, 26(1989).

60. Ti/C and W/C samples were prepared by I. K. Schuller, E. Ziegler.

61. Y. Lepetre, I. K. Schuller, G. Rasigni, R. Rivoria, R. Philip, and P. Dhez, Society of Photo-Optical Instrumentation Engineers, Proc. on Applications of Film Multilayered Structure to Figured X-ray Optics, 563, 258 (1985).

62. Si/C samples were prepared by H. Homma.

63. J. H. Underwood and D. T. Attwood, Physics Today 44 (1984).

64. Y. Lepetre, E. Ziegler, J. Appl. Phys. 60(7), 2301 (1986).

65. E. Ziegler, Y. Lepetre, and I. K. Schuller, Appl. Phys. Lett. 48(20), 10 (1986).

66. A. K. Petford-Long, J. Appl. Phys. 61(4), 1422 (1987).

67. "Tungsten and its Compounds", G. D. Rick, pg. 79-82 Pergamon Press Ltd. (1967).

68. R. B. Levy, M. Boudart, Science 10, 547 (1973).

69. L. H. Bennett, N. Erickson, Science 3, 563 (1974).

70. A. E. Newkirk, J. Amer. Chem. Soc. 77, 4521 (1955).

71. R. Kieffer and F. Kobbl J. Inorg. Chem. 262, 229 (1950).

72. E. Colavita, M. DeCrescenzi, L. Papagno, R. Scarmozzino, L. S.

Caputi, R. Rosei, and E. Tosatti, Phys. Rev. B 25(4), 2490 (1982).

73. G. Chiarello, E. Colavita, M. DeCrescenzi and S. Nannarone, Phys. Rev. B29(9), 4878 (1984).

74. J. R. Cameron, Phys. Rev. 90(5), 839 (1953).

75. R. W. Hill, Phys. Rev. 90(5), 845 (1953).

76. E. A. Taft and H. R. Philipp, Phys. Rev. 138(1A) (1965).

77. Edward D. Palik "Hand Book of Optical constant of Solids" (Academic Press, Inc), Tungsten(W) Table XII, P.555.

78. J. H. Weaver, C. G. Olson, and W. W. Lynch, Phys. Rev. B12(4), 1293 (1975).

79. P. E. Luscher, Surface Science 66, 167-188 (1977).

80. XPS [from C. M. Penchina, E. Sapp, J. Tejeda, and N. Shevchik, Phys. Rev. B10, 4187 (1974)] revealed that the N_{VI}, N_{VII} and O_{II} levels lie at 31.7, 33.9, and 46.3 eV respectively.

81. M. P. Seah and W. A. Dench, Surface and Interface Analysis, Vol. 1, No.1, 2(1979).

82. G. S. Painter and D. E. Ellis, Phys. Rev. B1, 4747 (1970).

83. R. F. Willis, B. Feuerbacher, and B. Fitton, Phys. Rev. 4(8), 2441(1971).

84. Ralph W. G. Wyckoff, "Crystal Structures Second Edition Volume 1", John Wiley & Sons, New York, 1960.

85. J. H. Westbrook and E. R. Stover, in "High - Temperature Materials and Technology (I. E. Campbell and E.M. Shrewood, des.) p.312. Wiley, New York, 1967.

86. V. Ern and A. C. Switendick, Phys. Rev. 137A, 1927 (15, March 1965).

87. Robert G. Lye and E. M. Logothetis, Phys. Rev. 147, 622 (15, July 1966).

88. James B. Conklin, JR. and Donald J. Silversmith, Int. J. Quantum Chem. Vol. IIs, 243 -255(1968).

89. J. F. Alward, C. Y. Fong, M. El - Batanouny, and F. Wooten, Phys. Rev. B. Vol. 12, No. 4, 1105(15 Aug. 1975).

90. H-R. Trebin and H. Bross, J. Phys. C:Solid state Phys. Vol.8, 1181(1975).

91. Hideo Ihara, Yukinobu Kumashiro, and Akio Itoh, Phys. Rev. B 12, No.12, 5465(15 Dec.1975).

92. A. Neckel, P Rastl, R Eibler, P Weinberger and K Schwarz, J. Phys. C 9, 579(1976).

93. A. Callenås, L. I. Johansson, A.N. Christensen, K. Schwarz annd J. Redinger, Phys. Rev. B 27, No. 10, 5934(15,May 1983).

94. A. L. Hagastrom, L. I. Johansson, S. B. M. Hagstrom, and A. Nørlund Christensen, Journal of Electron Spectroscopy and Related Phenomena, 11, 75-89(1977).

95. L. I. Johansson, P. M. Stefan, M. L. Shek, A. Nørlund Christensen, Phys. Rev. B 22, No.2, 6993(15 Nov. 1980).

96. David W. Fischer, Journal of Applied Physics, Vol. 41, 3922 (September 1970).

97. J. H. Weaver, A. M. Bradshaw, J. F. van der Veen, F. J. Himpsel, D. E. Eastman and C. Politis, Phys. Rev. B 22, No. 10, 4921(15 Nov. 1980).

98. L. I. Johansson, A. L. Hagstrom, B. E. Jacobson, S. B. M. Hagstrom, Journal of Electron Spectroscopy and Related Phenomena, 10, 259-271(1977).

99. S. Zaima, Y. Shibata, H. Adachi, C. Oshima, S. Otani, M. Aono, and Y. Ishizawa, Surface Science 157, 380-392 (1985).

100. A. Fujimori, Fijio Minami, and Nobuo Tsuda, Surface Science 121, 199-217(1982).

101. H. Raether, " Solid State Excitation by Electrons" , Springer Tracts in Modern Physics, Vol. 38, p93-94, Springer, 1965.

102. B. M. Biwer and S. L. Bernasek, Surface Science, 167, 207-230(1986).

103. C. J. Powell, Review of Modern Phys. Vol.48, No.1, (Jan.1976).

104. Worthington, C. R. and S. G. Tomlin, 1956, Proc. Phys. Soc. Lodon A 69, 401.

105. Bethe, H., 1930, Ann. Phys. 5, 325.

106. S. D. Bader, G. Zajac, A. J. Arko, M. B. Brodsky, T. I. Morrison, N. Zaluzec, J. Zak, R. L. Benbow and Z. Hurych, Phys. Rev. B 33, No. 6, 3636 (15 Mar. 1986).

107. G. Zajac, S. D. Bader, A.J. Arko, and J. Zak, Phys. Rev. B 29, No. 10, 5491 (15 May. 1984).

108. R. D. Bringans and H. Hochst, Phys. Rev. Vol. 30, No. 10, 5416(15 Nov. 1984).

109. J. Barth, F. Gerken and C. Kunz, Phys. Rev. B 31, No.4, 2022(15 Feb. 1985).

110. B. Sonntag, R. Haensel and C. Kunz, Solid State Comm. Vol. 7, p. 597-599,(1969).

111. "Electron Binding Energies for the Elements " Compiled by Gwyn P.Williams, National Sychrotron Light Source Brookhaven National Laboratory Upton, New York.

112. G. W. Simmons and E.J. Scheibner, J. Appl. Phys. 43, 693(19-72).

113. F. Pellerin and J.P. Langeron, Surface Sci. 126, 444(1983).

114. E. Bertel, Roger Stockbauer and Theodore E. Madey, Surface Sci. 141, 355(1984).

115. J. L. Robins and J.B. Swan, Proc. Phys. Soc. (London)76, 857 (1960).

116. P. E. Best, Proc.Phys.Soc.(London), 80, 1308(1962).

117. "Chemical Structure and Bonding", By Roger L. Dekock, and Harry B. Gray, Pg. 311, The Benjamin/ Cummings Publishing Company.

118. N.Thangprasert, P. A. Montano, D.L. Price, B.R. Cooper, E. Ziegler, I. K. Scheller, Y. Chan, H. S. Jin, D. Yan, and P. Lesser, Mat. Res. Soc. Symp. Proc. Vol. 122, 589-592(1988).

119. Identified from the line shape of the carbon AES (detailed information can be found from: N. Thangaparasert's Thesis,

West Virginia University).

120. International Conference on Silicon Carbide, University of South Carolina (1973).

121. W. J. Choyke and Lyee Patrick, Phys. Rev. Vol. 172, 769(19-68).

122. J. V. Shennan, Chem. Eng. Progr. Symposium, Series 80, 63 (1967).

123. Amorphous and Crystalline Silicon Carbide and Related Materials, Eds. G. L. Harris and C. Y. W. Yang, Springer Verlag Proceedings in Physics 34 (1989).

124. S. Adachi, M. Mohri and T. Yamashina, Surface Science 161, 479(1985).

125. J. J. Bellina Jr. and M. V. Zeller, Applied Surface Science 25, 380(1986).

126. F. Bozso, L. Muehlhoff, M. Trenary, W. J. Choyke, and J. T. Yates, Jr., J. Vac. Sci. Techn. A2(3), 1271 (1984).

128. R. Kaplan, Surface Science 215, 111 (1989).

128. A. H. Gomes De Mesquita, Acta Cryst. Vol. 23, 610(1967).

129. T. W. Barbee, in Procedings, Topical Conference on Low Energy X-Ray Diagnostics, AIP, NY (1980).

130. J. P. Henry, E. Spiller, and M. Weisskopf, Proc. Soc. Photo-Opt. Instrm. Eng. 316, 166 (1981).

131. J. G. Carter, R. H. Huebner, R. N. Hamm, and R. D. Birkhoff, Phys. Rev. 137, A639(1965).

132. D. L. Greenaway, G. Harbeke, F. Bassani, and E. Tosatti, Phys. Rev. 178, 1340(1969).

133. B. Vidal and P. Vincent, Applied Optics, 23, 1794 (1984). R. Rohlsberger et al, SPIE 1160, 26(1989).

134. R. Kubo, Can. J. Phys. 34, 1274(1956); J. Phys. Soc. Jap. 12, 570(1957).